Magnetisation of the Lunar Crust

Ruth Alexandra Carley

Thesis submitted for the degree of

Doctor of Philosophy

The University of Edinburgh

2010

Declaration

I declare that this thesis has been composed solely by myself and that it has not been submitted, either in whole or in part in any previous application for a degree. Except where otherwise acknowledged, the work presented is entirely my own.

Ruth A. Carley

May 16th 2011

Abstract

The Moon displays weak magnetic fields resulting from areas of the lunar crust that are remanently magnetised. The origins of the magnetic fields that produced this remanent magnetisation are still under discussion, and theories include among several, an ancient lunar dynamo, or processes occurring on the Moon as a result of impacts. Lunar crustal fields have been mapped globally by the Magnetometer (MAG) and Electron Reflectometer (ER) on the satellite Lunar Prospector, providing vector magnetic field measurements at an average altitude of 30 km, and estimates of the total surface field.

This thesis presents global and regional models of the magnitude and direction of lunar magnetisation within a layer, produced from both the MAG and ER data independently and jointly using several inversion methods. The inverse modelling techniques are based on those developed for terrestrial and Martian data sets, employing equivalent source dipoles as basis functions, and Green's functions relating a magnetic field observation to a spatially continuous magnetisation distribution. A unique magnetisation solution is selected having the smallest root-mean-square (RMS) magnetisation for a given fit to the data, controlled by a damping parameter. The non-uniqueness in magnetisation distributions and the determination of source parameters is discussed with the use of forward models to assist the interpretation of the crustal magnetisation models.

Suites of magnetisation models for layers with thicknesses between 10 and 50 km, and with different dipole depths, are able to reproduce both the ER and MAG data well. Inverse models utilising the scalar ER data have been developed successfully, resulting in a joint inversion of the ER and MAG data for one of the strongest magnetic anomalies on the Moon, Reiner Gamma.

The largest concentrations of strongly magnetised crust are, like the crustal fields themselves, located antipodal to the youngest large impact basins, and in some isolated areas associated with the strongest crustal fields. The magnetisation distributions show robust magnitudes with different data sets and modelling

techniques showing the extent of magnetised sources, but can not be used to infer the direction of the magnetising fields. Average magnetisation values in magnetised regions of 30-40 mA/m are similar to the measured magnetisations of the Apollo samples and significantly weaker than crustal magnetisations for Mars and the Earth. A global preference for a 30 km thick magnetised layer suggests that a dynamo field may be more consistent with these magnetisation models.

The magnetisation models in this thesis are the first global magnetisation models for the Moon, and the first to combine the vector MAG and the scalar ER data. These magnetisation models can be used to predict the crustal contribution to the lunar magnetic field environment at a particular location, and in the absence of reliable sample returns, provide valuable information on the magnitude of lunar crustal magnetisation.

Acknowledgements

This research was funded by the Natural Environment Research Council (NER/S/A/2006/14230), and I am grateful for this investment, including funding my visit to NASA Goddard Space Flight Center and several conferences.

While my declaration stands true, I would not have been able to carry out this research without the advice and support of many people. Firstly I would like to thank Kathy Whaler for her professional support and friendly nature. I am grateful for her 'door always open' policy and putting up with my many visits and questions throughout the duration of this research and the production of this thesis. Thanks also go to Mike Purucker for his part in the set up of this project and the provision of data and advice, and to Jasper Halekas for allowing access to the ER data. I would also like to thank my examiners Andrew Curtis and Benoit Langlais for their comments and helpful suggestions for the improvement of this thesis.

Many people have given me help and advice with my computing issues and I would specially like to thank the wonderful IT team of the Grant Institute, Roger Hipkin and Ciaran Beggan among several for advice with code writing, and Wyn Williams and Paul Palmer for the use of their machines.

My family and friend are always a great source of support and encouragement, and I would like to thank my parents for their love and patience, and putting up with my long absences. Thanks also go to my housemates Hanna and Vesna, and to Martyn, and my 'desk buddy' Louise, for their companionship.

And finally, a big thank you to ALL the staff and PhD students in the Grant Institute (too many to list!) and School of GeoSciences where this research was carried out, for providing a friendly and fun working environment.

Contents

List of figures……...xi
List of tables…….…..xix
Acronyms……..….xxi

Chapter 1: Introduction **1**

1.1 Magnetic fields on planetary bodies……...2
1.1.1 Dynamo fields…….....2
1.1.2 Induced fields ……..3
1.1.3 Fields from remanent magnetisation ……..4

1.2 Representing magnetic fields……..5
1.2.1 Spherical harmonic analysis.....5
1.2.2 Spatial magnetic power spectra……..6

1.3 Crustal magnetism……..8
1.3.1 Terrestrial crustal magnetism ……....8
1.3.2 Martian crustal magnetism ……...10
1.3.3 Lunar crustal magnetism……...11

1.4 The Moon……..12
1.4.1 The lunar crust ……..13
1.4.2 The lunar core ……...14
1.4.3 Lunar rocks ……...15

1.5 Magnetisation……16

1.5.1 Induced and remanent magnetisation……...17

1.5.2 Mechanisms for remanent magnetisation……19

1.5.3 Demagnetisation……...…20

1.5.4 Magnetic minerals……21

1.5.5 Magnetic properties of lunar rocks……...22

1.5.6 Paleointensities……..23

1.5.7 Paleopoles……24

1.6 Aims and outline of this thesis…….25

Chapter 2: The lunar magnetic field **27**

2.1 Observations of the lunar magnetic field……27

2.1.1 Impacts and antipodes……...……30

2.1.2 Isolated anomalies……30

2.1.3 High albedo features…..……32

2.1.4 Crustal field directions…….....33

2.2 Apollo surface data……...……35

2.2.1 Surface crustal fields…….37

2.2.2 Interaction with the solar wind…….38

2.3 Theories for the origin of the lunar magnetic fields ……38

2.3.1 A dynamo field……..39

2.3.2 Antipodal enhancements……...40

2.3.3 Impacts……..41

2.4 Sources for the magnetic anomalies…..……42

2.4.1 Statistical studies……..……42

2.4.2 Isolated sources and impact ejecta ……..…43

2.4.3 The lunar mare……..44

2.5 The Lunar Prospector Magnetometer and Electron Reflectometer……..44

2.5.1 The Lunar Prospector satellite…….44

2.5.2 The Magnetometer…….45

2.5.3 Magnetometer sensitivity and resolution…..……..46

2.5.4 The Electron Reflectometer……..……...…47

2.5.5 Sensitivity and resolution of the Electron Reflectometer…..……..…52

2.5.6 The magnetic environment of the Moon…….52

2.6 The Magnetometer and Electron Reflectometer data…..……..55

2.6.1 The LP-MAG data…….55

2.6.2 Isolation of crustal fields…..……. 57

2.6.3 Comparison of processing methods for the MAG data…..……...61

2.6.4 A spherical harmonic model ……63

2.6.5 The LP-ER data ……63

2.7 Comparison of the ER and MAG data……..……66

2.7.1 Regional comparison of the ER and MAG data…..……67

2.7.2 Qualitative comparison of the ER and MAG data…..……67

2.7.3 Correlation…..……70

2.8 Comparison of ER and Apollo data…..…….72

2.9 MAG and ER data for magnetisation modelling…..…….74

Chapter 3: Magnetisation modelling **75**

3.1 The use of magnetisation models…..…….75

3.1.1 Source parameters…..……76

3.1.2 Crustal field representation……..……76

3.2 Magnetisation modelling methods……77

3.2.1 Forward models…..……77

3.2.2 Inverse models…..……..78

3.2.3 Equivalent layer inversions…..…….……..80

3.2.4 Model resolution…..……...81

3.3 Finding a solution…..……82

3.3.1 Non-uniqueness…..……..……...82

3.3.2 Minimum norm solution…..……83

3.3.3 Constrained least squares solution……84

3.3.4 The effect of damping ……86

3.4 Constraints on the solution……...87

3.4.1 A priori and additional information……..87

3.4.2 Complementary data sets……..88

3.4.3 The Parker bound……...88

3.5 Input Parameters……..91

3.5.1 Layer thickness…….……91

3.5.2 Magnetic crustal thickness estimation from spectra…….……91

3.5.3 Equivalent layer depth……...93

3.6 Predicted fields and residuals…..……...93

Chapter 4: Equivalent source dipole magnetisation models 95

4.1 Magnetic dipoles as point sources…….……...96

4.1.1 The magnetic field from a single dipole…..……96

4.1.2 An ensemble of magnetic dipoles…..……..99

4.1.3 Contributions from dipoles ……100

4.2 The linear inverse problem with equivalent source dipoles…..……...101

4.2.1 Least squares inversion…..……...102

4.2.2 Damped least squares inversion……..103

4.2.3 Under constrained problems…..……...104

4.2.4 Model resolution and uncertainties…..……105

4.3 Input model parameters…..……..107

4.3.1 Dipole and data grid…..……...107

4.3.2 Dipole spacing…..……108

4.3.3 Dipole depth and layer thickness…..……109

4.3.4 Dipole directions…..…….110

4.4 Inversion method…..……...111

4.5 A test case…..……..113

4.5.1 The effect of noise on the solution……114

4.5.2 Including a damping parameter…..……..117

4.5.3 The effect of 'wrong' parameters…..……118

4.5.4 Fixing a magnetisation direction…..……118

4.5.5 Inversion of a single component of magnetic field data…..…...…….122

4.5.6 The resolution matrix…..……..123

4.6 Finding source parameters…..…….125

4.6.1 Finding a bulk magnetisation direction…..……..125

4.6.2 Depth and thickness…..……127

4.6.3 Spatial extent…..……...128

4.6.4 Vertical resolution…..……129

4.7 Non-uniqueness…..……..130

4.7.1 Distinguishing between different source models…..……...130

4.8 Summary of test models…….135

4.9 Application of the ESD technique to the Reiner Gamma region……...136

4.9.1 Input data and dipole grid……..137

4.9.2 Low resolution magnetisation models……140

4.9.3 High resolution magnetisation models……...145

4.9.4 Finding the bulk magnetisation direction……...…147

4.9.5 Investigating thickness and depth of the dipole layer…….150

4.9.6 The resolution matrix and covariance matrix……157

4.10 Application of the ESD technique to other regions…….159

Chapter 5: Spatially continuous global magnetisation models 161

5.1 Theoretical background…….…161

5.1.1 A minimum norm solution……..……163

5.2 The Solution…….……...164

5.2.1 Inversion…….165

5.2.2 The magnetisation solution…….167

5.3 Input model parameters……..168

5.3.1 The data…..…….169

5.3.2 Layer thickness ……...169

5.3.3 Threshold…..……...……170

5.3.4 Damping…….……..170

5.4 Magnetisation models from the spherical harmonic model data…….……...171

5.4.1 The effect of damping on the model solution……..172

5.4.2 The effect of damping on residuals…….178

5.4.3 Selected model solutions…..……179

5.4.4. The global distribution of residuals…..……..181

5.4.5. The effect of thickness on the model solution…….185

5.4.6. Magnetisation variation with depth……...191

5.5. Surface predictions from the continuous models……..193

5.6. Magnetisation models from the radial magnetic field data……195

5.6.1 Magnetisation solutions for the Reiner Gamma region……...196

5.6.2 Predictions and residuals……...196

5.7. Discussion of the continuous magnetisation models…….199

5.7.1 Magnetisations……...…….199

5.7.2 Inclinations and declinations…..……...……201

5.7.3 The fit to the data…..……...203

Chapter 6: Inverse magnetisation models with the ER data 205

6.1 Non linear inversion……205

6.1.1 Linearisation……...206

6.2 Inversion of the ER data for the Reiner Gamma region…..……209

6.2.1 Input data and dipole grid……..209

6.2.2 Starting magnetisation distributions……...211

6.2.3 Inversion of the 1°×1° binned ER data……..……..212

6.2.4 Inversions with the unbinned ER data…..……...219

6.2.5 Inversions with the squared 1°×1° binned ER data…..……...220

6.2.6 Inversions with shifted altitude surface data…..…….221

6.2.7 Inversions with different thicknesses…..…….221

6.2.8 Discussion of inversions with the ER data …….224

6.3 Joint inversion with the ER and MAG data ……...225

6.3.1 Formulation of the joint iterative inversion…..……226

6.4 Joint inversion of the ER and MAG data for the Reiner Gamma region……227

6.4.1 Joint inversion with different starting models…..……...228

6.4.2 Joint inversion for the Reiner Gamma region with different thicknesses 232

6.4.3 Discussion of the joint inversion….……233

Chapter 7: Summary and Discussion **235**

7.1 Summary of models…..……...235

7.2 Observations…..…….236

7.2.1 Directions…….237

7.2.2 Magnitudes…..…….238

7.2.3 Model thicknesses and source depths…..…….239

7.2.4 Magnetised sources…..…….240

7.3 Comparison of modelling techniques…….241

7.3.1 Comparison of the ESD and spatially continuous models……...241

7.3.2 Comparison of magnetisation solutions from MAG and ER data…...244

7.4 Comparisons with other magnetisation models…..…….246

7.3.1 Another magnetic dipole model……...246

7.4.2 A magnetic monopole model…….……...248

7.5 Comparative planetology……249

7.5.1 Magnetisation magnitudes…..……..249

7.5.2 Comparison of features…..……...252

7.6 Suggestions for future work……252
7.6.1 Improving estimations of magnetisation…..……254
7.6.2 Improving understanding of the sources…..……254
7.6.3 Further development of the ER and joint MAG-ER inversions…....255
7.6.4 Utilising crustal magnetisation models…..…….256

Chapter 8: Concluding remarks **257**

Bibliography **261**

Appendices **277**

1 Coordinate systems…..……...277
2 Regional maps of magnetic anomalies…..…….278
3 Altitude normalisation…….……..283
4 Distribution of points on a sphere……..284
5 Fitting a theoretical power spectrum…….…….285
6 Expression of the magnetic potential…..……287
7 Matrix format for equivalent source dipoles…..…….289
8 Formation of the normal matrix equations…..……290
9 The damped least squares solution……...……291
10 Under constrained normal matrix equations…..…..…….293
11 Formulations for the continuous magnetisation model…..……..294
12 Damped least squares solution for the continuous magnetisation model…….....297
13 Magnetisation solutions for selected regions…..……..298
14 Regional surface predictions from a spatially continuous model…..…….……..302
15 Simplification of joint matrix multiplication…..……..304

List of figures

Maps and graphs are plotted using Generic Mapping Tools (e.g Wessel and Smith, 1998), or MATLAB®.

1.1 Power spectra of magnetic fields at Mars, Earth and the Moon…..……7
1.2 Radial crustal fields for Mars, Earth and the Moon…..……...9
1.3 The internal structure of the Moon…..……..12
1.4 Lunar chronology…..…….13
1.5 Magnetisation direction defined by declination and inclination……...16
1.6 Schematic of a fundamental magnetic dipole…..……..17
1.7 Schematic hysteresis curve……..…….....18
1.8 Lunar paleointensities……...23

2.1 Map of the total lunar crustal field at altitude (spherical harmonic model)…..….29
2.2 Map of the total lunar crustal field at the surface (ER data)…….29
2.3 Labelled map of the total lunar crustal field at altitude…..……...31
2.4 Contour map of field magnitude over the Reiner Gamma region…..……...32
2.5 Vector components of the lunar crustal field at altitude……...34
2.6 Vector magnetic field of single dipoles……35
2.7 The Apollo 12 lunar surface magnetometer…..…….36
2.8 The Apollo landing sites……...36
2.9 The interaction of an expanding impact vapour cloud with a magnetic field…...41
2.10 The Lunar Prospector satellite……45
2.11 Schematic of a single axis of a fluxgate magnetometer……..46

2.12 Electrons reflecting from a surface magnetic field…….48
2.13 Schematic of an hemispherical analyser…….48
2.14 Electron velocity vectors in a converging magnetic field…..……..49
2.15 The magnetic environment of the Moon…..……53
2.16 The interaction of the solar wind with the Moon……54
2.17 Coverage of the low altitude MAG data from the lunar wake and geotail…….56
2.18 Histogram of the altitude distribution of low altitude MAG data……...57
2.19 Map of the total lunar crustal magnetic field at altitude (MAG data)……58
2.20 Radial magnetic field at 30 km for solar wind and wake and tail times…….61
2.21 Comparison of differently processed passes over the Reiner Gamma region…62
2.22 The surface locations of the unbinned ER data points……65
2.23 The binned and the unbinned ER data for the Reiner Gamma region……66
2.24 Comparison of the total magnetic field at altitude and at the surface for selected regions…….....68
2.25 Comparison of the ER data and spherical harmonic model prediction at the surface (same colour scale), with differences…..……...69
2.26 Comparison of the ER data and spherical harmonic model prediction at the surface (‘equal area’ colour scale).……69
2.27 Regional linear correlation coefficients for the ER data and the spherical harmonic model predictions…..……..72
2.28 Comparison of the ER data and Apollo surface magnetometer measurements..73

3.1 Illustrating forward model sources……...78
3.2 Example ‘trade-off’ curve for damped model solutions…..……..86
3.3 Geometry used for calculating the ‘Parker bound’……...89
3.4 Parker bound minimum magnetisations for different layer thicknesses……...90
3.5 Theoretical fit to the lunar spatial magnetic power spectrum…….……..92
3.6 Illustration of the definition of residuals ……..94

4.1 Geometry for equivalent source dipole models……97
4.2 Vector and scalar magnetic field of single dipoles…..……..……..100
4.3 The contribution to the field of a single dipole at distance……101

4.4 Schematic of the resolution matrix ……106
4.5 Schematic of dipole grid with border region of dipoles…….109
4.6 Representations of magnetised layers…..……110
4.7 Input magnetisation model for test case…..…….114
4.8 Plots of magnetisation solutions from the test case with added noise…..……...115
4.9 Maps of damped magnetisation solutions from the test case with noise……116
4.10 'Trade-off' curve for the test model with noise…..……...117
4.11 Plots of magnetisation solutions from a test case with 'wrong' parameters….120
4.12 Maps of damped magnetisation solutions from the test case with 'wrong' parameters…..……121
4.13 Maps of damped magnetisation solutions with fixed magnetisation direction for the test case…..…….122
4.14 A transect across the resolution matrix for the test case…….……..124
4.15 Plot of correlated dipoles…..……...……..124
4.16 Contoured misfits as a function of model inclination and declination for the test case…..……..126
4.17 Plot of misfits with thickness for discerning model thickness……..127
4.18 Comparison of total magnetisation solutions for the test case from different models…..…….....128
4.19 Cross section of total magnetisation solutions for the test case from different models……..129
4.20 Forward model magnetisations distributions with similar magnetic fields…..131
4.21 Classic dipolar field patterns from basic distributions of dipoles…..……132
4.22 Total magnetic field at altitude and the surface from different forward model magnetisation distributions……..134
4.23 Ratios of the maximum surface field to the maximum field at altitude for different forward model magnetisation distributions……135
4.24 The magnetic field at altitude and at the surface for the Reiner Gamma region …..137
4.25 Contour map of topography for the Reiner Gamma region……..138
4.26 The radial magnetic field data (from all regimes and from the wake and tail regions only) at 30 km altitude for the Reiner Gamma region……139

4.27 'Trade-off' curve for magnetisation models of the Reiner Gamma region…..141
4.28 Low resolution radial magnetisation solutions for the Reiner Gamma region ..….142
4.29 Low resolution three component magnetisation solutions for the Reiner Gamma region…..……..142
4.30 Predicted radial field from magnetisation models, and absolute residuals, for the Reiner Gamma region…..……..143
4.31 Histogram of exact residuals of predictions from magnetisation models for the Reiner Gamma region…..……..144
4.32 Predicted surface fields from magnetisation models for the Reiner Gamma region…..……...145
4.33 High resolution three component and total magnetisation solutions for the Reiner Gamma region (from all radial data)…..……146
4.34 High resolution three component and total magnetisation solutions for the Reiner Gamma region (from radial data in the wake and tail regions only)….146
4.35 Contoured misfit as a function of dipole inclination and declination for the Reiner Gamma region……..148
4.36 Magnetisation solutions in fixed directions for the Reiner Gamma region…..149
4.37 Predictions of the radial and surface fields from fixed direction models for the Reiner Gamma region…..…….150
4.38 Schematic diagram of the depths and thicknesses of model dipole layers used with the equivalent source dipole technique…..……...151
4.39 Three component and total magnetisation solutions for the Reiner Gamma region for models with different thicknesses…..……..153
4.40 Cross sections of the total magnetisation solutions for the Reiner Gamma region for models with different thicknesses…..…….154
4.41 Predicted radial field and the absolute residuals from magnetisation models with different thicknesses for the Reiner Gamma region…..……156
4.42 Predicted surface field from magnetisation models with different thicknesses for the Reiner Gamma region…..……156
4.43 A transect across the resolution matrix, and plot of correlated dipoles for magnetisation models of the Reiner Gamma region…..……158

4.44 Three component and total magnetisation solutions for the regions of Firsov, Crisium and Descartes….……160

5.1 Geometry for the spatially continuous magnetisation model….……162
5.2 Schematic showing the region of points retained in the sparse matrix system...166
5.3 Schematic of the estimation of vertically integrated magnetisation……...168
5.4 Trade-off curve for global models with different thicknesses (from three components of the spherical harmonic model data)……...172
5.5 Global magnetisation solutions with different damping parameters……..175
5.6 Three components magnetisation models with different damping parameters for the regions of Reiner Gamma and Descartes……..177
5.7 Profiles of the radial magnetisation of differently damped models, and the radial field for the Reiner Gamma region…….178
5.8 Histograms of radial residuals for models with different damping parameters..179
5.9 Profiles of predicted radial and total magnetic fields for the Reiner Gamma region with different damping parameters……...……..180
5.10 Global magnetisations at the top and bottom of a magnetised layer, and the vertically integrated magnetisation for different layer thicknesses…….182
5.11 Global distributions of exact, absolute and normalised residuals for the three components of magnetic field predicted from a magnetisation model…….184
5.12 Histogram of component residuals for predictions from models with different thicknesses…..……...186
5.13 Variation in misfit with layer thickness for global models with the same damping parameter……...187
5.14 Magnetisation solutions for the Reiner Gamma region from global models with different thicknesses…..…….189
5.15 Predicted fields and residuals for the Reiner Gamma region from global models with different thicknesses…….190
5.16 The decrease in magnetisation with depth in global magnetisation models….192
5.17 Cross sections showing magnetisation with depth for the Reiner Gamma region from global models with different thicknesses…..……192

5.18 Comparison of the 1°×1° binned ER data with surface field predictions from a global magnetisation model…….194
5.19 Regional comparison of the 1°×1° binned ER data with the surface predictions from global magnetisation models with different thicknesses……..194
5.20 Magnetisation solutions from global models with different damping parameters for the Reiner Gamma region (from radial magnetic field data)…..……197
5.21 Predictions of the radial fields, and absolute residuals, for the Reiner Gamma region from global magnetisation models…….198
5.22 Predictions of the total surface magnetic field in the Reiner Gamma region from global models with the radial field data…..……..198
5.23 Three component and total magnetisations at the surface for the preferred global magnetisation model from the spherical harmonic model data……...200
5.24 The inclination and declination of the surface magnetisation for the preferred global magnetisation model from the spherical harmonic model data……202

6.1 The ER data for the Reiner Gamma region (as figure 2.23)…..……..210
6.2 Correlation coefficients and misfits to the ER and MAG data with iterations from inversion of the ER data with different starting magnetisation distributions (Reiner Gamma region)…….…….213
6.3 The solution RMS magnetisation with iterations from inversion of the ER data with different starting magnetisation distributions (Reiner Gamma region)….214
6.4 Magnetisation solutions for the Reiner Gamma region from inversions of the 1°×1° binned ER data with different starting magnetisation distributions…..…215
6.5 Predictions of the surface data for the Reiner Gamma region from inversions of the 1°×1° binned ER data with different starting magnetisations…..……..217
6.6 Predictions of the MAG data for the Reiner Gamma region from inversions of the 1°×1° binned ER data with different starting magnetisations……...218
6.7 Magnetisation solutions for the Reiner Gamma region from inversions of the unbinned ER data…..……...219
6.8 The misfit to the ER and MAG data with iterations from inversion of the ER data with shifted surface altitudes (Reiner Gamma region)……...222

6.9 The solution RMS magnetisation with iterations from inversion of the ER data with shifted surface altitudes (Reiner Gamma region)……..223
6.10 The solution RMS magnetisation with iterations from inversion of the ER data with different layer thicknesses (Reiner Gamma region)……..223

6.11 Magnetisation solutions for the Reiner Gamma region from inversions of the 1°×1° binned ER data with different layer thicknesses……224
6.12 The misfit to the ER and MAG data with iterations from the joint inversion with different starting magnetisations and thicknesses (Reiner Gamma region)…..229
6.13 The solution RMS magnetisation with iterations from the joint inversion with different starting magnetisations and thicknesses (Reiner Gamma region)…..230
6.14 Magnetisation solutions for the Reiner Gamma region from joint inversions with different starting magnetisation distributions…..……..231
6.15 Magnetisation solutions for the Reiner Gamma region from joint inversions with different layer thicknesses……232

7.1 Comparison of the magnetisation solutions for the Reiner Gamma region from different modelling techniques using the radial magnetic field…….……242
7.2 Comparison of the magnetisation solutions for the Reiner Gamma region with different thicknesses and modelling techniques with the MAG data….……243
7.3 Comparison of the magnetisation solutions for the Reiner Gamma region from inversions with the ER and MAG data independently and jointly…..……...245
7.4 Alternative magnetisation solution of north-south oriented dipoles for the Reiner Gamma region shown with a solution from this study……...……247
7.5 Magnetic monopole representation of the Reiner Gamma region shown with an equivalent solution from this study ……..…….248
7.6 Three component and total global magnetisations for the Earth, Mars and the Moon….……250
7.7 Inclinations and declinations of crustal magnetisation directions for Earth, Mars and the Moon…..…….253

List of tables

2.1 Summary of the surface measurements from the Apollo missions…..……..37
2.2 Global correlation coefficients for the ER data and predictions from the spherical harmonic model…..……..71

3.1 Parker bound minimum magnetisations for different layer thicknesses……...90

4.1 Solution parameters for test models with noise, damping, and different parameters……..….119
4.2 Solution parameters for test models with fixed magnetisation direction…….....121
4.3 Solution parameters for test models with single input field direction…….....123
4.4 Comparison of solution parameters for the test models……..129
4.5 Dipole magnitudes and RMS magnetisations for forward model magnetisation distributions with similar magnetic field patterns…….…….133
4.6 Selected solution parameters for low resolution models of the Reiner Gamma region with fixed (radial) and variable direction dipoles…..……..141
4.7 Solution parameters for high resolution models of the Reiner Gamma region with fixed direction…..……...149
4.8 Solution parameters for variable direction magnetisation models of the Reiner Gamma region with different thicknesses, depths and damping parameters….152
4.9 Estimated source dimensions and volume for the magnetised region at Reiner Gamma…..……..155
4.10 Model and solution parameters for the regions of Firsov, Crisium and Descartes …….....159

5.1 Solution parameters for global models with different thicknesses and damping parameters (from three components of the spherical harmonic model data)….173

5.2 Solution parameters for selected global models with different thicknesses…...181

5.3 Solution parameters for different thickness models with the same VIM……188

5.4 Solution parameters for global for models with different damping parameters (from the radial magnetic field component)……..195

6.1 Solution parameters for inversions with the MAG and ER data independently and jointly for the Reiner Gamma region…..……233

7.1 Summary of modelling techniques and data sets used……236

Acronyms

ALSEP	Apollo Lunar Surface Experiments Package
ER	Electron Reflectometer/Reflectometry
ESD	Equivalent source dipole
GSE	Geocentric Solar Ecliptic
IMF	Interplanetary magnetic field
IRM	Isothermal Remanent Magnetisation
LP	Lunar Prospector
LSM	Lunar Surface Magnetometer
MAG	Magnetometer
MGS	Mars Global Surveyor
NRM	Natural Remanent Magnetisation
PDS	Planetary Data System
RMS	Root Mean Square
SPA	South Polar Aitken (basin)
SRM	Shock Remanent Magnetisation
SSR	Sum of squares of residuals
TRM	Thermo Remanent Magnetisation
UV	Ultra Violet
VIM	Vertically integrated magnetisation
VRM	Viscous Remanent Magnetisation

Units

Ga	10^9 years	μT	10^{-6} Teslas
Gcm	Gauss-centimetre	pT	10^{-12} Teslas
GPa	10^9 Pascals	Wb	Webbers
mA/m	10^{-3} Amps per metre	Am^2kg^{-1}	Amp metre squared per kilogram
nT	10^{-9} Teslas	$\mu_0 = 4\pi \times 10^{-7}$ H/m (Henrys per metre)	

Chapter 1

Introduction

Since the Apollo missions it has been known that, while the Moon possesses no global magnetic field, it has regions of weak magnetic field resulting from areas of the lunar crust that are remanently magnetised. The origins of the magnetic fields that produced this remanent magnetisation are still under discussion, with the main contenders being an ancient lunar dynamo, and processes occurring on the Moon as a result of impacts. Understanding the origins of the lunar magnetic fields has relevance to the understanding of terrestrial planets and their evolution, with implications for the magnetisation of smaller bodies, either through dynamo generation or other means of magnetic field generation or enhancement.

Measurements of the magnetic field around the Moon taken by the satellite Lunar Prospector (LP) have been used to map the lunar crustal remanent fields globally. Vector magnetic field data at the space craft altitude from the LP magnetometer (MAG), and indirect measurements of the intensity of surface magnetic fields with an electron reflectometer (ER) have allowed a more thorough study of lunar magnetism.

With the Moon now very much in the limelight of planetary exploration, the issues surrounding lunar magnetism still remain. The scientific objectives of the study of the lunar crustal fields are to understand the nature of the magnetised source regions and if possible, determine the origin of the fields and mechanisms that produced the remanent magnetisation. Interpretation of lunar magnetism relies on the determination of the distribution, magnitude and direction of the sources of

magnetisation. In the absence of extensive sampling, this is made possible with magnetisation models produced from the observed magnetic field data.

This study uses inverse modelling methods to produce global and regional models of the magnitude and direction of lunar magnetisation which can account for the observed magnetic fields at the surface and at altitude. The ambiguity in magnetisation distributions and determination of source parameters with these inverse methods is discussed with the use of forward models. The inverse modelling techniques are based on those developed for terrestrial and Martian data sets and give very weak magnetisations compared to the crustal magnetisations of the Earth and Mars. Crustal magnetisation models also permit the isolation of the crustal field contribution to the lunar magnetic field environment that can be used with other data sets or modelling methods.

1.1 Magnetic fields on planetary bodies

Magnetic fields are common features of many solar system bodies [de Pater and Lissauer, 2001]. They can be generated within the body by active magnetohydrodynamic dynamos, can result from magnetic induction from an internal field or interaction of an external magnetic field with a conductor, or can be from remanent magnetisation of rocks produced as a result of past magnetic fields.

1.1.1 Dynamo fields

Magnetohydrodynamic dynamos result from convection of a large region of a conducting fluid core which is in non-uniform motion [Stevenson, 1983]. The magnetic fields produced are planet-wide and can vary on time scales from years to billions of years [Stevenson, 2003]. Dynamo generated fields are present today in the Sun, the Earth, the gas giants, and the Galilean satellite Ganymede, but it is possible that dynamos could start in most differentiated planetary bodies if there is a mechanism for sustained convection [Stevenson, 1983]. Measurements from Mariner

10 [Ness et al., 1974] and recently from MESSENGER [Anderson et al., 2008] at Mercury suggest that Mercury has a weak, intrinsic magnetic field, perhaps from the end stages of an active dynamo [Russell, 1993] as the outer core solidifies.

For Jupiter and Saturn, the conducting fluid is super conducting hydrogen, while in Uranus and Neptune it is conducting hydrogen combined with water, methane and ammonia [Stevenson, 2003] and convection may arise from thermal or compositional gradients. In the terrestrial-like planets (including Jupiter's moon Ganymede), the field is generated in the conducting liquid iron-sulphur alloy outer core and is probably sustained by the presence of a growing solid inner core which allows release of gravitational potential energy.

While the conditions for planetary dynamos are not known precisely, the presence or past existence of a dynamo field allows certain assumptions to be made about the composition and processes of the interior of the body. The absence of an internal magnetic field at Venus may be due to the slow rotation of Venus, lack of convection, or the lack of an iron core [Stevenson, 1983]. Past dynamos are also suggested as a cause of the crustal fields at Mars and the Moon. The internal structure of Mars is inferred to be very similar to that of the Earth, so while a Martian dynamo may have been possible, the size inferred for the lunar core and thermal state of the Moon makes it unlikely to have been able to support a lunar dynamo by current dynamo theories [Stegman et al., 2003]. The prospect of the existence of a lunar dynamo then has implications for dynamo generation in small bodies.

The magnetic field generated from a magnetohydrodynamic dynamo is often predominantly dipolar and aligned close to the spin axis (e.g for Earth, Jupiter, Saturn, Ganymede and Mercury). However in some cases the field can also contain strong higher harmonics and be orientated at a large tilt angle to the spin axis (Uranus and Neptune have a strong quadrupole moment and tilt angles of 40-60°).

1.1.2 Induced fields

Planets are electrically conducting bodies and in the presence of a magnetic field can become host to induced fields. The inducing fields can be internal dynamo generated fields, or of external origin in the solar wind or interplanetary magnetic

field (IMF). The induced fields can be planet-wide, resulting from large scale (compared to the body) steady fields, or can occur on a regional scale from currents induced by small scale variations in an external field.

Induced fields can vary with location on the body (especially latitude) and vary with time. Their magnitudes are determined by conductivity and susceptibility, and can be used to reveal the conductivity structure of the body or of a region. This has been useful on Earth for exploration and at Jupiter's moons Europa and Callisto to infer the presence of a subsurface saline ocean [Khurana et al., 1998]. Induced fields on the Moon have been used to infer the internal structure of the Moon from electrical conductivity and magnetic permeability estimates [e.g Sonett, 1982, Hood, 1986]. At Venus and in cometary comae, interaction of the solar wind with charged particles in the atmosphere or exosphere also induces magnetic fields.

1.1.3 Fields from remanent magnetisation

Magnetic fields can also result from permanent remanent magnetisation of all or parts of the planetary body. A remanent magnetisation is a stable magnetisation which remains in certain minerals within a rock below its Curie temperature (the temperature above which magnetic grains lose their magnetisation) after the magnetic field in which it was acquired has been removed.

The scales of coherent remanent magnetisation are generally small compared to the planet's radius and so result in magnetic fields which vary significantly with location. Their strengths depend greatly on the strengths of the magnetising field, the type of magnetic minerals present and on any changes that might have occurred subsequent to magnetisation. The presence of remanent magnetisation implies the existence of magnetic minerals and of strong fields that existed long enough for the minerals to acquire a stable remanent magnetisation, thus providing some information on composition, and the past behaviour of local (to the body) magnetic fields.

Remanent magnetisation is a common feature of silicate solar system bodies [Hood, 1994], and is prominent on the Earth, Mars and the Moon, and also within

single grains in meteorites [e.g Stacey and Lovering, 1959] and on some asteroids [e.g Kivelson et al., 1993, Richter et al., 2001]. New results from MESSENGER at Mercury may reveal evidence for crustal remanent magnetisation, while the surface of Venus is likely to be too hot (above the Curie temperature for some magnetic minerals) to retain a magnetisation, or too 'new' (due to resurfacing) to have acquired a magnetisation in an ancient dynamo field [Stevenson, 2003].

1.2 Representing magnetic fields

The magnetic field data discussed and used in calculations in this thesis, and the magnetisation models produced, are in a lunar-centred spherical coordinate system specified in terms of co-latitude θ (90°-latitude) and longitude ϕ (in degrees), and radius r, with orthogonal vectors $\hat{\mathbf{r}}$, $-\hat{\boldsymbol{\theta}}$ and $-\hat{\boldsymbol{\varphi}}$ pointing outwards, south and east respectively. The spherical coordinate data locations are transformed from a 'selenographic' coordinate system [Hapgood, 1992] (See Appendix 1).

Altitude and topography are defined above the surface of a spherical Moon of radius 1737.1 km. The difference between the lunar polar and equatorial radii is ~ 2 km, so the ellipticity of the Moon is ignored (although deviations from sphericity might be apparent at the surface and low altitudes).

1.2.1 Spherical harmonic analysis

The magnetic induction, or flux density, **B** (here on called magnetic field) outside a source region ($\nabla \cdot \mathbf{B} = 0$) can be described by the gradient of a scalar magnetic potential ψ [e.g Stern, 1976]:

$$\mathbf{B} = -\nabla \psi \tag{1.1}$$

This potential satisfies Laplace's equation ($\nabla^2\psi = 0$). In a spherical geometry, the magnetic potential at regions outside a reference sphere of radius a ($r \geq a$), owing to internal sources (after external fields have been removed), can be expressed as a sum of spherical harmonics functions:

$$\psi = a\sum_{n=1}^{\infty}\left(\frac{a}{r}\right)^{n+1}\sum_{m=0}^{n}\left(g_n^m\cos(m\phi) + h_n^m\sin(m\phi)\right)P_n^m(\cos\theta) \tag{1.2}$$

where $P_n^m(\cos\theta)$ are the Schmidt quasi-normalised form of the associated Legendre polynominals of degree n and order m, and g_n^m and h_n^m the Gauss coefficients of the expansion. These coefficients can be determined up to a finite degree by observation of the magnetic field.

Such an expression for the magnetic potential provides a means to produce estimates of magnetic field at any location, and can also be used to infer some information about the sources of the field itself. The terms of the expansion represent multi-pole moments; $n = 1$ are dipole terms, $n = 2$ quadrupole, $n = 3$ hexapole and so on, and represent the contribution to the field from magnetic structures of different sizes. For degree n on a sphere of radius a, the wavelength Λ of the magnetised structure is:

$$\Lambda = \frac{2\pi a}{(n + \frac{1}{2})} \tag{1.3}$$

[Backus et al., 1996]. The relative importance of the n^{th} degree terms can be considered from a spatial magnetic power spectrum.

1.2.2 Spatial magnetic power spectra

The Lowes-Mauersberger power spectra R_n [Lowes, 1966] averages the mean square amplitude of the magnetic field for each harmonic n over the spherical surface of radius r, in which the sources are contained:

$$R_n = (n+1)\left(\frac{a}{r}\right)^{2n+4} \sum_{m=0}^{n} \left[(g_n^m)^2 + (h_n^m)^2 \right] \tag{1.4}$$

Figure 1.1 shows the Lowes-Mauersberger power spectra for the magnetic fields of the Moon, the Earth and Mars at their surfaces. The power spectra for the Earth is in two parts and shows the strong contribution from the core field up to about degree 15 or 16, and then contributions from crustal sources at higher *n*. Both the Moon and Mars show no sign of a clear break in slope that would imply the existence of a core field, as expected, and show an increase in power with degree resulting from smaller scale (compared to the planet) magnetised structures.

While the shape of the crustal spectra are similar for the Earth, Mars and the Moon, the crustal fields of Mars are an order of magnitude stronger than the crustal fields of the Earth, which in turn, are an order of magnitude stronger than the crustal fields on the Moon. This may be due to the carriers of the remanent magnetism, or the strengths of the magnetising fields, or both.

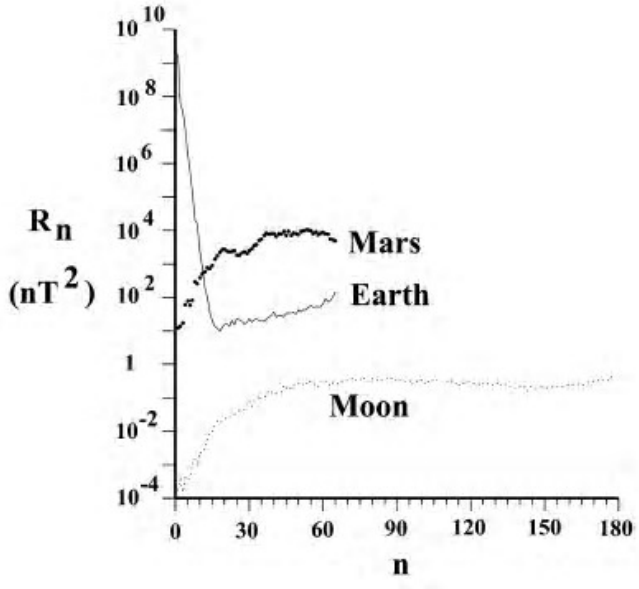

Figure 1.1: Comparison of the Lowes-Mauersberger power spectra at the surface, from recent determinations of the spherical harmonic coefficients for the Moon [Purucker, 2008], the Earth [Sabaka et al., 2004] and Mars [Langlais et al., 2004]. (From Purucker (2008)).

1.3 Crustal magnetism

Crustal magnetism is defined as magnetism originating from rocks below their Curie temperature [Purucker and Whaler, 2007]. For terrestrial-like planets, the increase in temperature with depth into the body means that it is generally only the thin crustal layer which can be magnetised [Wasilewski et al., 1979]. Crustal magnetic fields result from contrasts in crustal magnetisation and are called anomalies as they are 'anomolous' with respect to the non-crustal field, which is the core field for the Earth, and the absence of an internal field at the Moon or Mars. Magnetic fields measured around a planet are a vector sum of magnetic fields originating internally (from a dynamo, induction or remanent magnetisation) and externally (from the solar wind, within an ionosphere) to the planet, from which the crustal field has to be isolated. Figure 1.2 shows the radial component of the crustal fields for the Earth, Mars and the Moon. The crustal fields for these three bodies show very different magnitudes, scales and characteristics.

1.3.1 Terrestrial crustal magnetism

On Earth, most of the crust is magnetised, with different strengths in the magnetisation of the continents and the oceans due to the different relative contributions from remanent and induced magnetisations. At satellite altitudes of 350-550 km, terrestrial anomalies are mostly less than 10 nT, with some strong broadscale anomalies hundreds of km in extent up to 20 nT. The largest terrestrial crustal fields appear above continental cratons such as the Bangui anomaly in Central Africa and the Kursk anomlaly in the Ukraine [Langel and Hinze, 1998]. The radial component of the terrestrial crustal field (Figure 1.2A) also shows the 'magnetic stripes' of alternating polarity parallel to mid-ocean ridges which led famously to the description of sea floor spreading [Vine and Matthews, 1963] and magnetic field reversals.

Terrestrial magnetic anomaly maps reflect the physical and chemical differences in the crustal rocks, resulting from geological and tectonic processes.

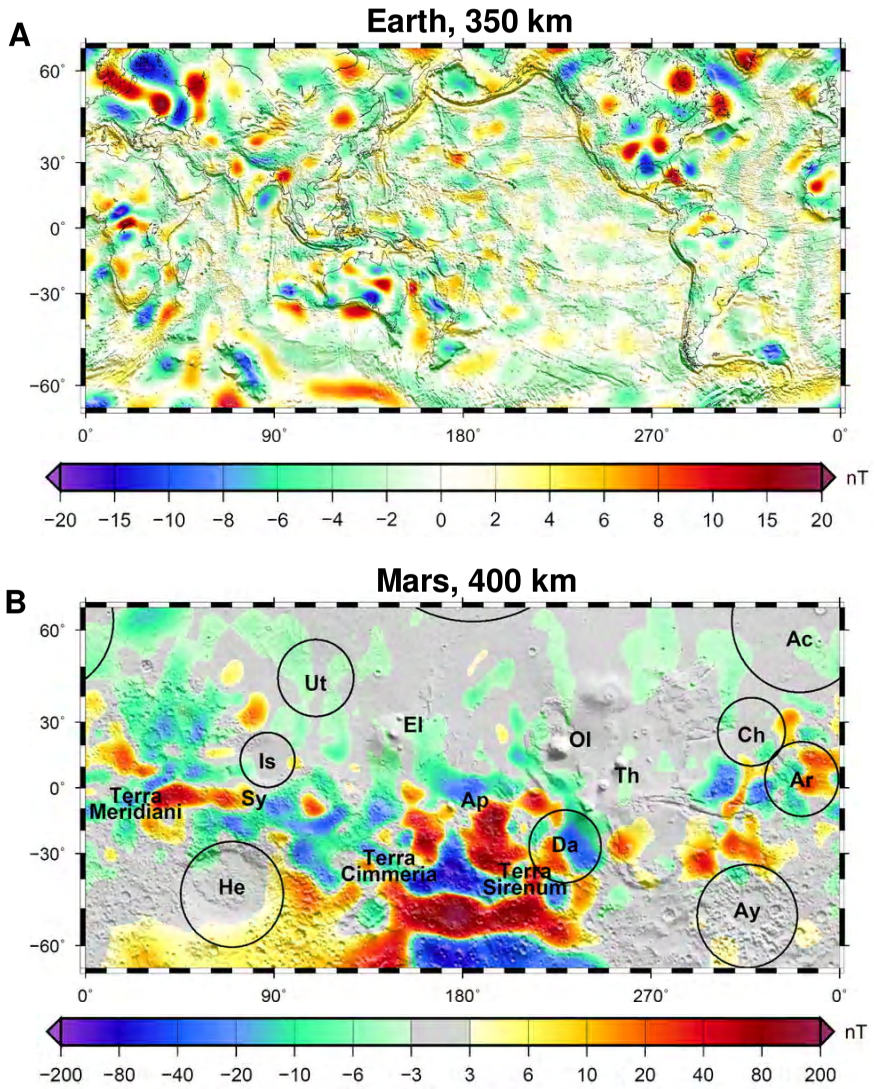

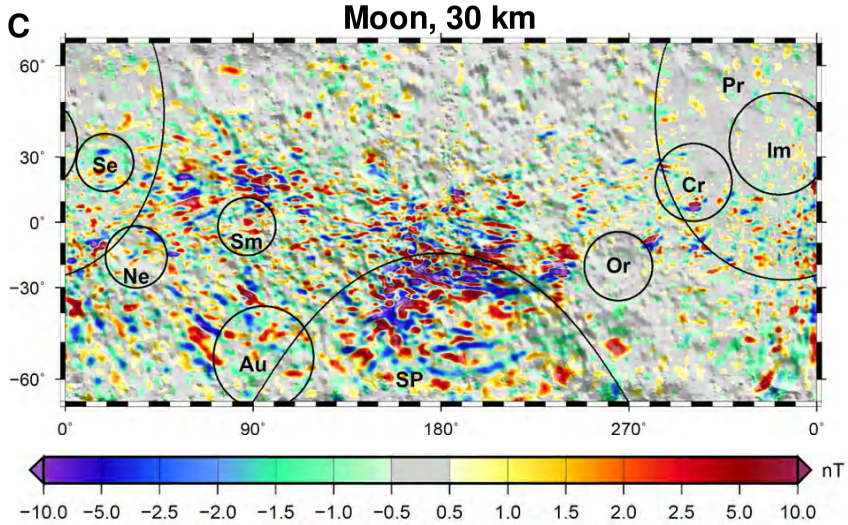

Figure 1.2: The predicted radial crustal magnetic fields for A: the Earth at an altitude of 350 km from the spherical harmonic model of Lesur et al. (2008), B: Mars at an altitude of 400 km based on the equivalent source dipole model of Langlais et al. (2004) with the rims of the largest impact basins labelled, and C: the Moon at an altitude of 30 km from the spherical harmonic model of Purucker (2008) with the rims of some of the impact basins indicated. (From Langlais et al. (2009)).

Spatial variations may represent variations in the crustal thickness, the distribution of magnetic minerals, thermal or mechanical history, and alterations such as fracture, shock, heating, and volcanic processes [Langel and Hinze, 1998]. Terrestrial magnetic anomalies are very useful in understanding the composition and structure of the Earth's lithosphere and they allow the reconstruction of the magnetic field history over billions of years.

Terrestrial crustal fields are also measured by airborne and shipborne surveys, offering much higher resolution than satellite surveys, showing surface anomaly fields of up to 1000 nT [Fowler, 2005] that vary over distances of <1 km. A recent study of the Vredefort crater in South Africa [Caporzen et al., 2005] which gives no significant feature on an aeromagnetic anomaly map showed very strong but spatially incoherent surface magnetisation. Even with the accessibility and variety of measurement techniques on Earth, and the wide variety of samples for many crustal regimes, the connections between many anomaly fields and the source body, even the strong Bangui anomaly, are not fully understood.

1.3.2 Martian crustal magnetism

The Martian crustal fields, measured with a vector magnetometer and electron reflectometer on Mars Global Surveyor (MGS), show very strong and localised magnetic fields of up to 200 nT at 400 km altitude. The younger northern hemisphere displays weak crustal fields, and the older southern hemisphere shows very strong crustal fields, one or two orders of magnitude stronger than the crustal field at Earth at similar altitudes [Acuña et al., 1998]. The large volcanic provinces on Mars are not associated with large magnetic anomalies, nor are the largest impact craters (labelled in figure 1.2B). The linear magnetic anomalies in the southern hemisphere have been interpreted by some as suggestive of tectonic processes in Martian early history [e.g Connerney et al., 1999].

Predictions of the Martian field at an altitude less than 200 km from the spherical harmonic model of Cain et al. (2003) gave fields of several thousand nT, suggesting that some fields at the surface could be of similar amplitude to the core

field of the Earth. It is thought that such strong remanent magnetic fields could only have been achieved in the presence of a Martian dynamo field, and that this dynamo ceased as the Martian core cooled or underwent a change in convective style [Stevenson, 2001], or as a result of multiple impacts to the planet [Roberts et al., 2009]. The present distribution of remanent fields then is the result of demagnetisation processes (such as heating from volcanoes, or impacts) subsequent to the cessation of the Martian dynamo.

1.3.3 Lunar crustal magnetism

The crustal fields on the Moon are very weak compared to those at the Earth and Mars and are two orders of magnitude less than that of the terrestrial crustal field at comparable altitudes, and four orders of magnitude less than the crustal field at Mars. The lack of lunar atmosphere allowed the low altitude orbit of the Lunar Prospector satellite (30 km), providing higher resolution measurements than those at the Earth and Mars, showing the fine-scale features of the lunar crustal fields.

The main features of the lunar crustal field, to be discussed in Chapter 2, are their association with the antipodes of the youngest large impact craters [Lin et al., 1988] and the presence of strong isolated anomalies. In general, the lunar Maria show weaker and more homogeneous magnetic fields, while the lunar highlands and the farside show stronger and more diverse fields. The large scale (<1 km to >500 km) magnetic anomalies imply the presence of relatively strong and coherent sources of remanent magnetisation.

With the ability of the lunar core to support a dynamo in debate, there have been many suggestions for the origins of these magnetising fields, and the mechanisms by which the remanent magnetisation was produced (reviewed by Fuller, 1974 and Dyal et al., 1974). The main contenders for the lunar paleofields (to be discussed in section 2.3) are an ancient lunar dynamo, or processes resulting from impacts. The distribution of the lunar crustal magnetic fields may not only represent physical or chemical variations in the crust, but also the location of magnetising fields.

1.4 The Moon

As the only other planetary body for which we have a significant mass of samples (~kg) and have visited, more is known about the structure and composition of the Moon than any planet other than the Earth. The Moon is thought to have formed from mostly silicate materials resulting from a collision of a Mars-sized object with the early Earth [Hartmann and Davis, 1975]. The impact ejected material from the crust and upper mantle of the early Earth, and the outer material of the impactor, which then accreted into the Moon.

Studies of the Apollo and Luna samples showed that the Moon, rather than being a primitive body, has undergone differentiation (chemical segregation) into a crust, mantle and core (Figure 1.3). The Moon's history has been dominated by impact events and volcanic activity, with lunar chronology based on the record of impacts (Figure 1.4). With the exception of some lava eruptions and small impacts, the Moon has been geologically inactive for the last 3.5 Ga (billion years).

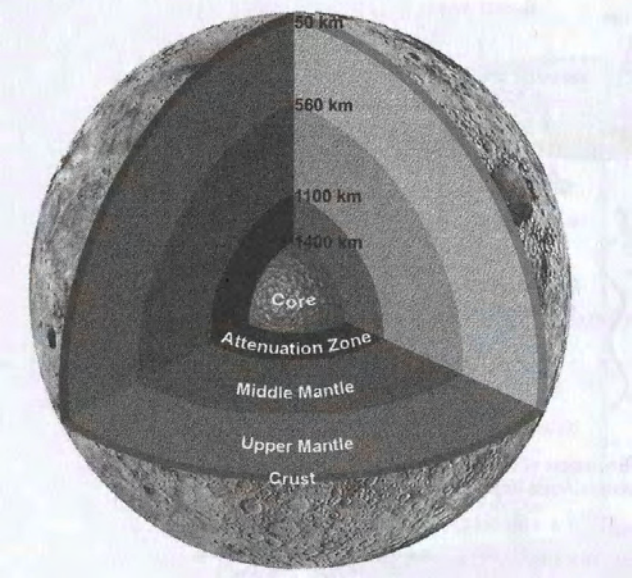

Figure 1.3: The internal structure of the differentiated Moon. (From Hiesinger and Head (2006)).

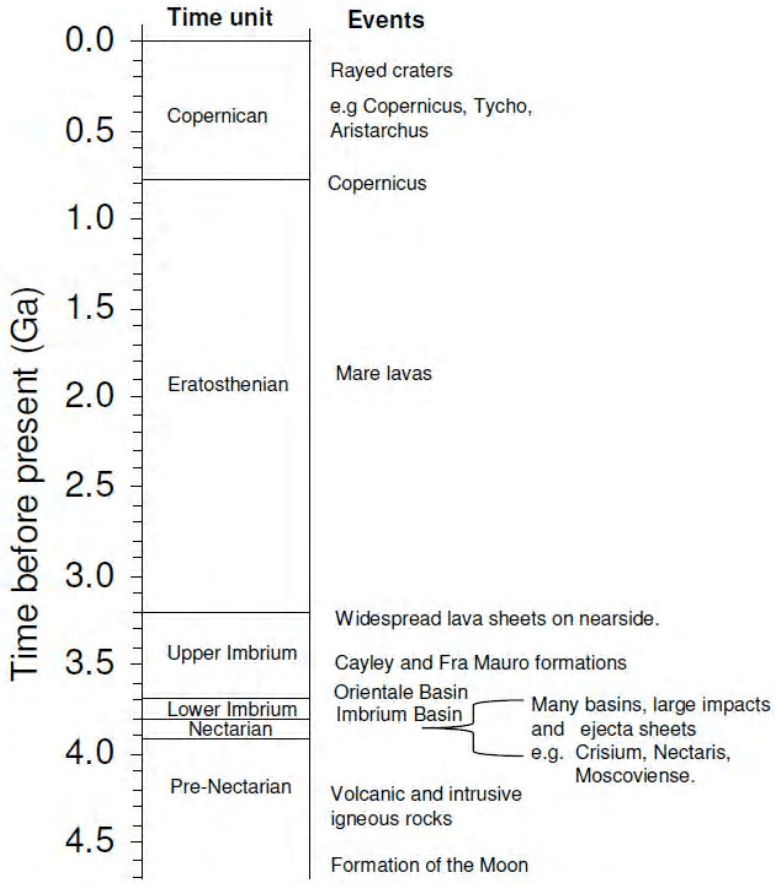

Figure 1.4: Lunar chronology. (Based on the lunar stratigraphy presented in Hiesinger and Head (2006), and details in Murray et al. (1981) and Heiken et al. (1991)).

1.4.1 The lunar crust

Magmatism early in the Moon's history led to a crust with varied thickness. The farside crust is thicker than the nearside crust, and recent reanalysis of the Apollo seismic data (perhaps biased by the region around the Apollo 12 and 14 sites), placed the lunar crustal thickness in the range 30-45 km [Khan and Mosegaard, 2002, Khan et al., 2000 and Lognonné, 2003]. Crustal thickness models derived from Lunar Prospector and Clementine gravity and topography data give a slighter higher average thickness of 49 ± 16 km, and show the thinning of crust in the centre of some major impact basins, surrounded by an annulus of thicker crust [Wieczorek et al., 2006].

Unlike the Earth whose crust is defined and altered by plate tectonics, the lunar crust is dominated by impact processes. These have altered the surface of the Moon over most of its lifetime producing a structurally disturbed and fractured crust and producing a layer of regolith, a fine-grained (< 1cm) unconsolidated debris covering the bedrock. Impacts on the Moon occur from impacts of microscopic dust particles onto grains of soil, up to major topographic and structural features hundreds of km across produced from impacting asteroids and comets. The Moon is host to one of the largest impact structures in solar system, the South Polar Aitken basin (SPA). Some of these larger impact basins then serve as sites for later volcanic and tectonic activity.

1.4.2 The lunar core

In other terrestrial planets, the metallic iron in the formation material is thought to have condensed into the substantial (core radius ≈ half planetary radius) observed iron cores. The heats of formation and from radioactive decay have ensured that these outer cores remained partially liquid, even to the present day, and in the case of the Earth and most probably Mars, permitting a planetary dynamo to result.

The size, state and composition of the lunar core, and hence its ability to support a lunar dynamo, is still in debate. A review of seismic measurements, moment of inertia and induced magnetic dipole moment for the Moon placed the size of a conducting core in the range 330-460 km [Hood, 1986]. The lower end of this estimate was reduced further to 220 km from improved moment of inertia estimates [Konopliv et al., 1998], and to 340 ± 90 km from the measurements of the induced dipole moment with Lunar Prospector magnetometer data [Hood et al., 1999]. Such a small core proves problematic when modelling the dynamo potential of the Moon [Stegman et al., 2003] but does not rule it out completely. Also, until recently, there has been a lack of evidence for a fluid metallic core at the Moon [Collinson, 1993]. Recent results from the lunar laser ranging experiment suggest that the outer core may still be partially liquid with energy being dissipated at the boundary between the molten core and a solid mantle [Williams et al., 2001].

If the observed crustal fields require the presence of an ancient lunar dynamo, then this implies the presence of a metallic core and places important constraints on its size and composition, and on the thermal state, formation and evolution of the Moon.

1.4.3 Lunar rocks

The Moon is the only planetary body for which we have samples from known locations. These can act as ground truths for local and regional geology, and magnetic properties. The basic chemistry and types of rock on the Moon are similar to terrestrial rocks. Differences occur due to the lack of atmosphere and water on the Moon and its impact history, and this makes lunar rocks magnetically different to terrestrial rocks.

There are two main geological terrains on the Moon; the highlands and the Maria, and four main types of lunar rock; pristine rocks, basalts, breccias and regolith [Heiken et al., 1991]. The highlands, generally 3 km above the mean lunar radius, are on the southern nearside and on the farside of the Moon. These formed from early melt and are the oldest surfaces and are consequently intensely cratered. Most of the rocks in the highland region have undergone extensive shattering or melting from meteoroid impacts, forming breccias and contributing to the lunar regolith. Highland material that remains unshattered is known as pristine lunar rock.

The lunar Maria were formed later from episodes of melting and volcanic eruptions of low viscosity basaltic lavas infilling some of the large impact craters. These are much younger at about 2-3 Ga and are nearly all on the nearside of the Moon, visible as the smooth dark regions. Lunar basalts are very similar to terrestrial basalts.

Lunar breccias are made up of fragments of older rocks that have been shattered, crushed and melted by meteoroid impacts and lithified or welded by shock. These are analogous to the products of meteorite impacts on Earth. Large impacts also result in ejecta deposits which can cover large areas of bedrock with ejecta blankets 2-3 km thick. This ejecta debris and the underlying bedrock are usually

covered by a layer of lunar regolith. The lunar regolith also results from impacts, both large and small, and the steady bombardment of the lunar surface by solar wind particles. Regolith is a complex mixture of rock fragments and impact glasses and covers most of the Moon's surface with a thickness between metres and tens of metres, with the near surface (~10 cm) uniformly mixed (gardened) by small and frequent impacts. The regolith also contains large boulders of the local bedrock and distal bedrocks from impact ejecta, allowing samples of different rock types to be collected from a limited number of landing sites.

1.5 Magnetisation

Magnetisation, **M** (Amperes per metre, A/m) is the magnetic dipole moment per unit volume of magnetised material [Lorrain et al., 1988]. Magnetisation direction can be defined by its inclination I_j (angle down from the horizontal) and declination D_j (angle clockwise from north) (Figure 1.5).

$$\tan I = \frac{-m_r}{\sqrt{m_\theta^2 + m_\phi^2}} \qquad (1.5a) \qquad \tan D = \frac{m_\phi}{-m_\theta} \qquad (1.5b)$$

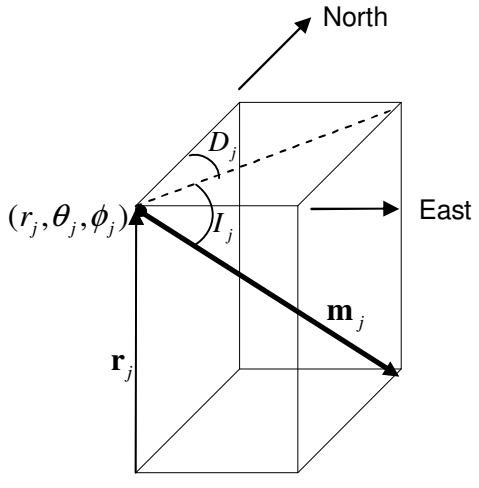

Figure 1.5: Magnetisation direction defined by declination and inclination. (Unit vectors in spherical coordinates with r outward, θ southwards, and ϕ eastward).

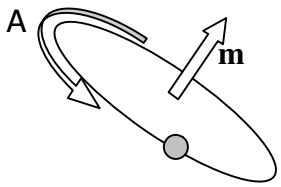

Figure 1.6: Schematic of a fundamental magnetic dipole **m** resulting from a current A from an orbiting electron.

Magnetisation results from the vector addition of magnetic moments **m** from individual atoms within a volume *V*:

$$\mathbf{M} = \frac{\sum_j \mathbf{m}_j}{V} \tag{1.6}$$

The magnetic moments of individual atoms result from the precession of each orbiting electron (Figure 1.6), and take no energy to sustain. For any one atom, these may be in an arbitrary direction or may add up to give an atomic magnetic moment.

1.5.1 Induced and remanent magnetisation

In the presence of a weak magnetic field **H** (~Earth's magnetic field magnitude), any material can acquire an induced magnetisation **M** which is proportional to the inducing field:

$$\mathbf{M} = \chi\mathbf{H} \tag{1.7}$$

The magnitude and direction of the magnetisation is determined by the constant of proportionality χ, the magnetic susceptibility. Magnetic susceptibility is the 'ease with which a material is magnetised' [Dunlop and Özdemir, 1997] and depends on the size, shape and mineralogy of the magnetic particle, the temperature, and the strength of the magnetising field. For most materials, χ is very small (typically on the order of 10^{-5}), and negative (diamagnetic) so that the induced field is anti-parallel

to the inducing field (due to the precession of electrons in the direction of the applied field producing a field in the opposite direction). For atoms with existing magnetic moments, these can align partially with the applied field, causing the material to acquire a large induced magnetisation parallel to the applied field (paramagnetic).

An induced magnetisation exists as long as an external field is present. When this field is removed, it will usually disappear as the randomness returns to the individual atomic moments. However in some materials, the atomic moments can align fully with the external field producing a large magnetisation, and under certain conditions this magnetisation can be 'frozen' into the rock, remaining after the external field is removed. This is known as a natural remanent magnetisation (NRM). This magnetisation can be strong due to the interaction between neighbouring atoms that forces their magnetic moments to align (ferromagnetism), or alternately align with different amplitudes (ferrimagnetic) or directions (antiferrimagnetic).

There is no simple relationship for a remanent magnetisation like equation 1.7 for induced magnetisation. The direction of a remanent magnetisation can be assumed to be parallel or anti-parallel to the direction of the magnetising field (paleo-field), but the magnetisation amplitude is a complicated function of the magnetising field described by a 'hysteresis curve', illustrated in figure 1.7.

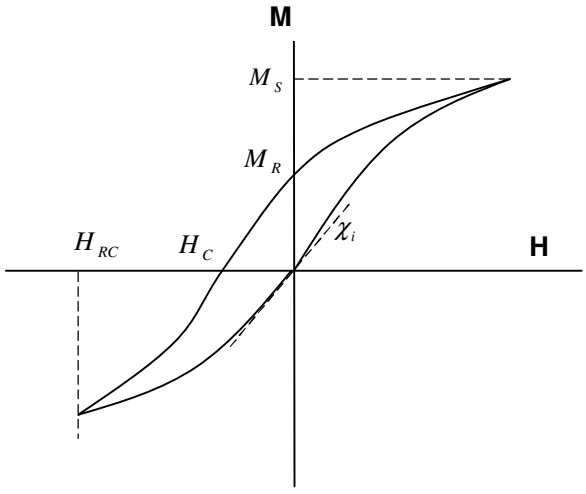

Figure 1.7: Schematic hysteresis curve for a sample with initial susceptibility χ_i, showing remanent magnetisation M_R, saturation magnetisation M_S, coercive force H_C, remanent coercivity H_{RC}.

The remanent magnetisation M_R remaining when a magnetising field is reduced and removed depends on the strength of the magnetising field, the initial susceptibility χ_i, and on the saturation magnetisation M_S (the strongest magnetisation that can be attained). If the external field is not sufficient for the saturation magnetisation to be reached then there is a different hysteresis curve with a weaker remanent magnetisation.

The relative importance of remanent magnetisation and the induced magnetisation $\mathbf{M}_i$ is expressed by the Koenigsberger ratio, Q:

$$Q = \frac{|\mathbf{M}_R|}{|\mathbf{M}_i|} = \frac{\mathbf{M}_R}{\chi \mathbf{H}} \tag{1.8}$$

The value of Q is very variable, depending on the different strengths and orientations of the magnetising and inducing fields, and the types of magnetic minerals, so that in some regions, the magnetisation can not be assumed to be parallel to the main field.

1.5.2 Mechanisms for remanent magnetisation

The 'freezing in' of acquired magnetisation to produce a remanence requires a mechanism. Magnetic carriers (ferromagnetic, ferrimagnetic and antiferrimagnetic) within rocks can retain a magnetisation through many processes (see for example Dunlop and Özdemir, 1997), but for the lunar case, the most probable mechanisms are thermo remanent magnetisation (TRM), shock remanent magnetisation (SRM) or isothermal remanent magnetisation (IRM).

Thermo remanent magnetisation is produced when a rock cools through the Curie temperature in the presence of a steady field. The Curie temperature is different for different materials, and is in the range ~500-700°C for the most common terrestrial magnetic minerals [e.g Dunlop and Özdemir, 1997]. The magnetisation is parallel (or anti-parallel) to the field, and the intensity is proportional to the strength of the field.

Shock remanent magnetisation is caused by shocking of a material in the presence of a magnetic field. Shock waves from impacts on the Moon can have pressures of several GPa, generating strong and stable SRMs [Cisowski et al., 1975]. Shock can also induce chemical or phase changes. Higher pressures from high impact velocities will cause melting, vaporisation or even ionisation of the projectile and target, opening the possibility for TRM. TRM requires the presence of a magnetic field for all or most of the duration of the cooling (which can be significant), while the magnetising field for SRM only has to exist while the shock wave passes through the rock.

Isothermal remanent magnetisation (IRM), or viscous magnetisation (VRM) is a magnetisation which is 'frozen in' without any change in temperature or pressure. This requires a strong magnetic field such as that from a planetary dynamo. The magnetisation is acquired as a linear function of log of time in an ambient field and is in the same direction as the field. Short term exposure to a strong (>1 mT) field can also result in an IRM. This was demonstrated by Strangway et al. (1973a) when (demagnetised) Apollo samples were exposed to strong magnetic fields on their return trip to Earth resulting in an IRM.

On Earth, IRM and TRM are the dominant forms of magnetisation, acquired in the presence of the strong, slowly varying global magnetic field, resulting in very high values of magnetisation. Wasilewski and Mayhew (1982) gave magnetisation values of up to 11 A/m for terrestrial crustal xenoliths, and values as high as 20 A/m have been reported for young mid-ocean ridge basalts [Nazarova, 1994]. For the Moon, the remanent magnetisations from IRM are not as strong, or stable, as those from TRM and SRM [Cisowski et al., 1973].

1.5.3 Demagnetisation

Processes which magnetise rocks can also alter or remove a remanent magnetisation. When a magnetised rock is heated or shocked, the remanence can be altered or removed. Heating such as from volcanism or other igneous or tectonic processes reduces the alignment of magnetic moments by thermal agitation. Above

the Curie temperature (or Néel point for ferrimagnets), there remains only partial, or no alignment, and the remanent (or induced) magnetisation is effectively destroyed. If there is no longer an ambient field then when this sample cools, or is shocked, it will no longer be magnetised.

If the ambient field changes (or if the rock is rotated), long term exposure to a field can also change or remove the magnetisation. The value of the field which reduces the magnetisation to zero is known as the coercive force H_C (see figure 1.7), and that which reverses the polarity of the saturation remanence is the remanent coercivity H_{RC}. An applied field with $H_{RC} > H > H_C$ will leave the rock with a non-zero remanent magnetisation in the opposite direction to that it had previously.

1.5.4 Magnetic minerals

Minerals capable of carrying an NRM for crustal magnetisation contain iron. These minerals are generally only a small percent (per volume) of a rock, and their magnetisation will depend on the shape and size of the grains as well as their magnetic history. Ferromagnetic materials such as metallic iron and nickel can carry the strongest magnetisations, while ferromagnetic and antiferrimagnetic materials such as some iron oxides, hydroxides and sulphides retain less, though still measurable, magnetisation. The magnetic properties of rocks can be quite variable and are not necessarily predictable by the rock type.

On Earth and Mars with oxidising atmospheres, the dominant magnetic carriers are iron oxides (with some titanium). For Earth, magnetite and its solid solutions with ulvöspinel are the most important magnetic minerals. The most strongly magnetised terrestrial rocks are mid-ocean ridge basalts where magnetite can form from hydration of basaltic crust (serpentinisation). Remanent magnetisations of these basalts can reach 20 A/m, but subsequent alteration of the magnetic grains reduces the magnetisations to 1-5 A/m [Nazarova, 1994]. In some terrestrial cases, hematite, pyrrhotite, and alloys of iron and nickel also contribute to the remanent magnetisation. Hematite, pyrrhotite, magnetite and metallic iron have been identified as magnetic carriers in Martian meteorites [van de Moortèle et al.,

2007, Rochette et al., 2005] and hematite has been detected at the surface of Mars [Christensen et al., 2001].

1.5.5 Magnetic properties of lunar rocks

The magnetic properties of the lunar rocks returned by the Apollo missions were studied in great detail by a variety of authors with the results summarised by Fuller and Cisowski (1987). The main magnetic carriers of NRM in lunar rocks are very different to those on Earth. The lack of water and oxygen on the Moon means that the iron in lunar rocks does not generally occur in iron oxides as on Earth, but as metallic iron. It is this metallic iron, Fe^0, mostly in the form of fine particles (single domain, uniformly magnetised), sometimes alloyed with nickel or cobalt or sulphur, that is the dominant magnetic carrier in lunar rocks [Fuller, 1974]. Some other magnetic minerals such as magnetite, titanomagnetite, ilmenite or spinel may be present, but it is the ferromagnetic iron and its alloys that carry the strongest remanent magnetisations.

Lunar soils and impact breccias can contain 0.1-2% metallic iron [Nagata et al., 1972, Lucey et al., 2006]. This iron is derived from the bedrock and is also added to the soils during impacts, such as in the reduction of iron-bearing phases in the presence of solar wind hydrogen [Housley et al., 1973] and also delivered in the meteoritic impactors. The iron in the lunar breccias gives them the largest measured NRMs with average mass normalised dipole moments of 10^{-3} Am^2kg^{-1} and largest normalised values up to 10^{-1} Am^2kg^{-1} [Fuller and Cisowski, 1987]. Much of the iron in the lunar soils however is in a 'superparamagnetic' state, which means that it cannot hold a remanent magnetisation [Nagata et al., 1970]. The Mare basalts contain iron bearing minerals but very little metallic iron, giving them lower NRM values at 10^{-3} - 10^{-7} Am^2kg^{-1}.

For most of the Apollo samples, both initial and recent paleomagnetic studies have not been able to establish if the NRM was of TRM or SRM in origin, and it is likely to be a combination of both [e.g Lawrence et al., 2008]. The lunar samples are

also susceptible to IRMs during transit to, and storage on Earth [Strangway et al., 1973a].

1.5.6 Paleointensities

A single rock can experience several episodes of magnetisation or demagnetisation, acquiring 'secondary' or even 'tertiary' 'overprinting' magnetisations. The natural remanent magnetisation of a rock is the vector sum of each episode of magnetisation and demagnetisation so that the rock retains a record of its history and the magnetic fields it has been exposed to. If the NRM is of TRM (or IRM) origin and has not been altered since its acquisition, the magnetisation can be related to the paleointensity, the intensity of the past magnetising field, through the hysteresis curve. The relationship between SRM and paleointensity is not, however, quantifiable.

Initial paleointenity studies of the Apollo samples, summarised in Fuller and Cisowski (1987) gave a variety of field magnitudes for rocks of different ages (measured with radioactive age determination techniques), plotted in figure 1.8.

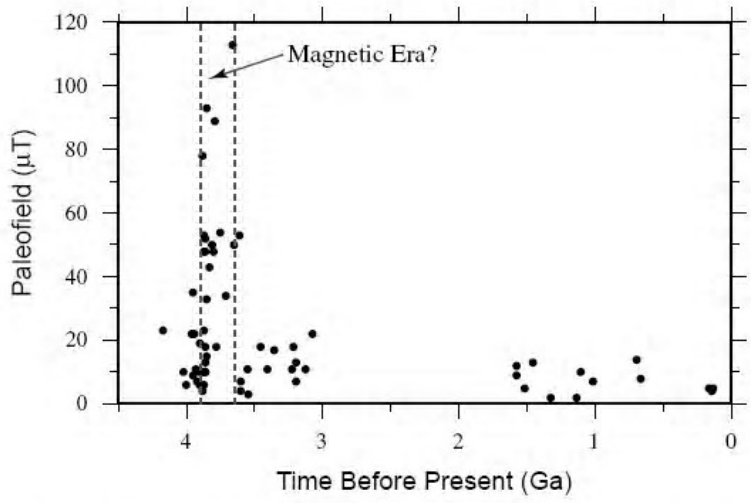

Figure 1.8: Paleointensities of the lunar magnetic field as a function of time inferred from the NRM of lunar samples. (From Wieczorek et al. (2006), based on data taken from Fuller and Cisowski (1987)).

Large paleointensities during the period 3.9-3.6 Ga were interpreted by many as indicating a short-lived lunar dynamo [e.g Fuller, 1998, Collinson, 1993] with lunar surface fields as strong as 10-100 μT, comparable to the magnitude of the Earth's surface magnetic field today.

However, a recent re-examination of the original paleointensity data raised some concerns over the reliability of many of these values due to measurement techniques, age determination of the remanence, and overprinted magnetisations [Lawrence et al., 2008]. Most of the Apollo samples have experienced some sort of impact related shock, perhaps resulting in their strong NRMs, and the period of increased field intensity inferred initially also coincides with the formation of the large impact craters, and a time of increased incidence of impact cratering [Cohen at al., 2000]. However, strong SRM should also occur over the rest of lunar history and the strong NRMs in this period especially may be consistent with a low intensity component of TRM acquired in a weak (few μT) field accompanied by a strong SRM [Fuller and Halekas, 2008].

Lawrence et al. (2008) made four new paleointensity measurements for different samples (with inferred TRM only) covering the time period 3.3-4.3 Ga using modern absolute and relative measurement techniques and these new measurements do not support the existence of 100 μT surface fields from a lunar dynamo in this period. Another recent paleointensity measurement from the oldest known unshocked lunar sample with TRM gave a paleointensity of at least 1 μT at ~4.2 Ga [Garrick-Bethell et al., 2009]. Studies of this sample revealed it had cooled slowly in a stable and strong magnetic field, supporting the existence of a long lived dynamo rather than transient magnetic fields from impact processes.

1.5.7 Paleopoles

On Earth, magnetised rocks are collected from geological units with known orientation, and their direction of magnetisation is used to determine the position of the pole of the assumed dipolar magnetic field in which they were magnetised. Paleopoles are used in the construction of ancient tectonic motions and polar wander.

The Apollo samples were not collected from lunar bedrock so can not offer information on lunar magnetisation directions.

For Mars and the Moon, paleopole locations can be estimated from magnetised regions if it is assumed they were magnetised in a dipolar dynamo field. Bulk magnetisation directions for isolated anomalies have been used to infer paleopole positions with varying degrees of confidence for Mars [Hood and Zakharian, 2001, Arkani-Hamed and Boutin, 2003, Langlais et al., 2004], and also for the Moon [Runcorn, 1980]. However, a review of paleopole locations for Mars [Ravat, 2006] showed that the paleopole locations are very much dependent on how the anomalies are modeled.

1.6 Aims and outline of this thesis

This thesis uses lunar crustal magnetic field data from the LP MAG and ER to produce the first global magnetisation models for the lunar crust, and the first regional magnetisation models produced from both the MAG and ER data. The aims of this thesis are:

- To quantify the magnetisation of the lunar crust in terms of the magnetisation magnitude and direction of sources.
- To develop an inverse method utilising both the vector MAG data and scalar ER data in the production of magnetisation models.
- To contribute to the understanding of the origin of lunar magnetism.

The present state of knowledge of lunar crustal fields, and the LP instruments and data sets are discussed in Chapter 2. After introducing the modelling methods used in this thesis in Chapter 3, the ‘equivalent source dipole’ and ‘spatially continuous’ methods of magnetisation modelling are discussed and implemented in Chapters 4 and 5 respectively to produce global and regional magnetisation models from the MAG data. Chapter 4 also includes a discussion on the ambiguity in magnetisation distributions and the determination of source parameters using forward

models. Chapter 6 then introduces a method for inversion with the scalar ER data, producing magnetisation models for a well known lunar magnetic anomaly, Reiner Gamma, from the ER data and jointly with the ER and MAG data.

The outcomes of the different modelling techniques are discussed in Chapter 7, comparing lunar crustal magnetisation with magnetisation models for the Earth and Mars, and making suggestions for further work. Chapter 8 then concludes with the implications of these magnetisation models for the aims of this thesis.

Chapter 2

The lunar magnetic field

Before the Apollo missions, the Moon was considered magnetically uninteresting. Magnetic field measurements from the Luna and Explorer missions showed no evidence of a global lunar magnetic field [e.g Dolginov et al., 1966]. The surprising discovery of large natural remanent magnetisations of the returned Apollo 11 samples [Runcorn et al., 1970] prompted the study of the lunar magnetic field resulting from these remanently magnetised rocks. Subsequent Apollo missions took magnetometers to the surface of the Moon to measure in situ crustal fields and the permanent and induced magnetic fields on the Moon. Later Apollo missions also included magnetometers on orbiting subsatellites. Analysis of all the Apollo data and samples revolutionised thoughts about the Moon and its magnetic history.

2.1 Observations of the lunar magnetic field

The first evidence of large scale crustal magnetic fields on the Moon came in the form of perturbations to the interplanetary magnetic field measured with Explorer 35 in the lunar wake and close to the lunar limb (near the terminator) [e.g Mihalov et al., 1971, Russell and Lichtenstein, 1975]. Source regions were identified as the lunar farside and highlands which were later confirmed from magnetometers on the Apollo 15 and 16 subsatellites and electron reflectometry (ER) measurements [e.g Russell et

al., 1977, Lin et al., 1976]. The Apollo subsatellites measured crustal fields from 1-100 nT at 100 km altitude, with the ER technique and surface magnetometer measurements showing even stronger surface fields with much regional variation [Anderson et al., 1975, Lin, 1979, Dyal and Gordon, 1973]. Observations from the Apollo subsatellites were from ~100 km altitude and the low inclination orbits confined observations to within about ± 35° from the equator.

The most recent and complete coverage of the lunar crustal magnetic fields comes from the NASA orbiting satellite Lunar Prospector (LP) (1998-1999). LP measured the magnetic field around the Moon at low altitude with a magnetometer (MAG), and made estimates of the surface field magnitude with an Electron Reflectometer (ER), providing the first global maps of the lunar magnetic field [Richmond and Hood, 2008, Purucker, 2008, Mitchell et al., 2008]. The Japanese space craft Kaguya (2007-2009), at an orbit of 100 km altitude, also carried a magnetometer (Kaguya-LMAG), and analysis of these data show good agreement with the LP data [Tsunakawa et al., 2010]. The global crustal fields from the analyses of the MAG and ER data by Purucker (2008) and Halekas et al. (2001) respectively are shown in figures 2.1 and 2.2.

The main features of the lunar magnetic field have been known since the Apollo missions, with the global maps from the MAG and ER data revealing additional detail in the low magnetic field regions. Maps of the lunar magnetic field from both the MAG and ER data show concentrations of strong magnetic fields antipodal to the youngest impact basins (these basins and their antipodes are shown by the white and black circles respectively in figure 2.2), and several other isolated strong anomalies. The ER data show very strong surface fields, of up to hundreds of nT in some regions, while the mare-filled impact basins show very weak surface fields.

The total field predicted at altitude from a spherical harmonic model for the Moon (see section 2.6.4) is shown in figure 2.3 (with a different colour scale to figure 2.1), where regions with total field > 5 nT, and more than ~3° in extent in this data set are labelled according to a coincident or nearby feature. Close-ups of the total magnetic field at altitude and the ER surface estimates are given in Appendix 2.

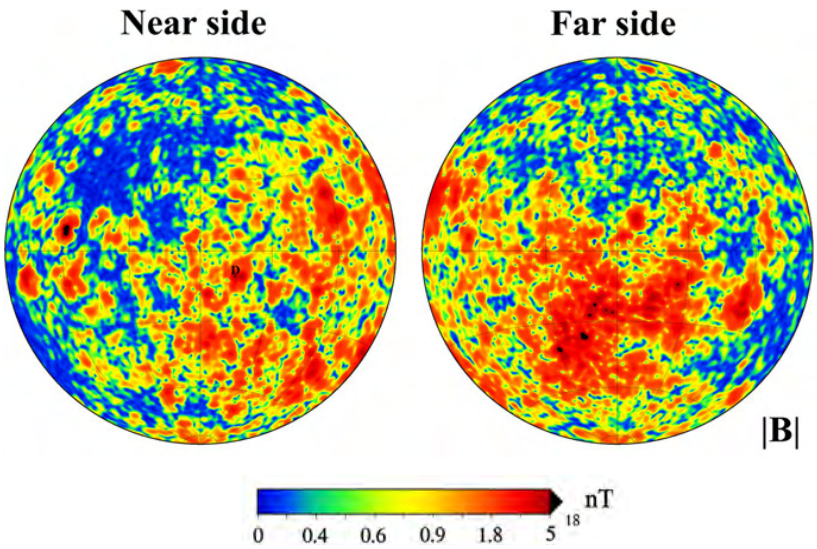

Figure 2.1: Global map of the total lunar crustal field at an altitude of 30 km, produced from a spherical harmonic model of the LP-MAG data (From Purucker (2008)).

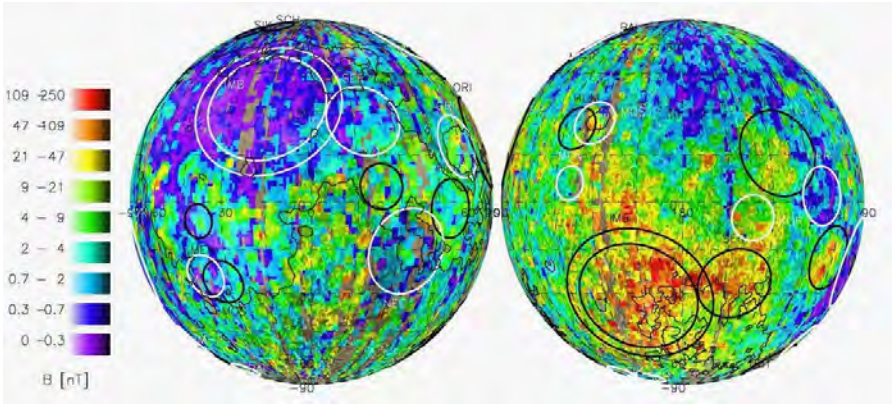

Figure 2.2: Global map of the total lunar crustal field at the surface estimated from electron reflectometry. The locations of major Nectarian and Imbrium aged impact basins (white circles) and their antipodes (black circles) are shown. (From Halekas et al. (2001)).

2.1.1 Impacts and antipodes

The most striking feature of the lunar magnetic field is that the largest concentrations of crustal fields are antipodal to the similarly aged youngest large impact basins of Imbrium, Serenetatis, Orientale and Crisium [Lin et al., 1988, Mitchell et al., 2008]. Analysis of the LP data also showed strong crustal magnetic fields in the region of the antipode of Nectaris [Halekas et al., 2001 and Hood et al., 2001], and many, but not all, of the antipodes of smaller impact basins [Hemant and Purucker, 2008], such as Mare Moscoveinse, close to the antipode of the Humorum basin [Halekas et al., 2003, Richmond and Hood, 2008], not shown in figure 2.3.

While the antipodes of the young impact basins show very strong magnetic fields, the large mare-filled impact basins themselves, and other lunar craters of all ages and sizes, show magnetic lows compared to their surroundings [Halekas et al., 2002], suggestive of shock demagnetisation. Impacts creating craters larger than 50 km diameter are expected to have demagnetised the crust to a depth of 10s of km [Halekas et al., 2001]. However, some older (pre-Nectarian/Nectarian), larger (>50 km diameter) impact basins show weak central magnetic fields, observed with both the ER [Halekas et al., 2003] and the MAG data [Purucker et al., 2006], such as the crater Planck, and Mendel-Rydberg.

2.1.2 Isolated anomalies

Aside from the impact antipodes, it is isolated features which make up the rest of the lunar crustal fields. Named by features they are associated with, or close to, anomalies at Reiner Gamma, a region of high albedo (light coloured), and Rima Sirsalis, a lunar rille, a sinous feature about 300 km long, have been studied since the Apollo era [e.g Anderson et al., 1977, Hood et al., 1979a]. The higher resolution LP data revealed more isolated anomalies, in the Descartes region [Halekas et al., 2001], close to the Apollo 16 landing site where the strongest surface fields were measured, the crater Gerasimovic in the Orientale impact ejecta sheet [Hood et al., 2001], two

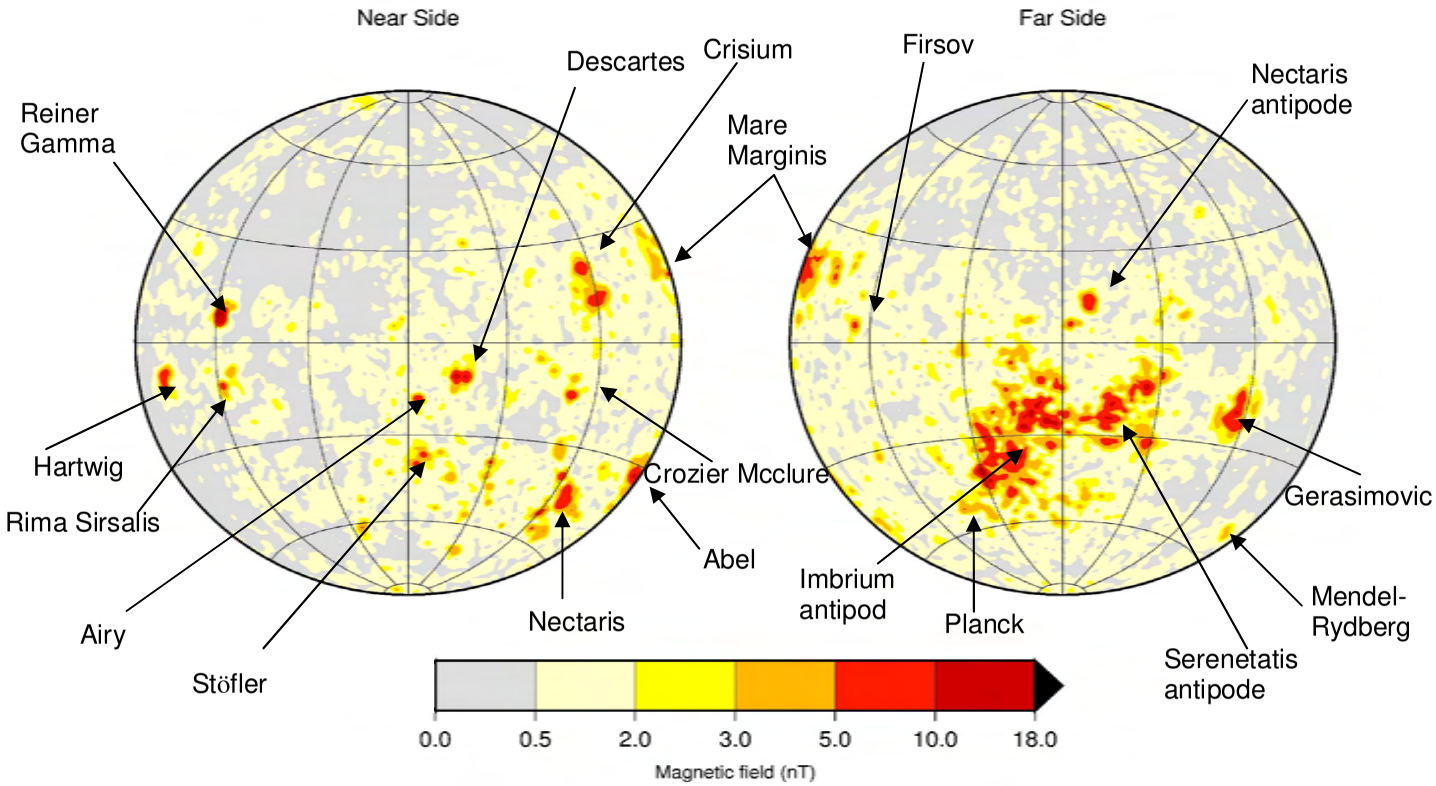

Figure 2.3: Global map of the total lunar crustal field at an altitude of 30 km produced from a spherical harmonic model of the LP-MAG data [Purucker, 2008] with selected regions labelled according to a coincident or nearby feature. (Note the colour scale is different from figure 2.1)

anomalies on the northern and southern edges of the Crisium basin, and Mare Marginis near the Orientale antipode [Richmond et al., 2005]. Richmond and Hood (2008) also identified several previously unmapped anomalies near to craters Abel, Hartwig and Stöfler on the nearside, and near to crater chains associated with the formation of the Nectaris basin.

2.1.3 High albedo features

Another interesting feature of the lunar magnetic field is that many of the strong anomalies are associated with regions of high albedo, often swirl-like in nature [e.g Hood and Schubert, 1980]. These swirls appear to have no topographic expression and are found in both the mare and the highlands, and may also be present on Mercury [Schultz and Srnka, 1980]. Most lunar swirls appear to be associated with high magnetic field regions, but not all high field regions have swirls.

The most famous of the lunar swirls is the Reiner Gamma feature (Figure 2.4), associated with one of the strongest magnetic anomalies on the Moon. The swirl pattern extends hundreds of km and exhibits regions of dark patches within the light areas, coinciding with the strongest magnetic fields.

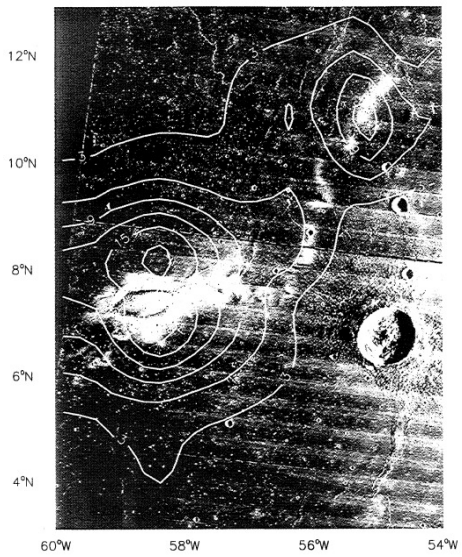

Figure 2.4: Contour map of magnetic field magnitude over the Reiner Gamma region at altitude 18-20 km. Contour interval 3 nT. (From Hood et al. (2001)).

Other high albedo features, though not with such complex swirl patterns, are observed in the Descartes region and near to Airy crater in the centre of the nearside highlands [Richmond et al., 2003, Hughes et al., 2006], and at the antipodes of Imbrium, Crisium, Orientale and possibly Serenetatis [Richmond et al., 2005, Hood and Williams, 1989].

It was initially suggested that the high albedo in these regions resulted from residues of relatively recent cometary impacts [Schultz and Srnka, 1980], with the magnetisation resulting from SRM in magnetic fields within the cometary coma [Gold and Soter, 1976]. Another impact origin theory suggested that meteor swarms could disrupt the regolith bringing lighter material to the surface [Starukhina and Shkuratov, 2004], but no suggestion for the magnetic field generation was proposed.

An issue with the impact origin of the swirl features is that cometary (or other) impacts would be expected to occur randomly on the Moon, not for example, preferentially at an impact antipode. An alternative origin for the lunar swirls is that they result from differential weathering (optical maturation) of the lunar regolith due to deflection of the solar wind particles by the magnetic anomaly [Hood and Schubert, 1980]. Bombardment with solar wind hydrogen and micrometeoroids is thought to darken the lunar surface with time. Strong local magnetic fields may be sufficient to shield the surface from solar wind ions, preserving the higher albedo in these regions. Numerical simulations of solar wind ion deflection by crustal magnetic fields can in principle explain the features of the observed albedo markings [Hood and Williams, 1989]. The swirl markings would then be old features resulting from the presence of the magnetic anomalies, proposed to be due to impact ejecta magnetised in a transient or dynamo field [e.g Halekas et al., 2001, Richmond et al., 2003].

2.1.4 Crustal field directions

The directions of the lunar crustal fields vary in magnitude and polarity over small scales, even below measurement resolution. Figure 2.5 shows the vector components of the lunar crustal field as produced from a spherical harmonic model

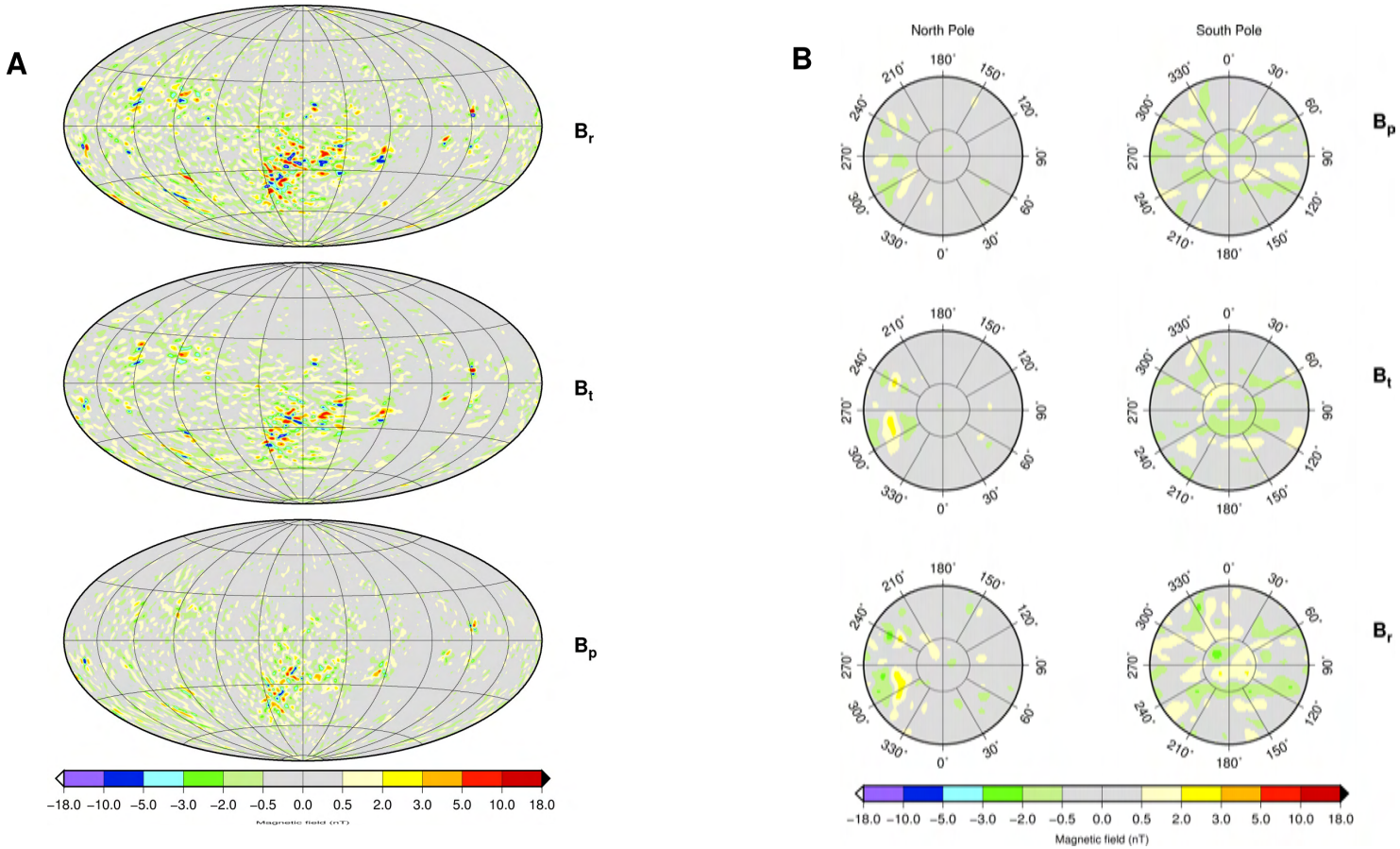

Figure 2.5: Vector components of the lunar crustal field at 30 km altitude, produced from the spherical harmonic model of the MAG data [Purucker, 2008], on 0.25° grid, for A: Lambert projection centred on the far-side, and B: polar regions from ±75° latitude. (Note the different ordering of the components).

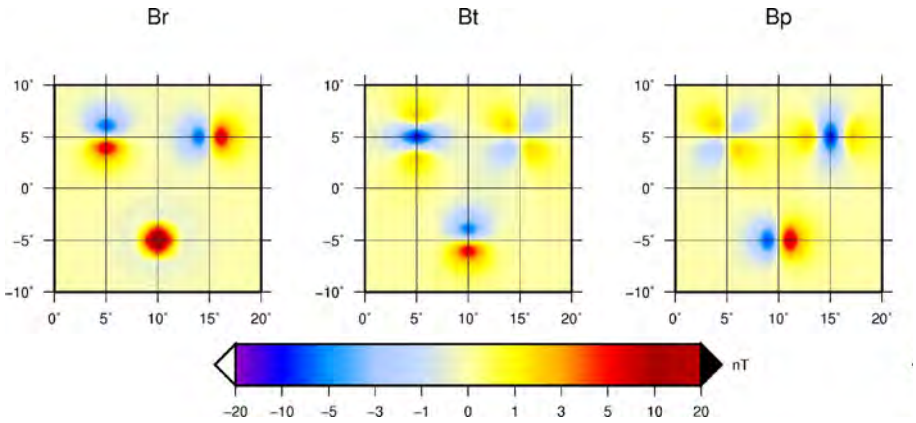

Figure 2.6: The three components of magnetic field for a horizontal (North-South) dipole at (5°N, 5°E), a horizontal (East-West) dipole at (5°N, 15°E), and a radial dipole at (5°S, 10°E).

for the Moon. It is interesting to note that many of the lunar anomalies take the characteristic form of a magnetic field resulting from a small homogeneously magnetised body, shown in figure 2.6 for horizontally and vertically orientated dipoles. These features may be suggestive of uniform magnetisation of sources in these regions, or could result from the coalescence of fields from different sources. Similarly, other anomalies appear to show linear features in one or several of the magnetic field directions which may or may not be related to linear features in the crust.

2.2 Apollo surface data

After Apollo 11, the other Apollo missions took magnetometers to the surface of the Moon as part of the Apollo Lunar Surface Experiments Package (ALSEP) (Figure 2.7). Apollo 12, 15 and 16 took a Lunar Surface Magnetometer (LSM) to continuously measure the surface magnetic field at a fixed location, and Apollo 14 and 16 took portable magnetometers to allow measurement of the surface magnetic field at different locations. These gave a total of nine static measurements of the lunar surface fields at the 4 different landing sites of the Apollo missions (Figure 2.8). As with the fields at the satellite, surface fields are a vector sum of fields of

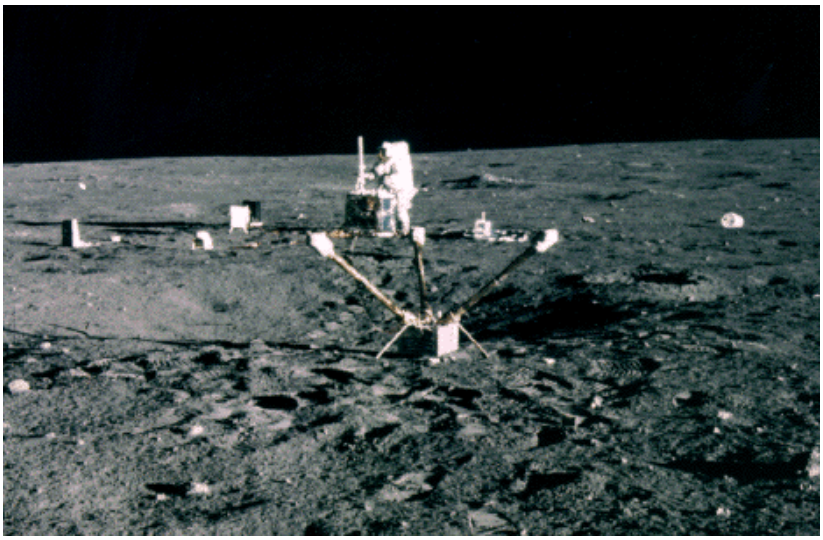

Figure 2.7: The Apollo 12 Lunar Surface Magnetometer, with its three orthogonal fluxgate sensors, deployed on the Moon (Image from the Apollo 12 photo archive, courtesy of the Lunar and Planetary Institute (LPI), Houston, Texas).

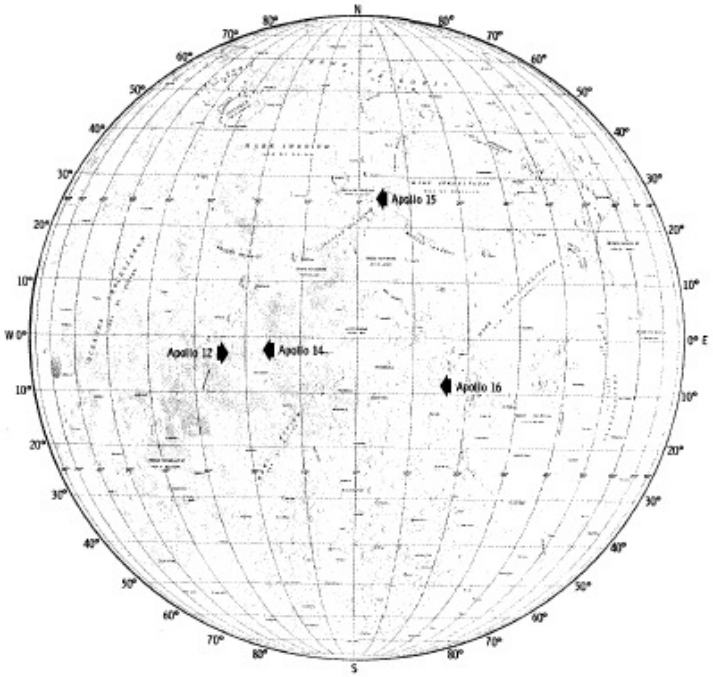

Figure 2.8: The Apollo Landing sites (from the Apollo 16 preliminary science report).

different origin (induced, solar wind, etc) and the crustal magnetic field at these locations was determined by taking time averaged data over a month.

2.2.1 Surface crustal fields

The crustal fields measured at the surface showed great variety in strength and direction both at different sites and at the same sites (see table 2.1). The strongest fields of ~ 300 nT were at the Apollo 16 landing site in a highland region covered with impact ejecta [Strangway et al., 1973b, Dyal et al., 1974], close to the Descartes region later recognised in the LP ER and MAG data. The weakest surface fields were at the Apollo 15 sites, in a mare region. The variation in strength and direction of the surface fields over a distance of only a few km suggest they are associated with strong localised sources of magnetisation close to the surface [Dyal et al., 1970].

Mission	**Region**	**Site**	**Location**	**Field** (nT)	**B_{up}** (nT)	**B_{east}** (nT)	**B_{north}** (nT)
Apollo 16	Descartes *(Highlands)*	ALSEP site Site 2 Site 5 Site 13 Rover Parking Site	8.9°S, 15.5°E (Sites separated by 7.1km)	231 180 125 313 121	-174 -179 120 -141 -42	-73 -10 -25 -209 -93	134 19 -25 -186 66
Apollo 15	Adjacent to Hadley Rille *(Mare plains)*	ALSEP site	26.1°N, 3.7°E	6±4	4±4	1±3	-4±3
Apollo 14	Fra Mauro formation *(Highlands, with bright ray ejecta)*	Landing site Site A Site C	3.7°S, 17.5°W (Sites separated by 1.2 km)	 103±5 43±6	- 93±4 - 15±4	 38±5 - 36±5	 -24±5 -19±8
Apollo 12	Eastern edge of Oceanus Procellarum *(Mare)*	Near to landing site	2.97°S, 23.35°W	36±5	- 26±1	12±1	-26±0.4

Table 2.1: Summary of the surface measurements from the Apollo missions. (The uncertainty in the Apollo 16 values is the largest at ± 25 nT). (Based on tables in Fuller and Cisowski (1987), supplemented with values from the Apollo preliminary science reports).

2.2.2 Interaction with the solar wind

On a planet-wide scale, the lunar magnetic fields are not strong enough to interact with the solar wind to produce a lunar magnetosphere. However, simultaneous investigations of surface magnetometer data and solar wind spectrometer data showed that the surface remanent magnetic fields interact with the solar wind on the day side of the Moon [Dyal and Parkin, 1972]. Measurements from the Apollo era are the only simultaneous measurement of the magnetic field at the lunar surface as well as at satellite altitude, and were also used to measure the fields induced in the Moon by interaction of the solar wind magnetic fields with the electrically conducting Moon.

Lin et al. (1998) also showed the deflection of the solar wind into a mini-magnetosphere several hundred km across at the Imbrium antipode. Numerical simulations of the interaction of the solar wind with lunar magnetic anomalies by Harnett and Winglee (e.g Harnett and Winglee, 2003) showed that localised mini magnetospheres could exist on the Moon. Comparisons of LP-MAG data from different local times also showed the presence of a mini magnetosphere over the Reiner Gamma region [Kurata et al., 2005].

Magnetic fields capable of standing off the solar wind protect the lunar regolith from solar wind bombardment as suggested for the lunar swirls, and can also prevent the implantation of solar wind hydrogen. The coincidence of magnetic fields at the lunar south pole with regions of low neutron content in shadowed craters, has been used to suggest that instead of implanted solar wind hydrogen, these regions may contain water ice [Schaler and Purucker, 2007].

2.3 Theories for the origin of the lunar magnetic fields

The magnetic fields responsible for producing the remanent crustal fields must be able to explain both the presence and the absence of crustal fields in different locations of the Moon and in rocks of different ages. The strong NRMs of the Apollo samples and the large regions of remanent magnetism might suggest the

existence of a past lunar dynamo; however the distribution of the lunar magnetic fields and concerns over some of the measured paleointensities called into question the need for a lunar dynamo in the formation of these features.

It was initially considered that the magnetising fields might have been enhanced early terrestrial or solar fields, however, this was not indicated by terrestrial paleomagnetic studies and such fields would not be steady over long periods of time. It is also conceivable that the crustal fields themselves were then the magnetising fields for other episodes of cooling or shock in an area.

The main theories for the lunar magnetising fields are discussed below. Each have shortcomings for satisfactorily describing all of the lunar crustal fields, and it is likely that a combination of different fields and mechanisms are required to explain the lunar crustal fields, with or without the need for a dynamo field. Given the highly cratered surface of the Moon, it is likely that impact processes are an important feature of lunar magnetism.

2.3.1 A dynamo field

If it were not for concerns over the ability of the Moon to support a lunar dynamo, it would be convenient to suggest that the lunar crust became magnetised in the presence of a global field from a lunar dynamo that is now extinct. Models of impact generated magnetisation and demagnetisation of a previously homogeneously magnetised crust have been shown to explain many of the larger features of lunar magnetism [Halekas et al., 2000 and Runcorn, 1975]. However, the magnetisation of antipodes without the magnetisation of impact basins of the same age casts some doubt on a dynamo field being responsible for all of the lunar crustal fields. Such large surface fields on a small body inferred to be responsible for the remanent fields, also present problems for a dynamo field given current dynamo theories [Stegman et al., 2003].

Though inconclusive, the ages of the magnetised areas and Apollo samples suggest the existence of a brief ‘magnetic era’ on the Moon from Pre-Nectarian to Imbrian times, ~3.6-3.9 Ga ago. The apparent demagnetisation of impact craters of

all ages requires a pre-magnetised crust from as far back as Pre-Nectarian times. The absence of anomalies within Imbrian and younger aged basins, and the apparently unmagnetised mare basalts, show that the field had disappeared by about 3.5 Ga, perhaps due to altered mantle convection patterns caused by the large impacts of Nectarian and Imbrium periods.

2.3.2 Antipodal enhancements

The association of lunar magnetic fields with impact antipopes has been explained by antipodal focussing of impact generated plasmas and amplification of an ambient magnetic field [Hood and Vickery, 1984, Hood, 1987, Hood and Huang, 1991]. The highly conducting plasma cloud produced by the excavation and vaporisation of material in a hyperveolocity (> 10 km/s) impact expands around the Moon, interacting with and compressing an existing magnetic field, amplifying it at the antipode (Figure 2.9). The surface field amplification is such that the ambient field does not have to be large so this mechanism does not require an existing dynamo field, but also does not rule out the existence of a dynamo field.

The impact ejecta also converges at the antipode producing high pressures (5-25 GPa) capable of shock magnetising the deposited impact ejecta [Hood and Artemieva, 2008]. Compressional seismic waves also converge at the antipode and unusual grooved terranes in the antipodal regions of Imbrium, Orientale, Serenetatis and Crisium [Richmond et al., 2005, Hood and Williams, 1989] are interpreted as being impact ejecta or resulting from the convergence of seismic waves [Schultz and Gault, 1975]. The seismic waves can also shock magnetise the antipode basement at depth and in this way the antipode geology may influence the final strength of the anomaly. For example, the strong magnetic field antipodal to Imbrium and Serenitatis coincides with the edge of the large South Pole Aitken basin, likely to contain more metallic iron from the impact, and the Crisium antipode is near to the crater Gerasimovic and the Orientale ejecta sheet. The absence of appreciable anomalies at many other antipodes may also be a consequence of the lack of magnetic material at those sites.

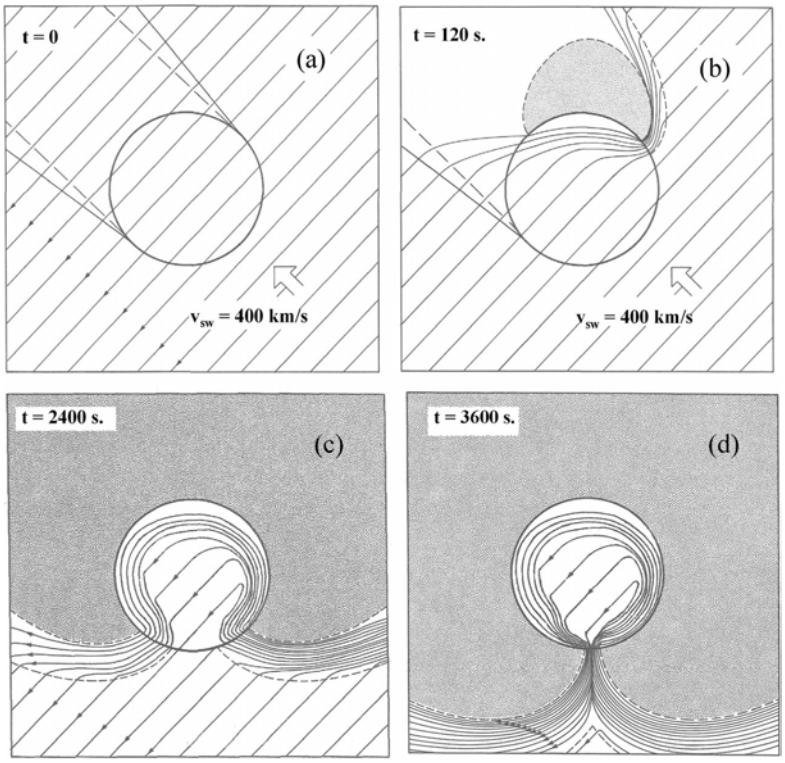

Figure 2.9: Schematic diagram of the interaction of an expanding impact vapour cloud (shaded) with a solar wind plasma (SW, incident at 400 km/s) and ambient magnetic field (parallel lines). (From Hood and Artemieva (2008)).

2.3.3 Impacts

Impacts can demagnetise or modify an existing magnetisation by shocking, heating or excavation [Langlais et al., 2009], and can produce and distribute metallic iron remanence carriers. Hypervelocity impacts are also capable of producing large transient magnetic fields [Srnka, 1977, Crawford and Schultz, 1988] which could magnetise the impact area. Transient fields generated by impacts are generally only surface fields and are only present for ~1 day. While this is long enough for micron sized iron grains to acquire a shock or rapid thermal remanence, large amounts of material would not become magnetised by TRM or SRM [Halekas et al., 2001], requiring instead a longer lived magnetic field in which to acquire a magnetisation of the impact melt. Some terrestrial impact craters are associated with magnetic features

[Pilkington and Grieve, 1992], but the magnetisation mechanism (SRM or TRM) is not conclusive.

While many of the lunar magnetic anomalies are associated with impacts or impact ejecta (see section 2.4), transient fields alone may not be sufficient to be able to explain all of the features of the lunar crustal field.

2.4 Sources for the magnetic anomalies

Beyond the general trend of the younger mare showing weaker fields than the older highlands, and the correlations with some impact basins and antipodes, there is little correlation of magnetic features with lunar geology. There is also little correlation of the observed fields with iron content derived from spectral studies [Lucey et al., 1995]. Joint analysis of lunar magnetic anomalies and topography [Frey et al., 2002], and gravity anomalies [Milbury et al., 2008] also did not show any clear correlation that might be expected for magnetised subsurface features.

The superposition of multiple episodes of magnetisation and demagnetisation, and the coalescence of magnetic fields from multiple sources complicates the determination of the sources. For example, the anomaly at the Imbrium antipode is also on the north west edge of the South Pole Aitken basin, the anomaly at the Crisium antipode is on the western edge of the Orientale impact ejecta sheet, and the magnetised Mare Marginis is in the vicinity of the Orientale antipode.

An initial suggestion that the main sources of lunar magnetic anomalies were impact ejecta [Strangway et al., 1973b, Hood et al., 1979b] was confirmed with recent studies attempting to link the location of the fields to geological features or materials [Halekas et al., 2001, Richmond et al., 2005].

2.4.1 Statistical studies

Statistical studies to identify the magnetic sources from lunar geological maps and photographs [Hood and Williams, 1989, Halekas et al., 2001, Richmond et

al., 2005], showed that most lunar anomalies were coincident with regions of impact ejecta. The antipodal regions were also correlated with high albedo regions, and ejecta and grooved terranes modified by seismicity [Moore et al., 1974, Schultz and Gault, 1975]. The association of magnetic anomalies with impacts is not necessarily surprising given that the magnetic carriers in lunar rocks are concentrated in impact breccias. The strongest surface fields (Apollo 16) were also in a region dominated by impact ejecta.

2.4.2 Isolated sources and impact ejecta

Many of the isolated anomalies have also been linked to basin ejecta and basin forming processes. The Descartes anomaly is associated with the Fra Mauro and Cayley formations which are primary and secondary ejecta from the Imbrium basin [Richmond et al., 2003]. Rima Sirsalis and Reiner Gamma are also approximately radial to the centre of the Imbrium basin, on an area that is likely to be impact ejecta [Hood et al., 2001].

The magnetic anomaly at Rima Sirsalis was originally thought to originate from the rille itself [Anderson et al., 1977], as a 'gap' in a uniformly magnetised crust or as the surface expression of a subsurface dyke [Srnka et al., 1979]. However, new observations from LP showed that the magnetic feature extended beyond the rille [Hood et al., 2001] and no other lunar rilles had associated magnetic fields [Halekas et al., 2001].

For magnetised regions where no ejecta are observed, the ejecta sources could be buried [Hood et al., 2001], or the source may be altogether different. For example, the strong arcuate magnetic features in the SPA region were suggested to be due to cross-cutting dykes perhaps infilling fractures produced from the large impact [Purucker et al., 2006]. Some ejecta blankets, such as Nectaris and Orientale are less magnetic, and the different field strengths of different regions could be attributed to compositional differences in the ejecta [Korotev, 1994].

2.4.3 The lunar mare

Both the MAG and ER data show very weak fields in the mare regions. Mare lava flows are not expected to demagnetise the crust beneath them, suggesting that the basins beneath them are not magnetised [Halekas et al., 2001]. However, weak fields over the mare could also mean that they are uniformly magnetised. Mitchell et al. (2008) calculated a very weak magnetisation for Mare Imbrium based on the fringing fields of craters within this basin, assuming it was uniformly magnetised. The fact that the mare are generally very thin (~500 m on the nearside [Heiken et al., 1991]), means that they could in fact be magnetised without producing observable anomalies [Wieczorek and Weiss, 2010].

2.5 The Lunar Prospector Magnetometer and Electron Reflectometer

The satellite Lunar Prospector, a NASA discovery mission, was launched on the 7th January 1998. This was the first lunar mission in 25 years to carry a magnetometer, along with 5 other instruments (including the Electron Reflectometer) [Binder, 1998]. The mission consisted of a 1 year primary mapping phase with the satellite in a near-circular polar orbit with a nominal altitude of 100 km and an extended phase with an elliptical orbit at a lower altitude (15-45 km) to perform higher resolution studies. The lower altitudes, with an average altitude of 30 km, offers better opportunities for resolving the crustal magnetic field. The 19 month mission ended on the 31st July 1999 with LP intentionally impacting into a crater near the South Pole.

2.5.1 The Lunar Prospector satellite

The LP satellite was a small, spin-stabilised drum shaped orbiter with three radial 2.5 m instrument booms to isolate instruments on them from spacecraft electronics and magnetic fields (Figure 2.10). The MAG-ER instrument was situated

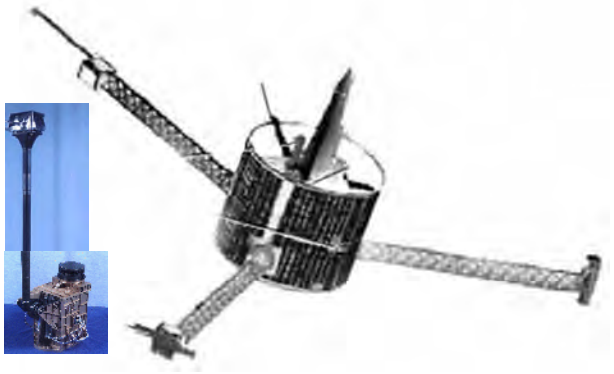

Details:
Mass (fully fuelled): 296 kg
Nominal spin rate: 12 rpm
Dimensions (of drum):
1.37m diameter, 1.28 m high
Boom length: 2.5 m
Primary mapping phase:
Orbit inclination 89.8°
Period: 118 minutes
Orbital velocity: 5,517 km/hour

Figure 2.10: An artist's impression of the satellite Lunar Prospector with inset, the MAG/ER instrument.

on the end of one of these booms, with the magnetometer extending 1.1 m from the ER instrument (Figure 2.10, inset). The LP orbit was designed so that the equatorial longitude crossing advanced approximately 1° per orbit. With an orbital period of 118 minutes, this means that during one day, LP mapped a 12-15° wide longitude swath on each side of the Moon and covered the Lunar surface twice a month.

2.5.2 The Magnetometer

The LP-MAG was similar to magnetometers on MGS (and previous missions such as Voyager, Magsat and Giotto), especially developed for low noise high stability applications [Acuña, et al., 1992]. The LP magnetometer was a tri-axial fluxgate magnetometer, able to measure three orthogonal components of the magnetic field. Each axis of the tri-axial fluxgate magnetometer utilised a ring-core geometry (Figure 2.11). This is sensitive to an external field, $\mathbf{B_o}$, parallel to the core. A toroidal ferromagnetic core (molybdenum-permalloy) is driven to magnetic saturation in alternate directions by a primary (P) driving coil [Ness, 1970]. In the absence of an external field, both halves of the core will saturate (and unsaturate) at the same time resulting in no net change of flux (and hence no induced voltage) in

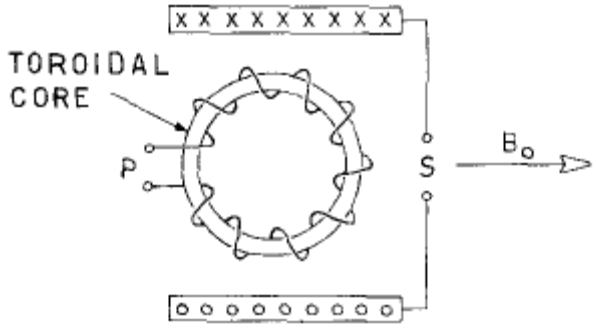

Figure 2.11: Schematic of a single axis of a fluxgate magnetometer sensor with ring-core geometry showing the primary (P) and secondary (S) coils in an external field B_o. (From Ness (1970)).

the secondary (S) coil. However, in the presence of an external field, each half of the core will saturate and unsaturate at different times as the external field adds to or subtracts from the induced field in each half of the core. There is hence a net change in the flux at each driven reversal which induces a voltage in the secondary coil that is twice the frequency of the driving signal [Ness, 1970]. The magnitude of the external field is given from the amplitude, phase and polarity of the induced signal.

2.5.3 Magnetometer sensitivity and resolution

Fluxgate sensors have a high sensitivity over a wide dynamic range with low noise levels, ideal for mapping the weak crustal fields at the Moon. The LP-MAG had a dynamic range of +/- 2 pT to +/- 65,536 nT, with this total range divided into 8 sub-ranges so that if the magnitude of the measured vector component exceeds a threshold value, the dynamic range of the magnetometer can be incremented or decremented to maintain a maximum digital resolution.

The noise level of the LP-MAG was low and shown to be stable over many months with a root mean square (RMS) value of 6 pT. The noise level of the instrument is determined by the stability of the zero level (of magnetism in the magnet core), and by the magnitude of the spacecraft's field contribution to each

value. A drift in the zero level, caused by residual magnetism in the magnet core, can be caused by thermal or mechanically induced stresses. The spinning of the LP spacecraft assisted in detecting zero level offsets, reducing systematic errors to < 0.5 nT. As well as instrument errors, there may be errors in the field direction due to orientation uncertainty after 'de-spinning' (relating the orientation of the magnetometer to the spacecraft axis), or errors in spacecraft telemetry. The magnetic environment of the satellite will also influence the reliability of the magnetometer measurement.

The magnetometer data were sampled 16 times a second and averaged in 5 second intervals. An RMS field value for the average was calculated as an indication of the field variability during the 5 second window. The spatial resolution of these values depends on the satellite altitude and the along-track and cross-track separations of the measurements. The along-track resolution of the MAG data is defined by the spacecraft trajectory and orbital progression. For a measurement averaged every 5 seconds, the along-track surface distance covered is ~ 7 km (depending on the altitude). This is an estimate of the smallest resolvable feature. The cross-track spacing is defined by the progression of the ground track with each orbit (~ 1° at the equator, ~30 km), and the location of repeat passes providing data at closer locations. Passes with spacing less than the altitude will be sensitive to the same internal signal, giving a resolution similar in magnitude to the altitude of observation.

2.5.4 The Electron Reflectometer

An Electron Reflectometer is a remote sensing instrument which indirectly measures the magnetic field at a planetary surface by detecting electrons reflected from local surface magnetic fields. Ambient electrons from the solar wind move helically along magnetic field lines and are reflected by regions of converging magnetic field lines resulting from magnetised regions of a planetary surface (Figure 2.12). This technique was first discovered using the plasma instruments on the Apollo 15 and 16 subsatellites which observed electrons travelling upwards from the

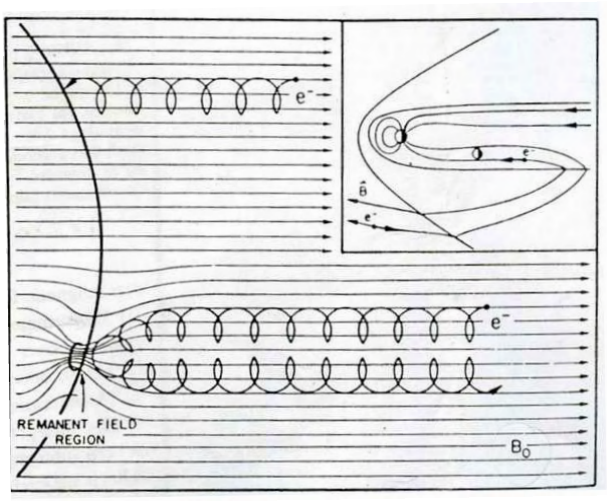

Figure 2.12: Schematic diagram of the reflection of electrons, e, from surface magnetic features, and absorption at the surface, in an ambient field, B_o. The inset shows one method of access of solar and interplanetary electrons into the Earth's magnetotail. (From Anderson et al. (1975)).

lunar surface over some regions of crustal magnetic field [Howe et al., 1974, Anderson et al., 1975].

The LP ER is based on the MGS ER instrument, a hemispherical electrostatic analyser [Carlson et al., 1983] with an inner and outer hemispherical plate with an adjustable positive potential between them (Figure 2.13). Electrons with certain energies (100s eV) and trajectories enter the shell through a hole in the outer plate. The entrance of the analyser is collimated to reduce the contamination from UV photons.

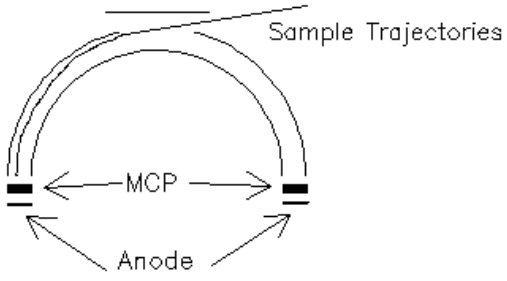

Figure 2.13: Schematic cross section of an hemispherical analyser with anode and microchannel plate (MCP). (From Halekas (2003)).

Electrons are focused onto an annular microchannel plate (MCP) which amplifies the signal, and are detected by an annular anode which determines the impacting position and hence the pitch angles (between the velocity vector of the electron and the magnetic field vector) of the electrons based on the magnetic field direction measured by the magnetometer [Halekas, 2003].

The surface field estimate from the ER is calculated from measurement of the pitch angle of the electron, α (between the velocity vector **v** and the magnetic field vector **B**) (Figure 2.14). The ambient field may be the interplanetary magnetic field or the Earth's magnetotail.

The motion of an electron (of charge q, mass m_e) in a magnetic field is determined by the Lorentz force

$$m_e \frac{d^2\mathbf{r}}{dt^2} = q\mathbf{v}\times\mathbf{B} = qvB\sin\alpha \tag{2.1}$$

so that in a uniform field **B**, the pitch angle is constant. As the electron approaches a surface that is remanently magnetised, converging magnetic field lines cause the pitch angle of the electron to increase (Figure 2.14), and the component of the

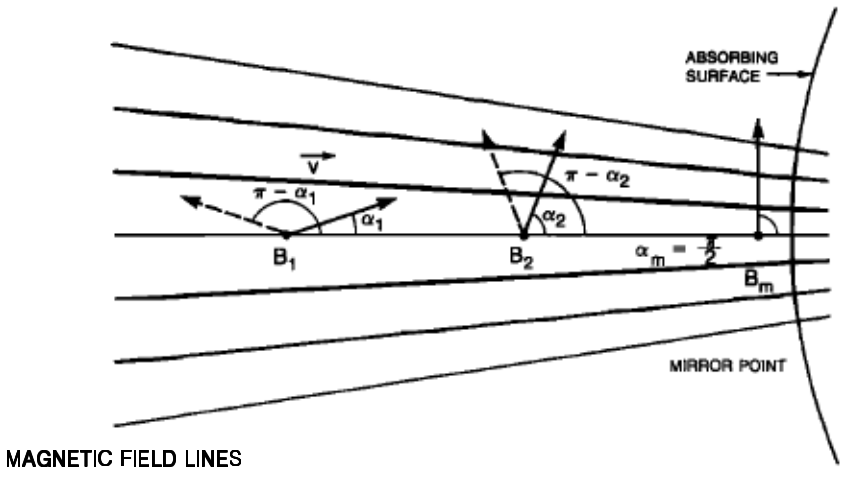

Figure 2.14: The velocity vectors, with increasing pitch angle, of an electron travelling along converging magnetic field lines, and its reflection (dashed lines). (From Acuña et al. (1992)).

electron's velocity parallel to the magnetic field to decrease. When the pitch angle reaches $\pi/2$ radians, the velocity of the electron increases in the opposite direction so that it is reflected back with pitch angle $\pi - \alpha$. This is known as the mirror point.

Conservation of the electron magnetic moment $\mu = {}^{1}\!/_{B}[{}^{1}\!/_{2} m_e v^2 \sin^2 \alpha]$, for an electron of initial incoming pitch angle α_1 in an external field B_1, gives the magnetic field at the mirror point, B_m as:

$$B_m = \frac{B_1}{\sin^2 \alpha_1} \tag{2.2}$$

The point at which the electron reflects depends on the initial velocity (electron energy) and the ambient magnetic field. If B_m is considered the surface magnetic field, for a given B_m and field at the spacecraft B_1, electrons that approach the surface with a pitch angle close to $\pi/2$ (less field aligned) will reflect before reaching the surface, and travel back up the magnetic field line. Electrons with initial pitch angles closer to 0 or π (more field aligned) would have reflected after reaching the surface, so are absorbed by the surface (other than < 5% that are Coulomb backscattered). On Mars, the ER technique detects fields at altitudes of approximately 170 km, due to atmospheric absorption of electrons [Mitchell et al., 2001].

If the pitch angle reaches $\pi/2$ before impact then it is reflected, otherwise it is absorbed. The 'cut-off angle' α_c, above which incoming electrons are no longer reflected, provides an instantaneous value of the ratio of the field at the space craft (provided by the magnetometer) to the field at the surface:

$$\sin^2 \alpha_c = \frac{B_{spacecraft}}{B_{surface}} \tag{2.3}$$

The cut-off angle can be determined from the pitch angle distribution measured with the ER, or can be calculated from the reflection coefficient *R*, the ratio of the upward to downward going flux of electrons, through $R = |\cos\alpha_c|$ [Halekas, 2003].

Assuming that the ambient magnetic field is uniform over distances larger than the distance between the spacecraft and the surface, the crustal magnetic field, B_c is calculated by subtracting the spacecraft field from the total surface field:

$$B_c = \left|\mathbf{B}_{surface} - \mathbf{B}_{spacecraft}\right| \geq B_{surface} - B_{spacecraft} = \frac{B_{spacecraft}}{\tan^2\alpha_c} \tag{2.4}$$

The surface field is a vector sum of the crustal field and the external field (approximately the field at the spacecraft) so a scalar subtraction is a good approximation to the crustal field. As the ER technique can only provide scalar values of surface field, this gives a lower bound estimate of the crustal field amplitude. The surface location of the reflecting point is determined from a straight line extrapolation of the magnetic field vector measured at the spacecraft with the magnetometer, to the surface (for a spherical Moon).

In regions of weak magnetic field (<10 nT), the deflection of electrons by electric fields is also significant. On the sunlit side of the Moon, photoelectrons are ejected, leading to a positively charged surface giving a potential of a few volts. The spacecraft itself can also become charged, distorting the trajectories of lower energy particles. The potential difference ΔU, between the spacecraft and the surface (typically 35 V on the night side, < 1 mV/m for 200 eV electrons) is found using electrons at multiple energies, *E* with different cut-off angles so that the correction for electrostatic reflection becomes

$$B_{crustal} \geq B_{spacecraft}\left[\frac{(1 - e\Delta U/E)}{\sin^2\alpha_c} - 1\right] \tag{2.5}$$

[Halekas, 2003]. Regions of large crustal field do not require correction for the effects of electric fields.

2.5.5 Sensitivity and resolution of the Electron Reflectometer

The ER technique can detect surface fields up to about 250 nT, beyond which the cut-off angle is too small to be resolved. For the electron energies used here (220-520 eV, lower than the Apollo ER), the cut-off angle can be determined to within 1.4° [Halekas, 2003]. The smallest surface fields detectable with the ER technique are ~0.2 nT. Such fields would not be detectable at altitude so the ER provides increased sensitivity for lunar crustal field measurements. However, these are lower bound scalar estimates with no polarity information.

The resolution of the ER technique is in principle determined by the gyroradius of the electron, $R_g = m_e v \sin\alpha / qB$. For typical electron energies in the solar wind and geotail (5-10 nT) this is as low as a few kilometres (e.g for an energy of 300 eV, the gyroradius is 5 km). The pitch angle distribution is measured every 2.5 seconds, during which the spacecraft moves 4 km. However, the response of the ER technique can depend on the spatial extent of the magnetic feature [Halekas et al., 2010].

Although the ER technique has been in use since the Apollo era, it is only recent studies which have been able to reveal its sensitivity to magnetisation with different spatial scales. Halekas et al. (2010) used simulations of electron motion in fields from magnetisation distributions with different strengths and spatial scales to show that the ER technique reliably detects surface fields from magnetisation distributions with wavelengths larger than 10 km, but has less sensitivity to smaller wavelengths. The lower bound estimates of the surface field from the ER technique can give a good approximation of the average surface field [Lin et al., 1976], but may, in some cases, be a significant underestimate of the strengths of the surface fields, especially in areas where there is very incoherent magnetisation.

2.5.6 The magnetic environment of the Moon

The magnetic environment of the Moon and the LP satellite changes with the location of the Moon with respect to the Earth (given in Geocentric Solar Ecliptic

(GSE) coordinates, see Appendix 1), and the location of the satellite with respect to the Moon. The plasma environment of the Moon consists of the solar wind and the Earth's magnetotail with its magnetosheath (Figure 2.15) produced by the interaction of the solar wind with the Earth's magnetic field. The Moon spends most of its orbit in the solar wind, a magnetised plasma flowing out from the Sun carrying the interplanetary magnetic field. The direction and strength of the field in the solar wind varies with time and depends on solar wind conditions (LP was operational close to a period of solar maximum).

For about 4 days each month the Moon is in the geomagnetic tail. This region has a steady magnetic field and contains the cylindrical magnetotail with two opposite polarity lobes separated by a neutral plasma sheet. The magnetotail region is bound by a bow shock formed magnetosheath and outer boundary, the magnetopoause. Magnetic fields in the magnetosheath can be strong and turbulent, varying on different time scales due to solar wind conditions and the orientation of the Earth's magnetic axis, such that the boundaries between the different regions (given in figure 2.15 in GSE longitude) are not static.

GSE longitude (°)	Regime
0-130	Solar wind
130-160	Magnetosheath
160-200	Magnetotail
200-230	Magnetosheath
230-360	Solar wind

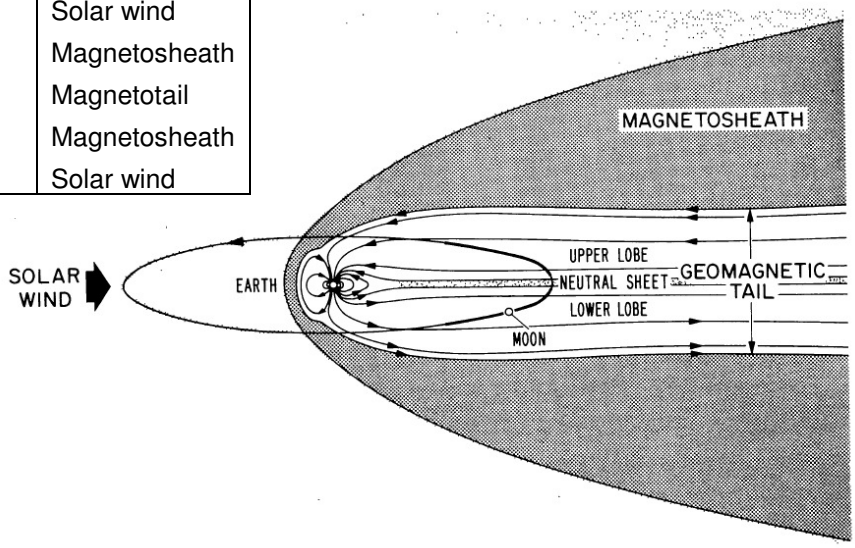

Figure 2.15: The magnetic environment of the Moon during a lunar orbit, showing the features in the geomagnetic tail region. (From Dyal et al. (1974)). Inset: Geocentric Solar Ecliptic (GSE) longitudes (see Appendix 1) for the different regimes.

In most regions, the lunar magnetic fields are not strong enough to stand off or divert the solar wind plasma, and it is absorbed by the surface on the day side. This leaves a plasma void (wake) behind the Moon (Figure 2.16) and can result in electrical currents at the lunar surface on the dayside which generate toroidal magnetic fields. While the nightside of the Moon is shielded from the solar wind, the solar wind on the day side can interact with the crustal magnetic fields [e.g., Harnett and Winglee, 2003, Kurata et al., 2005], modifying the field measured for a given region.

The contributions of the crustal field, induced fields, and external fields to the magnetic field measured around the Moon varies with the position of the Moon, the location on the lunar surface, and solar activity. Passes over the same area at different local times and in different regimes can show very different features. For most regions of the Moon, the external field is by far the largest component, with the magnetic field of the solar wind interplanetary plasma about 5-10 nT, and the strong fields in the Earth's magnetotail about 35 mT. Induced fields are generally smaller than the external field, but can be significant, as in the case of toroidal fields. The strongest crustal fields are only ~1 nT at 100 km altitude, and ~15 nT at 30 km altitude.

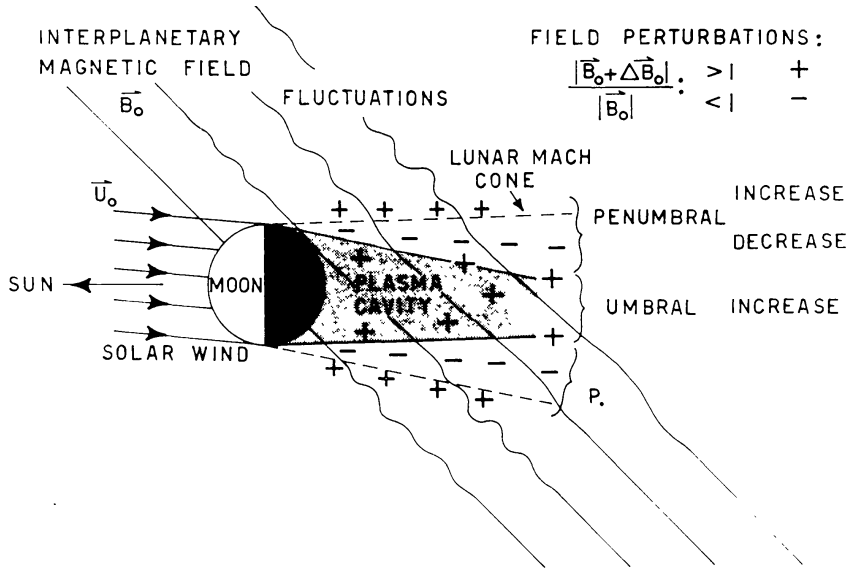

Figure 2.16: Schematic representation of the interaction of the solar wind (and interplanetary magnetic field) with the Moon to form the lunar wake. (From Ness (1970)).

The highest quality data for inferring the crustal magnetic field are measured under quiet plasma conditions where the external fields are minimal or easy to remove, and where time dependent induction fields and solar wind interaction are minimal. These regions are the steady magnetotail region and the lunar wake, where the Moon is shielded from the dynamic solar wind. Data from these regions are typically used for inferring the crustal magnetic field. Due to the resonant rotation of the Moon (same face facing Earth) and its orbit, it is not possible to have data from all regimes and all local times for all locations.

2.6 The Magnetometer and Electron Reflectometer data

The 5 second averaged LP-MAG data are available from NASA's Planetary Data System (PDS) with varying levels of processing. The MAG data used in this study have been processed and provided by M.E. Purucker (personal communication), and the processed ER data have been provided by J.S Halekas (personal communication). Although the ER technique does rely on the MAG data for the surface field estimations, the ER and MAG data sets can be considered as independent; the ER data are surface field estimates while the MAG data are at satellite altitude.

2.6.1 The LP-MAG data

The LP-MAG data from the PDS is provided as three orthogonal components of magnetic field at the satellite location in selenographic coordinates $B_x\ B_y\ B_z$, along with the latitude and longitude of the ground track of the satellite, the satellite attitude (above a sphere of 1737.1 km), the location of the Moon with respect to the Earth in GSE coordinates, the sense of the satellite path (ascending or descending), and a sun-pulse indicator to indicate if the satellite is in the sunlight or in the Moon's shadow. The selenographic $B_x\ B_y\ B_z$ of the level 1B (calibrated) data are

transformed into local spherical coordinates B_r B_θ B_ϕ using a simple matrix (see Appendix 1).

The LP-MAG recorded data continuously giving almost 100% spatial coverage except for interruptions for orbital maintenance burns or gaps from data contamination or processing limitations. Despite the high inclination of the LP orbit (89.8°), the ellipticity of the lower altitude orbit and its precession resulted in the least coverage at intermediate polar latitudes (~75°-85°) (see figure 2.17).

The MAG data used in this study are taken from the low altitude (< 66 km) phase of the LP mission and from the lunar wake and magnetotail times (1322217 data points) where the solar wind plasma densities are low and external field variations minimal. These data represent ~38% of the low altitude data set and offer excellent spatial coverage (Figure 2.17) at a range of altitudes from 10.637 km to 56.375 km (Figure 2.18).

To obtain the crustal field from the MAG data, the non-crustal fields must be removed. As there is no global coverage at any one altitude, the crustal field data can also be continued to a common altitude. The isolation of the crustal field and altitude normalisation can be limiting factors in the analysis of lunar crustal fields. When isolating the crustal field, uncertainties in the crustal field values arise not only from the magnetometer (e.g orientation, accuracy), but also from any remaining non-

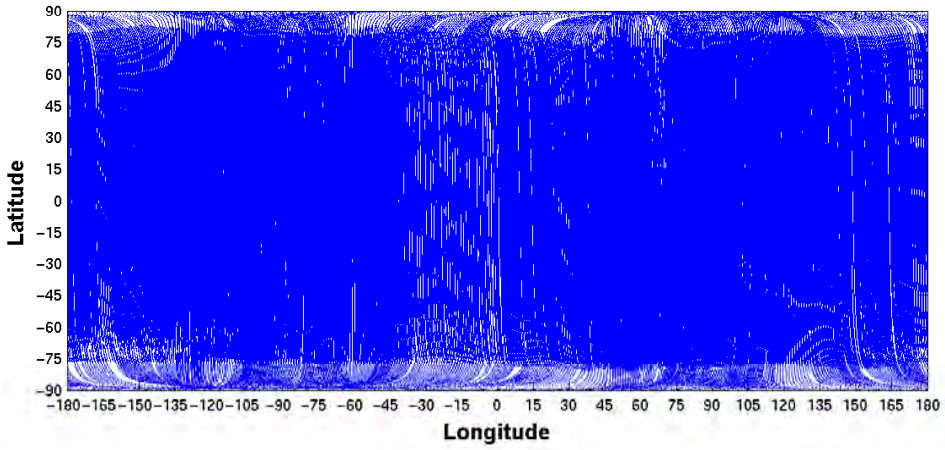

Figure 2.17: Coverage of the low altitude (~11-56 km) MAG data from the lunar wake and geotail regions.

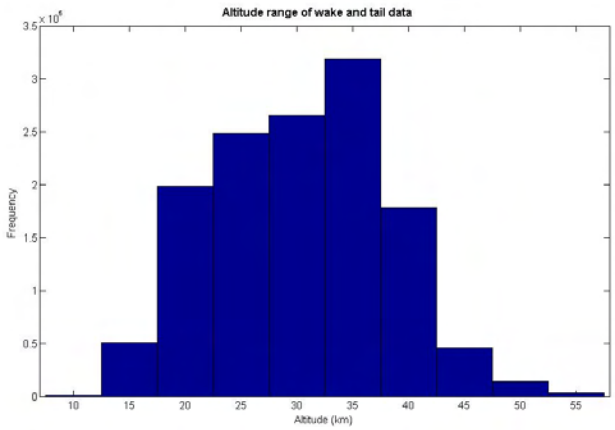

Figure 2.18: Histogram of the altitude distribution of the low altitude MAG data from the lunar wake and geotail regions.

crustal fields or amplification of noise during altitude normalisation. The overall noise level of the processed MAG data is dominated by the external magnetic field environment rather than any instrument uncertainty or spin averaging, and amounts to about 0.5 nT.

2.6.2 Isolation of crustal fields

The isolation of the crustal fields from the fields measured by magnetometers around the Moon has been approached in different ways. The first step is to remove long period external magnetic fields (such as the field in the solar wind, the magnetotail or globally induced fields) and then isolate the stable, time independent crustal magnetic field signature from any remaining short period external or induced fields (like small scale transient fields and plasma interactions) using adjacent passes. The consideration of adjacent passes for isolation of the crustal field was used with terrestrial data [Maus et al., 2002], where adjacent tracks with neighbouring passes with a significantly lower mean residual RMS on both sides were rejected.

Analysis of the Apollo subsatellite magnetometer data [Russell et al., 1975, Hood et al., 1981] minimised magnetic signals with large (> 20°) spatial wavelengths along the subsatellite track by fitting and removing a suitable low order polynomial

function for each component of the field for each orbit. This technique is known as detrending. Remaining shorter period external fields were removed by visually examining each orbit profile to identify features that repeated on adjacent passes. (Measurements from the surface magnetometers were also used to help reduce noise in the Apollo subsatellite data by removing the noise recorded at both the surface and the spacecraft).

Hood et al. (2001), Richmond et al. (2005), and Richmond and Hood (2008) applied a similar technique to the LP-MAG data, with continuation to constant altitudes of 30 km and 40 km using an empirical inverse power law [Richmond et al., 2005, Richmond and Hood, 2008] (see Appendix 3). Initially this technique resulted in only 40% coverage of the Moon with LP-MAG data [Hood et al., 2001], but the data editing technique was improved to produce better coverage by considering usable data outside of the lunar wake or magnetotail. This resulted in a global map of the internal magnetic field of the Moon by 2D filtering of the data from non-uniform locations [Richmond and Hood, 2008] (Figure 2.19). The cut-off of fields below 3 nT in this map ensures that external fields are not included.

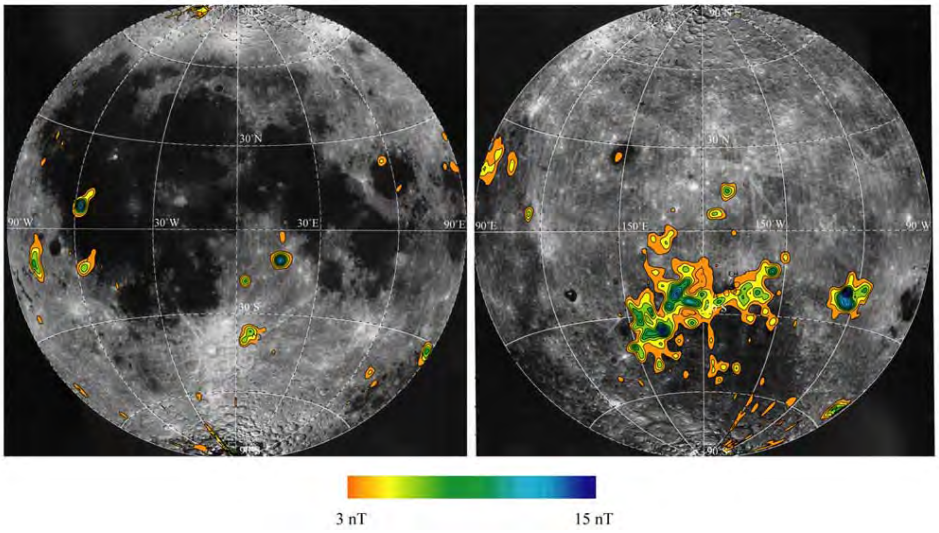

Figure 2.19: Global map of processed observations of the total lunar magnetic field from LP MAG data, normalised to 30 km. Background is the Clementine Albedo map. (From Richmond and Hood (2008)).

The MAG data used in this thesis, processed by M.E. Purucker, uses a new technique for external field removal [Purucker et al., 2006], based on techniques for the terrestrial magnetic field environment. The measured magnetic field **B** is parameterised into internal (crustal) and external magnetic fields in the near–lunar magnetic field environment through the use of spherical harmonic analysis,

$$\mathbf{B} = \mathbf{B}_{internal} + \mathbf{B}_{external} + \mathbf{B}_{toroidal}$$

$$= -\nabla\left[a\,\mathrm{Re}\left\{ \sum_{n,m} \left(\frac{a}{r}\right)^{n+1} t_n^m P_n^m e^{im\phi} \right\} \right] - \nabla\left[a\,\mathrm{Re}\left\{ \sum_{n,m} \left(\frac{r}{a}\right)^{n} \varepsilon_n^m P_n^m e^{im\phi} \right\} \right] + \nabla\times\left[\mathbf{r}\,\mathrm{Re}\left\{ \sum_{n,m} \left(\frac{a}{r}\right) \Psi_n^m P_n^m e^{im\phi} \right\} \right] \tag{2.6}$$

where a is the radius of the Moon, n and m spherical harmonic degree and order, $P_n^m(\cos\theta)$ the associated Legendre polynomials, and t_n^m, ε_n^m and Ψ_n^m the expansion coefficients describing the internal, external and toroidal magnetic field contributions respectively. Each of these components have different spatial characteristics such as a different dependence on the radial distance, r.

The parameterisation technique, as described in Nicholas et al. (2007) and Purucker (2008) ignores toroidal fields (particularly valid for data from the magnetotail and lunar wake), and assumes that the external field is a uniform potential field resulting from a dipole at distance, for each half orbit (pole to pole). The spherical harmonic expansion coefficients for the external field are then determined from the three components of the magnetometer data in a least squares sense. The dipole formulation and field uniformity is justified as both the Earth's field in the magnetotail and the Sun's magnetic field as expressed via the solar wind, can be assumed to be dipolar and not to change in direction and intensity over the course of a half orbit.

This method of external field removal was applied to data at all points of the Moon's orbit but is likely to be most effective in regions where the external field is stable over the half orbit period (~ 1 hour). The external fields parameterised with this method when the Moon is in the geotail have been shown to match

independently derived external field predictions from the T96 standard model for the description of the terrestrial magnetosphere [Purucker et al., 2006].

The external fields removed were generally small (~4 nT) but with some up to about 60 nT. After removal of the long period external field over each satellite half orbit, the crustal field was separated from the remaining smaller scale external field contamination by modeling the radial and theta components of the field for immediately adjacent passes using equivalent source dipoles (see section 4.1) fixed in the theta direction. The longitude span of three adjacent passes is small (2°) compared to the expected source size so the phi vector component (east-west) was not used in this stage of the process. This component is also the most affected by external fields. The equivalent source dipole formulation also immediately provides a means to reproduce field values at a preferred altitude, chosen here at 30 km.

The modeling of the radial and theta components of the field for adjacent passes, described in Purucker (2008) uses a conjugate gradient approach to solve for the magnitude of horizontal dipoles at the lunar surface directly beneath the observation points which produce the best fit to the field observations in a least squares sense. Sets of passes whose model field could not adequately reproduce the observed field were discarded so that the solutions represent the correlative parts of adjacent passes and hence the crustal fields common to those passes. As adjacent passes are separated by only ~2 hours, each solution is characteristic of a particular lunar regime. This correlative approach retains more passes than the selection approach of Richmond and Hood (2008), giving a higher resolution. The RMS misfits for each pass varied from 0.0055 nT to 0.13 nT (mean 0.0339 nT) for all passes and from 0.0055 nT to 0.12 nT (mean 0.0333 nT) for passes in the wake and tail only. This gives an indication of the fit of the model and an indication of the noise in the data.

The radial magnetic field maps at 30 km altitude for the wake and tail times and times when the Moon was in the solar wind are shown in figure 2.20. The fields in the solar wind are weaker than those in the wake and tail times, suggested by Purucker (2008) to be a consequence of the ‘suppression’ of fields by the solar wind to form mini magnetospheres.

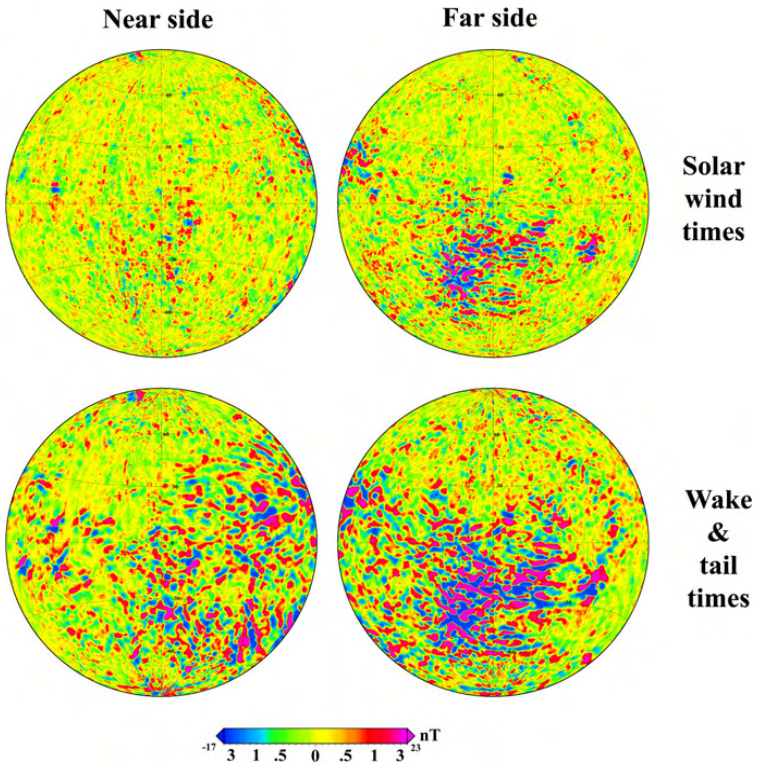

Figure 2.20: Global radial magnetic field maps at an altitude of 30 km for the near- and far-sides of the Moon, during periods when the Moon is in the solar wind (top) and in the lunar wake and geotail (bottom). (From Purucker (2008)).

2.6.3 Comparison of processing methods for the MAG data

Different processing techniques for the LP-MAG data yield very similar results for the lunar crustal magnetic field. Before altitude normalisation, with just the external fields removed, these data sets show excellent agreement over the strong magnetic feature Reiner Gamma. Comparison of the same passes for this region after detrending [Hood et al., 2001] and after a uniform external field had been removed [M.E. Purucker, private communication] are shown in figure 2.21.

Each of these processing methods offer some advantages over the other: The parameterisation technique, though not characterising all the fields in the lunar environment, offers an advantage over filtering of data because it can separate source fields whose spatial and/or temporal scales overlap, by performing an optimal separation of the model parameters. The residuals after parameterisation are small showing improved isolation of the crustal magnetic signature from the surrounding

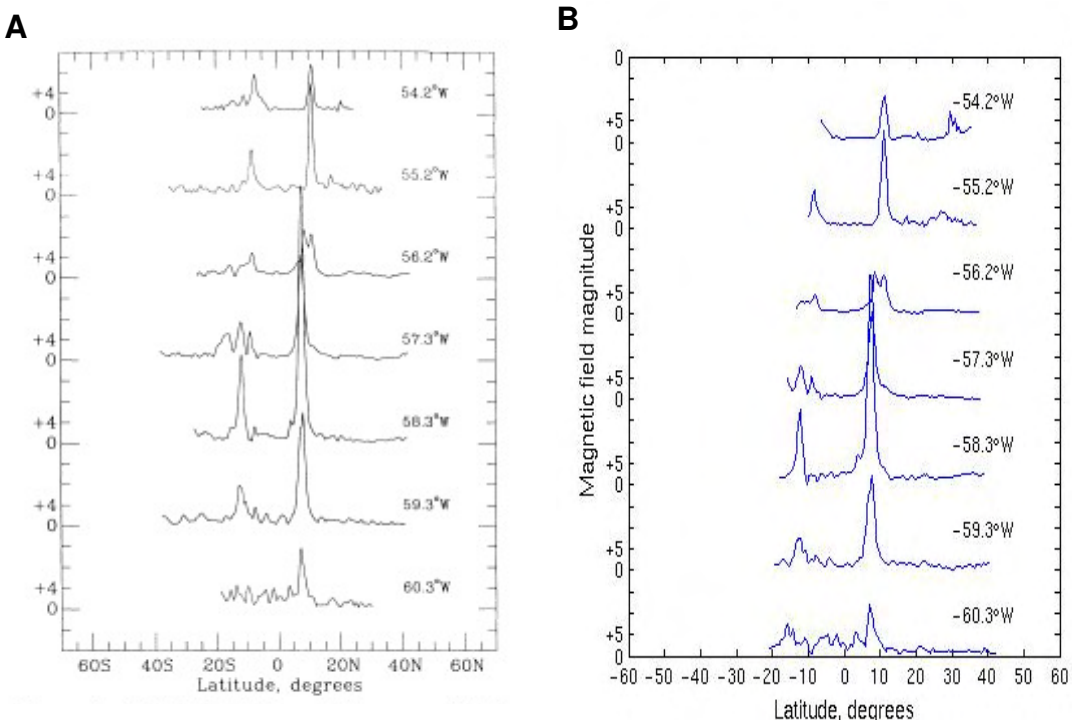

Figure 2.21: Comparison of the crustal field magnitude versus latitude for a series of LP passes over the Reiner Gamma region, as isolated by A: Hood et al. (2001) and B: M.E. Purucker (personal communication) for data for the same days. The space craft longitude is given for each pass.

fields. Detrending however, ignores the fact that the internal and external magnetic fields are potential fields, but this technique may be more effective at removing temporally varying fields.

The strongest crustal fields in the final lunar crustal field maps from Purucker (2008) and Richmond and Hood (2008) are in very good agreement, with the different processing methods giving slight differences (e.g the Reiner Gamma feature is the strongest in the map of Purucker (2008), while the Descartes anomaly is the strongest in the map of Richmond and Hood (2008)). The cut-off of fields below 3 nT in Richmond and Hood (2008) also ignores some of the lower magnitude anomalies, which they acknowledge. Analysis of the MAG data from the Japanese satellite Kaguya, again using the lunar wake and the tail environments, also show very good agreement with the LP-MAG data [Hayashida et al., 2009].

2.6.4 A spherical harmonic model

Purucker (2008) used the altitude normalised radial solutions for the wake and tail regions to construct a spherical harmonic model of the lunar crustal field up to degree 178 (see section 1.2.1). Only the radial field is used here in preference to including also the horizontal components as it is least susceptible to external field variations (Hayashida et al. (2009) suggested that that the horizontal components might be affected by surface currents generated by the varying interplanetary field). As the crustal field is a potential field, a single component of the field retains all the field information.

The data were binned into 1° longitude × 0.5° latitude bins (weighted by altitude for the median value of each bin) resulting in 99.2 % coverage. Unpopulated bins in the polar regions were supplemented with data from the solar wind times. Spherical harmonic terms up to degree 150 are considered robust [Purucker, 2008] and can be used to produce the scalar and vector components of the magnetic field at any location around the Moon, preserving the resolution of the original data set. In this study, the data were reproduced on a 'polar coordinate subdivision' point distribution [Katanforoush and Shahshahani, 2003] (see Appendix 4) at 30 km altitude, and on a rotated version of this grid to give improved polar coverage.

Predictions from the spherical harmonic model should be considered a minimum estimate of the strength of the crustal field at a given location as the model will result in some smoothing of the features, especially in the polar regions which are considered less reliable in the spherical harmonic reproduction. The error levels of these data are set by the accuracy of the MAG at less than 0.5 nT. This spherical harmonic representation of the lunar crustal field allowed analysis of some of the weaker crustal fields.

2.6.5 The LP-ER data

The ER data consist of the distribution of the electron pitch angles, or reflection coefficients, for different electron energies. The cut-off angle is used to

provide the surface field and hence the crustal field estimate. The pitch angle distribution of incoming electrons was measured every 2.5 seconds, but like the MAG data, not all of the data are usable for crustal field estimates.

There are a number of conditions which must be met for the ER technique to be valid. The magnetic field through which the electron travels must be steady on the time and spatial scales of the electron motion. The electrons in these energy ranges take less than 0.1 s to move past the spacecraft and back again (for pitch angles less than 80°) and during this time, the field must be constant. This is important for the application of conservation of the electron moment to estimate the surface field and the location of the surface reflecting point by linear extrapolation of the satellite field. This condition is met easily in the geotail and the lunar wake, but can be violated in the magnetosheath and where the crustal fields are very strong and/or are not coherent on a scale comparable to the electron gyroradius. Consequently, virtually all of the crustal field estimates from the ER technique are made from measurements in the lunar wake and geotail. If the spacecraft is in shadow, this also reduces the contamination of the detector from photoelectrons produced by UV radiation impacting on the detector.

Where the surface field is strong compared to the ambient field, there can be an error in the location of the magnetic field (of the order of the satellite altitude) as there may be significant curvature of the field lines. Strong fields may also produce mostly closed magnetic field lines, reducing the applicability of the ER technique. The surface field estimate depends on the location, the pitch angle and the field strength and orientation as well as the fine structure of the field. In general, it is the ER data of moderate magnitudes (few nT to tens of nT) which are most reliable with smaller statistical uncertainties.

Of all the measurements of the electron pitch angle distribution, there were 117647 usable data points. The ER technique is not sensitive to altitude so data from all altitudes can be used, but the largest source of data is from low-altitude passes. The ER data are provided as binned averages (with bins larger than the intrinsic resolution) to give almost global coverage, and as unbinned data points, which allow

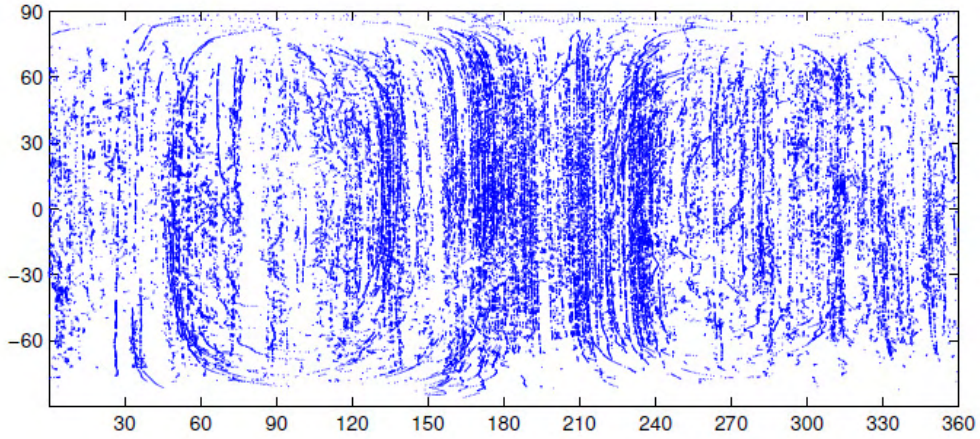

Figure 2.22: The surface locations of the unbinned ER data points.

better along-track coverage in some regions (Figure 2.22). The polar regions have the least coverage due to the spacecraft not being 'magnetically connected' to the surface.

The unbinned data points come with high statistical uncertainties, especially for fields big enough to be seen by the magnetometer at altitude, making this data set, particularly the larger magnitudes, less reliable. Values less than 0.2 nT (including negative values resulting from the estimates), are below the lower bound of the ER sensitivity.

The (equal angle) binned, average LP-ER data estimates of the surface magnetic field intensity are provided in 5°×5° and 1°×1° bins, 'boxcar smoothed' over 3°×3° areas. The binned data are mostly the crustal field estimates corrected for electrostatic effects, supplemented with some uncorrected field estimates. Bins with a very large uncertainty were discarded and bins near the poles were empty.

Binning and smoothing reduces the minimum crustal magnetic anomaly wavelength that is resolved but increases the surface coverage. The statistical uncertainties of each data point are also reduced providing a data set more conducive for inclusion in magnetisation models. The difference between the binned and unbinned data in terms of coverage, strength and variability can be seen more clearly on a smaller scale. Figure 2.23 shows the 1°×1° binned and unbinned ER data for the Reiner Gamma region.

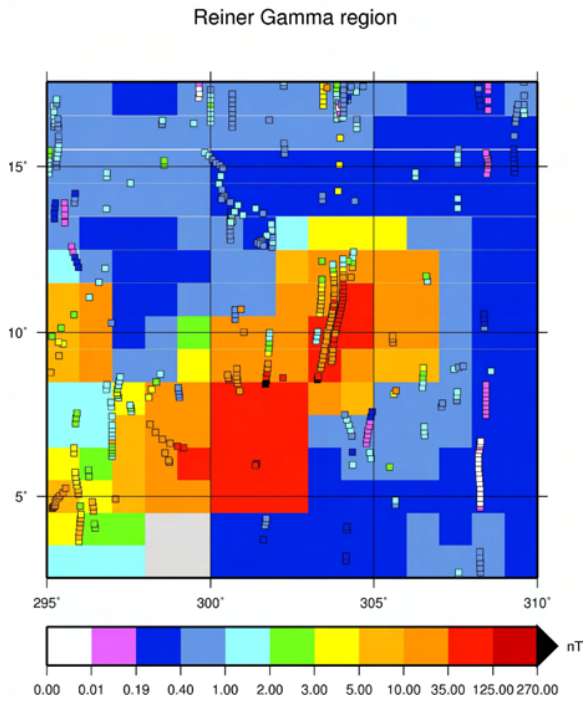

Figure 2.23: The 1°×1° binned ER data (background), and the unbinned ER data (small squares) for the Reiner Gamma region. (Grey represents the absence of data.)

2.7 Comparison of the ER and MAG data

The Moon is unique in that it is the only body other than the Earth for which we have magnetic field measurements at the surface as well as at satellite altitude (the ER on MGS could only detect fields at the top of the Martian ionosphere). The strength of a magnetic field diminishes with distance away from the source so that data measured at altitude is weaker than data measured at the surface. The 'fall off' with distance depends on the strength and size of the source ($B(z) \propto e^{-kz}$ for altitude z and source spatial wavelength k [Blakely, 1996]) with fields from small scale features being more strongly attenuated with distance.

The ER technique can detect weaker fields and fields from small scale sources, while the MAG can detect fields from regions with coherent fields with wavelengths larger than the observational altitude. With different measurement techniques and different sensitivities, uncertainties and resolutions, it is important to

assess how consistent the MAG and ER data sets are in order to use them appropriately to produce a magnetisation model which can account for the fields observed at altitude and the surface.

2.7.1 Regional comparison of the ER and MAG data

Both the MAG and ER data sets show the main features of the lunar magnetic fields described in section 2.1. For the strong field regions labelled in figure 2.3, the ER data also show strong surface fields (see Appendix 2). In most of these regions, there is no significant offset between the maxima of the magnetic anomalies detected by the two instruments (except perhaps for the regions near to craters Firsov and Airy) and the surface fields extend beyond the feature seen in the MAG data due to the sensitivity of the ER technique to weaker fields. However the actual spatial agreement of the ER and MAG data varies considerably for each region, showing the effect of noise and the variation in the response of the ER technique to different scales and magnitudes of fields. Some regions show clear features in the ER data, such as the anomaly at Reiner Gamma and near to the antipode of Nectaris, while other areas such as the anomaly at Descartes and Airy crater show less well defined features in the ER data set (Figure 2.24). The differences in the field distribution in some areas, if resulting from errors or mislocation, might make finding a magnetisation model, which fits both data sets equally well, difficult.

2.7.2 Qualitative comparison of the ER and MAG data

To assess the compatibility of the ER and MAG data sets, the spherical harmonic model of the crustal field at altitude [Purucker, 2008] was used to predict the total surface magnetic field. Figure 2.25 shows the 1°×1° binned ER data for mid-latitude regions, and the predictions at these locations from the spherical harmonic model of the MAG data, and their differences. Qualitatively, the ER and predicted surface fields are in remarkable agreement in terms of location of fields

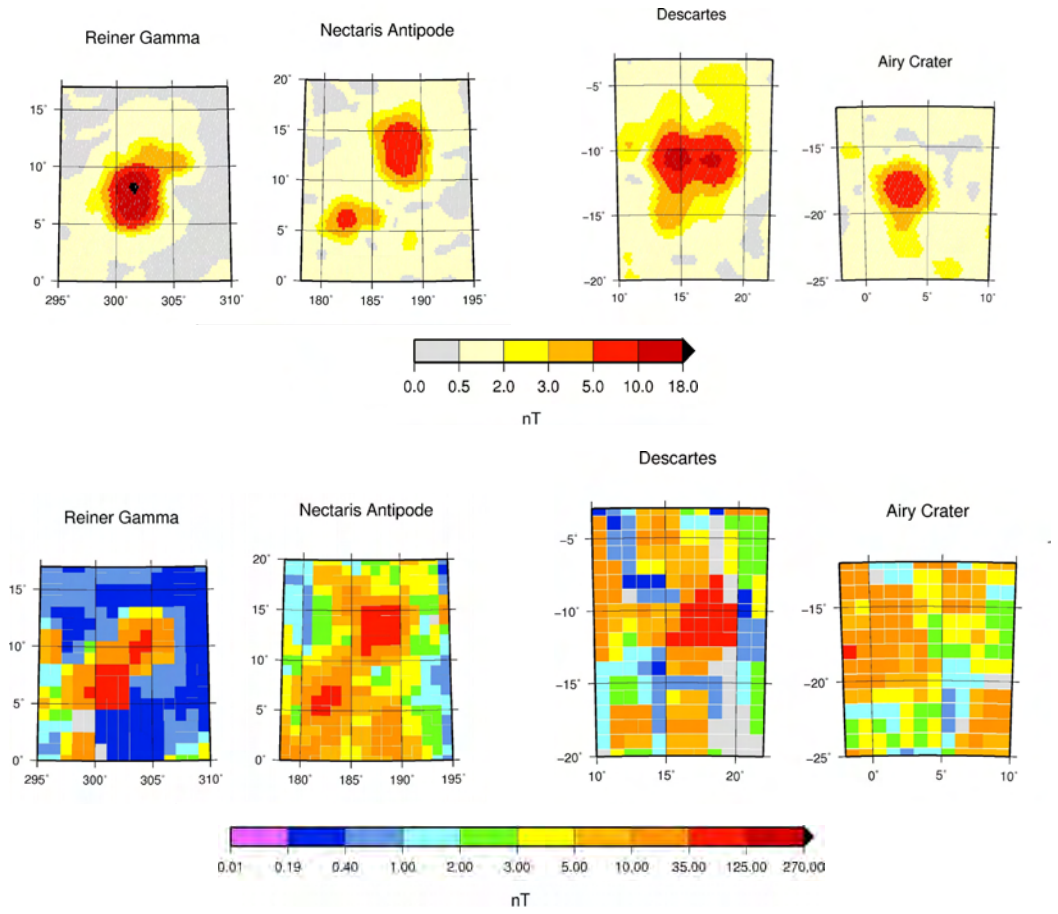

Figure 2.24: The total magnetic field at 30 km altitude produced from the degree 150 spherical harmonic model (top) and the 1°×1° binned ER data (bottom), for the anomalies at the Reiner Gamma region, near to the Nectaris antipode, Descartes and Airy crater.

and relative magnetic field magnitude, but the predicted surface data are much weaker. The discrepancy in magnitude, yet similarity in distribution, is emphasised in figure 2.26 which shows the ER and the predicted surface data again, each with an 'equal area[1]' colour scale.

The largest differences between the data sets occur in the regions of very strong (> 10s nT) or very weak (< few nT) magnetic field, with the strongest fields being under predicted by the spherical harmonic model and the weaker fields being over predicted. For example, the ER field estimates of the surface fields at the Imbrium antipode near the SPA basin are over 100 nT higher than the predictions

[1] Each colour bin contains the same number of data points.

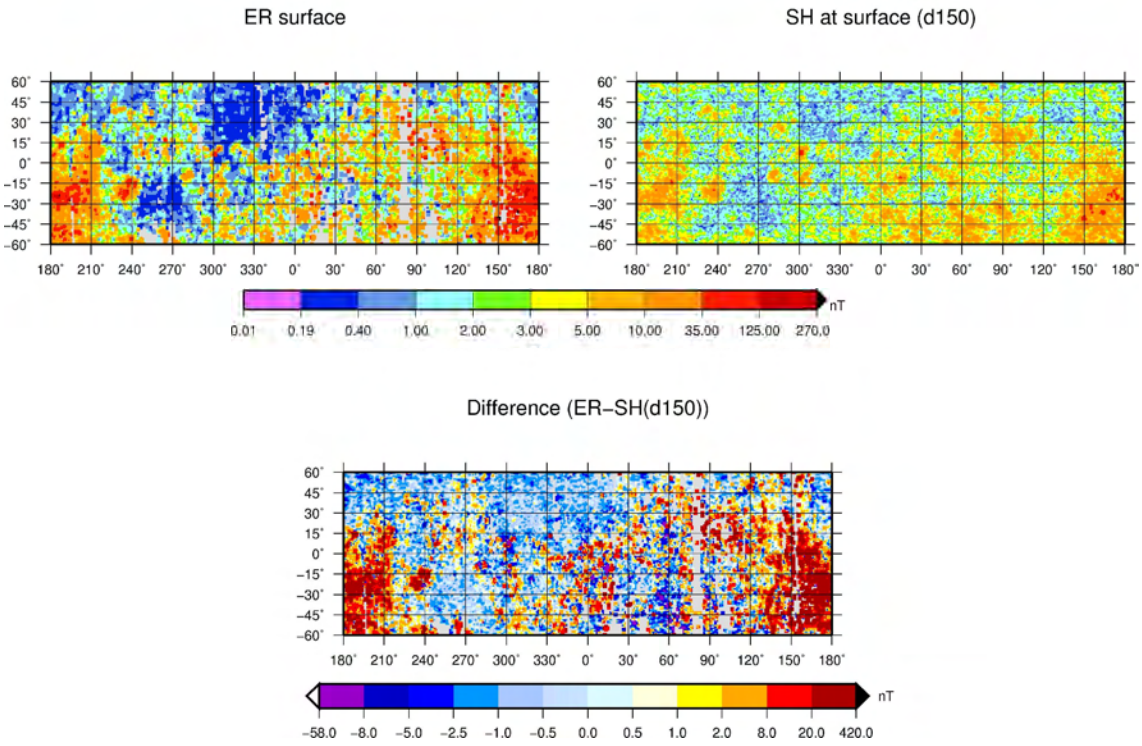

Figure 2.25: The ER data (top left), spherical harmonic model prediction at the surface (SH, degree 150, top right) and their differences (bottom) at the 1°×1° binned ER data locations for mid latitudes.

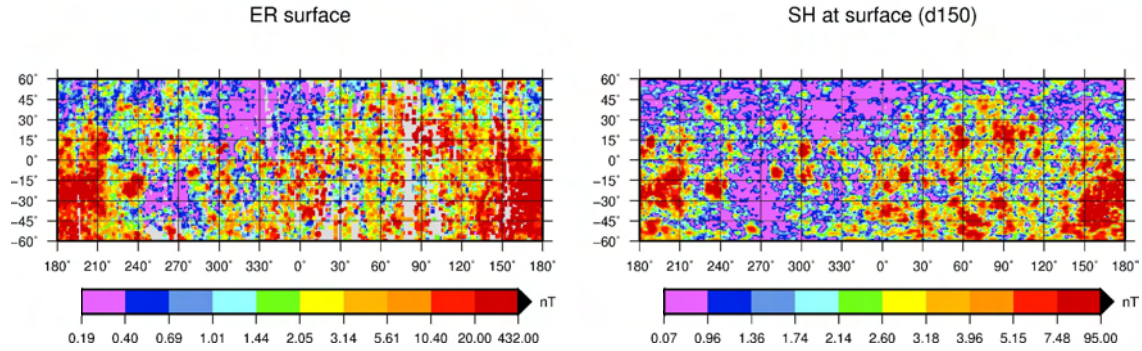

Figure 2.26: The ER data (left) and spherical harmonic model prediction at the surface (SH, degree 150, right) at the 1°×1° binned ER data locations for mid latitudes with ‘equal area’ colour scales.

from the spherical harmonic model. However, in the weak field regions (< 0 .2 nT) such as the Imbrium and Orientale basins, it is the predicted data that give the larger amplitude fields, if only by a few nT.

Stronger fields in the ER data result from the sensitivity of the ER technique to smaller wavelength, stronger features than the MAG, while over prediction of the weaker fields by the spherical harmonic model results from the amplification of smaller wavelength features when the data are predicted at the surface. Downward continuation of terrestrial magnetic fields measured at satellite altitudes of hundreds of km show amplitudes different to the fields of aeromagnetic surveys [Whaler, 1994].

2.7.3 Correlation

A quantitative comparison between the two data sets (x_i and y_i) can be achieved though the calculation of the linear correlation coefficient *r* [e.g Press et al., 1992]:

$$r = \frac{\sum_i (x_i - \bar{x})(y_i - \bar{y})}{\sqrt{\sum_i (x_i - \bar{x})}\sqrt{\sum_i (y_i - \bar{y})}} \tag{2.7}$$

A correlation coefficient of +1 or -1 represents a perfect positive or negative correlation respectively and a value of 0 represents a lack of correlation. Table 2.2 shows the global correlation coefficients for the ER data and the spherical harmonic model predictions of the data at the surface and at 30 km altitude. The predictions from the spherical harmonic model were made at the locations of the 1°×1° and 5°×5° binned ER data and also at the locations of the unbinned ER data which were then binned and smoothed following the method of processing for the ER data. For so many data locations (> 2500), these correlation coefficients are very significant (~100%). The lower correlation coefficient between the data at the unbinned locations is due to the very large magnitudes and statistical uncertainties of the individual ER data values, but the binned data sets show higher and more significant correlations.

Data points	Correlation coefficient at the surface	Correlation coefficient for the surface and 30 km
5°×5° grid	0.614	0.649
1°×1° grid	0.586	0.608
1°×1° grid (after binning and smoothing)	0.634	0.638
Unbinned	0.263	-

Table 2.2: Global correlation coefficients for the ER data and predictions from the spherical harmonic model at the surface and at 30 km altitude.

The higher correlation coefficients for the 5°×5° binned data and for the predictions at altitude with the surface ER data show that there is more agreement between the ER and MAG data on a larger scale. There is also more agreement if the predictions from the spherical harmonic model are treated in the same way as the ER data (i.e binned and smoothed).

To assess the correlation on a regional scale, correlation coefficients were also calculated for the 1°×1° binned data within regions of size 90°, 45°, 30°, 15°, 10° and 5°, shown in figure 2.27. Though not immediately obvious in figure 2.27, except in figure 2.27A, the local correlations in the regions of strongest and weakest total field are higher than correlations for mid-range magnitudes. Regions showing negative correlations occur for regions smaller than 30°, mostly in regions with few data points, and correlation coefficients of up to ± 1 occur for the smallest regions (though are not as significant in these regions).

Correlation coefficients for the global 1°×1° data sets (at the surface and an altitude) offset by ± 1° in latitude and longitude were also calculated to assess any obvious offset of the locations of the ER and MAG fields (due to possible location errors in the ER technique over regions of strong magnetic field). Higher correlation coefficients were not found for the offset data sets, suggesting that any mislocation of the ER data points is not significant on a global scale.

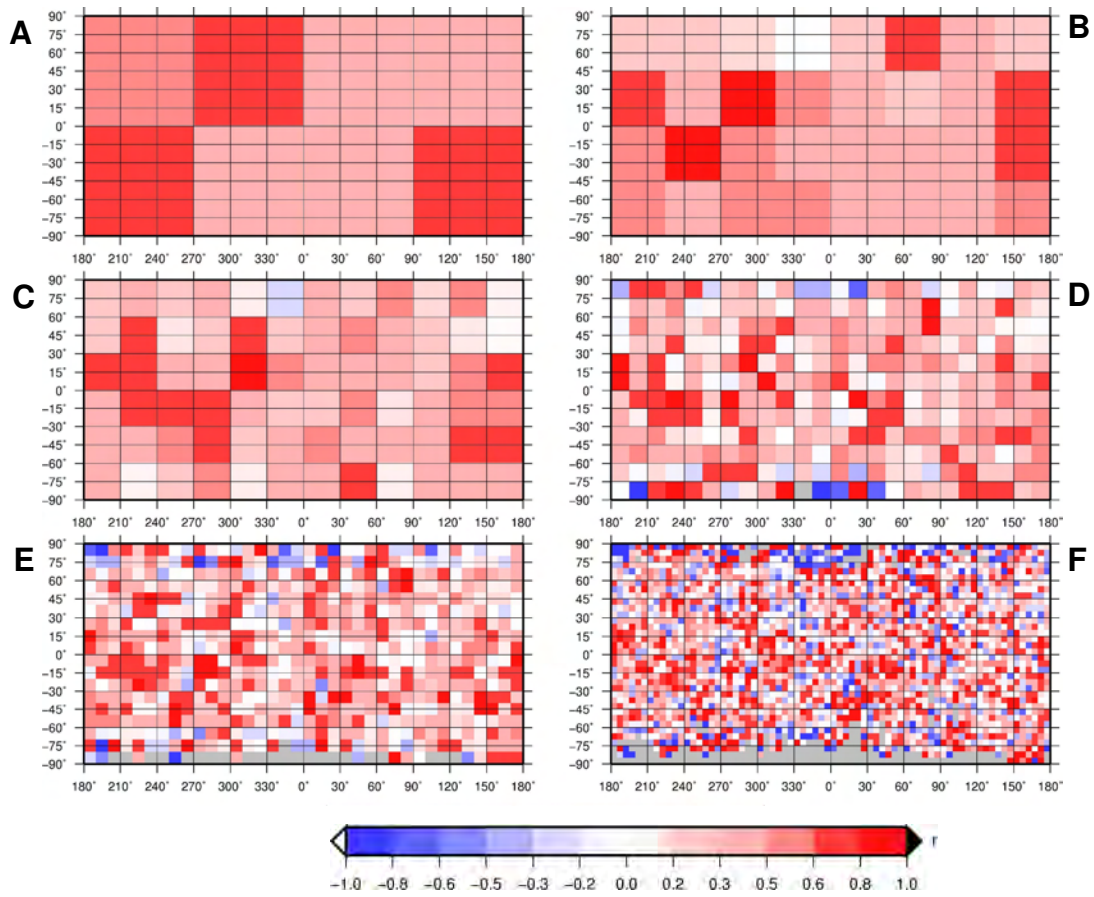

Figure 2.27: Linear correlation coefficients for the ER data and the spherical harmonic model prediction at the surface for the 1°×1° binned data in regions on scales of A: 90°, B: 45°, C: 30°, D: 15° E: 10°, and F: 5°.

2.8 Comparison of ER and Apollo data

As the ER data are surface field estimates it is interesting to compare them with the surface magnetic fields measured during the Apollo missions. The Apollo surface observations showed fields varying on sub-km scale, which would not be detected by the MAG but might be observed in the ER data. Figure 2.28 shows the 1°×1° binned ER data, the unbinned ER data and the surface measurements for the Apollo 12, 14, 15 and 16 landing sites. As expected, the surface fields measured with the LSM are much stronger than the estimated surface fields, but some of the

individual points of the unbinned ER data do show comparable magnitudes, though these may be displaced slightly.

The best agreements between the ER and the surface measurements are for the Apollo 12 site, with the least agreement at the Apollo 14 and 15 sites (though there were fewer ER data points for the Apollo 14 region). Strong surface fields are observed in the ER data near to the strong fields of the Apollo 16 site, and have perhaps been deflected by the nearby Descartes anomaly. The stronger surface fields measured with the LSM at the Apollo 15 site might result from features with spatial scales that even the ER technique cannot detect.

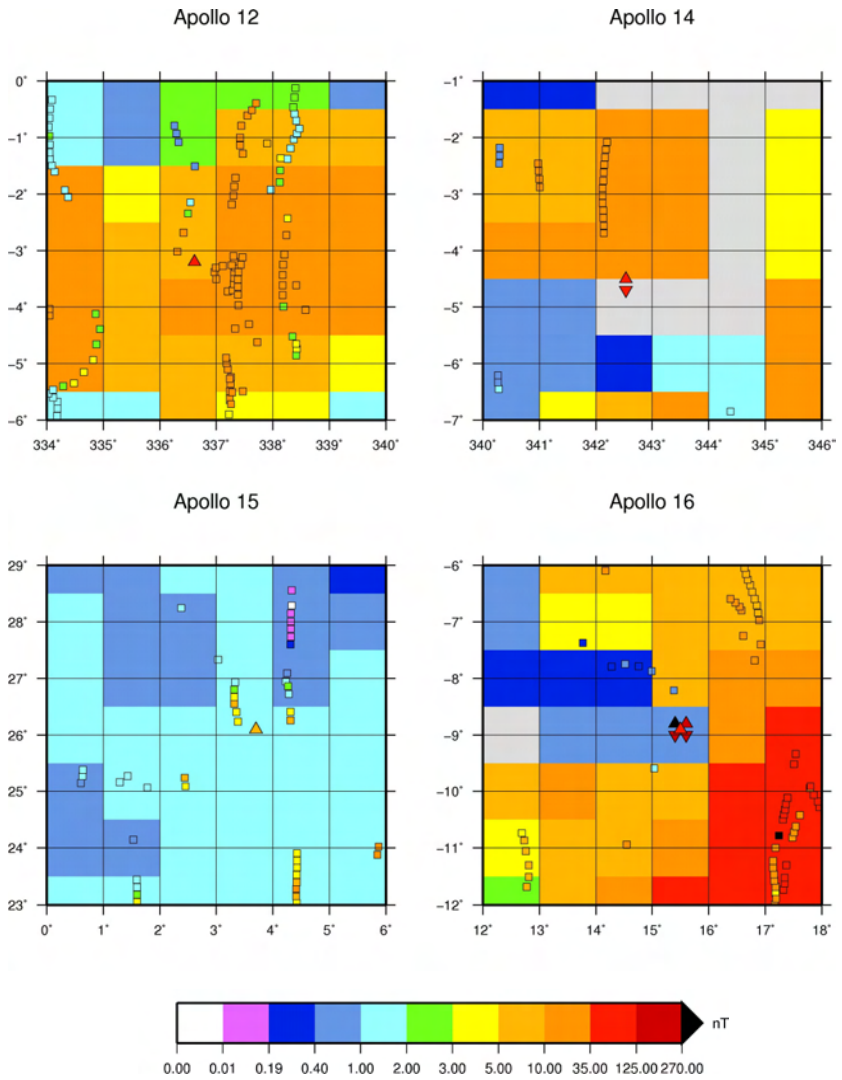

Figure 2.28: The 1°×1° binned ER data (background), the unbinned ER data (small squares) and the Apollo surface magnetometer measurements (triangles) for the Apollo 12, 14, 15 and 16 landing sites. (Grey represents absence of data.)

2.9 MAG and ER data for magnetisation modelling

Of the differently processed MAG and ER data, the lunar crustal magnetic field data used in this thesis are:

- The radial component of the crustal field from the MAG data at the satellite locations (normalised to 30 km altitude) provided by M.E. Purucker (personal communication).
- The three components of magnetic field predicted at 30 km altitude on a regular grid from the degree 150 spherical harmonic model of the internal magnetic field of the Moon produced from the MAG data [Purucker, 2008].
- The 1°×1° and 5°×5° binned ER data (J.S. Halekas, personal communication).
- The unbinned ER data (J.S. Halekas, personal communication).

Both the radial component of the MAG data and the unbinned ER data contain larger but less certain field values than the modelled and binned data. As the altitude normalisation was part of the process of separating the crustal field from remaining smaller scale external fields, MAG data at the original altitudes (not normalised or modelled) represent very noisy crustal fields and are not used in this study. The ER and the MAG data will be used independently and jointly to produce lunar crustal magnetisation models. The consistency of the two data sets suggests that crustal magnetisation models should be able to be produced to satisfy each data set reasonably well.

Chapter 3

Magnetisation modelling

Magnetic field observations alone are not enough to understand the nature of the source regions. Observations of crustal magnetic fields can be used with reasonable assumptions about the sources to produce models of the distribution of magnetisation in the crust with magnitude and direction. For the case of LP data, crustal magnetisation models would ideally be able to adequately account for both the MAG data at altitude and the ER data at the surface. As well as being able to describe the observed magnetic fields, magnetisation models should be able to provide information on the properties of the magnetised sources, namely the magnetisation contrast, source depth and dimensions.

3.1 The use of magnetisation models

The development of magnetisation models was driven by the need to isolate the crustal field of the Earth from the core field, and was later used as a means to study magnetisation [Parker et al., 1987]. For the Earth we have many in situ measurements of magnetisation to use with magnetic field data, but samples returned from the Moon are few, and did not allow any determination of magnetisation direction. Without extensive sampling, determination of the magnitude, direction and extent of magnetisation can be inferred from magnetisation models.

3.1.1 Source parameters

The aim of magnetisation modelling is to find as many source properties as possible. For lunar magnetic fields, the key properties are magnetisation direction and intensity, and source depth and dimensions (thickness and extent). On the Earth it is often (though not always) possible to assume that magnetisation is parallel (or anti-parallel) to the present dipolar field, with the magnetisation being induced over the continents and remanent for the oceanic crust. However, with the origin of the magnetising fields on the Moon unknown, magnetisation models for the Moon should be able to determine a magnetisation direction without any direction assumption. Magnetisation intensity is also an important parameter when considering the magnetising field (e.g paleointensities, section 1.5.6) and perhaps indicating the types of magnetic carriers, or layer thickness.

The depth at which sources are located within the crust can offer an important constraint on the sources themselves (e.g volcanic or ejecta) and on the magnetising field. However, with observations from satellite altitude comparable to the lunar crustal thickness, it may not be possible to resolve source depth and thickness from magnetisation models. Determination of depth and thickness, if possible, will be based on the results of a suite of models with different thicknesses and depths.

3.1.2 Crustal field representation

Representation of the sources of lunar crustal magnetic fields offers a means to predict the crustal contribution to the lunar magnetic field environment at a particular location. This is useful when considering the interaction of the solar wind with a planetary body, such as the mini-magnetospheres on the Moon, and the pathways of electrons used with the ER technique. Isolation of the crustal field, and indeed the crustal magnetisation, is also useful for comparative studies of the crustal fields of different planets, as in figure 1.2. Crustal field models rather than spherical harmonic models of the field can be a more accurate representation of the field if there is uncertainty in the field data.

3.2 Magnetisation modelling methods

Terminology note: When discussing magnetisation modelling, the magnetic field data are the crustal magnetic field with any non crustal fields removed (as described in section 2.6.2)

Magnetisation distributions can be produced from mathematical expressions of the relationship between model sources and the observed data using forward or inverse approaches. Forward methods specify values of chosen parameters of the modelled source, which are adjusted until the magnetic field they predict fits closely to the observed magnetic field. In contrast, inverse methods provide estimates of unknown model parameters which best fit the data. Forward methods are limited by the implication that the source is a simple isolated body with an assumed shape, while the more general inverse problems allow unknown parameters to be estimated. However, both forward and inverse models suffer from fundamental non-uniqueness.

3.2.1 Forward models

Forward methods make the assumption that the magnetised source can be represented by simple geometrical shapes or magnetic dipoles at known locations [Blakely, 1996]. Parameters such as exact location, size, and magnetisation are altered to give predicted magnetic fields close to the observed magnetic field. Forward models for magnetisation sources are often used on Earth as there is usually additional information from other geophysical techniques which can be included, and the direction of magnetisation may sometimes be assumed. Forward models have also been used on isolated anomalies on Mars [e.g Hood and Zakharian, 2001].

Additional information about sources of magnetisation on the Moon is severely lacking, making inverse models for lunar crustal magnetisation more attractive. However the first estimates of lunar magnetisation used forward models with Apollo subsatellite data. Hood et al. (1978) assumed source regions of fixed geometry (but not size) ranging from uniformly magnetised flat plates (with

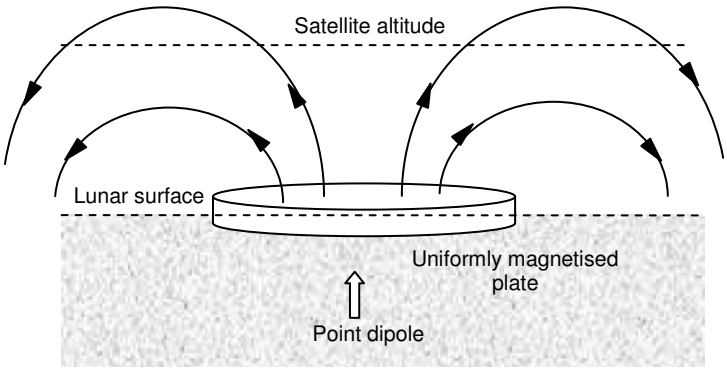

Figure 3.1: Source region models such as a buried point dipole, and a thin uniformly magnetised plate at the lunar surface (based on Hood et al. (1978)).

thickness ≤ subsatellite altitude) at the lunar surface, to point dipoles buried at depth with permanent magnetisation, separated by regions of unmagnetised material (Figure 3.1). Both of these source representations were shown to be consistent with the increasing complexity of the field with decreasing altitude [Russell et al., 1977]. These models showed that the bulk magnetisation direction of the modelled sources was independent of the source geometry, and that it was possible to determine the lateral positions and maximum sizes of the source regions, and to place limits on the dipole moments for the magnetised plates (per unit area) and buried dipoles. Determination of plate thickness and hence dipole moment per unit volume was not possible with Apollo data as vertical resolution was limited by the satellite altitude (~70-100 km for subsatellites) and data sampling rates [Russell et al., 1977].

While forward models can provide suitable estimates for source properties, this technique is generally not feasible for global data sets, or where the required assumptions (e.g magnetisation direction) may prove limiting for the magnetisation models.

3.2.2 Inverse models

Inverse theory allows unknown model parameters to be determined from the observed data. For the magnetic field inversions in this thesis, the aim is to obtain,

from the measured crustal magnetic field data, quantitative information about the distribution of the magnetisation in the lunar crust.

The inverse modelling methods for crustal magnetisation used in this thesis are based on methods used to represent the crustal fields using dipoles as basis functions [Purucker et al., 1996], or representing the magnetisation as a linear combination of Green's functions relating a magnetic field observation to a continuous magnetisation distribution within the crust [Parker et al., 1987]. The 'equivalent source dipole', and 'spatially continuous' methods have been previously successfully applied to terrestrial and Martian satellite data [e.g Whaler and Langel, 1996, Langlais et al., 2004, Whaler and Purucker, 2005]. The equivalent source dipole model can be used to solve for the magnetisation of dipoles in a fixed direction, or the intensity and direction of magnetisation, discussed in Chapter 4, while the continuous model solves for coefficients multiplying the Green's functions which are used to give the intensity and direction of magnetisation, discussed in Chapter 5.

Other approaches to the modelling of magnetised sources include the use of magnetic monopoles [Toyoshima et al., 2008], and a 'semi-inverse' approach where forward models are used initially to determine some source dipole characteristics which are then used as a priori information in an inverse model [Quesnel et al., 2007].

Inverse models that do not require assumptions about the magnetisation direction are particularly important for the lunar case where directions can not be assumed. If robust directional information can be inferred, this may offer a key constraint for determining the sources of the original magnetising fields. The different representations of the crustal magnetisation as equivalent source dipoles, or as a continuous model are expected to give similar solutions, as observed by Whaler and Purucker (2005) when comparing their continuous magnetisation model for the Martian crust with the equivalent source dipole model of Langlais et al. (2004).

3.2.3 Equivalent layer inversions

In order to conduct an inversion, assumptions must be made about the distribution and location of the magnetised sources. Given the lack of information about possible source locations and dimensions for the Moon, and the lack of clear correlations between magnetic anomalies with Clementine gravity and topography data [Frey et al., 2002], a reasonable assumption for the Moon is to confine magnetisation to a layer with constant thickness. The lack of horizontal boundaries is then not a restriction on the source extent, though the resulting magnetisation will be vertically averaged throughout the layer.

A component of the observed magnetic field B_i can be expressed in terms of the unknown magnetisations within a layer. The magnetisation distribution can be composed of discrete point dipoles with magnetisation m_j, related to the observations through a data kernel matrix G_{ij},

$$B_i = \sum_j^n G_{ij} m_j \tag{3.1}$$

or can be expressed as a continuous magnetisation $\mathbf{M}$ within a volume V which is a linear sum of Green's functions, $\mathbf{G}_i$, relating the magnetic field observation at location $\mathbf{r}_i$ to the magnetisation within the crust at location $\mathbf{s}$:

$$\mathbf{B}_i = \int_V \mathbf{G}_i(\mathbf{r}_i, \mathbf{s}) \cdot \mathbf{M}(\mathbf{s}) dV \tag{3.2}$$

These linear representations of the relationship between the observed field and magnetisation give rise to the generalised matrix form $\mathbf{B} = \mathbf{A}\mathbf{x}$:

$$\mathbf{B} = \mathbf{G}\mathbf{m} \quad \text{(a)} \qquad \mathbf{B} = \mathbf{\Gamma}\boldsymbol{\alpha} \quad \text{(b)} \tag{3.3}$$

with **G** the matrix of data kernels, **m** the vector of dipole magnetisations, **Γ** the 'Gram matrix' containing pairs of inner products of the Green's functions for all the data points, and **α** the vector of coefficients multiplying the Green's functions. With present computational power, inversions can involve many thousands, or hundreds of thousands, of data points and model parameters. Inverse problems with more data than parameters are described as 'over determined', whereas if the linear equations of 3.3 do not contain sufficient information for each of the model parameters to be determined uniquely, this is described as an 'under constrained' problem. The equivalent source dipole model can be formulated as over determined or under constrained depending on the number of data and dipoles used in each model, whereas the spatially continuous magnetisation model is infinitely under constrained.

Total magnetic field data (rather than the vector components) can also be used to produce magnetisation models, but the relationship between magnetisation and total magnetic field is non linear. Chapter 6 discusses the linearisation, and the resulting iterative inversion, for magnetisation modelling with the LP ER data, and joint inversion with the ER and MAG data.

3.2.4 Model resolution

The magnetic field measured by a satellite is a superposition of the fields from many sources, giving magnetic field distributions associated with magnetised features on the scale of the field resolution (~30 km for MAG data). However there are likely to be magnetisation variations on much smaller scales. Magnetisation models can only 'sample' magnetisation variations at a finite resolution (such as the dipole spacing) which may or may not be comparable to the true variation in the crustal magnetisation. As the model parameters are determined from the data, errors in the data are also mapped into errors in the estimated parameters and the models themselves can act to reduce the sampling resolution, as will be discussed in sections 4.2.4 and 4.5.6.

3.3 Finding a solution

There are many methods which could be used to solve the linear equations of 3.3 to find the magnitude and direction of a magnetisation solution. Where the number of data and parameters permit, the inversions can be carried out directly with the solution found after a single operation or series of operations. Models with more parameters may require iterative methods from a starting solution until there is convergence to a desired solution after a number of steps [Press et al., 1992].

However, inversion of magnetic field data will generally result in a non-unique solution. To restrict the number of available solutions and to find plausible models of magnetisation for interpretation, reasonable constraints can be incorporated into the model, or applied to model solutions.

3.3.1 Non-uniqueness

Any magnetisation distribution which fits a magnetic field is just one of an infinite number of magnetisation distributions that could also fit that field. For example, the sources of the Earth's crustal field, as mapped from satellite data do not unambiguously reflect features in the crust. Non-uniqueness can arise from the sampling of a finite number of data points used to represent the field, and the noise in these data [e.g Menke, 1989]. Another cause of non-uniqueness, outlined by Runcorn (1975), is that there are magnetisation distributions that produce no external magnetic field. These are known as annihilators of the magnetic inverse problem [Maus and Haak, 2003]. For the linear equations $\mathbf{B} = \mathbf{A}\mathbf{x}$, there exists an annihilator $\mathbf{a}$ for which $\mathbf{A}\mathbf{a} = 0$. Any amount of the annihilator can be added to the solution $\mathbf{x}$ which satisfies the data, without affecting the predicted field at the observation locations.

To select a unique, and suitable, solution from the myriad of potential solutions, constraints can be placed on the fit to the data, or on the model solution itself. Constraints reduce but do not remove non-uniqueness, and the inverse models

in this thesis produce a suite of possible magnetisation models rather than a unique solution. Examples of non-uniqueness are discussed in section 4.7.

3.3.2 Minimum norm solution

A unique solution can be found by imposing a constraint which gives preference to a particular solution with desirable properties, based on prior information. A constraint commonly used in inverse problems is that of minimising a norm of the solution (or its derivatives) [Backus and Gilbert, 1967, Shure et al., 1982]. Minimum norm crustal magnetisation solutions ensure that the magnetisation model has the minimum structure and/or amplitude required for a given fit to the data by minimising quantities related to the amplitude or spatial gradients. The true magnetisation is then at least as strong as the model on average, or with at least as much structure. However, it is recognised that imposed solution properties may present some difficulties in the interpretation of the magnetisation model produced if the constrained magnetisation solution is not representative of the true magnetisation.

For magnetisation models from magnetic field data, the usual choice of norm of the magnetisation solution is the '2-norm' which represents the minimum 'root mean square' (RMS) of the magnetisation amplitude. Parker (1971) and Parker et al. (1987) developed the minimum RMS magnetisation solution for magnetisation modelling for seamounts when finding an average magnetisation was more important than the distribution itself.

The form of the Gram matrix $\mathbf{\Gamma}$ in equation 3.3b is set up to ensure a solution with minimum amplitude [Shure et al., 1982] defined by the square of the amplitude norm:

$$\left\|\mathbf{M}\right\|^2 = \int_V \mathbf{M}\cdot\mathbf{M}dV = \boldsymbol{\alpha}^T\mathbf{\Gamma}\boldsymbol{\alpha} \tag{3.4}$$

For the magnetisation solution to equation 3.3a, the solution norm can be defined by $\mathbf{m}^T\mathbf{D}\mathbf{m}$ where the matrix $\mathbf{D}$ is a regularisation matrix which can be used to define

different norms. The solution '2-norm' in this case is given when **D=I**, the identity matrix:

$$\|\mathbf{m}\| = \sqrt{\mathbf{m}^T\mathbf{m}} = \sqrt{\sum_j^N m_j^2} \tag{3.5}$$

Different forms of the matrix **D** represent different norms of the solution vector.

Minimisation of a measure of the spatial gradient of the solution is another common solution norm used in inverse modelling. Both first and second derivatives of the model solution parameters within the horizontal layer (or vertically) can be used as a measure of roughness which is minimised, resulting in a smooth model solution [e.g. Constable et al., 1987]. The minimum roughness norm is complicated to apply as a constraint in magnetisation modelling due to the vector nature of the model solution and the input data. The matrix **D** becomes banded about the diagonal, and the elements of the Gram matrix $\boldsymbol{\Gamma}$ would be defined differently. However, rapid changes in geology and magnetisation processes over short distances are to be expected in the lunar crust, as seen on Earth, so minimisation of the RMS magnetisation amplitude norm is a more appropriate/less severe constraint on the inversion model.

3.3.3 Constrained least squares solution

In the presence of noise and uncertainty in the data, and differences between the model and actual source parameters (inhibiting the ability of the model to predict the data), a model which fits the data perfectly would be attributing noise to a crustal source. We therefore expect a residual, **v**, between the observed field **b** and the field predicted by the model:

$$\mathbf{b} + \mathbf{v} = \mathbf{A}\mathbf{x} \tag{3.6}$$

For a model with few a priori constraints on magnetisation direction or source geometry, a solution is sought for **x** which can best fit the observations. The simplest

way to asses the fit is to look at the 'sum of squares' of the residuals (SSR) between the observed data and the data predicted from the solution:

$$\mathbf{v}^T\mathbf{v} = (\mathbf{Ax}-\mathbf{b})^T(\mathbf{Ax}-\mathbf{b}) \tag{3.7}$$

A solution which has the smallest SSR, a 'least squares' solution [e.g Menke, 1989] contains no contribution from an annihilator and also minimises the RMS magnetisation [Whaler and Langel, 1996].

Unwanted features in the minimum norm solution due to noise in the input data can be reduced at the expense of the fit to the data by minimising a linear combination of the square of the solution norm, and the SSR weighted by a positive Lagrange multiplier, λ^{-1}, with respect to the solution vector **x**, so that:

$$\left[\mathbf{G}^T\mathbf{G}+\lambda\mathbf{D}\right]\mathbf{m}=\mathbf{G}^T\mathbf{b} \quad \text{(a)} \qquad \left[\mathbf{\Gamma}+\lambda\mathbf{I}\right]\boldsymbol{\alpha}=\mathbf{b} \quad \text{(b)} \tag{3.8}$$

(see sections 4.2 and 5.2, and appendices 9 and 12) [e.g Gubbins, 1983]. The forms in equation 3.8 assume that the noise in the data is uncorrelated and has zero mean. While the coordinate transformations of the measured vector data, and the removal of the external field may result in some shift or correlation in the noise levels, this is expected to be small so that the assumption of uncorrelated and zero mean noise should be valid, particularly for such a large data set. In equation 3.8a the regularisation matrix **D** incorporates the minimum norm constraint, with the parameter λ controlling the relative importance of the fit to the data versus the undesirable (e.g oscillatory, large variance) contributions to the solution. In the case when **D=I**, equation 3.8a becomes

$$\left[\mathbf{G}^T\mathbf{G}+\lambda\mathbf{I}\right]\mathbf{m}=\mathbf{G}^T\mathbf{b} \tag{3.9}$$

and, as in the case of equation 3.8b, the parameter λ controls the fit to the data versus the amplitude of the magnetisation solution, and is known as a damping parameter. Equations 3.9 and 3.8b are known as a 'damped least square solution'. If the matrix **D** were to represent spatial differences between model parameters, the

parameter λ would act as a smoothing factor giving a solution with minimum roughness. Similarly, the form of the Gram matrix could be altered to provide a solution in which a different solution norm is minimised.

3.3.4 The effect of damping

The amount of damping in equations 3.8b and 3.9 controls the 'trade-off' between the fit to the input data and the amplitude of the magnetisation solution. Solutions with a given norm and misfit are unique [Shure et al., 1982]. With no damping ($\lambda = 0$), solutions may fit the data exactly but are likely to consist of rapidly varying model parameters and large solution norms. This is discussed with examples in section 4.5. With a positive and increasing λ, the residual between the data and the model predictions increases, with the amplitude of the solution decreasing.

The ideal form of this trade-off is represented by the curve in figure 3.2; however, the shape of the trade-off curve can vary for different model representations. There are a range of values of damping parameters rather than an exact value which optimally minimises both the residuals and the magnetisation. A suitable value of damping parameter is one close to the 'knee' of curve, where models with similar fits to the data have lower magnetisation norms. An under

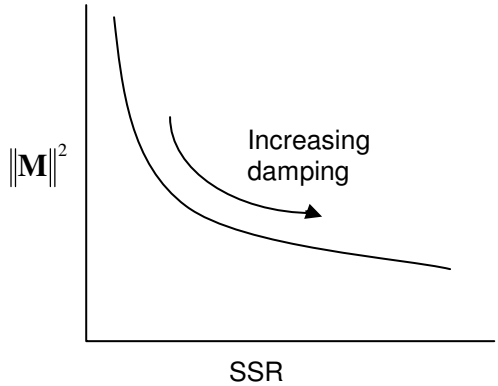

Figure 3.2: Example of a 'trade-off' curve with damping parameter, between the square of the norm of the model solution, and the sum of squares of the residuals (SSR) between the data and the model predictions.

damped solution may still contain features in the model which relate to noise in the data, while an over damped solution lacks detail in the model to adequately reproduce the source data.

3.4 Constraints on the solution

As well as minimisation of a norm and the SSR, further constraints can be applied to the model solution from complementary data sets, prior information, different processing techniques, or theoretical requirements. Additional constraints ensure that the solution is plausible, and where possible, geologically relevant.

3.4.1 A priori and additional information

On Earth, it is possible to produce very detailed crustal magnetisation models using a priori information such as ground truths, mineralogy, or other geological and geophysical data sets [e.g Hemant and Maus, 2005]. Source parameters such as magnetisation direction, source location or depth to the Curie isotherm (where the temperature exceeds the Curie temperature) are often known approximately before modelling. However for the Moon there is very little prior information which could be used with magnetisation modelling.

With terrestrial airborne magnetic data, techniques utilising the gradient of the magnetic field components [e.g Hood and McClure, 1965] can be used to determine the shape and location of magnetised sources. An approach known as Euler deconvolution can provide estimates of the depth and shape of sources [e.g Reid et al., 1990], while the 'tilt depth' technique [Miller and Singh, 1994] can reveal the location of the edges of a source. These techniques have been very successful and still are being developed and improved [e.g Stavrev et al., 2009, Salem et al., 2008]. The spectral content of the crustal fields has also been used to estimate source edges and depths [e.g Blakely, 1996]. However, the application of

these methods to satellite data and to a purely remanent crustal field has not been studied, and even the lowest altitudes of the LP satellite may be too high to make similar studies reliable.

3.4.2 Complementary data sets

For the Moon, the existence of magnetic field observations at altitude and at the surface can offer an important constraint for lunar magnetisation models; a chosen magnetisation distribution must be able to account for both data sets. If the solution contains a magnetic annihilator, these can produce non-zero magnetic fields in other component directions or at other locations, so such a solution would not be able to fit each data set as well as a solution without an annihilator.

On the Earth, other geophysical data sets can also be used to assist in the interpretation of magnetic anomalies. Structures identified in, for example, seismic, radar or resistivity surveys offer information on potential sources, and terrestrial gravity anomalies often correlate with magnetic anomalies. While there is gravity data for the Moon, there has so far been no clear correlation between lunar gravity and magnetic anomalies [Milbury et al., 2008].

3.4.3 The Parker bound

An analytical bound on the required magnetisation strength to account for the observed magnetic fields can be provided from ideal body theory and used to reject magnetisation solutions which are too weak, and to assist with the choice of damping parameter. Parker (2003) determined the smallest possible intensity of magnetisation within a layer (without any assumptions about direction), which could give the maximum observed field, B. For observations at an altitude of h_1 (Figure 3.3), the smallest possible intensity of magnetisation M_0 for a crust with thickness $h_2 - h_1$ is:

$$M_0 = \frac{12|B|/\mu_0}{[6+\sqrt{3}\ln(2+\sqrt{3})]\ln(h_2/h_1)} \approx \frac{1.4491|B|/\mu_0}{\ln(h_2/h_1)} \qquad (3.10)$$

[Parker, 2003] where μ_0 is the permittivity of free space, and B can be the maximum total or component field in Teslas. This magnetisation bound, the 'Parker bound' must be met somewhere in the model solution (maximum magnetisation >= M_0) and acts as a constraint for choosing an appropriate magnetisation solution. Although calculated from a single data point, the minimum magnetisation from equation 3.10 is not too different from the minimum magnetisations found when considering pairs of observations [Parker, 2003].

The maximum crustal field at an altitude of 30 km in the radial data in the lunar wake and tail region is 24.33 nT, and the maximum crustal field in the total field from the spherical harmonic model (degree 150) is 18.39 nT. These maxima are both over the Reiner Gamma region. Using these maxima with different layer thicknesses in equation 3.10, the Parker bound minimum magnetisations were calculated and are listed in table 3.1 and plotted in figure 3.4 as a function of layer thickness. If the altitude of the data is taken to be close to the surface (but not zero), the minimum magnetisations required to meet the maximum total surface field estimate from the 1°×1° binned ER data (73 nT, again over the Reiner Gamma region) are lower than the values listed in table 3.1.

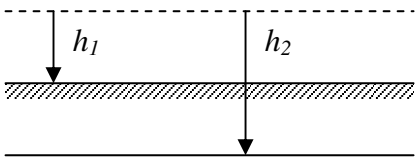

Figure 3.3: Schematic of the geometry used for calculating the Parker bound

Thickness (km)	M_0 (mA/m) (for $B_{\max}$ =18.39 nT)	M_0 (mA/m) (for $B_{r_{\max}}$ = 24.33 nT)
5	137.6	174.5
10	73.7	93.5
15	52.3	66.4
20	41.5	52.7
25	35.0	44.4
30	30.6	38.8
35	27.4	34.8
40	25.0	31.8
45	23.1	29.4
50	21.6	27.4

Table 3.1: Parker bound minimum required magnetisations for layers with different thicknesses, for the maximum total magnetic field from the spherical harmonic model of the lunar crustal field, and the maximum field value in the radial component in the lunar wake and tail region.

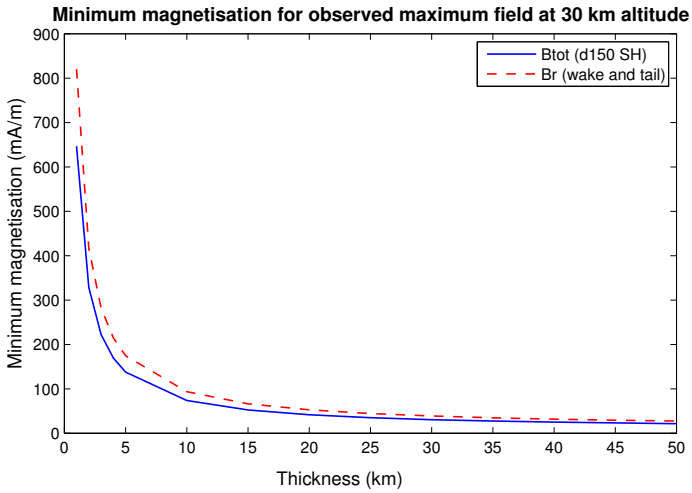

Figure 3.4: Plot of the Parker bound minimum required magnetisations with layer thickness ($h_2 - h_1$, figure 3.3) for the maximum total magnetic field from the spherical harmonic model of the lunar crustal field (d150 SH, blue solid line), and the maximum field value in the radial component in the lunar wake and tail region (red dashed line).

3.5 Input Parameters

The equivalent source dipole technique and the spatially continuous magnetisation model assume that the magnetisation is confined to, and spread vertically, in a single layer with fixed dipole depth and layer thickness. The physical model parameters required as inputs to the equivalent source dipole inversion are layer thickness, dipole depth, and dipole spacing (and dipole direction if assumed), and for the spatially continuous inversion, layer thickness only.

3.5.1 Layer thickness

For the Earth, the whole of the crust down to the Curie isotherm or the crust/mantle interface (whichever is shallower) can be considered to be magnetised in the presence of the global magnetic field. However for the Moon, while the potentially magnetisable crust is still the region down to the Curie isotherm or crust/mantle boundary, the actual region of the crust which is magnetised will depend on the extent of the magnetising fields and the sources. For example, magnetisation may exist as a thin layer of impact ejecta or mare basalt (~500 m) or could exist in the entire crust from the surface down to the Curie isotherm several 10s of km beneath the surface. Using the demagnetisation signatures of large (> 50 km) craters, an upper limit of the thickness of a magnetised layer at the Moon was given as ~50 km [Halekas et al., 2002].

3.5.2 Magnetic crustal thickness estimation from spectra

An estimate of the thickness of the magnetised crust for the Moon can be made by fitting a theoretical power spectrum to the observed power spectrum of the spherical harmonic model of the lunar crustal field (Figure 1.1). Voorhies et al. (2002) give the theoretical power spectrum of degree n, $\{R_n(r)\}$, expected from a

large number of uncorrelated dipoles with random magnetic moments scattered on a sphere of radius r_x within the body sphere of radius a as:

$$\{R_n(r)\} = A_x n(n+½)(n+1)\left(\frac{r_x}{a}\right)^{2n-2}\left(\frac{a}{r}\right)^{2n+4} \qquad (3.11)$$

where the constant A_x is determined by the number of dipoles used, their mean square moments, and geometrical factors. Following Voorhies et al. (2002), the source radius r_x and constant A_x for the log of the theoretical spectrum with the least squares fit to the log of the observed spectrum were found for different sections of the spectrum (see Appendix 5). The best fitting power spectrum for degrees 1 to 150 is shown in figure 3.5 with the observed power spectrum. The higher degree terms fit better to the theoretical model than the lower degree terms, which are perhaps dominated by noise from unmodelled external fields.

The best fitting source sphere radius of 1711.4 km gives a globally averaged source depth of 25.73 km. The globally averaged source depth varies from ~14 to 30 km depending on which parts of the spectrum are fit (see Appendix 5). The estimated

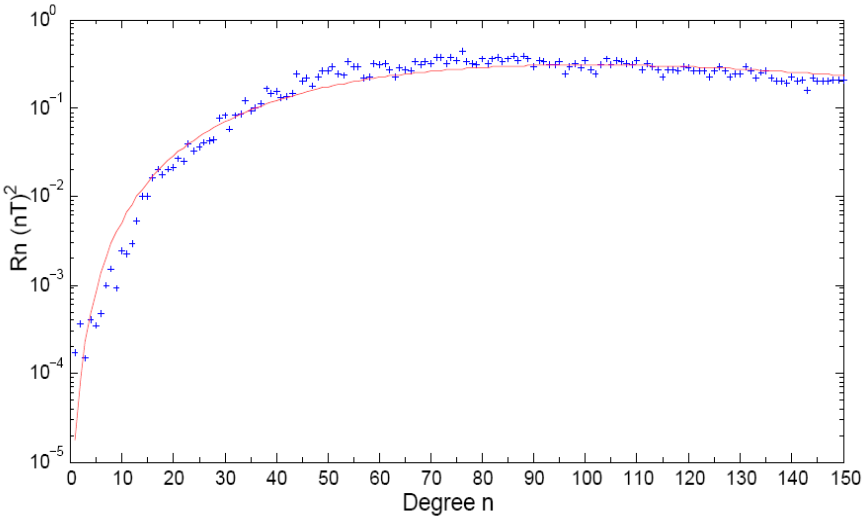

Figure 3.5: The spatial magnetic power spectrum for the lunar crustal field up to degree 150 at the surface (blue crosses) with the two parameter theoretical curve fitted through it (red line) expected from a spherical shell of randomly oriented dipoles.

source depth from this technique is considered to be closer to the layer thickness than the layer half thickness as the theoretical spectrum may overestimate the true depth of sources that are correlated over scales larger than the dipole spacing [Voorhies et al., 2002]. Although this 'spectral thickness' does not take into account any correlation of the sources, or variations in layer thickness which would be expected for some regions of the Moon, a layer thickness of 25-30 km serves as a first estimate for the global average magnetic crustal thickness of the Moon.

3.5.3 Equivalent layer depth

For equivalent layer magnetisation models it is also possible to place the layer at depth within the crust representing a subsurface or buried source. Magnetised sources could be intrusive, or buried by subsequent volcanism or impact ejecta. Layered basalts are observed in some subsurface radar studies from Apollo 17 and the Lunar Radar Sounder on Kaguya [Peeples et al., 1978, Ono et al., 2009].

The layer depth of models in this thesis is varied for the equivalent source dipole technique. The depth of a layer could also be raised above the surface to represent local topography, but this will not be considered.

3.6 Predicted fields and residuals

The model solutions can be used to predict the magnetic field at any location. This allows the study of the distribution of the residuals at the original input data locations, or prediction of the field with a denser distribution than the starting data. Histograms of the residuals can be used to identify the nature of the residuals and any systematic biases in the data or components. The magnetic field at the surface can also be predicted and compared to the ER observations.

A damped solution will mostly produce field values that under predict the field, so as well as considering the exact residuals, defined as $data - predictions$, it is also useful to consider absolute residuals, defined as $|data| - |predictions|$. In this

way, a positive absolute residual signifies an under prediction of the data while a negative absolute residual signifies an over prediction of the data (see figure 3.6A). Exact residuals will result in ambiguities in over or under prediction of the vector component field depending on the 'sign' of the value (Figure 3.6B). As the largest residuals are likely to be in regions of stronger field values, it is also useful to consider normalised residuals to show where the misfit is significant with respect to the field at that point. Normalised residuals are defined as

$$Normalised\ Residual = \frac{data - predictions}{data} \times 100 \tag{3.12}$$

which, assuming that the predicted field is of the same sign as the data, gives a positive residual for an under prediction of the data and a negative residual for an over prediction.

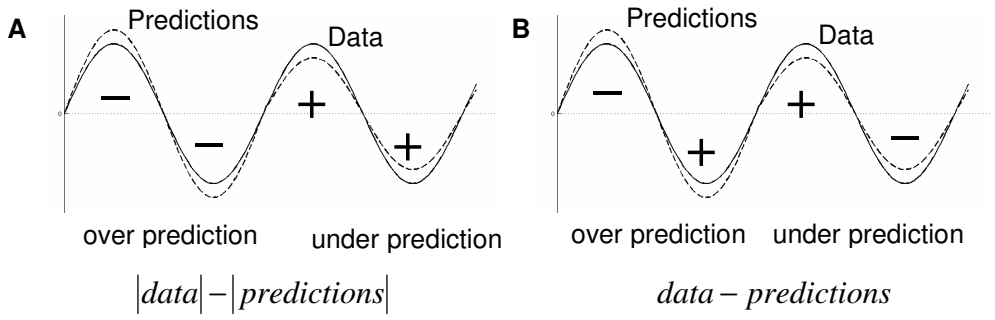

Figure 3.6: The 'sign' of A: absolute residuals, and B: exact residuals, for over or under prediction of the data by the model. Solid line is the data, dashed line the predictions from the model.

Chapter 4

Equivalent source dipole magnetisation models

A layer of equivalent source dipoles can be used to represent a crustal magnetic field and crustal magnetisation by assuming that the crust can be divided into magnetised blocks [Mayhew, 1979]. While magnetisation varies right down to the atomic scale, with the magnetic domains of each grain of a magnetic material combining to give the total observed field originating from that region of rock, the volume averaged magnetisation of each block can be represented by a magnetic dipole at its centre. A magnetic field at an observation point can be represented by the superposition of the fields from each of these source dipoles. As a discrete formulation of magnetisation, the equivalent source dipole technique has the advantage of being amenable to both global and regional magnetic studies. In this thesis, the equivalent source dipole technique will be applied to regions of isolated anomalies.

The equivalent source dipole technique has been used with the radial component of the MGS magnetometer data, solving for dipole magnitudes with fixed direction [Purucker et al., 2000], and with the three components of the Martian field solving for the three components of magnetisation globally [Langlais et al., 2004, Chiao et al., 2006].

4.1 Magnetic dipoles as point sources

The magnetic point dipole is defined as a dipole of negligible length compared to the distance between the source and the observation points. The equivalent source dipole technique looks at the contributions of point source dipoles within the lunar crust, to the magnetic field at satellite altitude.

4.1.1 The magnetic field from a single dipole

The magnetic potential $\psi_j(\mathbf{r}_i)$, at an observation point $\mathbf{r}_i$ at satellite attitude, arising from a magnetic dipole at location $\mathbf{r}_j$ within the lunar crust with magnetic moment $\mathbf{m}_j$ is:

$$\psi_j(\mathbf{r}_i) = \frac{\mu_o}{4\pi}\mathbf{m}_j \cdot \nabla_j \frac{1}{R_{ij}} \tag{4.1}$$

where ∇_j is the gradient operator (in spherical coordinates) with respect to (r_j, θ_j, ϕ_j) and R_{ij} is the distance between the dipole location and the magnetic field observation point.

This formulation uses spherical polar coordinates (r, θ, ϕ) (Figure 4.1) assuming a spherical Moon of radius 1737.1 km and is based on Dyment and Arkani-Hamed (1998) and Von Frese et al. (1981).

The dipole moment $\mathbf{m}_j$ is defined by the dipole moment magnitude m_j (units Am^2), and the direction $\mathbf{w}_j$,

$$\mathbf{m}_j = m_j \mathbf{w}_j \tag{4.2}$$

defined by an inclination I_j and declination D_j.

$$\mathbf{w}_j = (-\sin I_j, -\cos I_j \cos D_j, \cos I_j \sin D_j)^T \tag{4.3}$$

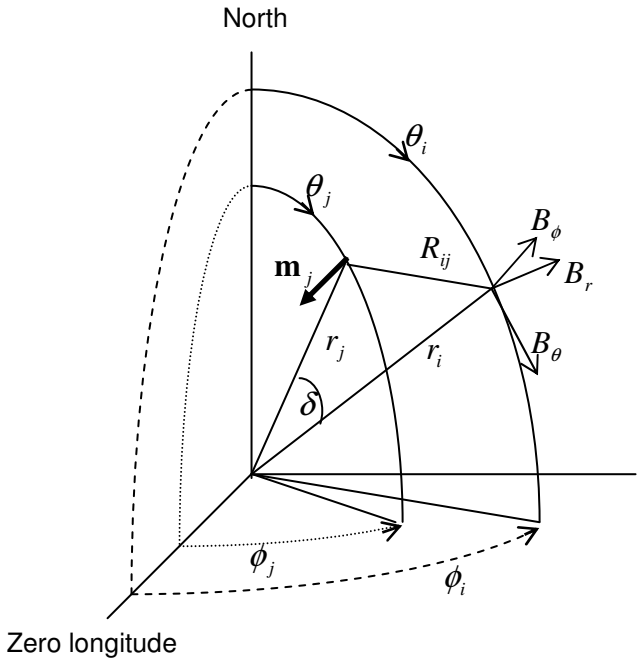

Figure 4.1: Geometry of the source point, observation point and the associated unit vectors in spherical coordinates. (***B*** is outwards so that r points outward from the origin, θ points southwards, and ϕ points eastwards). (Based on Dyment and Arkani-Hamed (1998)).

Applying the gradient operator in equation 4.1 and following the notation of Dyment and Arkani-Hamed (1998), the potential can be expressed as

$$\psi_j(\mathbf{r}_i) = -\frac{\mu_o}{4\pi}\frac{(m_{j_r}A_1 + m_{j_\theta}B_1 + m_{j_\phi}C_1)}{R_{ij}^3} = -\frac{\mu_o}{4\pi}\frac{m_j(w_rA_1 + w_\theta B_1 + w_\phi C_1)}{R_{ij}^3} \quad (4.4)$$

(see Appendix 6),where

$$\begin{aligned} R_{ij} &= \left|\mathbf{r}_i - \mathbf{r}_j\right| = (r_i^2 + r_j^2 - 2r_ir_j\cos\delta)^{1/2} \\ A_1 &= r_j - r_i\cos\delta \\ B_1 &= r_i(\cos\theta_i\sin\theta_j - \sin\theta_i\cos\theta_j\cos(\phi_i - \phi_j)) \\ C_1 &= -r_i\sin\theta_i\sin(\phi_i - \phi_j) \end{aligned} \quad (4.5)$$

with the angle δ between the position vectors to the dipole location and the magnetic field observation point (see figure 4.1).

The magnetic field $\mathbf{B}_j(\mathbf{r}_i)$, at position $\mathbf{r}_i$, predicted from a dipole at location $\mathbf{r}_j$ is given by the negative gradient of the potential so that:

$$\mathbf{B}_j(\mathbf{r}_i) = -\nabla_i \psi_j(\mathbf{r}_i) = \frac{\mu_o m_j}{4\pi} \nabla_i \left(\frac{(w_{r_j} A_1 + w_{\theta_j} B_1 + w_{\phi_j} C_1)}{R_{ij}^3} \right) \tag{4.6}$$

Applying the gradient operator again, the magnetic field vector $\mathbf{B}_j(\mathbf{r}_i)$, of component p ($p = 1,2,3$ for r_i, θ_i, ϕ_i) can be expressed in matrix form where the contribution of the dipoles can be considered in terms of magnitude only (equation 4.7a and 4.7c) (for a set direction $\mathbf{w}_j$), or magnitude and direction independently (4.7b and 4.7d):

$$\mathbf{B}_j(\mathbf{r}_i) = [\mathbf{H}_{ij}\mathbf{w}_j] m_j \quad \text{(a)} \qquad \mathbf{B}_j(\mathbf{r}_i) = \mathbf{H}_{ij}\mathbf{m}_j \quad \text{(b)} \tag{4.7}$$

$$B_j(\mathbf{r}_i)_p = (\mathbf{H}_{ij}\mathbf{w}_j)_p m_j \quad \text{(c)} \qquad B_j(\mathbf{r}_i)_p = (\mathbf{H}_{ij})_p \mathbf{m}_j \quad \text{(d)}$$

Matrix $\mathbf{H}$ is the 3×3 dipole source function matrix relating the contribution of the components q ($q = 1,2,3$ for m_r, m_θ, m_ϕ) of the dipoles to the components p of the magnetic field. $(\mathbf{H}_{ij})_p$ is the pth line of the $\mathbf{H}$ matrix. Using the notation of Dyment and Arkani-Hamed (1998), the elements of $\mathbf{H}$ are:

$$H_{11} = \frac{-\mu_o}{4\pi R_{ij}^3}\left[\frac{3AA_1}{R_{ij}^2} + \cos\delta\right] \quad H_{12} = \frac{-\mu_o}{4\pi R_{ij}^3}\left[\frac{3AB_1}{R_{ij}^2} - \frac{B_1}{r_i}\right] \quad H_{13} = \frac{-\mu_o}{4\pi R_{ij}^3}\left[\frac{3AC_1}{R_{ij}^2} - \frac{C_1}{r_i}\right]$$

$$H_{21} = \frac{-\mu_o}{4\pi R_{ij}^3}\left[\frac{3BA_1}{R_{ij}^2} - \frac{B}{r_j}\right] \quad H_{22} = \frac{-\mu_o}{4\pi R_{ij}^3}\left[\frac{3BB_1}{R_{ij}^2} + D\right] \quad H_{23} = \frac{-\mu_o}{4\pi R_{ij}^3}\left[\frac{3BC_1}{R_{ij}^2} + E\right] \tag{4.8}$$

$$H_{31} = \frac{-\mu_o}{4\pi R_{ij}^3}\left[\frac{3CA_1}{R_{ij}^2} - \frac{C}{r_i}\right] \quad H_{32} = \frac{-\mu_o}{4\pi R_{ij}^3}\left[\frac{3CB_1}{R_{ij}^2} - F\right] \quad H_{33} = \frac{-\mu_o}{4\pi R_{ij}^3}\left[\frac{3CC_1}{R_{ij}^2} + G\right]$$

where

$$
\begin{aligned}
A &= r_i - r_j \cos\delta \\
B &= r_j(\sin\theta_i \cos\theta_j - \cos\theta_i \sin\theta_j \cos(\phi_i - \phi_j) \\
C &= r_j \sin\theta_j \sin(\phi_i - \phi_j) \\
D &= \sin\theta_i \sin\theta_j + \cos\theta_i \cos\theta_j \cos(\phi_i - \phi_j)
\end{aligned}
\qquad
\begin{aligned}
E &= \cos\theta_i \sin(\phi_i - \phi_j) \\
F &= \cos\theta_j \sin(\phi_i - \phi_j) \\
G &= \cos(\phi_i - \phi_j)
\end{aligned}
\qquad (4.9)
$$

4.1.2 An ensemble of magnetic dipoles

When multiple dipoles (*nx*) are considered, there is a dipole source function (**H**) for each dipole at the observation location so that the field at the observation point becomes the sum of the contributions from each dipole:

$$B(\mathbf{r}_i)_p = \sum_j^{nx} (H_{ij} w_j)_p m_j \quad \text{(a)} \qquad B(\mathbf{r}_i)_p = \sum_j^{nx} \sum_q^3 (H_{ij})_{pq} m_{j_q} \quad \text{(b)} \qquad (4.10)$$

where equation 4.10a represents the contribution from dipoles with fixed direction, and equation 4.10b the contributions from dipoles with variable direction.

To simplify this notation, the individual source functions **H** for all of the dipoles and observation locations can be included in a single matrix **G** so that the entire set of observations **B** can be represented as:

$$\mathbf{B} = \mathbf{Gm} \qquad (4.11)$$

The size of the **G** matrix (M×N) is determined by the number of dipole parameters in the vector **m** of dipole moments (size 3*nx*), or magnitudes (size *nx*), and the number of components of magnetic field used at each of the *mx* observation locations in the vector **B** . For **m** to represent magnetisation, the dipole moment per unit volume (A/m) instead of dipole moment (Am^2), the volume of the crust encasing the dipole becomes a coefficient in the terms of the **G** matrix. The volume is defined by the dipole spacing (1° ≈ 30.0 km on the Moon) and layer thickness.

An observed magnetic field is related to the crustal magnetisation of a grid of dipoles by a set of linear equations through the source function matrix **G,** so that the components of the magnetic field at an observation point can be simply expressed as dot products of parts of the matrix:

$$B(\mathbf{r}_i)_p = \mathbf{G}_{i_p} \cdot \mathbf{m} \tag{4.12}$$

where $\mathbf{G}_{i_p}$ contains the *p*th line from the **H** matrix for the observations at location $\mathbf{r}_i$ for each of the dipoles (see Appendix 7).

4.1.3 Contributions from dipoles

The magnetic field from a set of magnetic dipoles will depend on their orientation, as well as the model parameters of depth, thickness and spacing. The three components of magnetic field from a single dipole with different orientations are shown in figure 4.2. For a global distribution of dipoles and observation points, the matrix **G** can be very large ($>10^9$ elements for data and dipoles with 1° spacing) and computation of the matrix elements can be lengthy. However, the influence of a

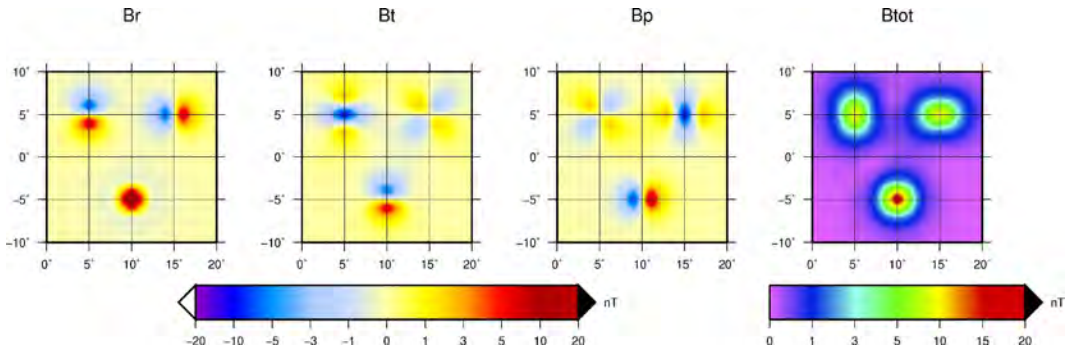

Figure 4.2: The three components and total magnetic field at 30 km altitude for a horizontal (North-South) dipole at (5°N, 5°E), a horizontal (East-West) dipole at (5°N, 15°E), and a radial dipole at (5°S, 10°E). (Magnetisation 5 A/m in the centre of blocks 0.25°×0.25°×30 km thickness).

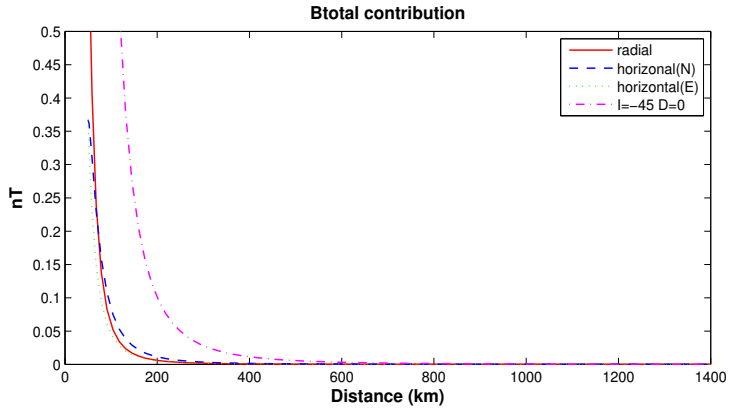

Figure 4.3: The contribution of a single radial (red solid line), horizontal (North, blue dashed line), horizontal (East, green dotted line) dipole, and dipole with Inclination -45° and Declination 0° (pink dot-dash line), to the total magnetic field at an observation point (30 km altitude) as a function of distance. (Magnetisation 0.1 A/m in the centre of block 0.5°×0.5°×40 km thickness).

single dipole decays rapidly with distance (equation 4.6) so that dipoles beyond a certain distance from an observation point will have a minimal contribution to the field at that point (Figure 4.3). The sparseness of the **G** matrix can be exploited by only considering dipoles within a certain distance from the observation point (e.g making the matrix **G** for only selected dipoles, or setting to zero any element in **G** from a dipole beyond a certain distance).

4.2 The linear inverse problem with equivalent source dipoles

For a known distribution of dipoles, the magnetic field they produce can be calculated (equation 4.11). If instead it is the magnetic field **b** that is known, resulting from an unknown magnetised source, the inverse problem here is to solve for the dipole parameters **m,** for a collection of dipoles which can successfully reproduce the observed magnetic field with a small residual **v**:

$$\mathbf{b} + \mathbf{v} = \mathbf{Gm} \tag{4.13}$$

The observations vector **b** contains vector magnetic field data, and the **G** matrix can be assembled as the source function matrix for all or each of the components of the observed magnetic field data, and for dipoles with pre-assigned or solvable directions. It is not possible however, to solve for a single component of magnetisation only without setting the other components to zero (solutions for just the M_r, M_θ or M_ϕ component of magnetisation alone are not necessarily similar to the components when solved for together).

4.2.1 Least squares inversion

As discussed previously, the inverse problem is non-unique and there are an infinite number of solutions which are capable of reproducing the data. For an over determined problem, the linear equations 4.11 contain enough information to determine each parameter, so that there exists a unique 'least squares solution'. This is the case when there are more observations than dipole parameters (M>N), and the least squares residual is non zero since in general there is no exact solution for **m** which can satisfy all of the linear equations. Minimisation of the sum of squares of residuals

$$\mathbf{v}^T\mathbf{v} = (\mathbf{Gm}-\mathbf{b})^T(\mathbf{Gm}-\mathbf{b}) \tag{4.14}$$

between the observations and the predictions from the model, with respect to **m**, leads to the normal matrix equations:

$$\mathbf{G}^T\mathbf{Gm} = \mathbf{G}^T\mathbf{b} \tag{4.15}$$

(See Appendix 8). The matrix $\mathbf{G}^T\mathbf{G}$, of size (N×N) (the smaller of the dimensions of matrix **G**), is square and symmetric with positive diagonal elements and has an inverse so that the least squares solution is given by:

$$\mathbf{m} = \left[\mathbf{G}^T\mathbf{G}\right]^{-1}\mathbf{G}^T\mathbf{b} \tag{4.16}$$

4.2.2 Damped least squares inversion

The stability of the inversion in equation 4.16 and the physical relevance of the magnetisation solution, depends on the sensitivity (conditioning) of the matrix $\mathbf{G}^T\mathbf{G}$ to noise in the data or uncertainty in the models. A well-conditioned matrix has a small condition number, and discrepancies between $\mathbf{b}$ and the predictions by the model will not have great significance to the solution. An ill-conditioned matrix, however, with a large condition number, while providing a magnetisation solution which fits the data very well, is very sensitive to small changes in $\mathbf{b}$ which can result in large variations in the values of $\mathbf{m}$ obtained by the inversion

The conditioning of the matrix $\mathbf{G}^T\mathbf{G}$ depends on the geometry of the model dipoles and the data locations, and also on the dimensions of the $\mathbf{G}$ matrix. For the geometrical set ups (thickness, depth, altitude, spacing) in these models, the condition value for the $\mathbf{G}^T\mathbf{G}$ matrix can be very large ($> 10^{10}$). This results from the high degree of colinearity in the columns of the matrix $\mathbf{G}$ since the contributions from different dipoles to observations points with similar distances between them are similar. In this case, while a solution can be found, it will be high amplitude and variable and may contain annihilators which give no contribution to the observed field or change to the fit to the data. A similar difficulty in choosing a solution was encountered by Langlais et al. (2004) who found that for almost identical residuals between the observed and predicted fields, the magnetisation changed dramatically, without creating any coherent magnetic field at the satellite altitude.

The damped least square inversion provides a stable and meaningful solution to the linear equations 4.11. Minimisation of the square of the 2-norm of the solution vector,

$$\|\mathbf{m}\|^2 = \mathbf{m}^T\mathbf{m} \tag{4.17}$$

and the SSR (equation 4.14), weighted by a parameter λ^{-1}, gives the solution:

$$\mathbf{m} = \left[\mathbf{G}^T\mathbf{G} + \lambda\mathbf{I}\right]^{-1}\mathbf{G}^T\mathbf{b} \tag{4.18}$$

(see Appendix 9). The addition of even a small value of λ to the diagonal elements of the matrix $\mathbf{G}^T\mathbf{G}$ significantly reduces its condition number, with the elements of the matrix $\left[\mathbf{G}^T\mathbf{G}+\lambda\mathbf{I}\right]^{-1}$ being smaller than those of the matrix $\left[\mathbf{G}^T\mathbf{G}\right]^{-1}$. This causes a reduction in the magnetisation values of the model solution, at the expense of a small increase in the residuals (see figure 3.2) so that the resulting solution still fits the data well, but is not affected by small changes in the input data (e.g noise). A damped least squares inversion with equivalent source dipoles was applied to the Martian data set by Chiao et al. (2006).

4.2.3 Under constrained problems

If the linear equations of 4.11 do not contain sufficient information for each of the model parameters to be determined uniquely (under constrained), the matrix $\mathbf{G}^T\mathbf{G}$ is singular and there is no unique minimum least squares solution to equation 4.15. This may be the case when there are more dipole parameters than observations (N>M) so that there are an infinite number of solutions for $\mathbf{m}$ with zero residual which satisfy all of the linear equations in 4.11.

Where the misfit is zero, a unique solution is found by minimising the RMS magnetisation, which gives the solution

$$\mathbf{m}=\mathbf{G}^T\left[\mathbf{G}\mathbf{G}^T\right]^{-1}\mathbf{b} \tag{4.19}$$

(see Appendix 10). The matrix $\mathbf{G}\mathbf{G}^T$ is of size (M×M), again the smaller of the dimensions of the matrix $\mathbf{G}$. As with the solution to the over determined problem, the stability of the inversion in equation 4.19 can be improved by allowing a non zero misfit with the inclusion of a damping parameter:

$$\mathbf{m}=\mathbf{G}^T\left[\mathbf{G}\mathbf{G}^T+\lambda\mathbf{I}\right]^{-1}\mathbf{b} \tag{4.20}$$

Most of the data and dipole parameter set ups in this thesis will involve more observations than dipole parameters, being over determined inversions rather than under constrained ones.

4.2.4 Model resolution and uncertainties

As long as there are sufficient data, the inherent resolution of the resulting equivalent source dipole model is set by the dipole spacing of the dipoles used to represent an area of the crust. However, if the dipole parameters being solved for are not independent, the model resolution decreases, independent of the data. An assessment of the 'independence' of each model parameter can be made from the 'model resolution matrix' **R**, an N×N matrix which relates the 'closeness' of the minimum magnetisation least squares estimate of the solution to a true solution ($\mathbf{b} = \mathbf{G}\mathbf{m}_{true}$) [Menke, 1989].

$$\mathbf{m} = \mathbf{R}\mathbf{m}_{true}$$

with (4.21)

$$\mathbf{R} = \left[\mathbf{G}^T\mathbf{G} + \lambda\mathbf{I}\right]^{-1}\left[\mathbf{G}^T\mathbf{G}\right]$$

for the case with more observations than dipole parameters (N>M).

Without damping, **R** would be the identity matrix and each model parameter is uniquely determined ($R_{ij} = \delta_{ij}$). As the damping parameter increases, **R** deviates from the identity matrix by spreading around the matrix diagonal (Figure 4.4), effectively correlating the solution of one dipole with adjacent dipoles so that the model solutions are weighted averages of the true model parameters. The spreading around the matrix diagonal indicates how well each of the model parameters can be resolved and the trace of the resolution matrix (the sum of the diagonal elements) indicates the effective number of parameters that can be independently resolved. The trace of **R** decreases as the damping parameter increases.

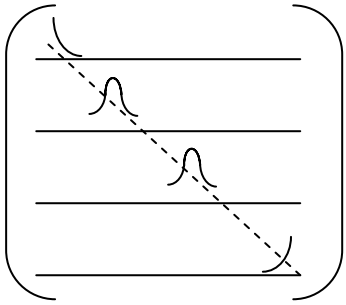

Figure 4.4: Schematic of the spreading of the values on selected rows of the resolution matrix representing a decrease in the model resolution. (Based on Menke (1989)).

Assuming that the data are uncorrelated and have equal and independent variance (not necessarily true in all cases but not invalid), the variance of the data, σ_d^2 can be estimated from the SSR and the degrees of freedom of the data given by the number of data points M and the trace of the resolution matrix $tr(\mathbf{R})$:

$$\sigma_d^2 = \frac{SSR}{M - tr(\mathbf{R})} \tag{4.22}$$

An estimate of the uncertainties in the model parameters σ_m, resulting from the inversion and variance of the data σ_d^2 can be attained from the covariance matrix of the model parameters, **C**, defined as

$$\mathbf{C} = \sigma_d^2 \left[\mathbf{G}^T\mathbf{G} + \lambda\mathbf{I}\right]^{-1} \tag{4.23}$$

[Menke, 1989] (in the over-determined case). An N×N matrix, the diagonals of **C** give the variances of each model parameter σ_m^2 and the off-diagonal elements of **C** indicate the correlations between the model parameters.

4.3 Input model parameters

The linear equivalent source dipole inversion for crustal magnetisation requires as inputs:

- Vector magnetic field data (single or multiple components) at specified locations (latitude, longitude and altitude)
- Locations of source dipoles (latitude, longitude and depth)
- Stated dipole spacing
- Vector of dipole directions if fixed
- Thickness of model layer
- Damping parameter

These inputs will determine the conditioning of the matrix $\mathbf{G}^T\mathbf{G}$ and the stability and success of the inversion.

4.3.1 Dipole and data grid

The distribution of dipoles, and also data, in the model should be as geographically homogeneous as possible to allow a stable solution [Covington, 1993]. The distribution of dipoles chosen here places dipoles homogeneously on a sphere using a polar coordinate subdivision [Katanforoush and Shahshahani, 2003] (Appendix 4). While this distribution gives equally spaced (equal volume) dipoles globally on a sphere, the coverage in the polar regions is limited, however, the dipole grid can be rotated to provide cover in the polar regions if required.

An equivalent source dipole model for a regional rather than a global data set should include all dipoles likely to contribute to the field observations in the area. The rapid fall off with distance of the contribution of a dipole to the field at the observation location (Figure 4.3) means that dipoles beyond ~400 km have negligible contribution to the observation location. This corresponds to a value for the angle δ (in figure 4.1) of about 15°, and for an orbital altitude of 30 km is

equivalent to the distance to the horizon from the satellite. A studied region therefore requires the contribution of dipoles from out to about 15° angular distance. These 'border dipoles' at the edges of the region of interest help to improve the solution in the central region by allowing contributions to the observed field from magnetised areas outside the region of interest. The data region is chosen to be coincident with the dipole grid (with the border dipoles) to avoid any edge effects from the chosen geometry and dipole and data grids.

4.3.2 Dipole spacing

Prediction of magnetic field measurements from the equivalent source dipole technique requires that the distance from the dipole to the observation location is greater that the dipole spacing (R_{ij} > dipole spacing (in km)). For observations at 30 km altitude, this gives a maximum dipole spacing of ~1°. For surface observations, this limit requires the dipoles to be located at a depth greater than their spacing.

The size of each individual block of magnetisation should ideally be within the range where magnetisation variation has a geological significance, and from which the finer scale features of the observed field can be still be predicted. Decreasing the dipole spacing increases the number of dipoles required, making regional rather than global models of crustal magnetisation favourable computationally. The spacing of the dipoles used in each model was determined by the amount of computer memory required for storing the **G** matrix, and the computation time for the inversion. Global magnetisation models for Mars with the equivalent source dipole technique [Langlais et al., 2004, Purucker et al., 2000, Chiao et al., 2006] were limited to dipole spacings of >1.4° which represents over 80 km on the Martian surface.

In the equivalent source dipole inversions of this thesis for regions only, the central region of interest is represented by a grid of dipoles with latitude spacing 0.25° (~7.58 km) centred on the region, with a 10-15° wide border of dipoles with 0.5° spacing (~15.15 km) (Figure 4.5). A lower resolution border is used to maximise

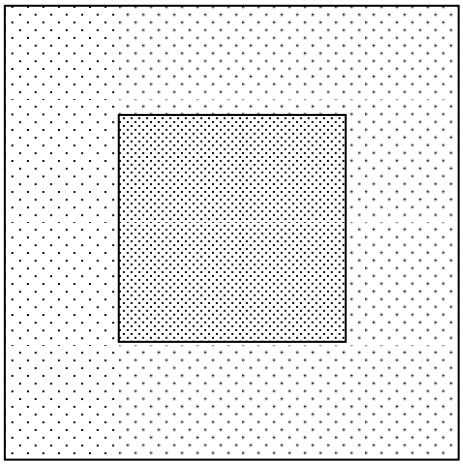

Figure 4.5: Schematic representation of the dipole grid with dense coverage in the central region of interest, and larger dipole spacing in the border region.

the number of dipoles in the central region (the change in resolution does not affect the results of stability of the inversion). Test models use a lower resolution square grid with 0.5° spacing in the central region and 1° spacing in the border. These spacings allow the inclusion of the border region dipoles and data over the extended region without overloading the computations, and also providing enough resolution within the selected area.

4.3.3 Dipole depth and layer thickness

The dipole depth and layer thickness defines the assumed layer of magnetisation. This can be thick or thin, starting at the surface, or buried under nonmagnetic material (Figure 4.6). While the depth of the dipoles may be anywhere within the magnetised layer, the requirement for surface observations that the dipoles should be located at a depth greater than their spacing, places them beneath the surface. Very thin layers for substantial regions (> few degrees) are therefore not possible to model with this equivalent source dipole technique due to computational limitations on the number of dipoles that can be used (thin layers require smaller spacing between dipoles). For these models, the dipole depth is chosen to be at the

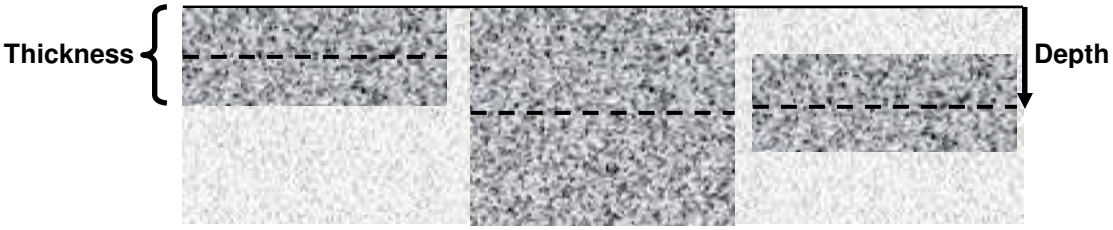

Figure 4.6: Thickness and depth of magnetised layers (grey) within the crust for a thin magnetised surface layer (left), thick magnetised surface layer (centre), and buried magnetised layer (right) surrounded by nonmagnetic material (light grey).

centre of the magnetised layer so that for a layer starting from the surface, the depth is half the thickness, while for a buried layer a depth ≥ ½ thickness can be chosen.

The dipole spacing and layer thickness define the volume encasing each dipole which will influence the strength of the dipole magnetisation in the model. In general, a thinner layer will require higher magnetisation values to produce the observed magnetic field than a thicker layer (though the relationship will also depend on the direction of the dipoles). However, the depth of the dipole enters into the representation of magnetic field in a non linear way through the distance term R_{ij} and the dipole position vector $\mathbf{r}_j$ in equations 4.8, so that it is not possible for magnetisation values for certain model parameters to be 'extrapolated' to different model parameters (e.g magnetisation of a layer at depth $2d$ is not twice a strong as magnetisation in a layer at depth d).

4.3.4 Dipole directions

If using equivalent source dipoles as a means to represent the magnetic field, the direction of the dipoles is not important [Mayhew, 1979], though the use of radial dipoles ensures the predicted anomalies are centred over their sources. For magnetisation distributions, it is desirable that the direction should be meaningful. If the magnetisation direction is assumed (for example, on Earth magnetisation of the continents is often assumed to be in the direction of the main field), the inclination and declination of the source dipoles are specified. With the dipole directions fixed

in advance, it is then just the magnetisation intensity that is solved for in the inversion.

For the Moon and for Mars where there is no present core field, or in regions on the Earth where the remanent magnetisation is more significant than the induced magnetisation, a magnetisation direction can not be assumed. If a region is expected to be homogenously magnetised (e.g parallel to an ancient field), then a fixed inclination and declination can be used. It may then be possible to estimate this direction by carrying out the inversion for magnetisation intensity with different fixed values of inclination and declination.

Identification of a suitable fixed direction was demonstrated by Nicolosi et al. (2006) with an iterative equivalent source dipole inversion on synthetic data, and with an isolated terrestrial magnetic anomaly. They found that the minimum misfit to the observations occurs when the model dipole directions coincide with or are close to the actual source direction. This was successful for a range of complex synthetic source geometries and magnetisation directions, with different input and model parameters, and the real terrestrial example directions were consistent with local measured paleomagnetic directions.

4.4 Inversion method

For a given set of observations and a grid of dipoles with a stated spacing, layer thickness and dipole depth, the required components of matrix $\mathbf{G}$ are calculated using equations 4.8. The matrix is built up in sections considering the contribution of each component of the dipoles to each component of the field (see Appendix 7). For very large data and dipole grids, the $\mathbf{G}$ matrix can be made in sections which are combined to carry out the matrix multiplication $\mathbf{G}^T\mathbf{G}$, and $\mathbf{G}^T\mathbf{b}$ (for the over determined case). The damping parameter is then added to the diagonal elements of $\mathbf{G}^T\mathbf{G}$.

The inversion to produce the solution in equation 4.18 or 4.20 is implemented in MATLAB®, using the 'back-slash' command, which selects the most appropriate

algorithm from LAPACK, a library of routines for large linear systems, depending on the structure of the matrix.

The suitability of the solution with different damping parameters is assessed by calculating the fit to the data with the sum of squares of residuals of the model prediction and the data,

$$SSR = (\mathbf{Gm} - \mathbf{b})^T (\mathbf{Gm} - \mathbf{b}) = \mathbf{b}^T\mathbf{b} - \mathbf{m}^T\mathbf{G}^T\mathbf{b} - \lambda\mathbf{m}^T\mathbf{m} \tag{4.24}$$

(see Appendix 9), the misfit per data point,

$$misfit = \sqrt{\frac{(\mathbf{Gm} - \mathbf{b})^T (\mathbf{Gm} - \mathbf{b})}{M}} \tag{4.25}$$

and the RMS magnetisation:

$$RMS(m) = \sqrt{\frac{\mathbf{m}^T\mathbf{m}}{N}} \tag{4.26}$$

The maximum total magnetisation for individual dipoles was also calculated to ensure the Parker bound criterion was met (see section 3.4.3).

Global crustal magnetisation models from equivalent source dipoles for the Earth and Mars [Purucker et al., 1996 and 2000, Langlais et al., 2004], where formation of the inverse of the matrix $\mathbf{G}^T\mathbf{G}$ was computationally impractical, used an iterative conjugate gradient approach to solve equation 4.15. This technique generates a new solution to the linear equations at each step *k*, based on a 'search direction' defined by minimising the gradient of the residual $\mathbf{G}^T\mathbf{b} - \mathbf{G}^T\mathbf{G}\mathbf{m}_k$ or $\mathbf{b} - \mathbf{G}\mathbf{m}_k$, after the *k*th iteration, until an acceptable fit and solution to the data are found [e.g Press et al., 1992].

4.5 A test case

Although the equivalent source dipole technique has been used before to produce minimum magnetisation models for crustal magnetisation, just what can be inferred about a source from this technique alone has not really been considered. A set of simple forward models was used to investigate what information about a magnetised source can actually be inferred from this modelling technique. This is necessary to avoid erroneous conclusions and interpretations.

These tests look at:

- the effect of noise and damping on the final solution
- the effect of the model parameters on the final solution
- inversions with a single field component
- inversions with fixed magnetisation directions
- identification of the source thickness, depth, and magnetisation direction
- the model resolution

The forward model consisted of a square dipole grid with 1640 dipoles at 0.5° spacing at depth of 15 km and layer thickness 30 km. The central 65 dipoles were given north-south horizontal magnetisations of 0.07 A/m (Figure 4.7) and the dipoles were used to produce the three components of magnetic field at 6480 locations on a regular grid with 0.25° spacing at an altitude of 30 km. These magnetic field observations (maximum total field 6.6 nT) were then used as input data for inverse models. For even this simple geometrical set up (thickness, depth, altitude, spacings) the condition number of the matrix $\mathbf{G}^T\mathbf{G}$ is very large (~10^7). This high condition number meant that the inversion of the exact synthetic data could not quite reproduce the initial input magnetisation model (zero values in the radial and phi magnetisations were perturbed by $\pm$ 10^{-5} and $\pm$ 10^{-4} A/m respectively, while magnetisation values in the theta direction were in the range 0.07 $\pm$ 0.0007 A/m). However, the resulting model had the same RMS magnetisation as the input model (to at least 6 significant figures), and a negligible misfit to the input data.

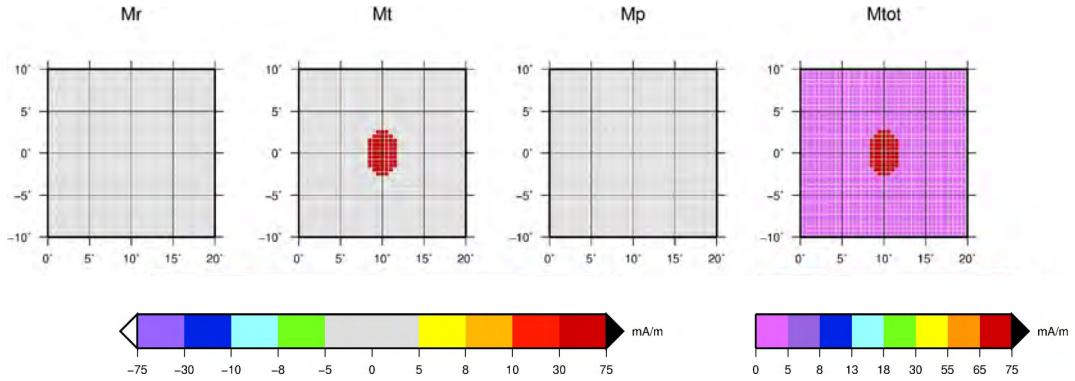

Figure 4.7: The input magnetisation model for the test case. Dipoles with 0.5° spacing, at a depth of 15 km in a layer of thickness 30 km. Horizontal magnetisation of 0.07 A/m.

4.5.1 The effect of noise on the solution

Gaussian distributed, zero mean random noise with standard deviations from 0.001 pT to 10 pT, was added to the predicted observations to use as 'noisy' input observations for the inversion. With only these very small amounts of noise, the magnetisation solution from the inversion diverged from the input distribution into large and unphysical distributions spread across all three magnetisation directions (shown in figure 4.8B-D and 4.9A) with large RMS magnetisations and increased misfits comparable to noise added to the observations (see table 4.1.1).

The 'spreading', or aliasing of the solution into the other components of magnetisation results from terms in the **G** matrix, relating to the contribution of the dipoles to the field in each of the component directions. As the phi and theta components of the field are weakest, they are more affected by noise, which might explain the stronger spreading in this case into the phi and theta components of magnetisation.

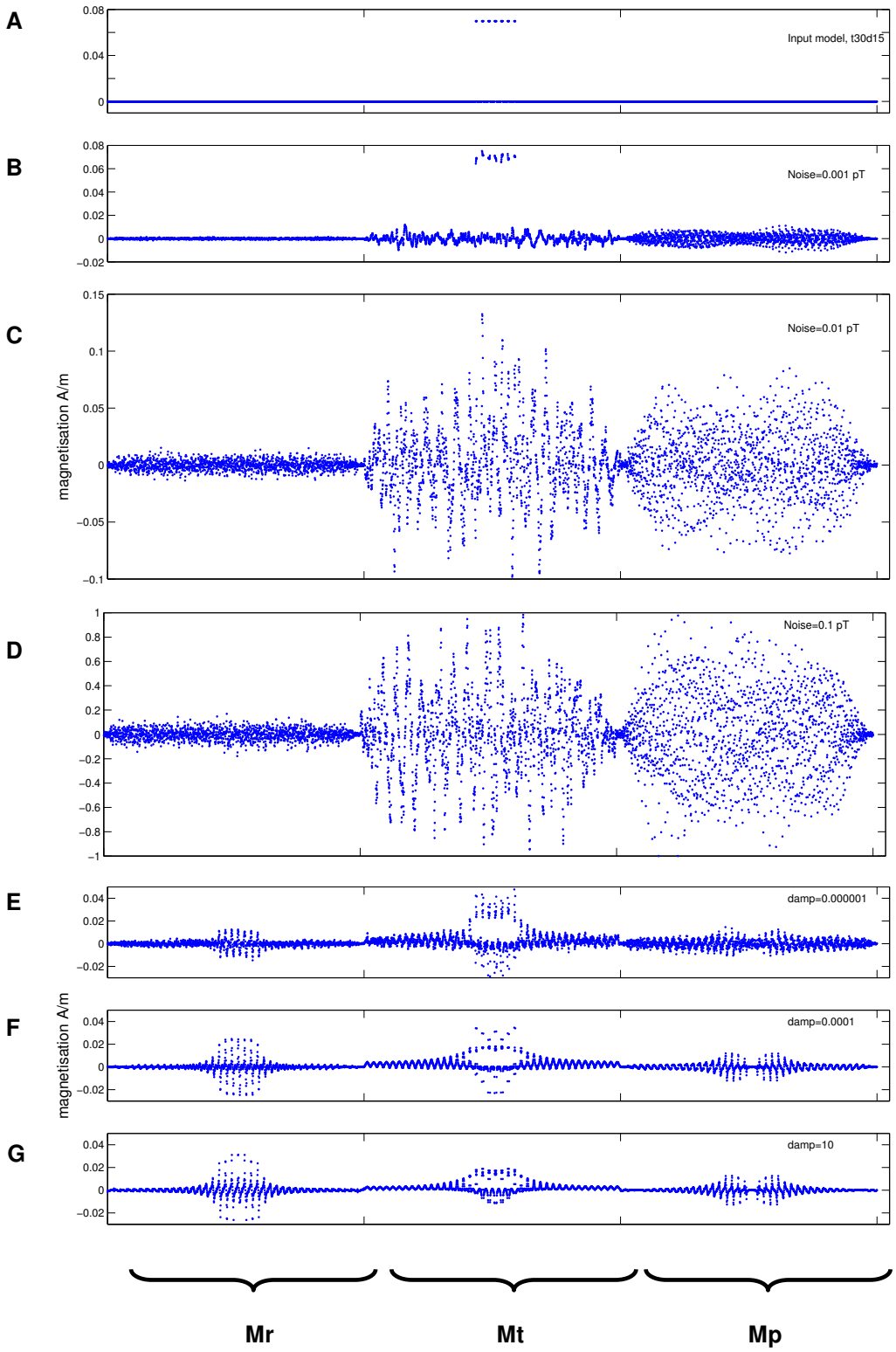

Figure 4.8: The three components of magnetisation (Mr, Mt, Mp) plotted per dipole for A: the input model (thickness 30 km, depth 15 km, t30d15), B-D: solutions from input data with added noise of 0.001 pT (B), 0.01 pT (C) and 0.1 pT (D), and E-G: damped solutions from input data with 0.01 pT added noise with damping parameters of 10^{-6} (E), 10^{-4} (F) and 10 (G). (Note the different amplitude scales).

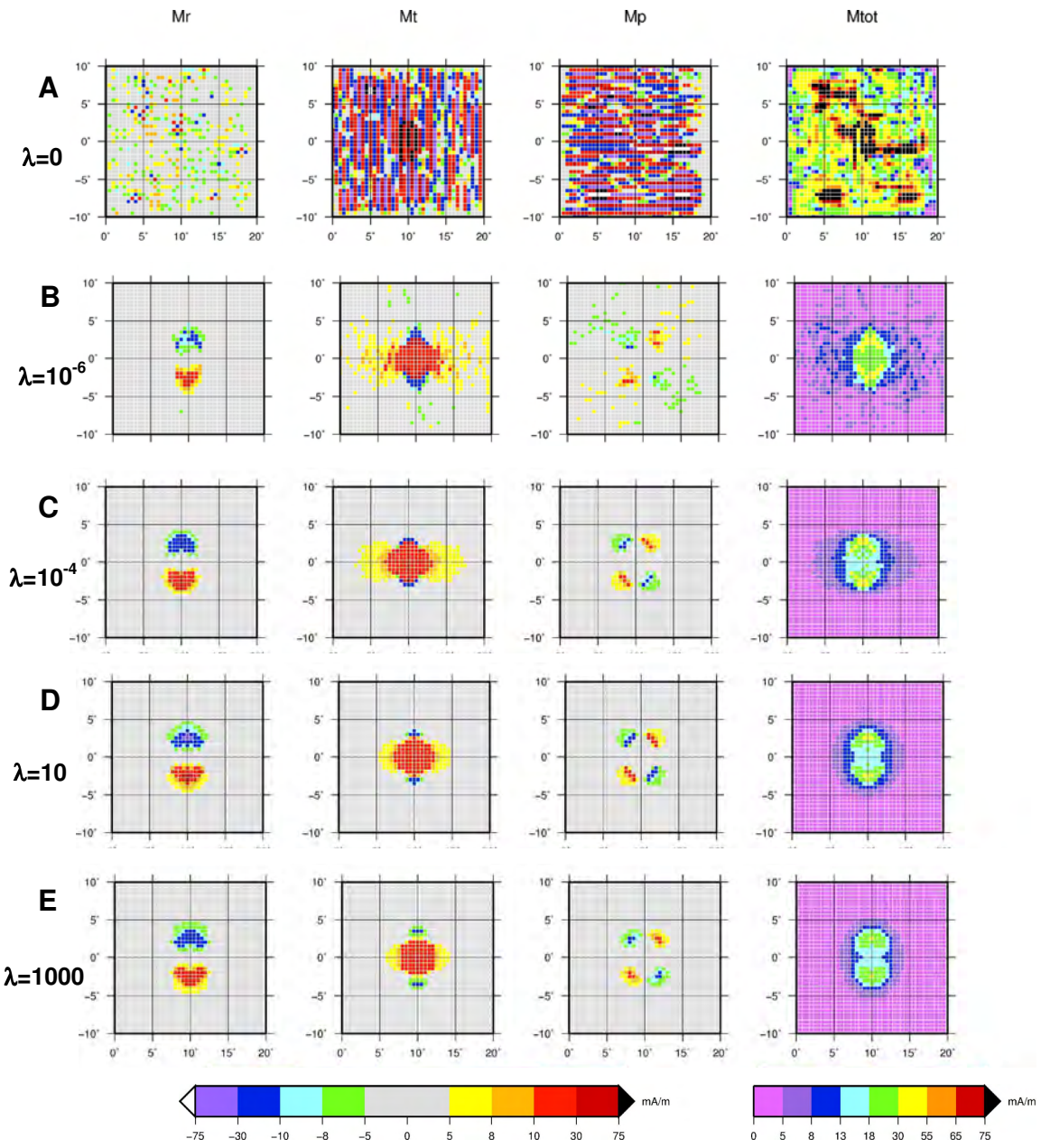

Figure 4.9: Maps of the three components of magnetisation and total magnetisation for solutions from the input data with 0.01 pT noise with different damping parameters.

4.5.2 Including a damping parameter

To improve the solutions from the noisy input data, the $\mathbf{G}^T\mathbf{G}$ matrix was damped for the inversion with the data with 0.01 pT standard deviation noise, as an example. Small damping parameters (<<1) were sufficient in this case to significantly reduce the RMS magnetisation, and provide a solution closer to (but weaker than) the input model (see figures 4.8E-G, 4.9B-E and table 4.1.2).

The 'spreading', or leakage, of the magnetisation solution into the radial and phi components increases as the damping parameter is increased, decreasing the magnetisation in the theta direction. This 'smoothing out' of the magnetisation reduces the RMS magnetisation and increases the misfit to the data, as smaller scale higher magnitude variations are lost as the damping parameter is increased. This is seen in the magnetisation maps of figure 4.9. The trade-off curve for the misfit and the RMS magnetisation is shown in figure 4.10. The damping parameters suitable for this model with this noisy data set are from 10^{-2} to 10 (as shown by the 'knee' of the trade-off curve). Smaller damping parameters leave more unlikely features in the magnetisation model (Figures 4.8E and F and 4.9B and C), and larger damping parameters may spread the magnetisation too much (Figure 4.9E).

It is worth noting that the 'smoothing out' of the magnetisation appears to give a distribution similar to the directions and relative magnitudes of the components in the input field (see figure 4.2 for the horizontal (North-South) dipole). This is again a consequence of the terms in the **G** matrix.

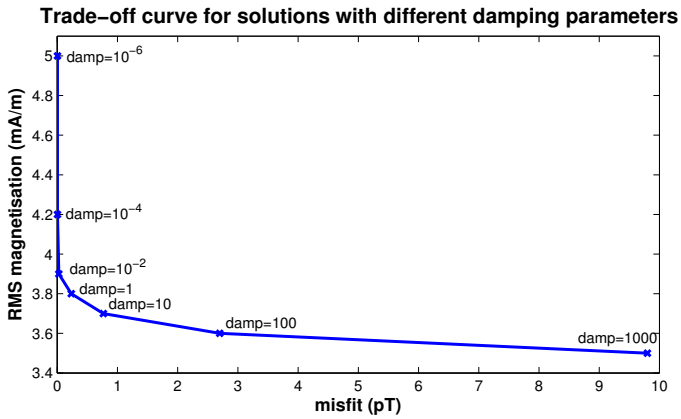

Figure 4.10: 'Trade-off' curve of RMS magnetisation and misfit for damped solutions from the input data with 0.01 pT noise.

4.5.3 The effect of 'wrong' parameters

It is unlikely that the location of the dipoles and the parameters of thickness and depth used in these models are the same as those of the magnetic sources responsible for the magnetic field observed around the Moon. The model parameters of thickness and depth in this test case were changed slightly from 30 km and 15 km respectively in the forward model, to 31 km and 15.5 km, and 32 km and 16 km, and changed drastically to 20 km and 10 km. These new models were then used to calculate a new **G** matrix and the inversion carried out with the data from the original model.

Small changes to the model parameters have a similar effect to the addition of noise, in that the **G** matrix with the new model parameters now cannot account for all the observations. The model magnetisation solution is again spread across the three component directions (though smoothly in this case as the input data are not noisy) (Figure 4.11A-C), giving a higher RMS magnetisation for the models closest to the input thickness (see table 4.1.3). However, in general, it would be expected that the thicker models result in lower magnetisation values than thinner models due to the presence of the thickness as a coefficient in the terms of the **G** matrix (in the volume factor). Thicker models then have larger terms in the **G** matrix than thinner models, resulting in solutions with lower RMS magnetisations.

If these 'wrong parameter' solutions are also damped, the RMS magnetisation is reduced further (see table 4.1.4) by spreading the solution into the radial direction (Figure 4.11D and E, and figure 4.12). A suitable damping parameter for these models is again around 10, by observation from the trade-off curves and model solutions.

4.5.4 Fixing a magnetisation direction

Instead of solving for the three components of magnetisation, the model dipole directions were fixed successively in the radial, theta and phi components, and the inversion carried out for noisy input data with different damping parameters (in

Noise, pT (standard deviation)	**RMSmag.** (A/m)	**Misfit** (pT)
0	0.0080	$<10^{-5}$
0.001	0.0085	$<10^{-4}$
0.01	0.0245	0.0086
0.1	0.2361	0.0876
1	2.4331	0.854
10	26.9818	8.6

Table 4.1.1: Solution parameters from noisy input data.

Damp.	**RMSmag.** (A/m)	**Misfit** (pT)
10^{-6}	0.0050	$<10^{-2}$
10^{-4}	0.0042	$<10^{-2}$
10^{-2}	0.0039	0.029
1	0.0038	0.234
10	0.0037	0.768
100	0.0036	2.70
1000	0.0035	9.80

Table 4.1.2: Solution parameters from noisy (0.01 pT) input data with damping.

Model	**RMSmag.** (A/m)	**Misfit** (pT)
T30 d15	0.0080	$<10^{-5}$
T31 d15.5	0.0091	0.00010
T32 d16	0.0103	0.00019
t20 d10	0.0060	0.00326

Table 4.1.3: Solution parameters from models with 'wrong' layer thickness (t) and dipole depths (d).

Damp.	**RMSmag.** (A/m)	**Misfit** (pT)
0.000001	0.0058	0.003
0.0001	0.0054	0.006
0.001	0.0053	0.012
10	0.0049	1.0
100	0.0048	3.6
1000	0.0047	13.2

Table 4.1.4: Solution parameters from the 'wrong' model with thickness 20 km and depth 10km, with damping.

this case, noise of 0.01 nT was used as the smaller $\mathbf{G}^T\mathbf{G}$ matrix was less sensitive to noise in the data). The resulting solutions in these directions were not the same as the individual components found when the direction was not fixed (Figure 4.13). (These fixed direction solutions with lower damping parameters also exhibited 'edge effects' at the edge of the dipole grid).

When the model direction was fixed in the same direction as the input (theta), the misfits were lowest (see table 4.2) and a solution close to the input was returned (see figure 4.13B). The radial direction in this case also has misfits similar to the model fixed in the theta direction (due to non-uniqueness, to be discussed in section 4.7). The phi direction, however is not consistent with the source direction at all, resulting in a very spread out and unphysical magnetisation distribution and a misfit

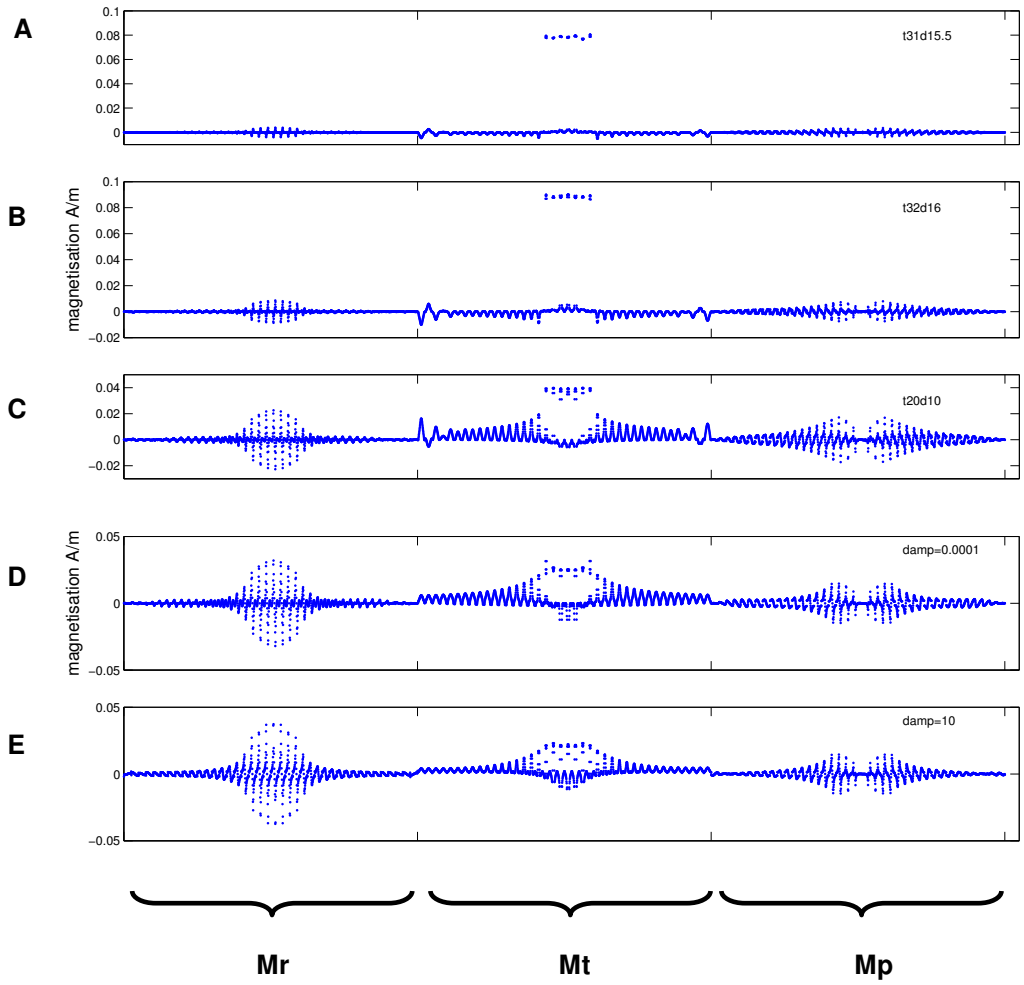

Figure 4.11: The three components of magnetisation (Mr, Mt, Mp) plotted per dipole for A-C: solutions for the model with thickness (t) and depth (d) respectively of, 31 km and 15.5 km (A), 32 km and16 km (B), 20 km and 10 km (C), and for D-E: damped solutions for the model thickness 20 km and depth 10 km with damping parameters of 0.0001 (D) and 10 (E). (Note the different amplitude scales).

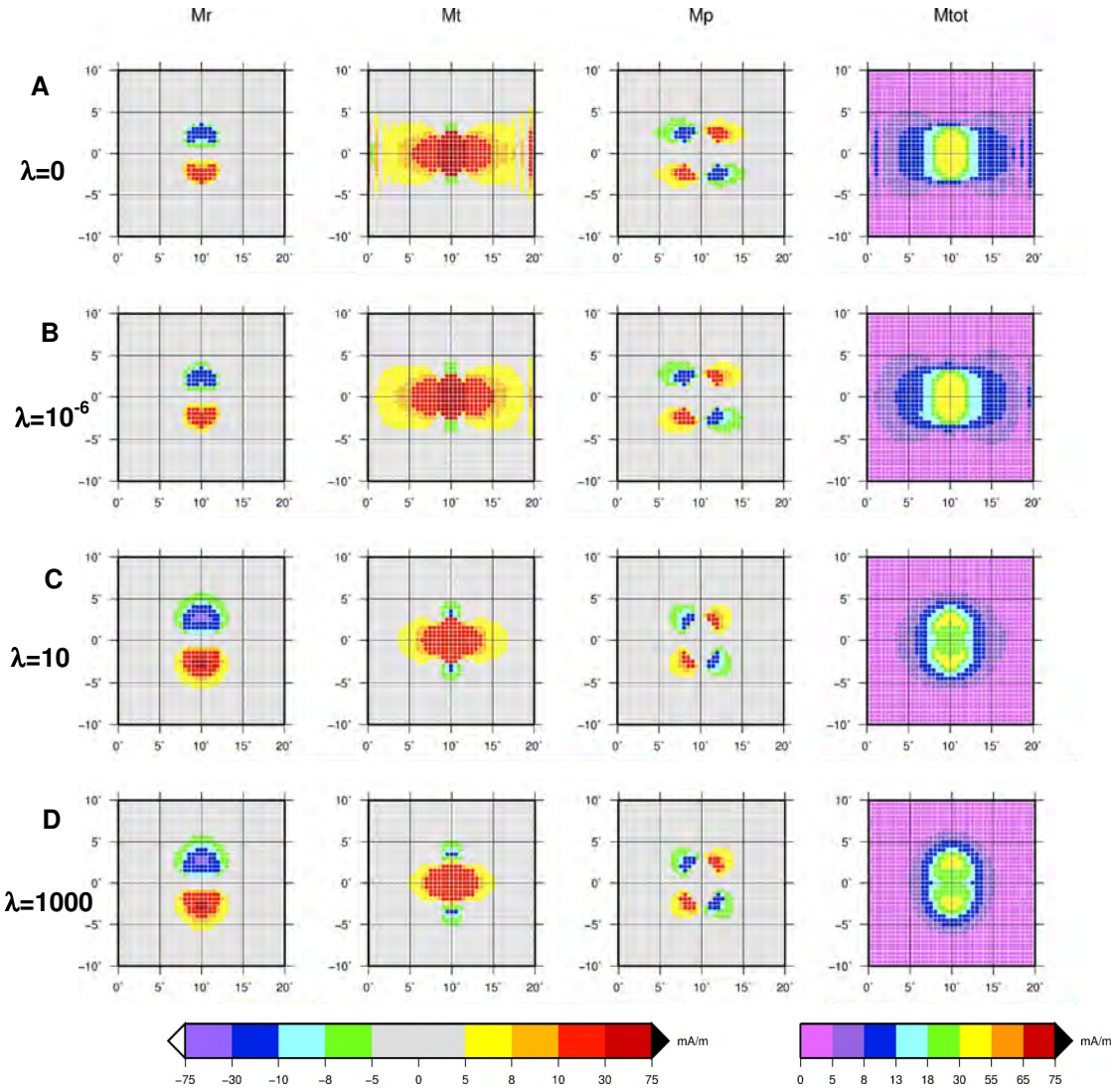

Figure 4.12: Maps of the three components of magnetisation and total magnetisation for damped solutions for the model with 'wrong' parameters of thickness 20 km and depth 10 km with different damping parameters.

Radial			Theta (north-south)			Phi (east-west)		
Damp.	**RMSmag.** (A/m)	**Misfit** (nT)	**Damp.**	**RMSmag.** (A/m)	**Misfit** (nT)	**Damp.**	**RMSmag.** (A/m)	**Misfit** (nT)
0	0.0254	0.0157	0	0.0363	0.0096	0	0.2243	0.2703
1	0.0111	0.0158	1	0.0139	0.0098	1	0.1242	0.2708
10	0.0096	0.0161	10	0.0135	0.0099	10	0.0771	0.2763
100	0.0088	0.0172	100	0.0131	0.0118	100	0.038	0.2965

Table 4.2: Solution parameters for damped, noisy (0.01 nT) models with fixed magnetisation directions.

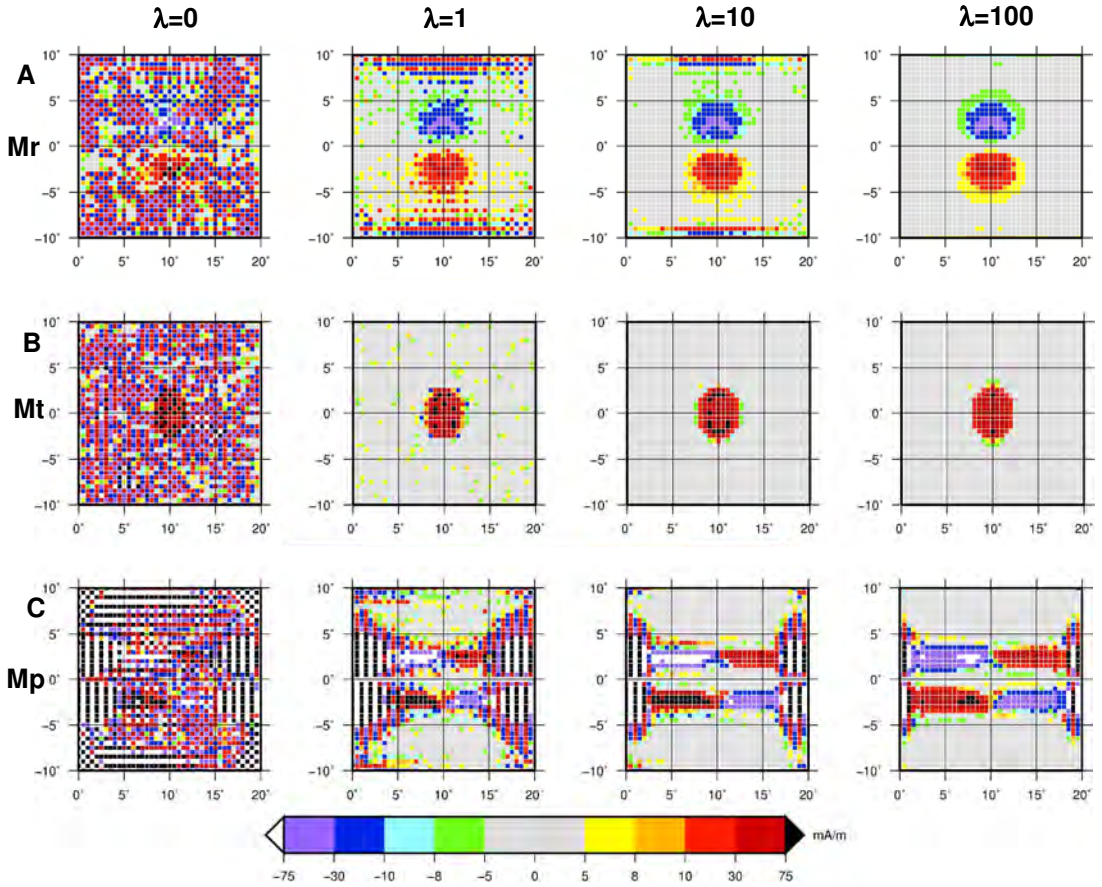

Figure 4.13: Damped magnetisation solutions from noisy (0.01 nT) input data with the direction of magnetisation fixed in A: the radial direction, B: the theta direction, and C: the phi direction.

an order of magnitude larger than for the model fixed in the theta direction (see table 4.2). Solutions with a fixed direction have slightly higher magnetisations since there can be no spreading of the solution into other component directions (though there is some spreading into the opposite direction).

4.5.5 Inversion of a single component of magnetic field data

If only one component of the vector data is used in the inversion instead of three, the resulting output solutions for each component of magnetisation are almost

Components	RMSmag. (A/m)	Misfit (pT)
Ball	0.0038	0.234
Br	0.0036	0.288
Bt	0.0037	0.303
Bp	0.0034	0.387

Table 4.3.1: Solution parameters with single input field direction with no noise, and damping parameter =1.

Components	RMSmag. (A/m)	Misfit (pT)
Ball	0.0038	0.352
Br	0.0036	0.381
Bt	0.0037	0.395
Bp	0.0034	0.467

Table 4.3.2: Solution parameters with single input field direction, with 1 pT noise and damping parameter =1.

identical to the solution produced from using all three components of the data with and without noise (see table 4.3.1 and 4.3.2). This shows the redundancy in the field components of potential fields where a single component of the field contains all the field information. The size of the **G** matrix can then be reduced by two-thirds if only one (rather than three) of the field components are used.

4.5.6 The resolution matrix

The resolution matrix (equation 4.21) was produced for the test case **G** matrix set up solving for the three components of magnetisation of 1640 dipoles (0.5° spacing, depth 15 km, layer thickness 30 km), from the three components of the field at 6480 data locations (0.25° spacing). For damping parameters of 1 and 10, the trace of the resolution matrices, and hence the effective number of independent parameters rapidly decreased to 1495.6 and 1125.3 respectively compared to the identity matrix **R** with trace=3×1640=4920. For a square grid of dipoles with three magnetisation directions, this means the effective resolution is about 1°, equivalent to ~ 30 km, the altitude of the data.

Figure 4.14A shows a transect across the resolution matrix with a damping parameter of 10, at row 1000. While the R_{ii} term is still the largest, some of the other terms in the resolution matrix are also significant. As well as spreading near to the diagonal (into the surrounding 2 or 3 dipoles at the same latitude and surrounding latitudes (see Figure 4.14B and figure 4.15), representing correlated magnetisation

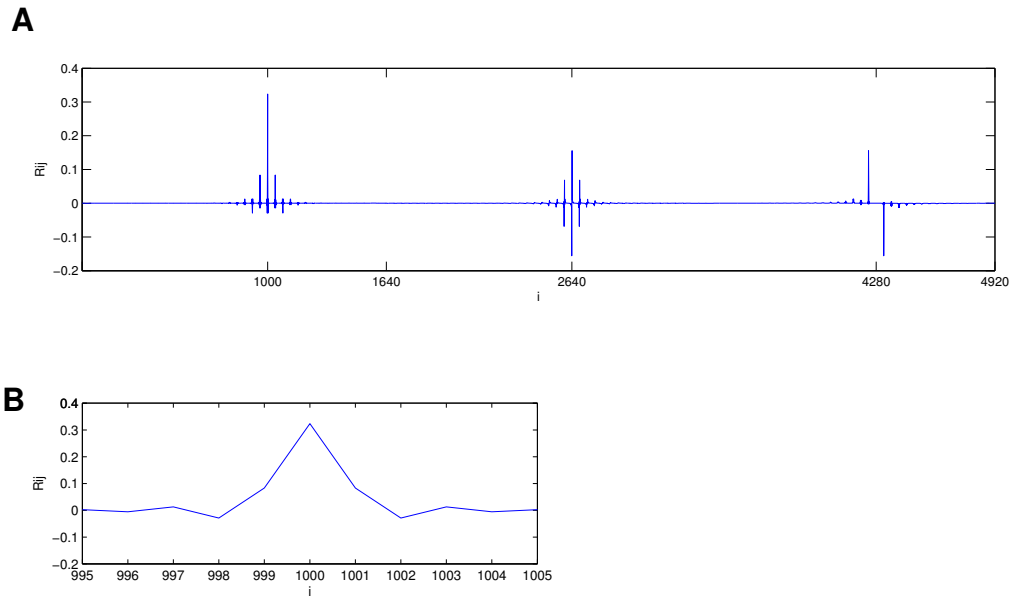

Figure 4.14: A: A transect across the resolution matrix **R** (of size 4920×4920), with a damping parameter of 10, at row i=1000, and B: a close up around the R_{ii} point.

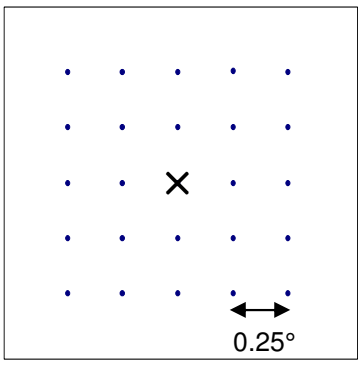

Figure 4.15: A portion of the dipole grid showing the 1000th dipole (×) and surrounding dipoles which have correlated magnetisation solutions.

solutions, there is also 'leakage' into the component directions of this 1000th dipole (near to i=1000+1640 and i=1000+(2×1640)) (see Appendix 7 for the **G** matrix ordering). This spreading reduces the value of the diagonal elements and hence reduces the trace of the resolution matrix. A close up around the R_{ii} point for i=1000 (Figure 4.14B) shows the spreading of the diagonal term into the surrounding 2 or 3 dipoles, showing the resolution decrease to about 1°.

4.6 Finding source parameters

A key aim of the inversion of real data is to try to identify the source parameters of magnetisation direction, depth, thickness and source extent. The minimum magnetisation solutions will spread out the magnetisation distribution, but it is still possible to constrain some of the source parameters.

4.6.1 Finding a bulk magnetisation direction

Although the damped least squares inversion spreads out the magnetisation solution, in this case, when the three components of magnetisation are solved for, the dominant magnetisation direction in the model is the same as the input magnetisation direction. There are however also strong magnetisations in the radial direction. If it can be assumed that the source is homogeneously magnetised, it might be possible to estimate the source magnetisation direction from the three component magnetisation solution, though this may not be reliable.

A better means of finding the magnetisation direction of a homogeneously magnetised source is to solve for the magnetisation intensity of dipoles with a fixed direction. The fixed direction can be varied with different combinations of inclination and declination, as in Nicolosi et al. (2006), to find a solution with the smallest misfit. This technique was tested for this direct inversion set up by fixing the input source magnetisation direction of the central 65 dipoles (of the input model in figure 4.7) and using the three components of the magnetic field predicted at an

altitude of 30 km (on the 0.25° spaced grid) from this source distribution in the inversion (keeping the same model parameters of depth and thickness). An arbitrary inclination of I =52° and declination D =38° were used.

The model values of inclination and declination were changed in 10° steps (D, -180 to 180, I, -90 to 90) and for each pair of I and D, the directions were input into the **G** matrix and the inversion carried out (using the same damping parameter for each inversion). This was carried out for non-noisy and noisy (0.1 nT standard deviation) input data using damping parameters of 0 and 10.

Contoured values of the misfit between the observations and the predictions for models with different I and D values for the damped non-noisy and noisy input data are shown in figure 4.16. There is a minimum in each case at or near to the values of inclination and declination which match the input values. (This also gave a minimum in the opposite direction with I=-52°, D=-142°). However, the minimum is very broad and the misfits here are very small, below the noise level where noise was added to the input data, perhaps due to the high altitude of the data (compared to Nicolosi's 600 m). While this technique appears successful in finding a direction close to the source direction, even with noise and for different damping parameters, when applied to real data the results may be less satisfactory. Also, when testing this

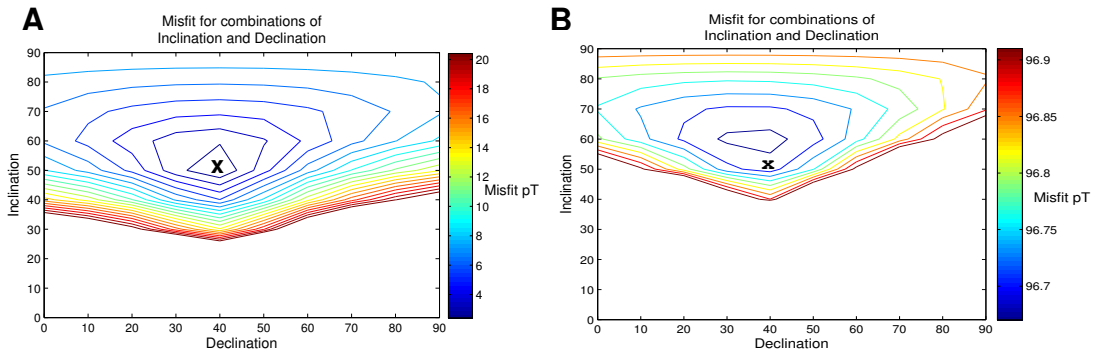

Figure 4.16: Contoured misfit as a function of model inclination and declination for A: the non-noisy input data and B: the noisy (0.1 nT) input data. The input values of I =52° and D =38° are marked 'X'. Contour intervals are A: 1 pT (up to 20 only), and B: 0.03 pT (up to 96.9 only).

technique with a single component of vector observations only, the minimum directions in these cases were parallel to the direction of the component observation. All three components of the vector magnetic field data are therefore required for this technique to give the input source magnetisation direction.

4.6.2 Depth and thickness

The synthetic data were also used to ascertain whether source depth and thickness could be constrained. Magnetisation solutions were produced with different model parameters of depth and thickness. While the magnetisation distributions for each set of parameters were quite similar, the misfit and RMS magnetisations were slightly different. Even in the presence of noise (0.01 pT) and with damping, the model with the best fit to the data in this case was the model with parameters matching the input thickness of 30 km (depth 15 km) (Figure 4.17). This is of course for a simplified input model with constant depth and thickness (and thickness = 2×depth) but this result suggests that it might be possible to discern some information about the source parameters with real data.

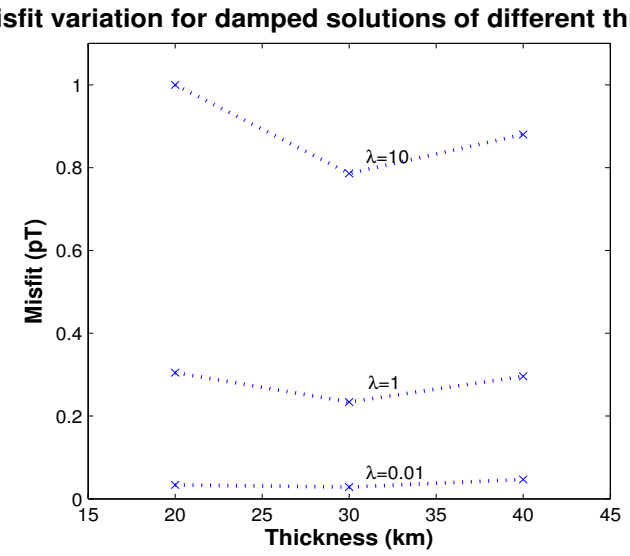

Figure 4.17: Misfits for model solutions from noisy data (0.01 pT) for models with different thicknesses (and depths) showing a minimum at the input thickness of 30 km for each damping parameter λ.

4.6.3 Spatial extent

Comparison of the total magnetisation in the model solutions with the input magnetisation (Figure 4.18 and table 4.4) shows that the spreading of the magnetisation into different component directions reduces the total magnitude of the solution and results in a lateral smearing of the source feature. However, the shape of the feature is still in agreement with the shape of the input source.

The lateral smearing of the source is a consequence of the model not having any fixed geometry (other than vertically). These models also include non magnetised material since the whole layer of dipoles will not necessarily require a magnetisation to be able to fit the data.

The model sources have gradual rather than distinct boundaries. Figure 4.19 shows a cross section across the models and the input source at 0° latitude. Using the 'width at half maximum' as an estimate for the edge of the model source, the inferred spatial extent of the source from different models can be compared. The cross section of figure 4.19 also emphasises the reduction in the magnetisation strength in the minimum RMS magnetisation models.

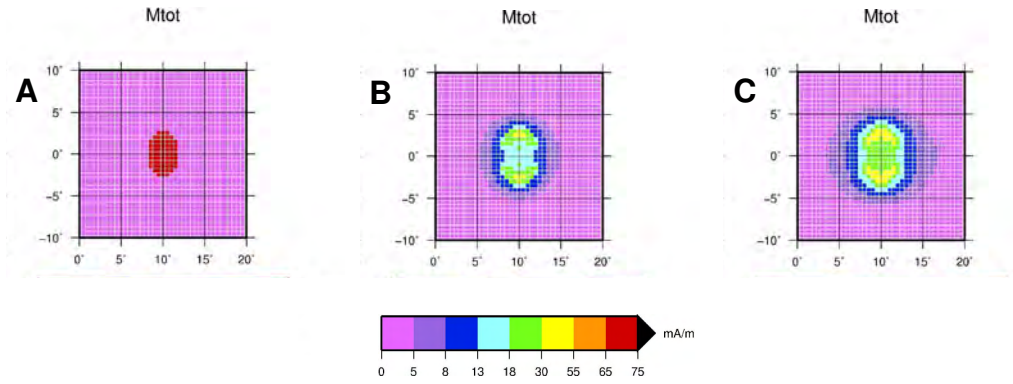

Figure 4.18: Maps of the total magnetisation of A: the input model (thickness=30 km, depth=15 km), B: a damped model from noisy data (damping parameter=10, noise =0.01 pT) and C: a damped solution for a model with different model parameters (damping parameter=10, thickness= 20 km, depth=10 km).

Model	RMSmag. (A/m)	Misfit (pT)	Max. magnetisation (A/m)	Dimensions (°)
Input	0.0080	$<10^{-5}$	0.070	5×3
0.01 pT noise, λ=10	0.0037	0.768	0.035	7×6.5
Thickness 20 km, depth 10 km, λ=10	0.0049	1	0.043	7.2×6.8

Table 4.4: RMS magnetisation, misfit, maximum magnetisation and source dimensions (from the width at half maximum) for final damped solutions with noise and different model parameters compared to the input model.

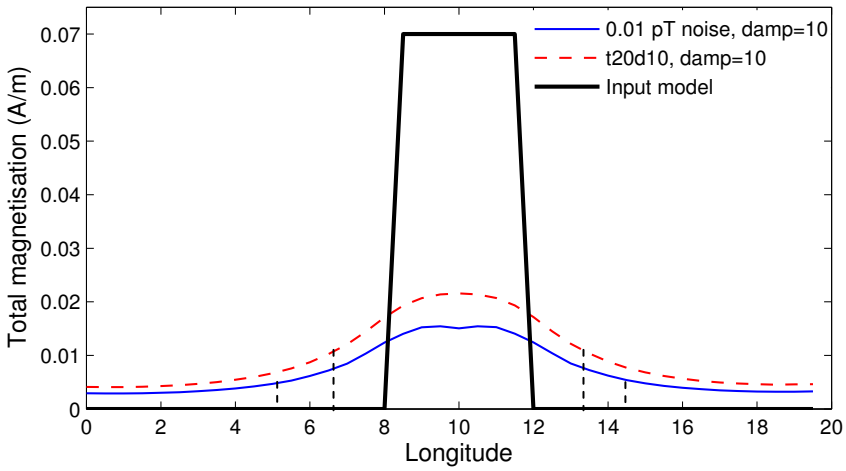

Figure 4.19: Cross section at latitude 0° for final damped solutions with noise and different model parameters (thickness (t) 20 km, depth (d) 15 km) compared to the input model. Longitude locations are marked at the 'half maximum'.

4.6.4 Vertical resolution

When the observation altitude is large compared to the thickness of the layer, the satellite is not sensitive to the difference between the distance to the top of the layer and to the bottom of the layer. To assess the vertical resolution potential of data at 30 km altitude, the forward test model was divided into two layers of dipoles at depth 5 km and 15 km (each of thickness 10 km) with different magnetisations in each layer. The inverse model solution with two layers returns the magnetisation for each layer as an average magnetisation for the two layers. With data at 30 km altitude, no depth resolution is expected due to the vertically averaging effect of the satellite observations.

4.7 Non-uniqueness

The resulting magnetisation solutions from these damped least squares inversions are the minimum RMS solution for a particular fit to the data, but there are other magnetisation distributions with different RMS magnetisations that fit the data equally well. This was hinted at in the fixed direction model where a positive and negative radial direction distribution of magnetisation was almost as good a fit to the data as the homogeneous theta direction distribution.

The three components of magnetisation from a homogenous purely theta direction magnetisation distribution (as figure 4.7 but now with 93 dipoles of magnitude 0.19 A/m and spacing 0.25° within a total grid of 6480 dipoles) and the magnetic field they produce are shown in figure 4.20 along with 3 other similarly sized magnetisation distributions which give a similar magnetic field pattern. This is a classic 'dipolar' magnetic field pattern, also reproducible from a single horizontal dipole and other basic distributions of dipoles with much stronger magnetisations (Figure 4.21). (This field pattern can also be produced from a 'hole' in a homogenously horizontally magnetised crust.) The relative sizes of the lobes of the field components depend on the individual magnetisation distribution in this case, but the single maximum value of the total field at 30 km altitude is the same in each of the models even though the number of dipoles with non-zero magnitude, and the RMS magnetisations are very different (Table 4.5). The strength of the magnetisation in each distribution depends on the number of non-zero magnitude dipoles and their directions. The larger the area of magnetisation (the more non-zero magnitude dipoles), the smaller each individual dipole magnetisation needs to be to produce the same field.

4.7.1 Distinguishing between different source models

As shown previously, the damped least squares inversions of the dipolar field pattern return a minimum magnetisation solution which favours the style of magnetisation model of figure 4.20A4, i.e. a complex distribution of differently

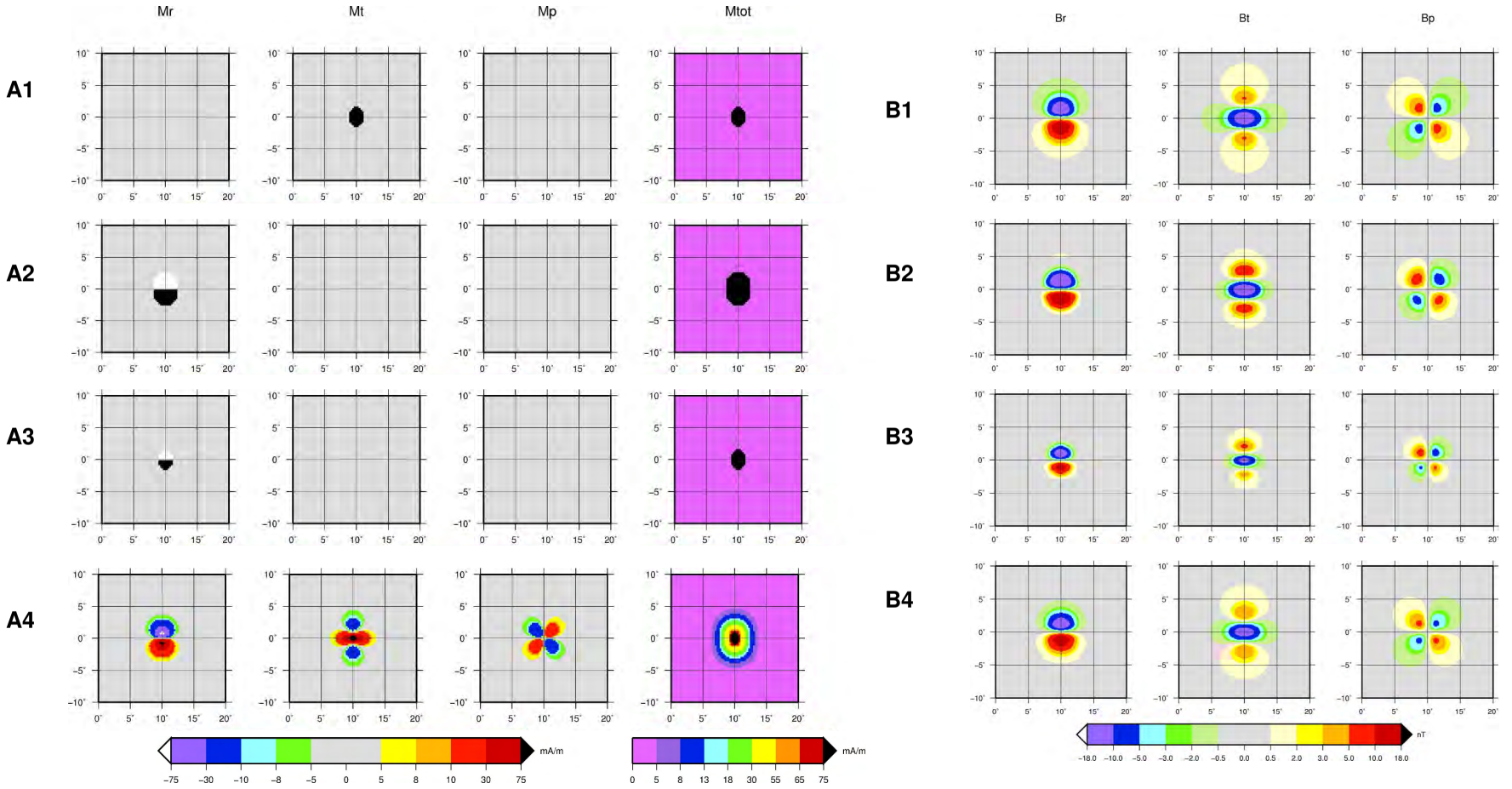

Figure 4.20: A: The three components and total magnetisation for 6480 dipoles in blocks of 0.25°×0.25°×30 km thickness, and B: the components of magnetic field they produce at 30 km altitude, for distributions with horizontal dipoles (1), vertical dipoles (2 and 3), and a complex magnetisation distribution (4).

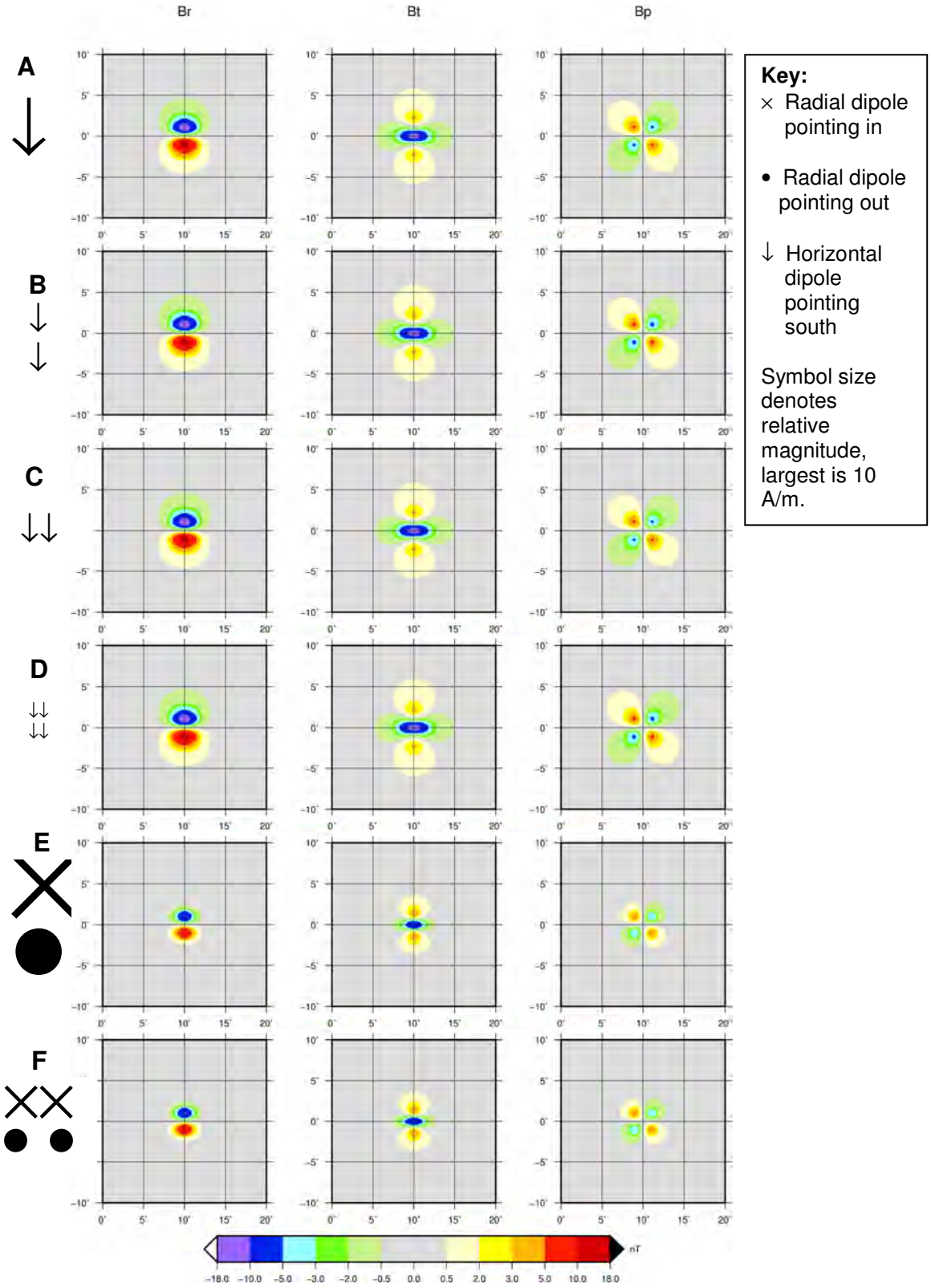

Figure 4.21: The three components of magnetic field at 30 km altitude for basic magnetisation distributions with horizontal and vertical dipoles producing a 'dipolar' field with the same single total maximum field. (Dipole block 0.25°×0.25°×30 km thickness.)

Distribution		Dipole magnitude (A/m)	RMSmag. (A/m)
Single dipole	(fig. 4.21A)	10.00	0.0717
Double	(fig. 4.21B)	5.164	0.0524
Double	(fig. 4.21E)	20.15	0.2044
Double	(fig. 4.21C)	5.054	0.0513
Quartet	(fig. 4.21F)	10.25	0.1470
Quartet	(fig. 4.21D)	2.609	0.0374
Complex	(fig. 4.20A4)	varied	0.0079
93 dipoles	(fig. 4.20A1)	0.272	0.0188
275 dipoles	(fig. 4.20A2)	0.115	0.0135
93 dipoles	(fig. 4.20A4)	0.198	0.0137

Table 4.5: Dipole magnitudes and RMS magnetisations for different models giving a classic dipolar field pattern with the same single maximum total field at altitude.

magnetised dipoles. While the minimum magnetisation solution may provide some information on the source, to distinguish between different potential source models, additional information is required. Each of the models in figures 4.20 and 4.21 meet the Parker bound constraint for the maximum field observation at satellite altitude, but the magnetic field at the surface can represent another constraint as each of these distributions produces different surface magnetic fields.

Figure 4.22 shows the total field at altitude and the total surface field for the 10 different models in figure 4.20 and 4.21, and table 4.5. While the fields at altitude are very similar, there are more differences in the surface predicted fields, especially between the 'basic' models (Figure 4.22A) and the 'more complex' models (Figure 4.22B).

The surface fields are much stronger for the simple models with fewer dipoles, representing a smaller region of the crust, since each dipole is more strongly magnetised. Figure 4.23 shows the ratio of the maximum surface field to the maximum field at altitude for these 10 different models showing the number of non-zero magnitude dipoles and the RMS magnetisation as a measure of the amplitude variation of the solution. The larger the region covered by the source (more dipoles), the 'smoother' the distribution is and the lower the surface field is. Observations of very strong surface fields therefore may indicate a more compact source since the decrease in the strength of the field with altitude is greater for smaller sources.

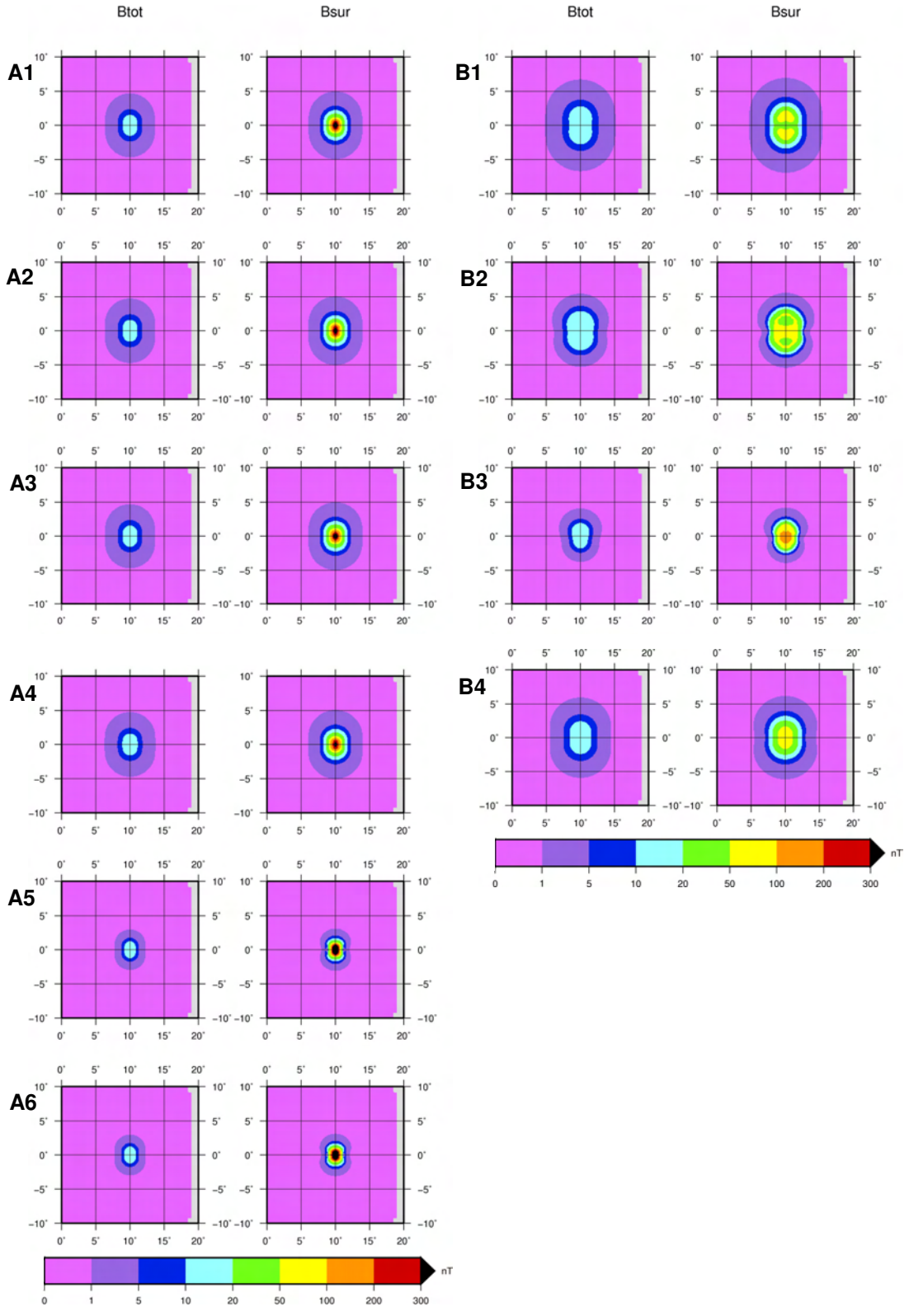

Figure 4.22: The total magnetic field at an altitude of 30 km (Btot) and at the surface (Bsur), for A: the simple magnetisation distributions (as in figure 4.21) and B: the more complex magnetisation distributions (as in figure 4.20).

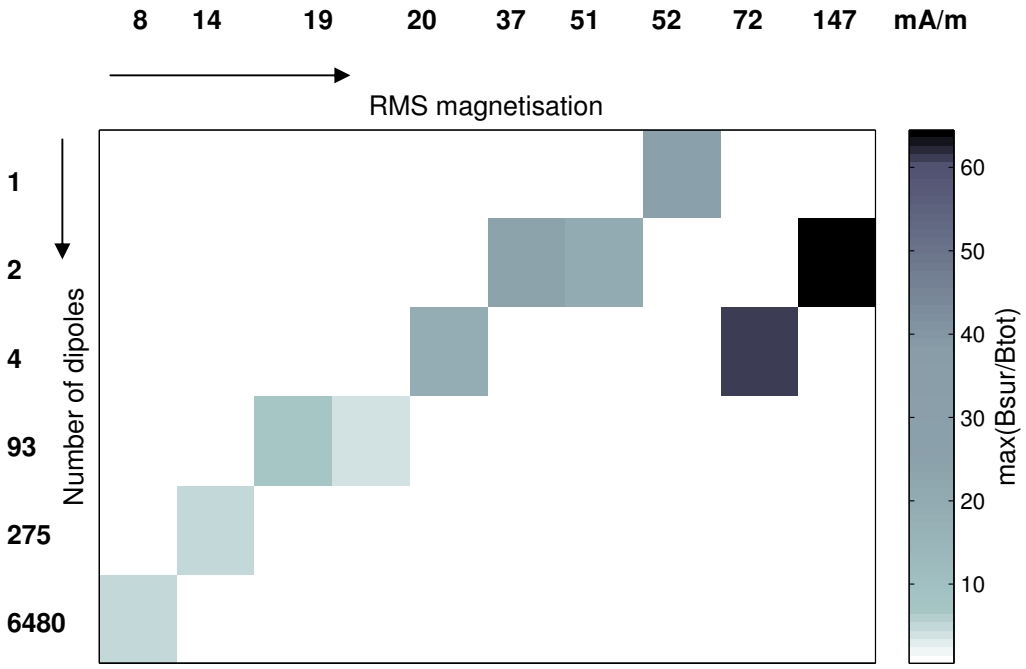

Figure 4.23: The ratio of the maximum surface field to the maximum total field at altitude for models with different numbers of non-zero magnitude dipoles and different RMS magnetisations.

4.8 Summary of test models

The tests described in sections 4.5-4.7 have led to useful conclusions that will help in the interpretation of the models obtained from real data. As real data will not be able to be exactly represented by the model parameters, the inversion will require damping to produce a physically reasonable magnetisation solution. The resulting solution will always be the solution with the minimum RMS magnetisation for the particular model parameters of depth and thickness, giving a particular fit to the data. As a result, the model solution may be much weaker in magnetisation and larger in physical extent than the actual source.

This 'simplest' magnetisation solution, though minimal in magnitude, is in some sense a more complicated solution in that the magnetisation direction varies over a small region and is thus less likely to represent a true solution from real sources. While we may not expect magnetisation in a single direction on the Moon,

there may not be a mechanism for producing rapidly spatially varying magnetic field directions for isolated anomalies. Inversion for the three components of magnetisation direction is not conducive to finding the magnetisation direction of a homogenously magnetised source, even when the direction is fixed. This is an important observation since not assuming a magnetisation direction in this inverse modelling technique was intended as an advantage rather than a disadvantage.

Despite the doubt over the validity of the magnetisation directions, these models are capable of fitting the data well and can provide other information of relative magnetisation magnitudes, source shape, and an estimation of the depth and thickness of the source layer.

These test cases have used simple source models with very small amounts of noise and small damping parameters. Real data will contain noise of a higher magnitude and therefore larger damping parameters will be required to generate an interpretable solution. This will result in a solution with a low RMS magnetisation and a poorer fit to the data, but should still be representative of the source. Inclusion of the ER data in these inversions will offer a significant advantage over inversion of the data at satellite altitude alone by imposing constraints on the strength of the surface field and thus the magnetisation distribution.

4.9 Application of the ESD technique to the Reiner Gamma region

The strong isolated anomaly in the Reiner gamma region offers an excellent location on which to apply the equivalent source dipole technique of magnetisation modelling. As discussed in section 2.1.3, the Reiner Gamma region correlates with a region of high albedo. The magnetic anomaly consists of a main anomaly over the high albedo feature, with an extension to the north east, with magnitudes of over 10 nT at 30 km altitude and over 70 nT at the surface (see Figure 2.4 and Figure 4.24). There is good spatial agreement between the MAG and ER data for this region making inclusion of the ER data as a constraint for this region promising. This anomaly is in the lowland plains (average elevation of -1.6 km) and has no topographic expression (see figure 4.25).

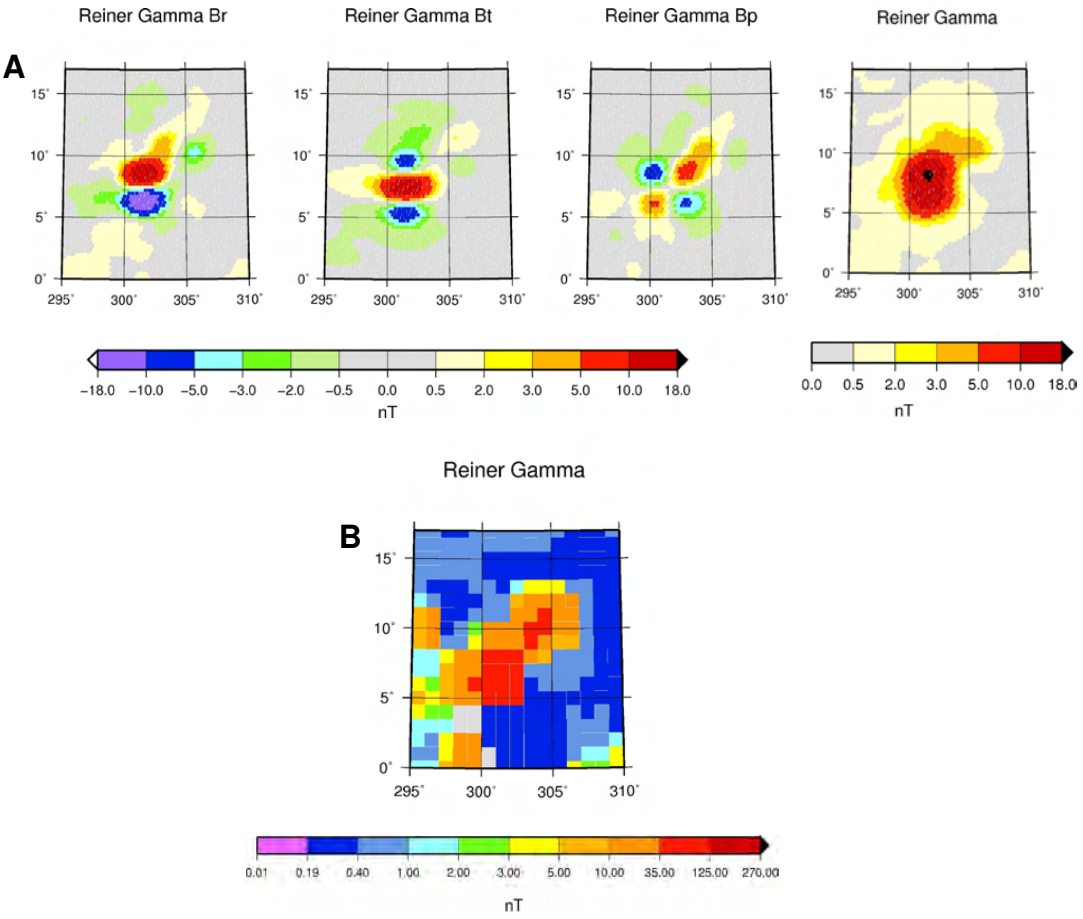

Figure 4.24: A: The three components and total magnetic field at 30 km altitude for the Reiner Gamma region reproduced from the spherical harmonic model, and B: the 1°×1° binned surface estimates from the ER data.

4.9.1 Input data and dipole grid

The data sets used for the production of magnetisation models with the equivalent source dipole technique are the altitude normalised (30 km) radial magnetic field data at the satellite ground track latitude and longitude from all lunar regimes (Figure 4.26A), and the selected wake and tail data from this set (Figure 4.26B). The data from all regimes are noisier than the wake and tail data, with the north east extension of the main anomaly feature suppressed slightly. It is expected

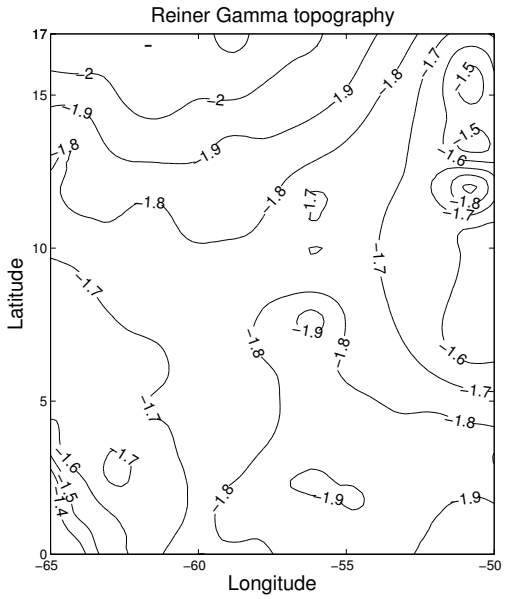

Figure 4.25: Contour map of topography (in km) for the Reiner Gamma region from Clementine topography data. Contour interval 0.1 km.

that the wake and tail data will be more suited to the production of magnetisation models, but both data sets are used with the inversion initially to check this.

The model dipoles for the Reiner Gamma region consisted of a 'low resolution' polar coordinate subdivision of points with a central region of 591 dipoles at 0.5° spacing, with a 25° border region with 4074 dipoles with 1° spacing, and a 'high resolution' grid with a central region of 4126 dipoles at 0.25° spacing, with a 10° border region with 3571 dipoles with 0.5° spacing (a smaller border was required with an increased number of dipoles but this did not affect the stability of the solution). While the resulting model resolution is not expected to be as high as 0.25° due to the correlation of model parameters (see section 4.5.6), the higher resolution model will provide a smoother magnetisation solution for the Reiner Gamma region. The dipole depths and layer thicknesses were varied to give a variety of surface layers and buried layers (Figure 4.6).

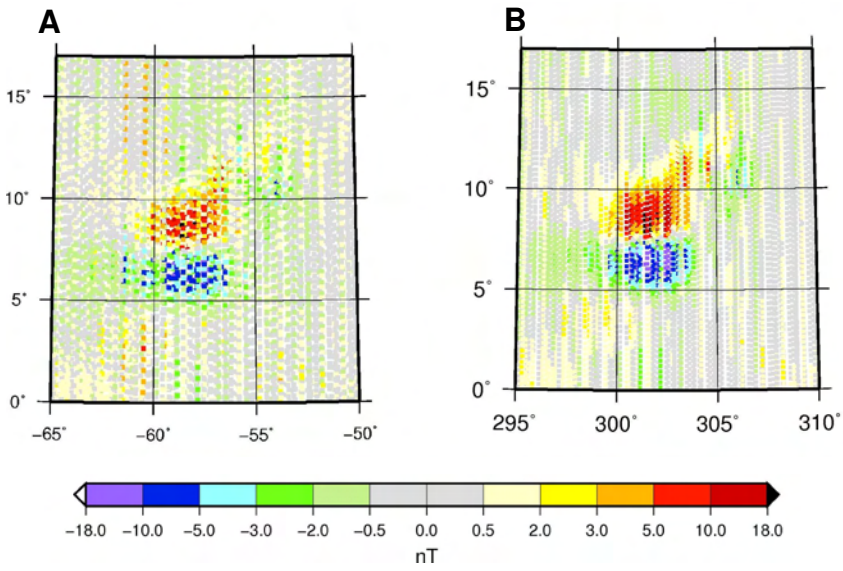

Figure 4.26: The radial magnetic field data at 30 km altitude for the Reiner Gamma region from A: all lunar regimes and B: lunar wake and geotail times only. Note: As pass-by-pass data locations are plotted, grey represents low fields and white gaps are the absence of data.

The radial magnetic field data for all lunar regimes coincident with the low resolution grid contained 271,166 data points, of which every other data point (135583 points) or less were used. There were 41800 wake and tail data coincident with the area covered by the high resolution dipole grid.

Components of the **G** matrix for models solving for the magnitude of dipoles with fixed directions, and for the magnitude and direction of dipoles, were each produced from equations 4.8. For the number of data and dipole parameters in this region, the linear equations in equation 4.11 were over determined and the inversion was carried out for a range of damping parameters using equation 4.18. The solution was used to calculate the RMS magnetisation and the misfit to the data for this region (including the border).

4.9.2 Low resolution magnetisation models

An initial equivalent source dipole magnetisation model for the Reiner Gamma region used the radial magnetic field data from all regimes and the low resolution dipole grid. The dipole depth was chosen close the spectral depth at 20 km (see section 3.5.2), with a layer thickness of 40 km. Magnetisations for dipoles fixed in the radial direction were solved for, and also the magnetisation and direction of variable direction dipoles.

The RMS magnetisations and misfits for the radial dipole magnetisation solutions with damping parameters ranging from 0 to 12,000 are shown in table 4.6A and plotted as a 'trade off' curve in figure 4.27. Figure 4.28 shows the magnetisation solutions with some of these damping parameters. The choice of 5 mA/m as a 'cut off' for the magnetisation strength is somewhat arbitrary, but gives a magnetisation distribution coincident with magnetic field distribution when the solution is suitably damped. All of these magnetisation solutions have dipoles with magnetisations larger than the Parker bound for this thickness.

As expected, solutions with small damping parameters show unphysical solutions with high RMS magnetisations and rapid oscillations in the dipole directions, as the model tries to fit all the data including noise. However, as the damping parameter increases, the RMS magnetisation and the spatial variability of the solution quickly decrease as the form of the model solution stabilises. The damping then acts to reduce the magnitude of the smaller scale large amplitude features of the solution, but retains the same pattern. The misfits for this region change very little with the different damping parameters (see table 4.6A).

When the direction of the dipoles was not fixed (Table 4.6B), the misfits and the RMS magnetisations decreased slightly compared to the fixed direction solutions. The radial magnetisation in these models is not as strong as the magnetisation for the radial dipoles as the magnetisation solutions spread into the theta and phi directions (Figure 4.29).

What is immediately obvious is that the magnetisation distribution in the component directions is coincident with and similar to the magnetic field distribution

A

Damp λ	Misfit (nT)	RMSmag. (mA/m)
0	0.732	664
1	0.733	98.7
10	0.734	25.3
50	0.734	11.4
100	0.734	9.45
200	0.734	8.46
500	0.734	7.72
800	0.734	7.42
1000	0.734	7.28
1500	0.734	7.03
2000	0.734	6.84
5000	0.735	6.19
6000	0.735	6.05
8000	0.736	5.81
10000	0.736	5.61
12000	0.737	5.45

B

Damp λ	Misfit (nT)	RMSmag. (mA/m)
100	0.730	12.1
500	0.731	5.44
1000	0.732	4.31
6000	0.733	2.88

Table 4.6: Selected misfits and RMS magnetisations for magnetisation models of the Reiner Gamma region with different damping parameters for A: radial dipoles and B: variable direction dipoles, from the radial data in all lunar regimes. Model thickness, 40 km, dipole depth, 20 km, 0.5° spaced central dipoles, 1° spaced border dipoles.

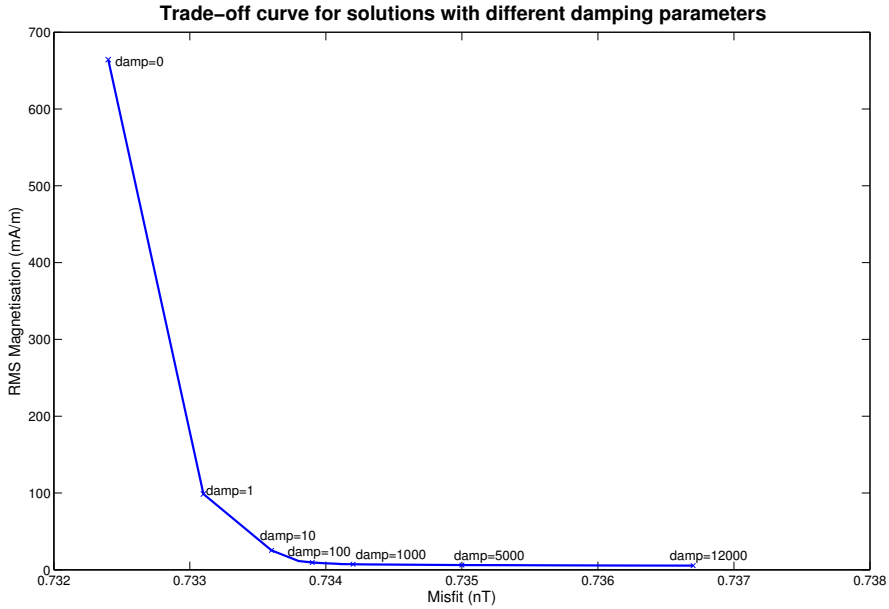

Figure 4.27: Trade-off curve of RMS magnetisation and misfit for magnetisation models with radial dipoles of the Reiner Gamma region with different damping parameters from the radial data in all lunar regimes. Model thickness 40 km, dipole depth, 20 km, 0.5° spaced central dipoles, 1° spaced border dipoles.

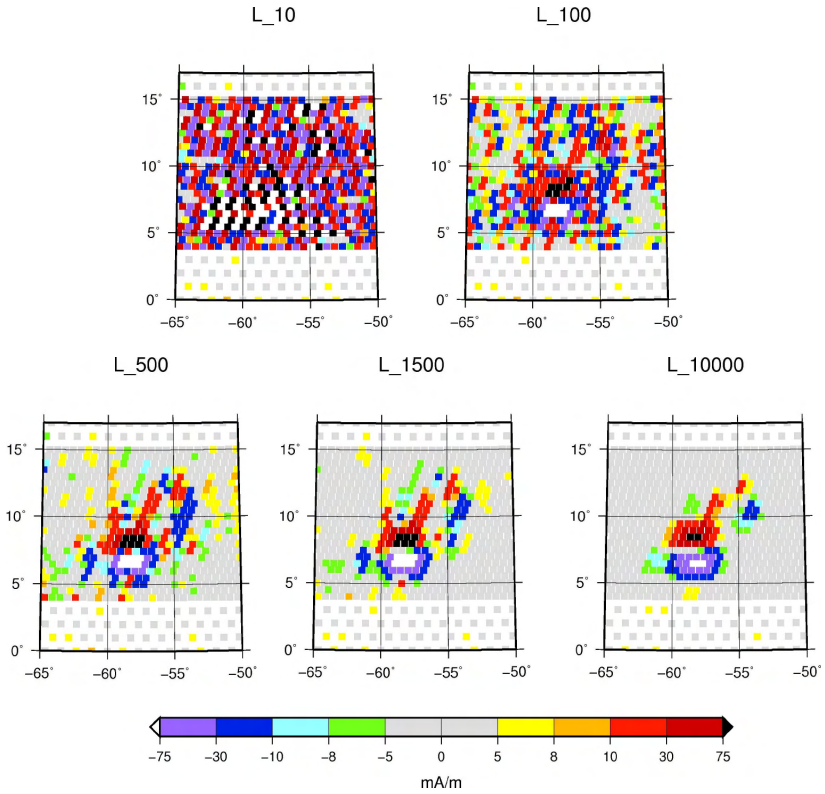

Figure 4.28: Magnetisation solutions for radial dipoles for the Reiner Gamma region with different damping parameters (L) from the radial data in all lunar regimes. Model thickness 40 km, dipole depth, 20 km, 0.5° spaced central dipoles, 1° spaced border dipoles.

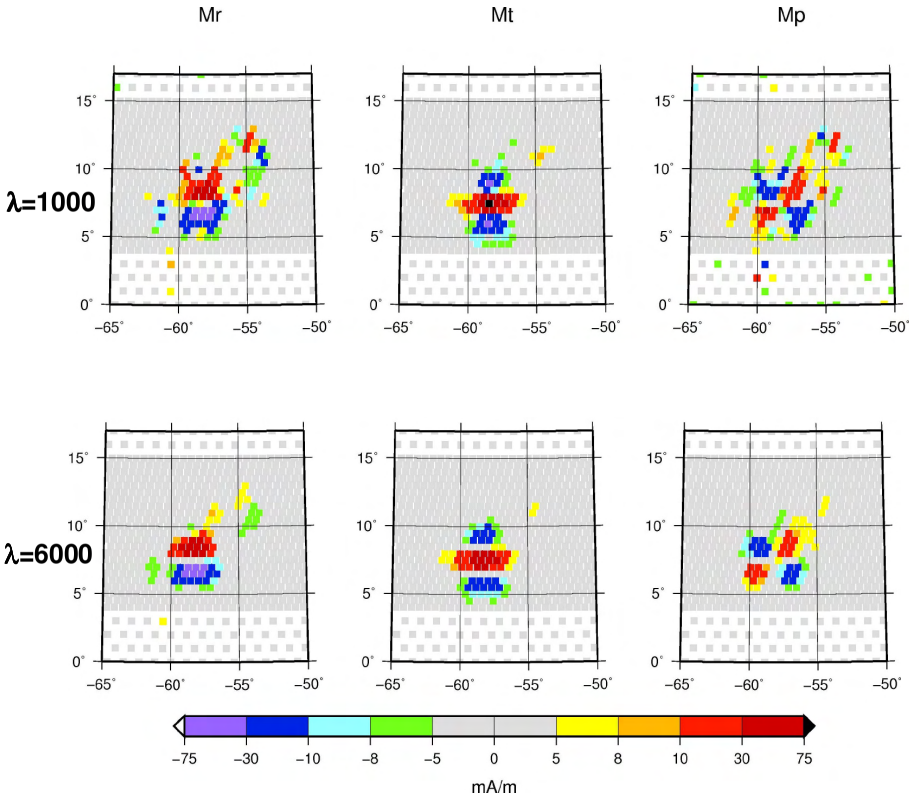

Figure 4.29: Three component magnetisation solutions for the Reiner Gamma region with damping parameters (λ) of 1000 and 6000, from the radial data in all lunar regimes. Model thickness 40 km, dipole depth, 20 km, 0.5° spaced central dipoles, 1° spaced border dipoles.

(compare figure 4.24A with figure 4.29). The magnetisation solution is also very robust for a range of magnetised layer thicknesses, dipole depths and damping parameters. When the magnetisation is confined to a single direction (in this case radial), the solution is also very similar in distribution to the input radial field. The likeness of the magnetisation distribution to the magnetic field distribution is a consequence of the minimum magnetisation solution and inhibits the interpretation of the magnetisation directions. However, as the misfits are lower for solutions with variable direction dipoles compared to the solutions with fixed dipole directions, most subsequent models solve for three components of magnetisation rather than in a fixed direction.

The misfits to the data of this minimum magnetisation solution, though larger than the expected noise in the input data, are still not unacceptably large, especially given the variability of the input data from all lunar regimes. Figure 4.30 shows the predictions of these data by the three component magnetisation model with a damping parameter 1000, and the absolute residuals (see section 3.6). The model predicts the data very well and the residuals result from under and over prediction of the varying input data, and the use of the damping parameter. The zero mean of the

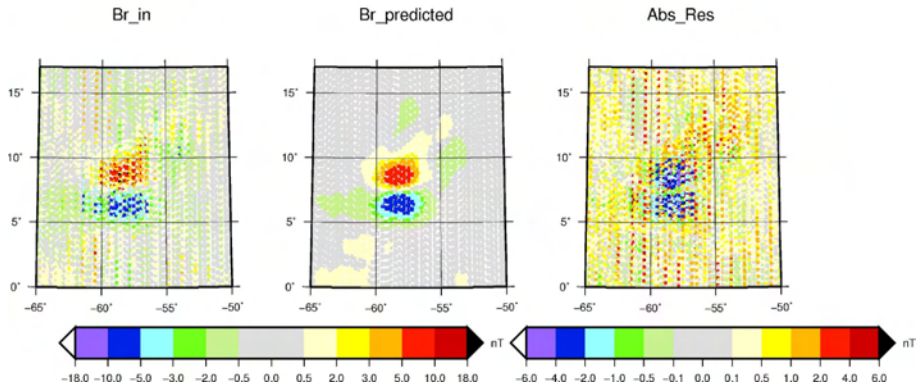

Figure 4.30: The input (left), and predicted radial field (centre) in all lunar regimes, with the absolute residuals (right) for the Reiner Gamma region from the three component magnetisation model with damping parameter 1000. Model thickness 40 km, dipole depth, 20 km, 0.5° spaced central dipoles, 1° spaced border dipoles. Note: As pass-by-pass data locations are plotted, grey represents low fields and white gaps are the absence of data.

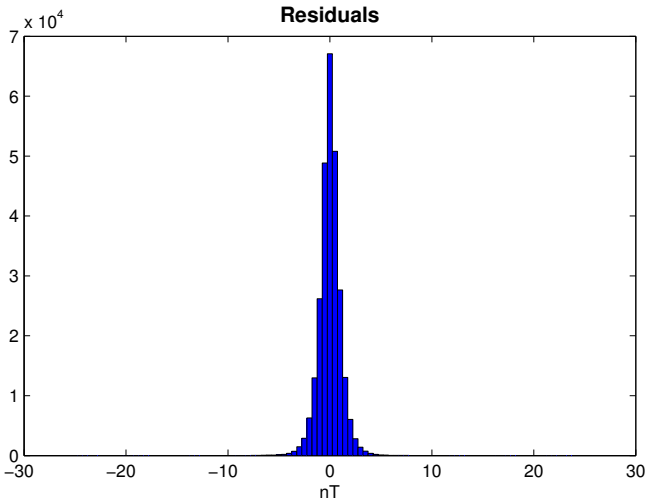

Figure 4.31: Histogram of exact residuals for the Reiner Gamma region from predictions from the three component magnetisation model with damping parameter 1000. Histogram bin size 0.5 nT. Model thickness 40 km, dipole depth, 20 km, 0.5° spaced central dipoles, 1° spaced border dipoles.

residuals in this region, shown in the histogram of residuals in figure 4.31, shows that the equivalent source dipole model is a reasonable representation for the magnetisation in this area. Most of the residuals are small but some are large, giving a strongly peaked distribution with long tails, following a more Laplacian-type distribution than a Gaussian distribution.

The model solutions of figure 4.29 can also be used to predict the total field at the surface to compare with the ER observations. The surface predictions at the ER locations in figure 4.32 give the rough shape of the surface field but with much weaker magnitudes. The model with a higher damping parameter predicts the surface shape better and gives lower surrounding surface fields as observed, but cannot predict the strong magnitudes estimated from the ER technique. While the minimum RMS magnetisation solution can fit the input data at altitude, the under prediction of the ER data suggest that stronger, and perhaps smaller scale magnetisation features are required to fit the ER data.

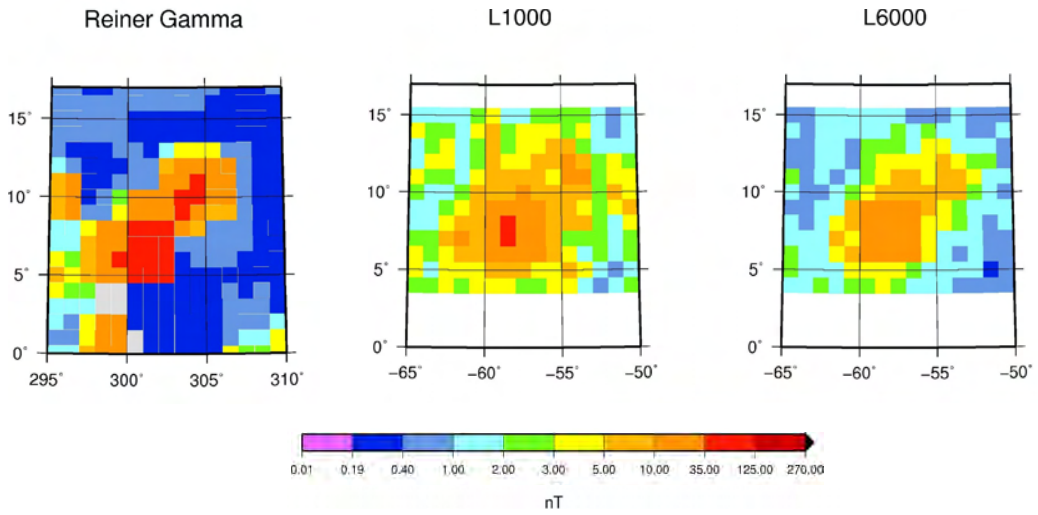

Figure 4.32: The 1°×1° binned ER data for the Reiner Gamma region (left) and the predicted total magnetic field at central latitude locations from the three component magnetisation models with damping parameters of 1000 (centre) and 6000 (right), from the radial data in all lunar regimes. Model thickness 40 km, dipole depth, 20 km, 0.5° spaced central dipoles, 1° spaced border dipoles.

4.9.3 High resolution magnetisation models

The blocky nature of the model solutions of figure 4.29 can be improved by using closer spaced dipoles. A higher resolution dipole grid with dipoles at depth 20 km and layer thickness 40 km was used to find the magnitude and direction of magnetisation from the radial magnetic field data in all lunar regimes, shown for damping parameters of 1000 and 2000 in figure 4.33. While it is not anticipated that the magnetisation solutions be completely smooth, these higher resolution models, even with a damping parameter of 2000, reveal some north-south magnetisation artefacts, probably relating to data from orbits with particularly high magnetic field measurements, since when radial data from the wake and tail regions only were used (Figure 4.34), these features no longer occurred.

The magnetisations produced from the inversion of the wake and tail radial data are very similar to the magnetisations produced from the radial data in all regimes, but are stronger and show a larger and stronger source coincident with the

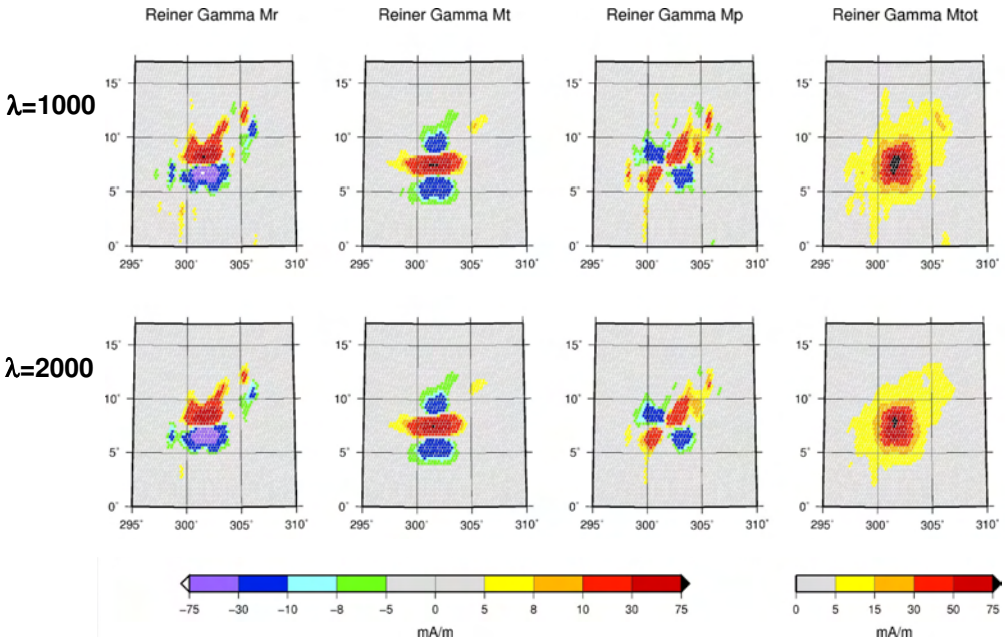

Figure 4.33: Three component and total magnetisation solutions for the Reiner Gamma region with damping parameters of 1000 and 2000, from the radial data in all lunar regimes. Model thickness 40 km, dipole depth, 20 km, 0.25° spaced central dipoles, 0.5° spaced border dipoles.

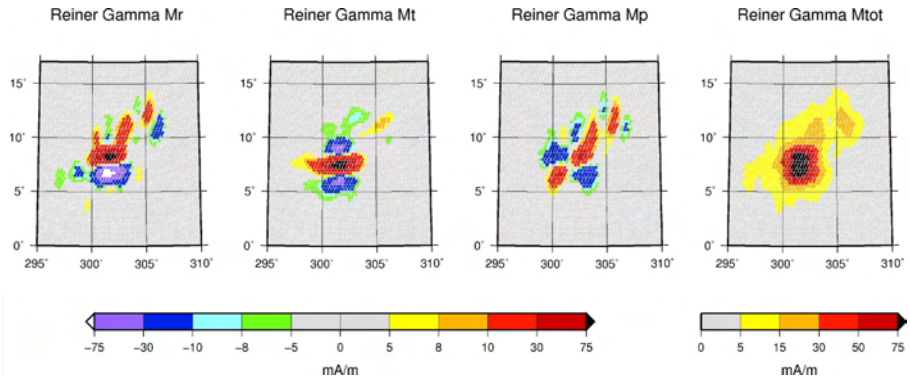

Figure 4.34: As figure 4.33 with a damping parameter of 1000, from the radial data from the wake and tail regions only.

north east extension of the main Reiner Gamma anomaly. The models with the wake and tail data also have a lower misfit than the models with the radial magnetic field data in all lunar regimes. This confirms that data from the lunar wake and geotail regions are preferred, but not essential, for magnetisation modelling by giving a better fit to the input data and fewer potential artefacts in the model solution.

4.9.4 Finding the bulk magnetisation direction

Following the method described in section 4.6.1 for finding a bulk magnetisation direction, magnetisation models were produced for dipoles with fixed inclination values incremented in 30° steps and declination values incremented in 45° steps. An attempt to find the best fitting direction requires all three components of magnetic field at 30 km altitude from the spherical harmonic model. The dipole depth used this time was 15 km with layer thickness at 30 km and a damping parameter of 1000 was used. Figure 4.35 shows the contoured misfit as a function of model inclination and declination for the Reiner Gamma region. As in the test case, the difference in misfits for each combination of inclination and declination are very small. The minimum misfit here occurs for an inclination of 90°. The highest misfits, and hence the least compatible magnetisation direction for the Reiner Gamma magnetic anomaly, occurs for horizontal dipoles in the east-west direction (I=0°, D=±90°). This is in agreement with the magnetisation solutions produced for dipoles fixed in the radial, theta (horizontal north) and phi directions (horizontal east), using the wake and tail radial data, which gave the smallest misfits and RMS magnetisation for the radial dipoles and largest misfits and RMS magnetisations for the horizontal east dipoles (Table 4.7). The magnetisation distribution in the radial, theta and phi directions (Figure 4.36) shows similar features to those from models with variable direction dipoles, with the most difference in the horizontal east direction as expected.

When these fixed direction models are used to predict the input data and the total field at the surface, the radial dipoles give the best fits in each case (without

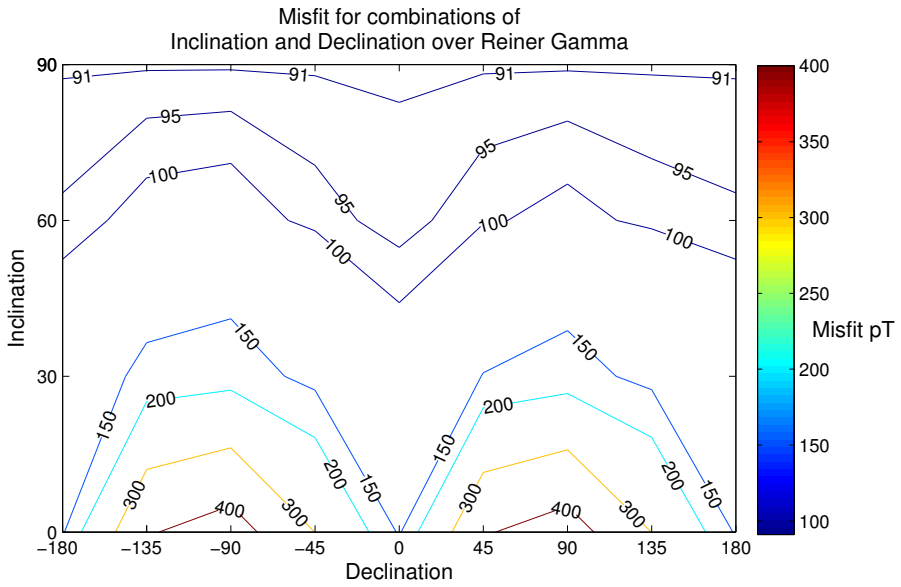

Figure 4.35: Contoured misfit as a function of dipole inclination and declination for the magnetisation solutions for the Reiner Gamma region from the three components of magnetic field at 30 km altitude from the spherical harmonic model. Damping parameter 1000, model thickness 30 km, dipole depth 15 km, 0.25° spaced central dipoles, 0.5° spaced border dipoles.

reaching the highest surface magnitudes) and the horizontal north dipoles also give reasonable fits (Figure 4.37). These predictions highlight the incompatibility of the horizontal east dipoles which cannot correctly predict the patterns of the magnetic field at altitude or at the surface.

The preferred bulk magnetisation direction in the radial direction as opposed to the horizontal north direction is surprising given the form of the magnetic anomaly for Reiner Gamma. Though this highlights the non-uniqueness of magnetisation models as discussed in section 4.7 for a similar anomaly pattern, the preference for radial dipoles raises the issue of bias in the direction solution to the radial component used in the production of the spherical harmonic model of the lunar crustal field data (see section 2.6.4).

	Radial	Theta (horizontal north)	Phi (horizontal east)
Misfit (nT)	0.724	0.737	0.821
RMSmag. (mA/m)	14.5	17.1	24.1

Table 4.7: Misfits and RMS magnetisations for magnetisation models of the Reiner Gamma region with damping parameter 1000, with dipoles fixed in the radial, theta and phi directions from the radial data in the wake and tail. Model thickness 30 km, dipole depth, 15 km, 0.25° spaced central dipoles, 0.5° spaced border dipoles.

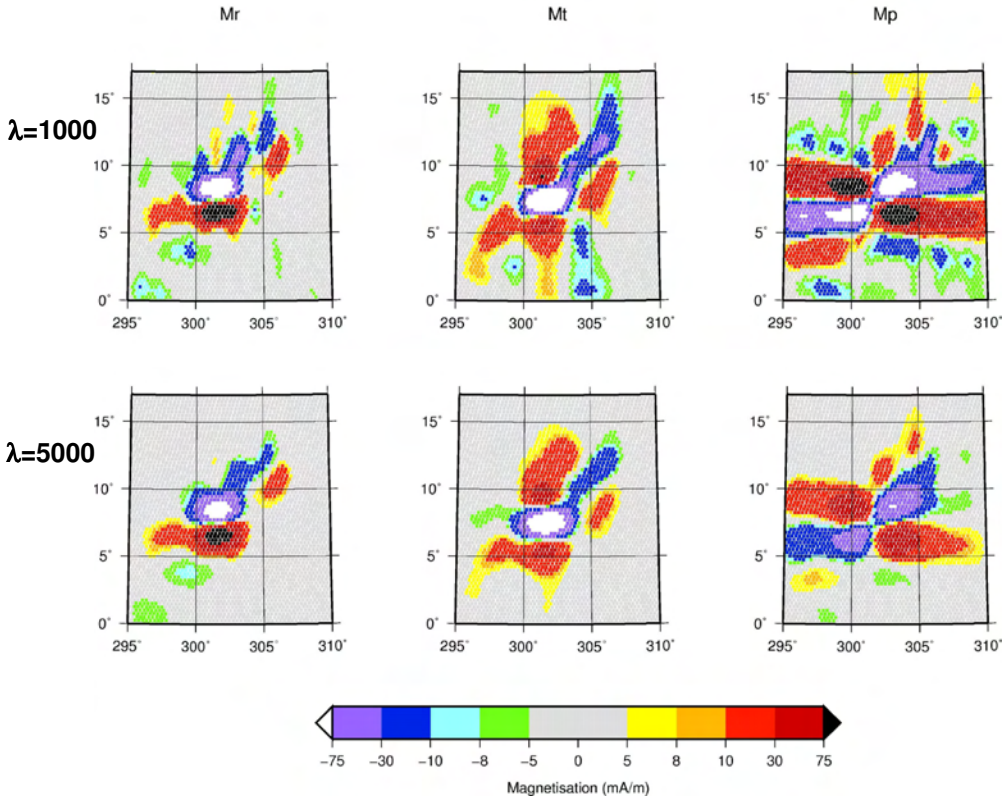

Figure 4.36: Magnetisation intensities for dipoles fixed in the radial (left), theta (horizontal north, centre) and phi (horizontal east, right) directions for the Reiner Gamma region with damping parameters of 1000 and 5000, from the radial data in the wake and tail. Model thickness 30 km, dipole depth, 15 km, 0.25° spaced central dipoles, 0.5° spaced border dipoles. (The directions are opposite to other magnetisation solutions due to the fixed direction of the dipoles).

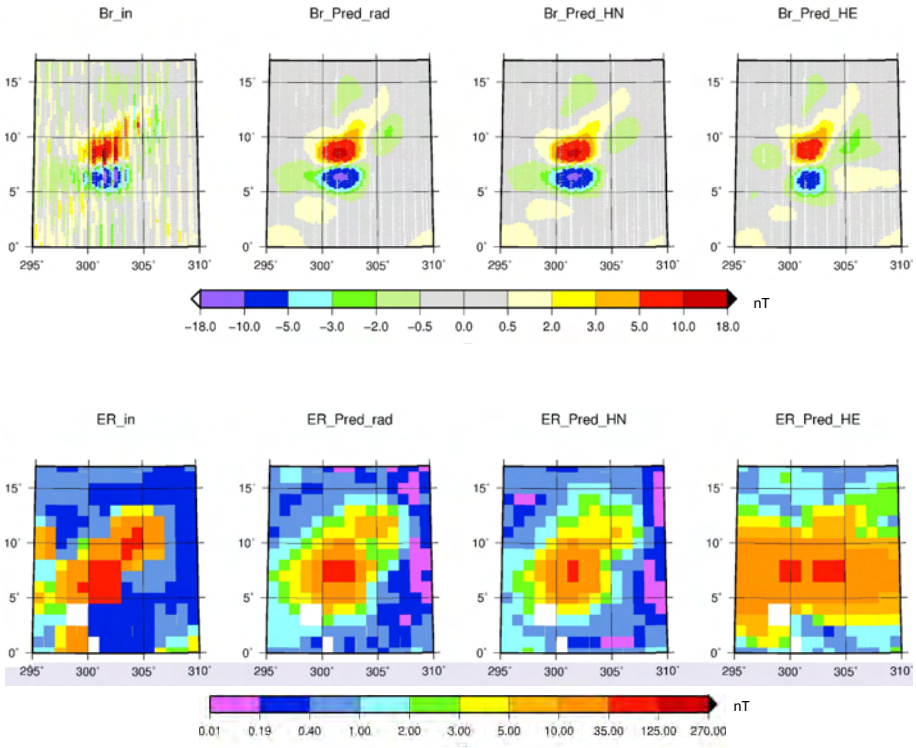

Figure 4.37: The input (left) and predicted radial field in the wake and tail (top) and surface field at the 1°×1° binned ER data locations (bottom) from models with dipoles fixed in the radial (rad), theta (horizontal north, HN) and phi (horizontal east, HE) directions for the Reiner Gamma region with a damping parameter of 1000. Model thickness 30 km, dipole depth, 15 km, 0.25° spaced central dipoles, 0.5° spaced border dipoles.

4.9.5 Investigating thickness and depth of the dipole layer

Using the radial magnetic field data from the wake and tail, high resolution magnetisation models with variable direction were produced for dipole layers with a variety of depths and thicknesses representing surface layers (with depth=thickness), thin buried layers (thickness < depth), and thick buried layers (thickness > depth) (Figure 4.38). As these inversions are computationally intensive, selected damping parameters of 500, 1000 and 5000 were used rather than using a whole range of damping parameters. These are suitable damping parameters with slight over or under damping depending on the model thickness and depth.

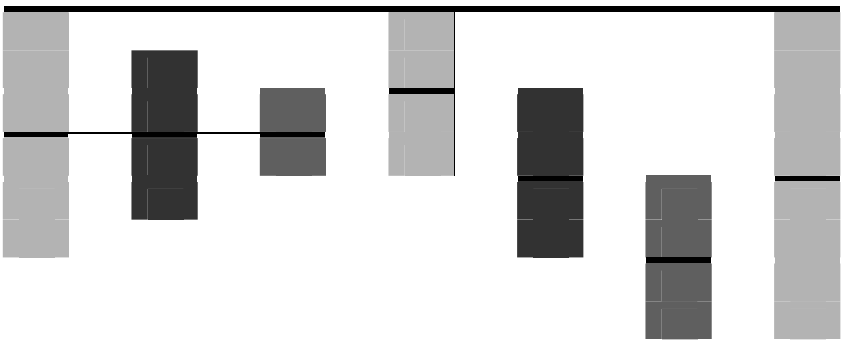

Figure 4.38: Schematic diagram to scale of the depths and thicknesses of dipole layers used to produce magnetisation models for the Reiner Gamma region, representing surface layers (with depth=thickness, light grey), thin buried layers (thickness < depth, grey) and thick buried layers (thickness ≥ depth, dark grey).

For all of these models, the solution outputs and the magnetisation distributions group very well into surface layers and thick and thin buried layers. The RMS magnetisations, misfits to the MAG and ER data (with border region) and correlation coefficients between the predicted and observed MAG and ER data are given in tables 4.8. The lowest misfits and best correlations between the predictions and the observations occur for the surface layers, and the highest misfits and lowest correlations for the thick buried layers. Thinner surface and buried layers have slightly larger RMS magnetisations than comparable thicker layers. All of these models contain dipoles with magnetisations above the Parker bound and are good fits to the data, with misfits slightly lower than the models produced from the radial data from all lunar regimes. Magnetisation solutions with a damping parameter of 1000 for the models with set depth (15 km) and thicknesses of 10, 20 and 30 km (Table 4.8A) are shown in figure 4.39. These models are representative of a surface layer, a thin buried layer and a thick buried layer.

The magnetisation distributions are very similar in shape for the surface layers and the thick and thin buried layers, being similar to and coincident with the component directions of the magnetic field, and each showing the extension of the feature to the north east. Thinner representations of the source are more magnetised than thicker representations, as expected due to the presence of thickness as a

A (Depth =15 km)

Thickness (km)	**Damping** λ	**Misfit** (nT)	**RMSmag.** (mA/m)	**Misfit to ER** (nT)	**Correlation coefficients** **Br**	**ER**
30	500	0.718	7.1	5.27	0.790	0.684
20	500	0.721	9.6	5.03	0.788	0.709
10	500	0.732	15.8	5.00	0.783	0.739
30	1000	0.720	6.5	5.13	0.745	0.704
20	1000	0.725	8.7	5.13	0.747	0.721
10	1000	0.748	13.8	5.41	0.778	0.739
30	5000	0.734	5.2	5.01	0.782	0.741
20	5000	0.756	6.6	5.24	0.775	0.748
10	5000	0.851	8.1	6.04	0.745	0.730

B (Thickness = 20 km)

Depth (km)	**Damping** λ	**Misfit** (nT)	**RMSmag.** (mA/m)	**Misfit to ER** (nT)	**Correlation coefficients** **Br**	**ER**
10	500	0.716	8.3	6.38	0.791	0.612
15	500	0.721	9.6	5.03	0.788	0.709
20	500	0.725	11.3		0.785	
30	500	0.742	14.8	5.05	0.776	0.757
10	1000	0.719	7.5	5.38	0.747	0.656
15	1000	0.725	8.7	5.13	0.747	0.721
20	1000	0.732	10.1		0.746	
30	1000	0.758	12.6	5.51	0.736	0.744
10	5000	0.739	5.9	5.16	0.783	0.704
15	5000	0.756	6.6	5.24	0.775	0.748
20	5000	0.780	7.0		0.764	
30	5000	0.841	7.5	6.02	0.731	0.736

C

Thick. (km)	**Depth** (km)	**Damp.** λ	**Misfit** (nT)	**RMSmag.** (mA/m)	**Misfit to ER** (nT)	**Correlation coefficients** **Br**	**ER**
20	10	500	0.716	8.3	6.38	0.791	0.612
30	15	500	0.718	7.1	5.27	0.790	0.684
40	20	500	0.720	6.9			
20	10	1000	0.719	7.5	5.38	0.747	0.656
30	15	1000	0.720	6.5	5.13	0.745	0.704
40	20	1000	0.722	6.2			
20	10	5000	0.739	5.9	5.16	0.783	0.704
30	15	5000	0.734	5.2	5.01	0.782	0.741
40	20	5000	0.735	4.9			

Table 4.8: RMS magnetisations, misfits to the MAG data (with border region) and the ER data (for selected models only), and correlation coefficients between the predicted and observed MAG and ER data, for variable direction magnetisation models of the Reiner Gamma region from the radial data in the wake and tail with different damping parameters for A: variable layer thickness with set depth 15 km, B: variable depth with set thickness 20 km and C: variable surface layer thickness. 0.25° spaced central dipoles, 0.5° spaced border dipoles.

coefficient in the terms of the **G** matrix in equation 4.11. However, the expected linear inverse relationship between the magnetisation and the layer thickness is destroyed by the presence of the damping parameter in the inversion.

Each of the models in figure 4.39 has magnetisations exceeding 75 mA/m, with the thin buried layer having the strongest and most spread out region of magnetisation. The surface layers show a more compact magnetisation solution requiring a smaller magnetised source to give the best fit to the input data. Figure 4.40 shows sections across the total magnetisation for the models in figure 4.39 at

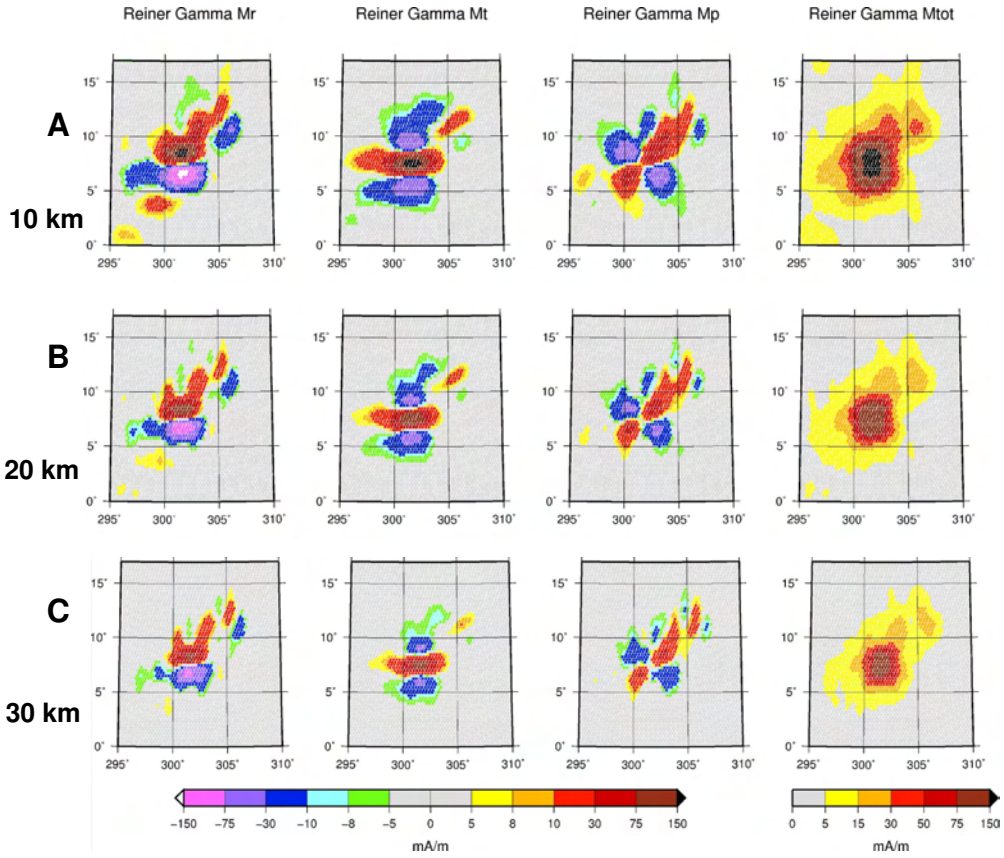

Figure 4.39: Three component and total magnetisation solutions for the Reiner Gamma region with a damping parameter of 1000, from the radial data in the wake and tail for models with dipole depths of 15 km and thicknesses of A: 10 km (thin buried layer), B: 20 km (thick buried layer) and C: 30 km (surface layer). 0.25° spaced central dipoles, 0.5° spaced border dipoles. Note the extended scale compared to previous figures.

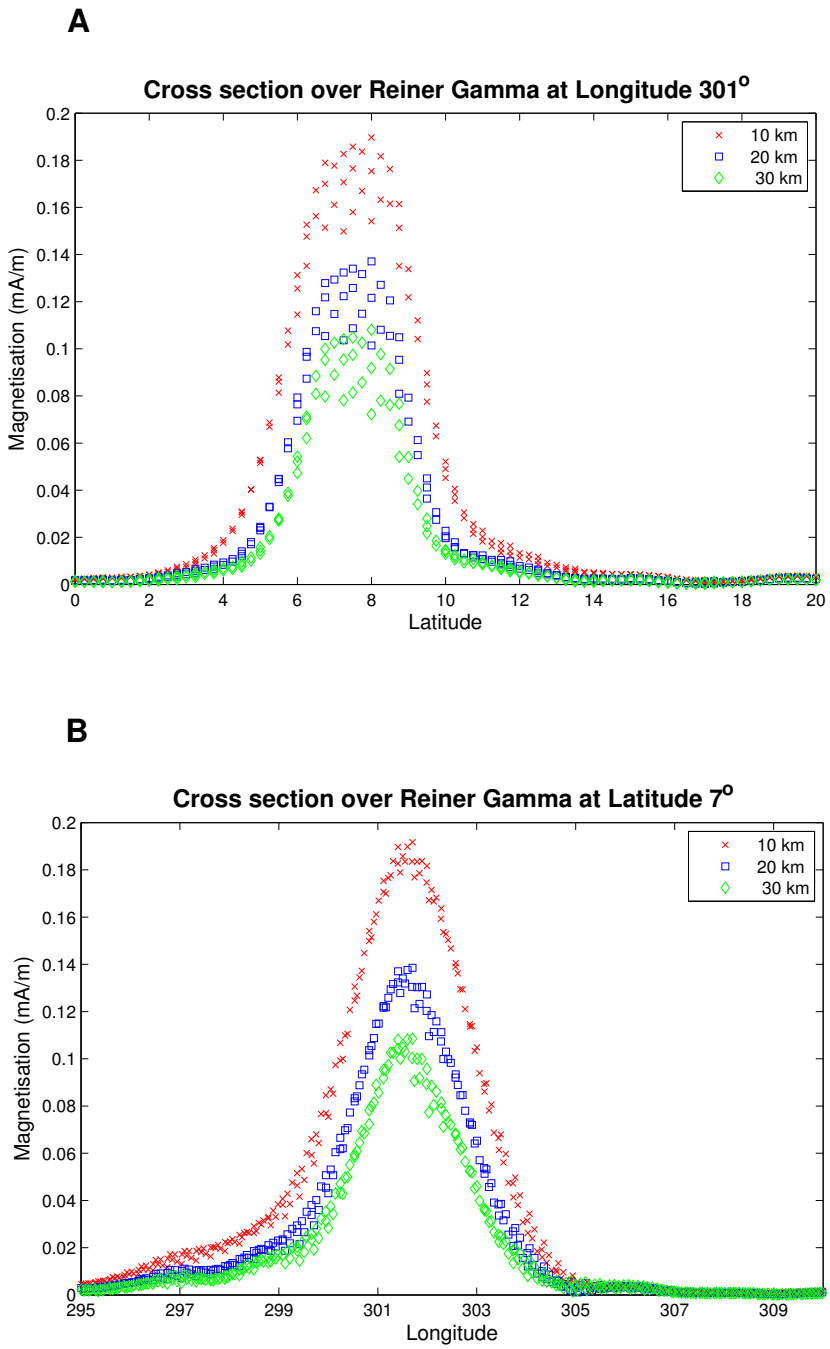

Figure 4.40: Cross sections of the total magnetisation at A: 301° longitude and B: 7° latitude, for the magnetisation solutions for the Reiner Gamma region with a damping parameter of 1000, from the radial data in the wake and tail for models with dipole depths of 15 km and thicknesses 10 km (red cross), 20 km (blue square) and 30 km (green diamond). 0.25° spaced central dipoles, 0.5° spaced border dipoles. As the dipole grid is not square, the longitude cross section consists of several sections closest to 301° longitude, giving a less ordered pattern.

Thickness (km)	**Latitude** extent (°)	**Longitude** extent (°)	**Volume** $\times 10^3$ km^3
10	3.96	3.16	112.6
20	3.33	1.89	113.3
30	2.92	1.42	112.0

Table 4.9: Estimate of the source dimension and volume for the Reiner Gamma source from the 'width at half maximum' total magnetisation models from the radial data in the wake and tail for models with dipole depths of 15 km and thicknesses 10 km, 20 km and 30 km. 0.25° spaced central dipoles, 0.5° spaced border dipoles.

301° longitude and 7° latitude, with the widths at half maximum listed in table 4.9. While the difference in the source size is significant (1° is equivalent to 30 km), it is interesting that the volume of these sources are almost identical (Table 4.9).

Figure 4.41 shows the predicted radial field and the absolute residuals for the model solutions of figure 4.39. The predictions are good (correlation coefficients >0.74) with some larger under and over predictions of the data over the strongest regions, again due to the variability of the input data. Each of these models shows some over prediction of the radial field around the edge of the anomaly, more so in the surface layers, resulting from the spreading of the magnetisation feature with damping (the surface layers seem less damped with a damping parameter of 1000 than the buried layers).

When these models are used to predict the surface fields (Figure 4.42), they can all reproduce the rough total field pattern but cannot predict the strengths estimated from the ER technique. The surface layers are better at predicting the stronger fields and the strong central anomaly, but the buried layers are slightly better at giving the weaker surface fields around the main anomaly and have slightly higher correlation coefficients for the ER data than the surface layers.

Despite producing magnetisation models for a range of thicknesses and depths, it is not possible to determine an 'ideal' depth or thickness for this region. The misfits and correlation coefficients for all these models are similar but the smallest misfits and highest correlation coefficients with the input (MAG) data are for the thinnest surface layers, with the predictions from the buried layers less

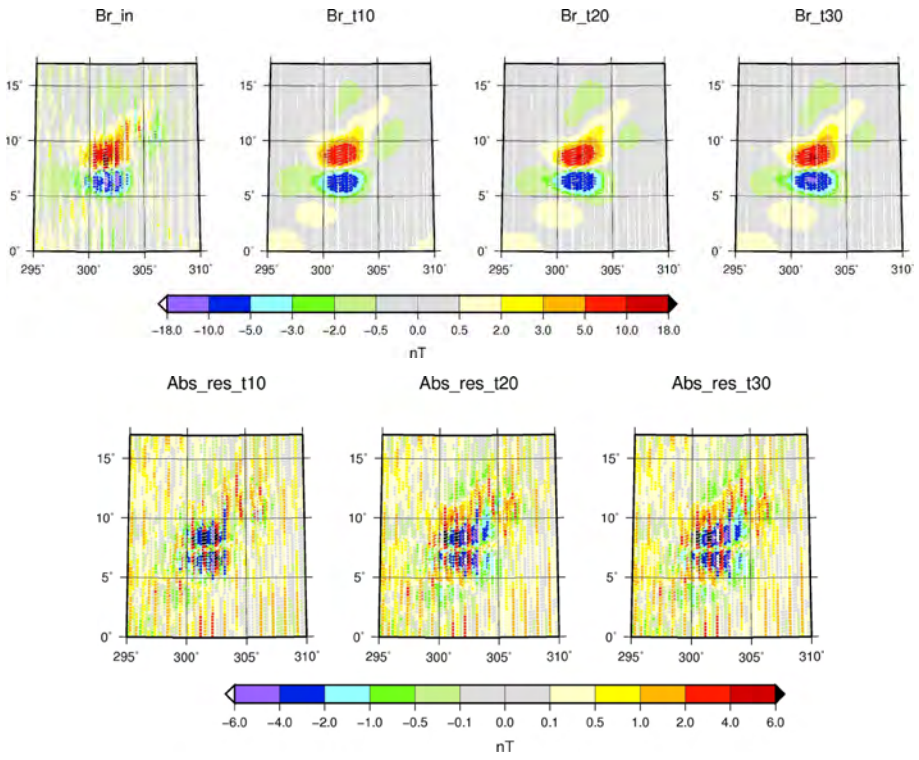

Figure 4.41: The input and predicted radial field (top) and the absolute residuals (bottom) for the Reiner Gamma region from the three component magnetisation models with damping parameter 1000 for model depth of 15 km and thicknesses (t) of 10 km, 20 km and 30 km. 0.25° spaced central dipoles, 0.5° spaced border dipoles, from radial data in the wake and tail region.

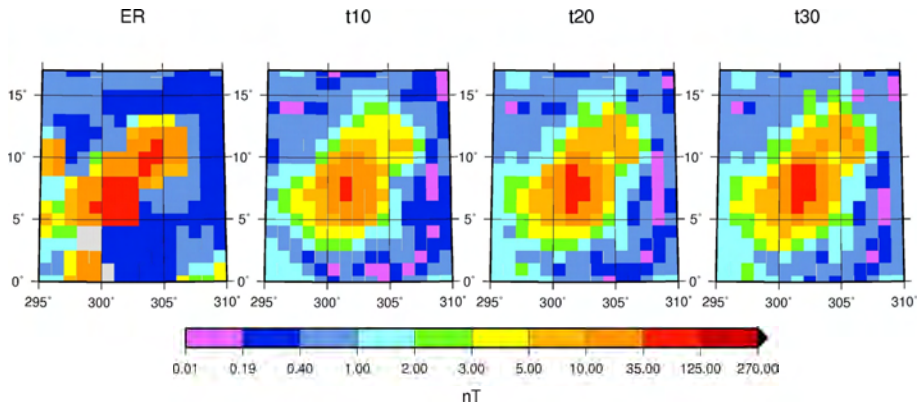

Figure 4.42: The 1°×1° binned ER data for the Reiner Gamma region (left) and the predicted total magnetic field at the same locations from the three component magnetisation models with damping parameter of 1000 for model depth of 15 km and thicknesses (t) of 10 km, 20 km and 30 km. 0.25° spaced central dipoles, 0.5° spaced border dipoles, from the radial data in all lunar regimes.

(though not significantly so) consistent with the input data. When considering the predictions of the ER data, the best fitting model for both the MAG and ER data (see table 4.8) are the models with depth 15 km and thickness 20 km and 30 km. Interestingly it is not the thinner models or models with higher RMS magnetisation (stronger and with smaller scale features) which fit the ER data better as might be expected.

4.9.6 The resolution matrix and covariance matrix

The model resolution matrix and covariance matrix were produced from the **G** matrix for the three component magnetisation model from the radial data in the wake and tail for the model with dipole depth 15 km and layer thickness 30 km and a damping parameter of 1000. For a total of 3×7697 dipole parameters, the trace of the resolution matrix is only 1503. Focussing on the central region of dipoles, the trace for these parameters is even less at 232. This massive reduction in the number of independent parameters results from the 'leakage' of the solution into component directions and into adjacent dipoles as observed in section 4.5.6. The nature of this dipole grid (the polar coordinate subdivision grid) also gives more closer 'nearest neighbours' than the square grid used in the test case, reducing further the values of the diagonal terms.

A section of the transect across the resolution matrix at row 1000 (Figure 4.43A) shows how small the terms in the resolution matrix are (< 0.03) and the leakage into the surrounding dipoles, featured in figure 4.43B. The effective resolution of this model in the central region is ~1°, comparable to the altitude of the observations (30 km). With the actual model resolution much less than the intrinsic model resolution (the dipole spacing), a coarser dipole grid could have been used, reducing the requirement for computation power and time. However, dipoles with larger spacing would have to be placed at greater depths when incorporating the surface ER data (see section 4.3.2).

Using the trace and the SSR for this model (2.17×10^4 nT for λ=1000) in equation 4.22, the variance of the data is estimated at 0.539 nT^2. The estimated

uncertainties in the model parameters σ_m (from the diagonal elements of the covariance matrix in equation 4.23), for the central region dipoles, are 19-23 mA/m. These uncertainties are reduced to 9-10 mA/m if a damping parameter of 5000 is used, but the effective resolution is still ~1°. The uncertainties are high compared to the values of the magnetisation solution in many locations, even when the data are assumed to have equal variance, which is probably not the case for these radial data. However, despite these uncertainties, these models are still able to provide information on the magnitude and distribution of the magnetisation responsible for the magnetic anomaly over the Reiner Gamma region.

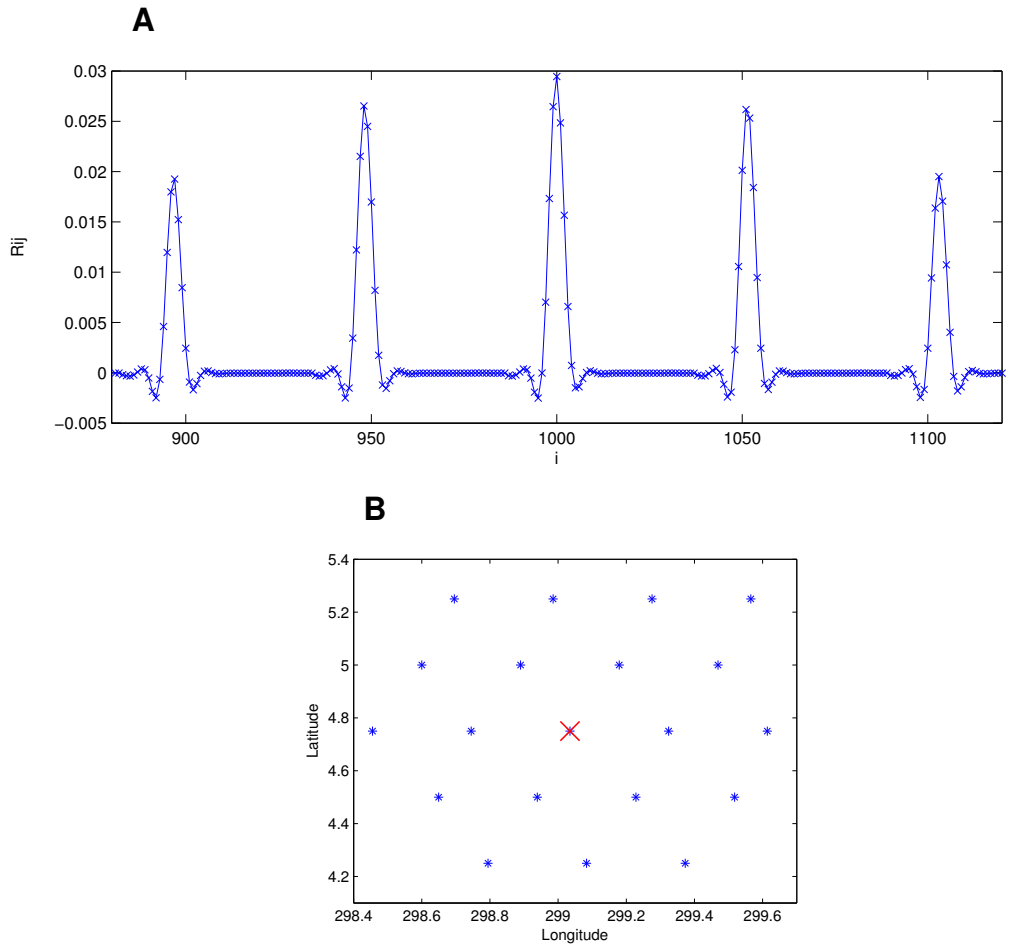

Figure 4.43: A: A transect across the resolution matrix **R** (of size 23091×23091) at row *i*=1000 for the three component magnetisation model from the radial data in the wake and tail for the model with dipole depth 15 km and layer thickness 30 km. 0.25° spaced central dipoles, 0.5° spaced border dipoles. B: The *i*=1000 dipole (red cross) and the surrounding dipoles which have correlated magnetisation solutions (blue stars).

4.10 Application of the ESD technique to other regions

This in depth study of the application of the equivalent source dipole technique to the Reiner Gamma region, although producing models which fit the MAG very well and also the ER data, have not allowed other information about the source, namely thickness, depth and direction to be determined. With this in mind, the application of the equivalent source dipole technique to other regions has only focussed on trying to find a suitable solution for a set layer thickness only. Using wake and tail radial data, with a high resolution dipole grid, three component magnetisation models were produced for regions near Firsov crater, Descartes and the Crisium basin.

The chosen magnetisation solutions for these regions are shown in figure 4.44, with the solution parameters in table 4.10. The magnetisation solutions for these regions are very similar to the components of the field at 30 km altitude, as was the case with the Reiner Gamma models. The total magnetisations coincide with the total field magnitude (see Appendix 2). Each of these regions have smaller RMS magnetisations than the Reiner Gamma region, with magnetisations within the layer exceeding 30 mA/m. The Firsov and Crisium models give slightly better fits to the data in their region than the Reiner Gamma model, while the Descartes model has a higher misfit, perhaps as a result of the choice of the layer depth and thickness.

Region	Thickness (km)	Depth (km)	Damping λ	Misift (nT)	RMS mag. (mA/m)
Firsov	30	15	2000	0.602	4.3
Crisium	30	15	1000	0.614	5.2
Descartes	20	30	3000	1.15	9.4

Table 4.10: Model and solution parameters for the regions of Firsov, Crisium and Descartes from the radial data in the wake and tail. 0.25° spaced central dipoles, 0.5° spaced border dipoles.

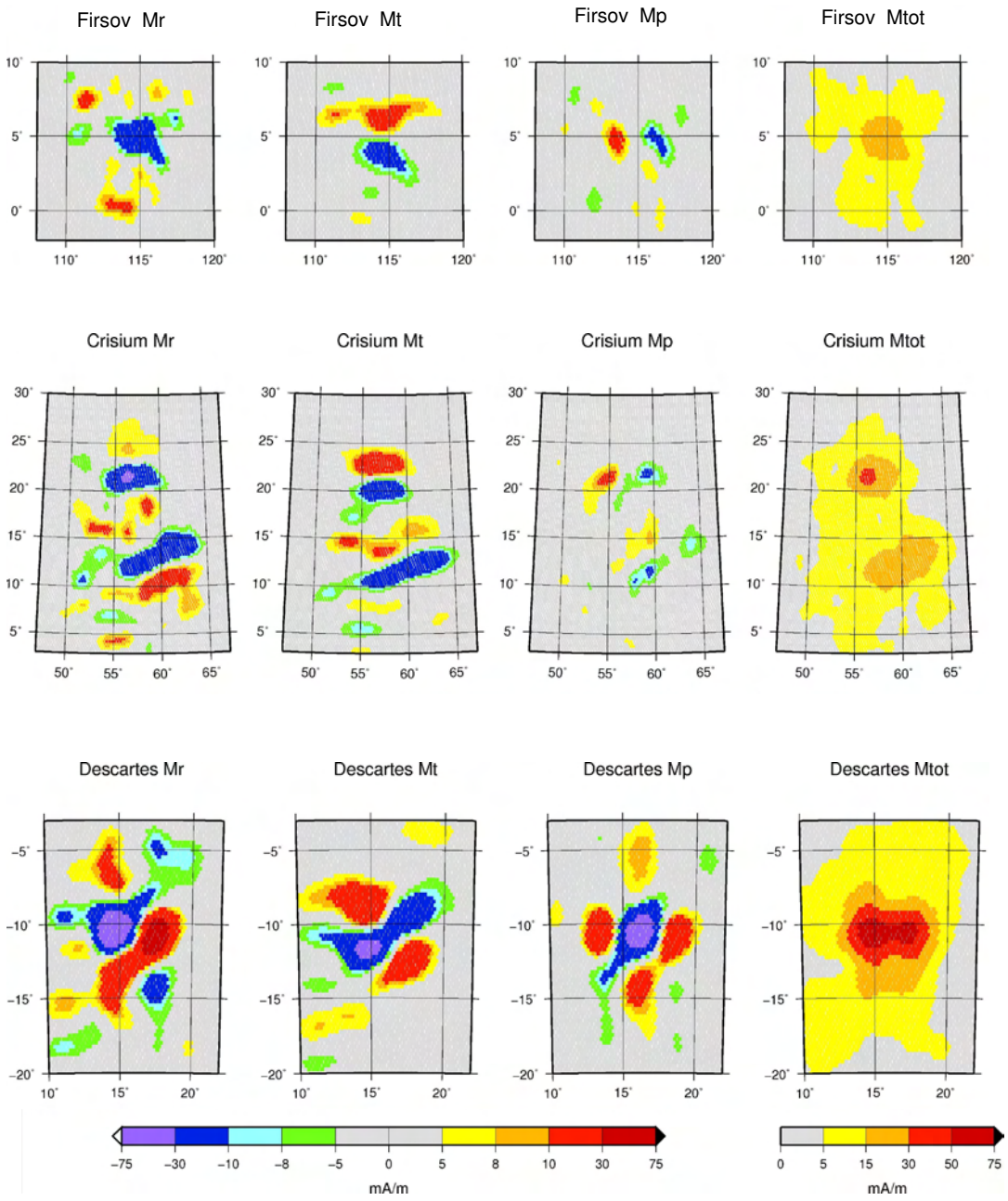

Figure 4.44: Three component and total magnetisation solutions for the regions of Firsov (top) in a 30 km thick layer with damping parameter 2000, Crisium (middle) in a 30 km thick layer with damping parameter 1000, and Descartes (bottom) in a 20 km thick layer with damping parameter 3000, from the radial data in the wake and tail. 0.25° spaced central dipoles, 0.5° spaced border dipoles.

Chapter 5

Spatially continuous global magnetisation models

A spatially continuous magnetisation distribution involves expressing the spatial distribution of magnetisation as a linear combination of Green's functions. The magnetisation of a layer of constant thickness is produced without any assumption about the magnetisation direction or spatial resolution. This method is suitable for inversion of global data sets, as applied to the terrestrial case [Whaler and Langel, 1996], and Mars [Whaler and Purucker, 2005], and preserves the resolution of the original data set. The codes used for the production of the models in this chapter are taken from the work of Whaler and Purucker (2005) and adapted for the lunar case.

5.1 Theoretical background

Similarly to the equivalent source dipole technique, this method considers the effect of the magnetisation vector within a crustal layer of set thickness and volume, on the magnetic potential at the satellite location. In this case, the magnetisation vector $\mathbf{M}(\mathbf{s})$, is at a non-specific location $\mathbf{s}$ within the crustal layer of thickness t and total volume V (Figure 5.1), giving the magnetic potential ψ_i at the satellite at position $\mathbf{r}_i$

$$\psi_i = \int_V \mathbf{H}(\mathbf{r}_i, \mathbf{s}) \cdot \mathbf{M}(\mathbf{s}) dV \tag{5.1}$$

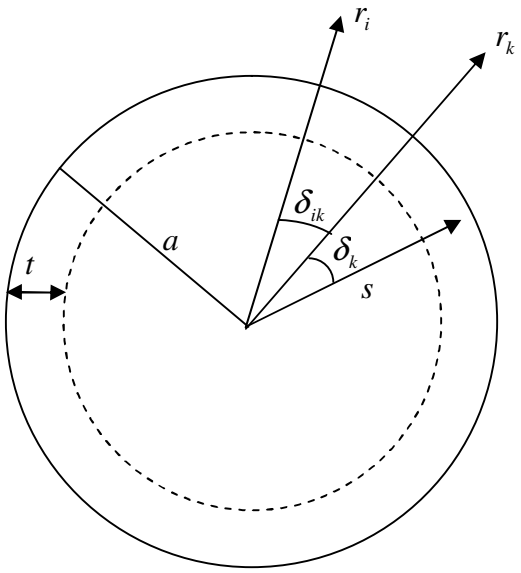

Figure 5.1: Schematic cross section through the Moon with radius a showing the magnetised layer of thickness t (not to scale), the observation locations r_i and r_k separated by angle δ_{ik} and the location s of the magnetisation vector at an angle δ_k to r_k. (Based on Jackson (1990)).

where **H** is the Green's function relating the magnetisation at **s** to the magnetic scalar potential at point $\mathbf{r}_i$, [Parker et al., 1987, Jackson, 1990]:

$$\mathbf{H}(\mathbf{r}_i,\mathbf{s}) = \frac{\mu_o}{4\pi}\nabla_s \frac{1}{|\mathbf{r}_i - \mathbf{s}|} \tag{5.2}$$

with ∇_s, the gradient operator with respect to the position **s**.

Taking the negative gradient of the potential, the *pth* component of the observed magnetic field $\mathbf{B}_{i_p}$, (in spherical polar coordinates) at the satellite location can be expressed as:

$$\mathbf{B}_i^{(p)} = \int_V \mathbf{G}^{(p)}(\mathbf{r}_i,\mathbf{s})\cdot\mathbf{M}(\mathbf{s})dV \tag{5.3}$$

with **G** now the Green's function of the problem given by

$$\mathbf{G}^{(p)}(\mathbf{r}_i,\mathbf{s}) = -\frac{\mu_o}{4\pi}\hat{\mathbf{I}}_i^{(p)}\cdot\nabla_{r_i}\nabla_s \frac{1}{|\mathbf{r}_i - \mathbf{s}|} \tag{5.4}$$

with $\hat{\mathbf{I}}_i^{(p)}$ the unit vector in the direction of the local orthogonal components. Each Green's function depends on the cosine of the angular separation ($\mu_k = \cos\delta_k$) between the observation point and the point *s* within the magnetised crust (see figure 5.1 and Appendix 11), and the values of **G** fall off quickly as μ_k decreases. As long as no two observation locations are identical, the Green's functions form a linearly independent set of basis functions [Parker et al., 1987].

5.1.1 A minimum norm solution

There are an infinite number of distributions $\mathbf{M}(\mathbf{s})$ in equation 5.3 that could produce the observed magnetic field. A unique minimum norm solution for **M** (in three component directions) can be expressed as a linear combination of the Green's functions with expansion coefficients α_i:

$$\mathbf{M}(\mathbf{s}) = \sum_{i=1}^{3mx} \alpha_i \mathbf{G}(\mathbf{s}, \mathbf{r}_i) \tag{5.5}$$

[Shure et al., 1982], where mx is the number of data locations.

The '2-norm' $\|\mathbf{M}\|$ of the magnetisation amplitude (RMS magnetisation) can be expressed as:

$$\|\mathbf{M}\| = \sqrt{\int_V \mathbf{M}\cdot\mathbf{M}dV} = \sqrt{\boldsymbol{\alpha}^T \boldsymbol{\Gamma} \boldsymbol{\alpha}} \tag{5.6}$$

where $\boldsymbol{\Gamma}$ is known as the Gram matrix, and $\boldsymbol{\alpha}$ is the vector of expansion coefficients. The Gram matrix is a 'data by data' matrix (size $3mx \times 3mx$) containing all the possible pairs of inner products of the basis functions for the field components *g* and *p* (*g*,*p*=1,2,3) at positions $\mathbf{r}_i$, and $\mathbf{r}_k$:

$$\Gamma_{ik}^{(gp)} = \int_V \mathbf{G}^{(p)}(\mathbf{r}_i, \mathbf{s}) \cdot \mathbf{G}^{(g)}(\mathbf{r}_k, \mathbf{s}) dV \tag{5.7}$$

Inputting the magnetisation solution (equation 5.5) into equation 5.3, the set of magnetic field observations **B** can be represented as:

$$\mathbf{B} = \mathbf{\Gamma}\boldsymbol{\alpha} \tag{5.8}$$

In this case, the forms of the Gram matrix elements are set up to ensure a solution with minimum RMS magnetisation. The forms of these elements described in Jackson (1990), Whaler and Langel (1996) and Appendix 11, can be expressed in terms of elementary functions depending on the cosine of the angular separation of data points, $\mu = \cos\delta_{ik}$ and the ratios of the radii, $\rho = a^2 / r_i r_k$:

$$\Gamma_{ik}^{(gp)} = \left(\frac{\mu_o}{4\pi}\right)^2 (\hat{\mathbf{I}}_i^{(p)} \cdot \nabla_i)(\hat{\mathbf{I}}_k^{(g)} \cdot \nabla_k)\left[\frac{4\pi}{a} Q(\mu, \rho)\right] \tag{5.9}$$

Jackson (1990) shows that the function *Q* takes the form of elliptical integrals which take a long time to evaluate. When the magnetised layer is thin (with respect to the radius), it is possible to accurately approximate the function *Q* and hence the elements of $\mathbf{\Gamma}$ avoiding lengthy calculations of elliptical integrals [Whaler and Langel, 1996]. The exact expressions are simplified when $\mathbf{r}_i$, and $\mathbf{r}_k$ are at concentric or antipodal points where $\mu = \pm 1$, and the calculation can be made more accurate by using the exact expressions for these points.

As the elements of $\mathbf{\Gamma}$ are integrals of products of the Green's functions, for large angular separations, they become very small and can be assumed to be zero, making the Gram matrix numerically sparse.

5.2 The solution

A solution for the expansion coefficients $\boldsymbol{\alpha}$ in equation 5.8, is sought which minimises the RMS magnetisation (equation 5.6) for a given fit to the data. A 'least squares' solution can be found from

$$\mathbf{B} = (\boldsymbol{\Gamma} + \lambda \mathbf{I})\boldsymbol{\alpha} \tag{5.10}$$

[Shure et al., 1982, Parker and Backus, 1982] where **I** is the identity matrix and λ represents a (positive) damping parameter controlling the relative importance of the fit to the data and the RMS magnetisation (see Appendix 12), in similar fashion to the damping parameter used with the equivalent source dipole method. The sum of squares of residuals S^2 can be expressed as:

$$S^2 = \lambda^2 \boldsymbol{\alpha}^T \boldsymbol{\alpha} \tag{5.11}$$

[Shure et al., 1982].

5.2.1 Inversion

For a large data set it is impractical to solve equation 5.10 directly (input data at 1° spacing would require a Gram matrix with $>10^{10}$ elements). Whaler and Langel (1996) dealt with this size constraint by basing the expansion of the solution in equation 5.5 on only a subset of the data points ('depleted basis') [Parker and Shure, 1982], however this decreased the resolution of the model. In order to make the solution tractable and to preserve the resolution of the input data set, the numerical sparseness of the Gram matrix can be exploited, and an iterative conjugate gradient method for sparse matrix systems [Purucker et al., 1996] was used to solve equation 5.10.

Following the method of Whaler and Purucker (2005), the Gram matrix elements were calculated for combinations of data points (equation 5.9) using approximate functions for Q when $-1 < \mu < 1$ and exact expressions when $\mu = \pm 1$. Due to the arrangement of data points, there may not be a point where $\mu = -1$, so the data points closest to the antipodal points (r_k', figure 5.2) are sought within a 'search arc' (e.g $\mu + 1 < 10^{-7}$), and these Gram matrix elements calculated from the exact expressions. The 'search arc' will depend on the spacing of the data points. Closely spaced points will have several near-antipodal points, and the accuracy of the

solution, particularly of the calculated magnetisation distribution and the predicted field, is increased by increasing the size of the 'search arc' (e.g with 0.5° spaced data points, the 'search arc' was increased to $\mu + 1 < 10^{-6}$).

The values of the elements in the Gram matrix will depend on the layer thickness and the locations of the data points, but most of the elements in the Gram matrix are small (< 0.1). Only Gram matrix elements for coincident points and those with absolute values above a stated threshold were retained so that the number of elements stored did not exceed the memory capabilities of the system (~2×10^9 elements). This is equivalent to retaining elements for pairs of data points in a hemispherical cap around each data point and its antipode (Figure 5.2).

The solution for $\boldsymbol{\alpha}$ in equation 5.10 was found using the iterative conjugate gradient method for sparse matrix systems [Purucker et al., 1996], implemented in a FORTRAN90 code (by Whaler and Purucker, 2005). Convergence of the iterations was defined by satisfying equation 5.10 to a tolerance of:

$$\left\| \mathbf{B} - (\boldsymbol{\Gamma} + \lambda \mathbf{I})\boldsymbol{\alpha} \right\| < 10^{-10} \tag{5.12}$$

within the maximum stated number of iterations, set at 500.

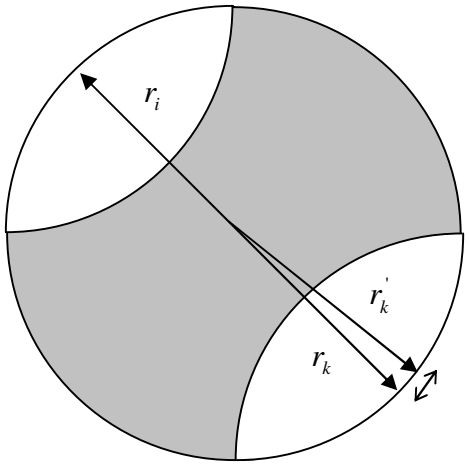

Figure 5.2: Schematic showing the region of the majority of retained data points used in the calculation of the matrix elements (white) for an observation at location r_i with antipode at r_k and near-antipodal point r_k'.

The convergence of this iterative technique was improved by preconditioning the components in equation 5.10 using Jacobi scaling:

$$\frac{B_i}{\sqrt{(\Gamma_{ii}+\lambda)}} = \left[\frac{\Gamma_{ik}+\lambda\delta_{ik}}{\sqrt{[(\Gamma_{ii}+\lambda)(\Gamma_{kk}+\lambda)]}}\right]\alpha_k\sqrt{(\Gamma_{kk}+\lambda)} \qquad (5.13)$$

(with δ_{ik} now being Kronecker delta and summation over *k* implied). The diagonals of the damped Gram matrix become unity and this set of equations is solved for $\alpha_k\sqrt{(\Gamma_{kk}+\lambda)}$ rather than α_k so the preconditioning factor needs to be removed after the solution is found.

5.2.2 The magnetisation solution

The coefficients $\boldsymbol{\alpha}$ are used to evaluate the three components of the continuous distribution of magnetisation (equation 5.5), and to predict the field (equation 5.8) at specified locations and at the input field locations to calculate residuals. The RMS magnetisation in this case for the whole volume of magnetised crust can also be calculated (equation 5.6), though this is a less useful value on a global scale.

Calculations for the magnetisation distribution and the predicted field utilise all values of $\mathbf{G}$ or $\boldsymbol{\Gamma}$ (rather than using a threshold) and use the exact functions for data points near both coincident and antipodal locations using a 'search arc'. This results in some small discrepancies between the 'point by point' misfits and the global values. This is most prominent with the smallest damping parameters.

Calculation of the magnetisation distribution requires the Green's functions and an output grid of specified spacing for the entire globe or for a region of interest, at a specified depth within the magnetised layer. In this way, the magnetisation at a global or regional scale can be studied at different depths within the magnetised layer.

The representation of the magnetisation as a linear combination of Green's functions (equation 5.5) gives a magnetisation solution that decreases with depth into the magnetised layer [Whaler and Purucker, 2005]. Any depth variation in the magnetisation models with different layer thicknesses can be averaged out by calculating the vertically integrated magnetisation (VIM), the sum of the product of the magnetisation at each interval with the depth interval (units, kA). By producing the magnetisation solution at different depths within the layer, the VIM was estimated using the trapezium rule (Figure 5.3).

5.3 Input model parameters

The spatially continuous model for crustal magnetisation requires as inputs:

- Vector magnetic field data (single or multiple components) at specified locations (latitude, longitude and altitude)
- Thickness of model layer
- Threshold for retaining significant elements of the Gram matrix
- Maximum number of iterations and convergence tolerance
- Damping parameter

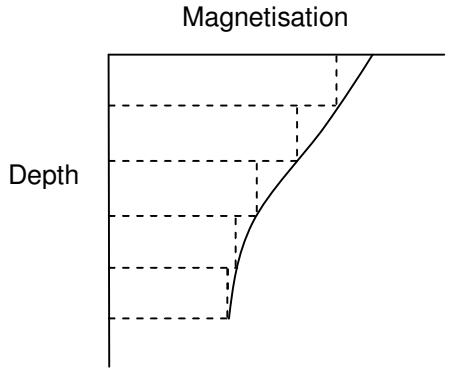

Figure 5.3: Schematic showing the decrease in the magnetisation solution with depth in these models, and the method of estimation of the vertically integrated magnetisation for a single location.

5.3.1 The data

For a global magnetisation model, the global data sets used with this method are the three components of magnetic field at 30 km altitude produced from the spherical harmonic model, and the altitude normalised (30 km) radial component of magnetic field. The data from the spherical harmonic model were produced on a 1° spaced polar coordinate subdivision grid (Appendix 4) consisting of n=35812 data locations. The number of elements in the Gram matrix when three components of data are used is $(3n)^2$. Data closer than 1° significantly increase the computation time and number of iterations. With a single component of magnetic field data (the radial component), the number of elements in the Gram matrix is n^2 so a higher resolution data set can be used.

The radial magnetic field data set consisted of over 3 million data points unequally spaced, at the original observation locations. To provide an equally spaced sub set of these data, the data points closest to the locations of the polar coordinate subdivided grid with spacing 0.5° were selected. The selection of data points was then varied by shifting the grid by 0.25° in latitude and longitude to test if the choice of data selected has a significant impact on the results from the model. Models were produced using the radial data for all lunar regimes, and for just the data from when the satellite was in the lunar wake and the geomagnetic tail. The data were treated as if they had the same variance and were uncorrelated.

5.3.2 Layer thickness

As the spatially continuous distribution of magnetisation is for the entire Moon, the layer thickness chosen has to reflect the expected global magnetisation thicknesses. Layer thicknesses between 5 km and 60 km were tried, focussing on layers with thicknesses of 10 km, 30 km and 50 km, representing thin or thick layers with respect to the globally estimated magnetic thickness of 26 km (see section 3.5.2). These thicknesses satisfy the thin layer approximation. The thickness influences the size of the elements in the Gram matrix, with thinner layers having

smaller values so fewer elements are retained for the same threshold value. It would be possible to consider a buried layer with this set up if the radius was reduced by the distance to the top of the buried layer, but this was not considered in these models.

5.3.3 Threshold

The threshold value determines how many of the Gram matrix elements will be retained. For a layer of 30 km thickness (with damping parameters of 0 and 20,000), threshold values from 0.1 to 10 retained from 9.18 % to 0.988 % of elements respectively with very little difference (to within less than 0.05 %) in the sum of squares of residuals and the solution norm for each of these models (with the same damping parameter) showing that within this range, the solution is stable with respect to the threshold.

Damping does not affect the number of elements retained but does reduce the number of iterations required for the solution to converge. When no damping was used, models with higher thresholds took longer to converge as they contained fewer matrix elements. The threshold value must also allow enough elements to be retained to allow the solution to converge to a suitable result. Thresholds imposed for the Martian case retained down to 0.21 % of the Gram matrix elements and still provided acceptable solutions [Whaler and Purucker, 2005].

A threshold value of 1.5 was suitable for the models with layer thickness from 8 km to 60 km, retaining between 1.3 % and 3.7 % of the elements of the Gram matrix. This corresponds to retaining elements for data points separated by up to 20°.

5.3.4 Damping

The form of damping applied to equation 5.10 is different to the damping applied to the equivalent source dipole model in equations 4.18 and 4.20. In this case, the damping is applied directly to the matrix $\mathbf{\Gamma}$ which is square, to solve for the Green's functions coefficients, instead of to the 'parameter by parameter' matrix of

the equivalent source dipole method solving for magnetisation directly. However, damping the linear equations in 5.10 has a similar effect to the damping in equations 4.18 and 4.20 by reducing the magnetisation norm of the solution at the (small) expense of increasing the residuals (Appendix 12). Damping parameters between 0 and 100,000 were used with these models to find the most suitable damping parameter for each set of data and layer thickness. As a result of the inclusion of the damping parameter in the Jacobi scaling (equation 5.13), a model with a larger damping parameter will require fewer iterations to converge to the required tolerance.

5.4 Magnetisation models from the spherical harmonic model data

Using the three components of magnetic field at 30 km altitude from the degree 150 spherical harmonic model as input data, continuous magnetisation model solutions were found for magnetised layers with thicknesses of 10 km, 30 km, and 50 km for a range of damping parameters from zero to 100,000. All of these models converged within 80 iterations or less and gave magnetisation solutions satisfying the Parker bound for their layer thickness and the maximum value of the predictions from the spherical harmonic model. Residuals between the predicted and input magnetic fields, defined as 'exact', 'absolute', and 'normalised' (see section 3.6) were calculated.

Unlike models with Martian and terrestrial data [Whaler and Purucker, 2005, Whaler and Langel, 1996], convergent solutions were found when no damping was used (λ=0). Despite giving a zero misfit (equation 5.11), and hence fitting noise inherent in the spherical harmonic model data, the non damped solutions did not have substantially higher norms than many of the damped solutions, yielding 'reasonable' magnetisation models, without large variation in magnitude. This convergence without the use of a damping parameter may result from the use of fewer data points than in the Martian case (Whaler and Purucker (2005) use >100,000 data points), and the inability of the 'depleted basis' method in the terrestrial case to provide a non-damped solution. The convergence with zero

damping does not seem to be the result of the 'smooth' nature of the input data from the spherical harmonic model, as recent terrestrial magnetisation models with this method also use data predicted from spherical harmonic models [Whaler and Purucker, 2010].

5.4.1 The effect of damping on the model solution

Magnetisation solutions for each layer thickness can be found for a large range of damping parameters while still giving a reasonable fit to the input data (see table 5.1). The global correlation coefficients are all high (> 0.94) and the globally averaged misfits in these models are all within the range of the estimated uncertainty in the data values (~0.5 nT), although there will be larger misfits over the regions with larger fields.

Plotting the 'trade-off' curves (Figure 5.4) for the model and fit parameters for these differently damped models requires the square of the magnetisation norm

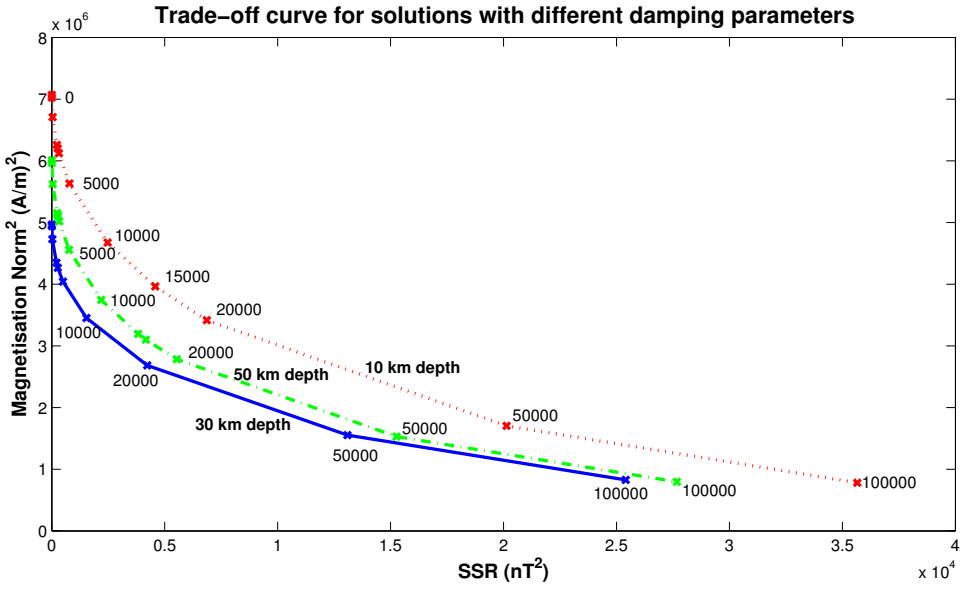

Figure 5.4: Trade-off curve of the square of the magnetisation norm and the sum of squares of residuals (SSR) for global models with 10 km, 30 km and 50 km thickness and different damping parameters. (From the three components of the spherical harmonic model data with 1° spacing).

	10 km				30 km				50 km			
Damping λ	**SSR** (nT^2)	**Norm** (A/m)	**Misfit** (nT)	**Iterations**	**SSR** (nT^2)	**Norm** (A/m)	**Misfit** (nT)	**Iterations**	**SSR** (nT^2)	**Norm** (A/m)	**Misfit** (nT)	**Iterations**
0	0.00	2658.58	0.0000	80	**0.00**	**2228.35**	**0.0000**	**30**	0.00	2451.34	0.0000	25
100	0.49	2650.68	0.0021	68	0.30	2222.63	0.0017	30	0.51	2442.71	0.0022	25
1000	41.42	2589.85	0.0196	39	27.44	2174.86	0.0160	26	44.99	2370.96	0.0205	24
3000	317.42	2474.22	0.0544	27	206.82	2085.21	0.0439	24	327.05	2240.05	0.0552	22
5000	783.93	2373.18	0.0854	22	500.20	2009.91	0.0682	22	763.94	2134.85	0.0843	21
10000	2475.23	2161.91	0.1518	16	**1535.56**	**1858.08**	**0.1196**	**18**	2189.36	1935.10	0.1428	18
20000	6868.29	1848.30	0.2528	12	4227.49	1637.96	0.1984	14	5530.75	1668.37	0.2269	15
50000	20132.75	1305.44	0.4329	9	**13087.66**	**1245.78**	**0.3490**	**11**	15261.46	1236.74	0.3769	11
100000	35657.70	883.50	0.5761	7	25409.35	909.40	0.4863	8	27672.58	892.62	0.5075	9

Damping λ	**Correlation coefficients**		
	Br	**Bt**	**Bp**
100	1.000	1.000	1.000
1000	1.000	>0.999	>0.999
5000	0.999	0.999	0.999
10000	0.998	0.998	0.998
50000	0.990	0.990	0.989
100000	0.985	0.985	0.983

Correlation coefficients		
Br	**Bt**	**Bp**
1.000	1.000	1.000
1.000	>0.999	>0.999
0.999	0.999	0.998
0.998	0.997	0.996
0.985	0.983	0.980
0.976	0.974	0.969

Correlation coefficients		
Br	**Bt**	**Bp**
1.000	1.000	1.000
>0.999	>0.999	>0.999
0.999	0.997	0.997
0.997	0.993	0.992
0.977	0.969	0.964
0.962	0.954	0.946

Table 5.1: Solution parameters and model outputs for the global models with 10 km, 30 km and 50 km thickness with different damping parameters, from the three components of the spherical harmonic model data with 1° spacing. (Bold are the model solutions plotted in figure 5.5 and 5.6).

and the sum of squares of residuals (rather than the RMS magnetisation and the misfit) to give a 'knee' to curve. These trade-off curves give ideal damping parameters for these layer thicknesses between 5000 and 50,000, which highlights the subjectivity of the choice of the damping parameter.

The three component magnetisations and the total magnetisation produced at the surface for a model with 30 km thickness produced with damping parameters of 0, 10,000 and 50,000 are shown in figure 5.5. The magnetisations for the layers with 10 km and 50 km thickness show the same pattern of the magnetisation as the 30 km layer but with slightly higher amplitudes, showing that the magnetisation pattern, but not amplitude, is robust. The similarity between the differently damped models also shows that the magnetisation features in these models are very stable with respect to the damping parameter and the layer thickness. The solutions with zero damping show many smaller scale positive and negative features as the model attempts to fit all features of the data including noise.

As the damping parameter is increased, the magnitude of the magnetisation decreases and the smaller, perhaps unphysical (where noise is being fitted), features of the model are smoothed out. This is illustrated by looking close up at features in the model solutions in figure 5.6 which shows the three component magnetisations over the regions of Reiner Gamma and Descartes, and figure 5.7, a profile through the radial magnetisation component of the models for the Reiner Gamma region. Figures 5.6 and 5.7 show that while the magnetisation amplitudes do decrease with increased damping, the change in the magnetisation amplitude is by less than a factor of 3 for damping parameters from 0 to 100,000.

Figure 5.7 also shows the radial magnetic field, and small fluctuations in the field at the edge of the main feature (at about the noise level) can be seen. These fluctuations in the data may be the cause of the fluctuations of the radial magnetisation at the edge of the main feature. As the damping parameter is increased, the magnitude of the magnetisation reduces and the fluctuations in the magnetisation solution are smoothed out. The 'smoothing out' of the magnitude variations broadens the magnetisation feature slightly but it is always narrower than the signature it produces in the magnetic field.

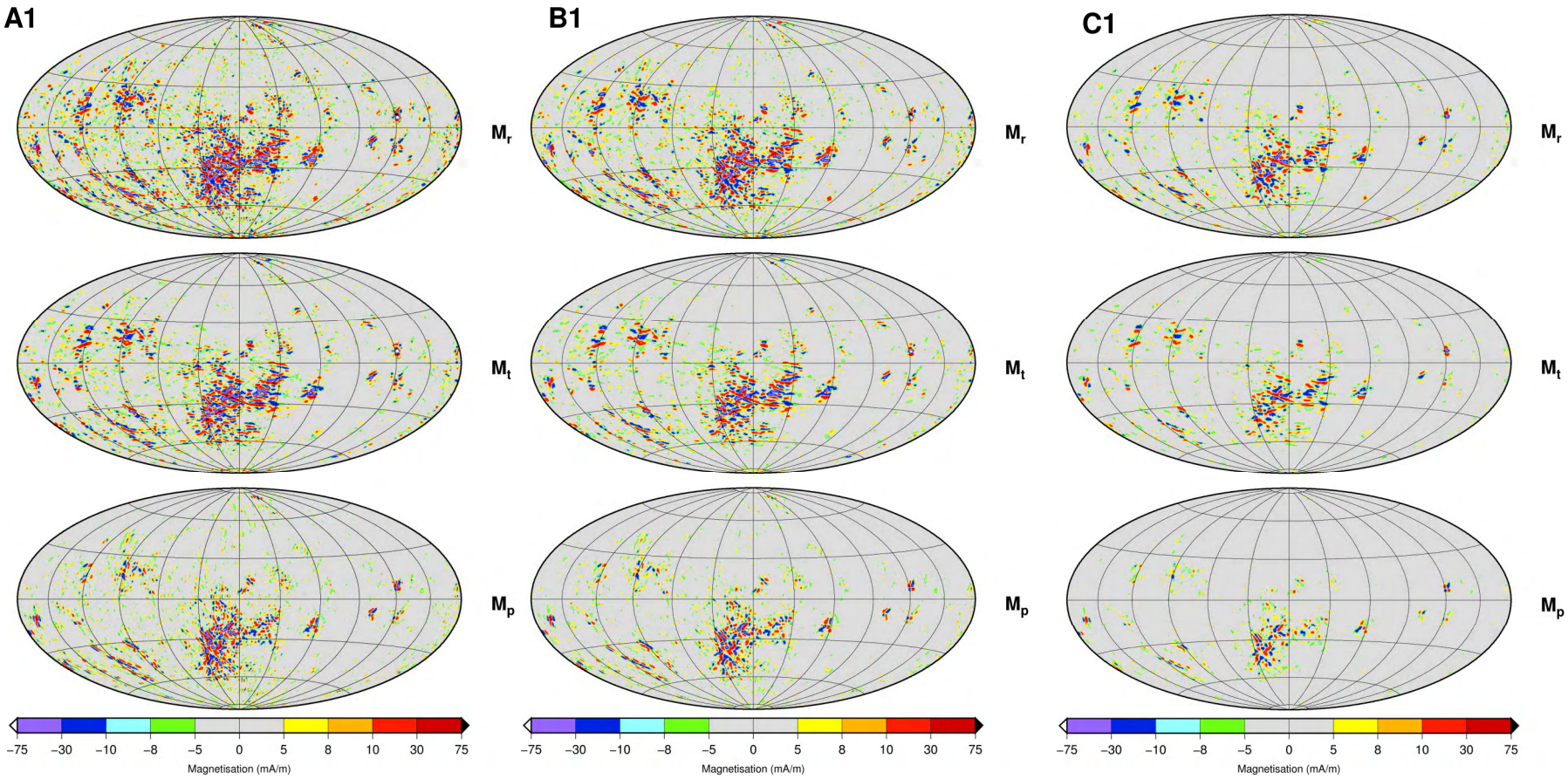

Figure 5.5, caption overleaf.

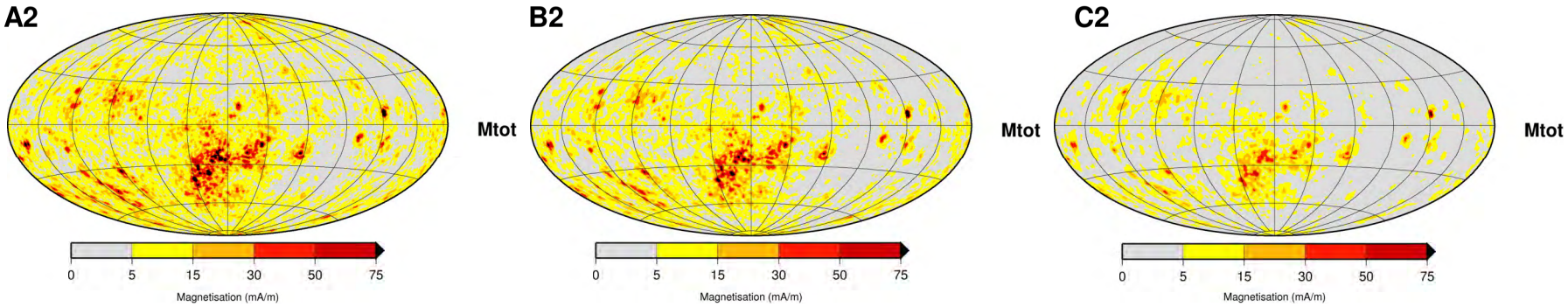

Figure 5.5: Three component magnetisations (1) and total magnetisation at the surface (2) for models with 30 km thickness from three components of the spherical harmonic data at 30 km altitude, with damping parameters A: λ=0, B: λ=10,000, and C: λ=50,000. Lambert projection centred on the far side, 0.5° gridded points.

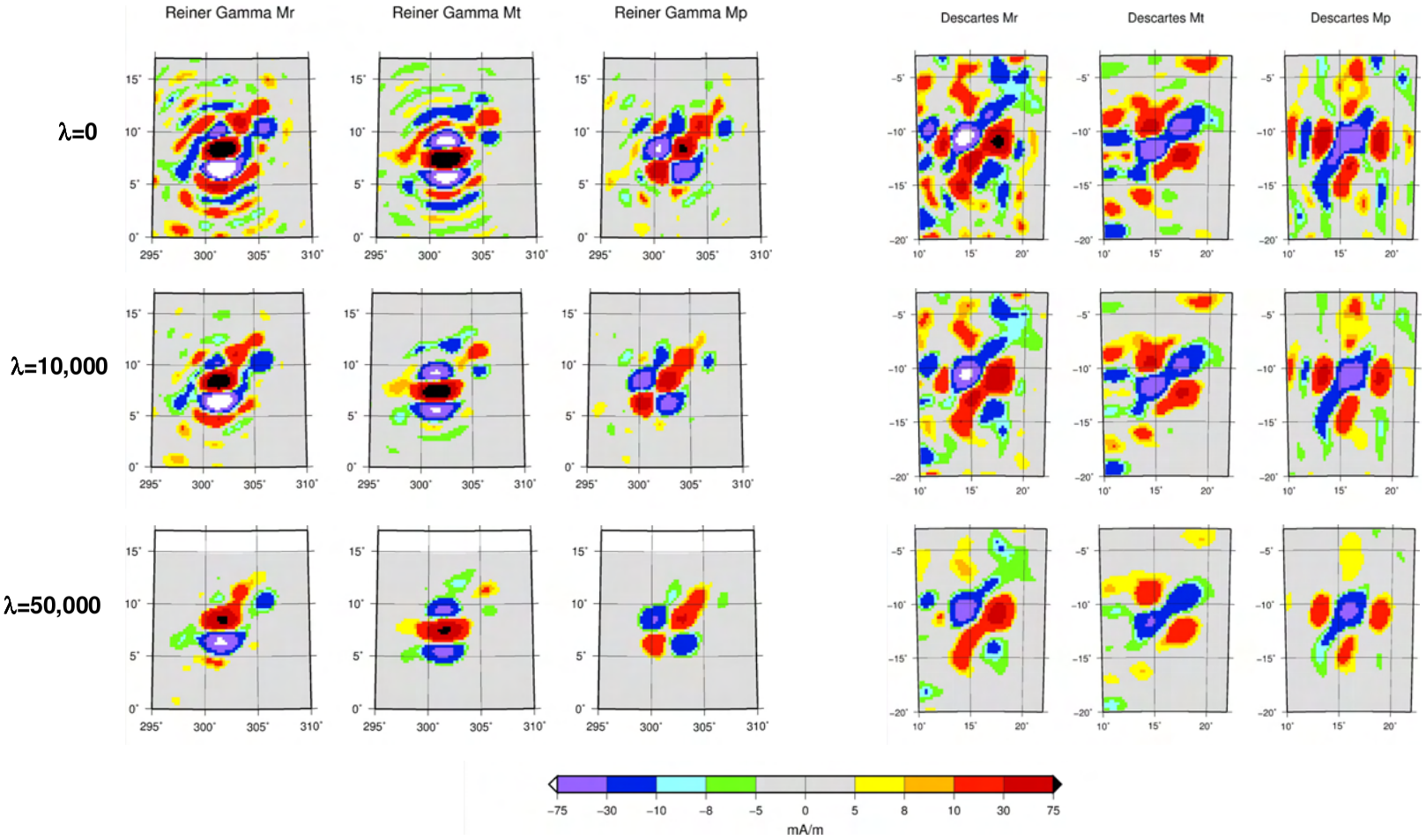

Figure 5.6: Three components of magnetisation at the surface for the regions of Reiner Gamma (left) and Descartes (right) for models with 30 km thickness from three components of the spherical harmonic data at 30 km altitude, with λ=0, λ=10,000 and λ=50,000. Lambert projection, 0.25° gridded points.

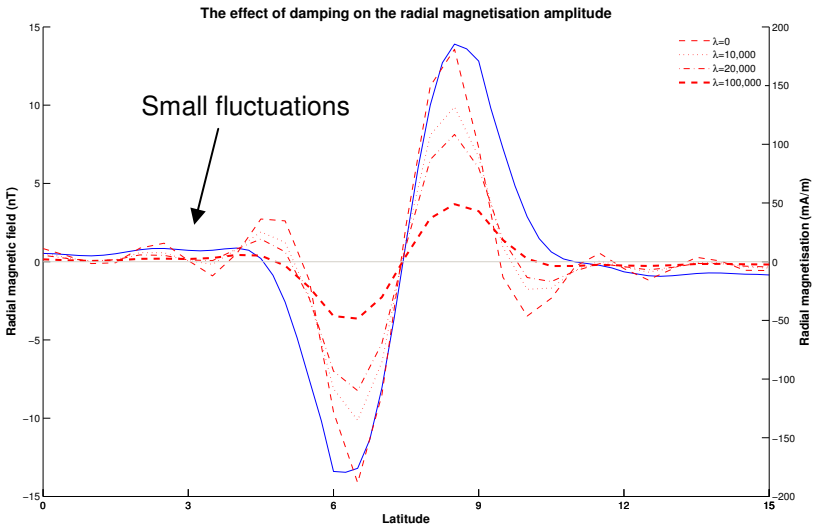

Figure 5.7: The radial magnetisation solution (red, dotted) for a profile over Reiner Gamma at longitude 301°, showing the effect of damping with damping parameters of 0, 10,000, 20,000 and 100,000. The radial field (blue, solid) is shown for the same profile.

5.4.2 The effect of damping on residuals

The smoothing out of magnitude variations the magnetisation solution with increased damping results in increased residuals between the model predictions and the input data. Histograms of the exact residuals for models with different damping parameters show the increase in the larger residuals for larger damping parameters (Figure 5.8). Some of the small residuals result from a mis-prediction of the sign of the component field which occurs for some regions of weak magnetic field. Residuals from all of these models have zero mean and are more strongly peaked and broadly flanked than a Gaussian distribution.

Profiles of the radial and total predicted field from damped models for the Reiner Gamma region in figure 5.9 show that as damping is increased, the anomaly in the predicted field is suppressed over the maxima but increased slightly over the edges of the anomaly feature. This results in the over prediction of the radial field at the edge of the main anomaly (Figure 5.9A), and a slight over prediction of the total field for lower damping parameters (Figure 5.9B).

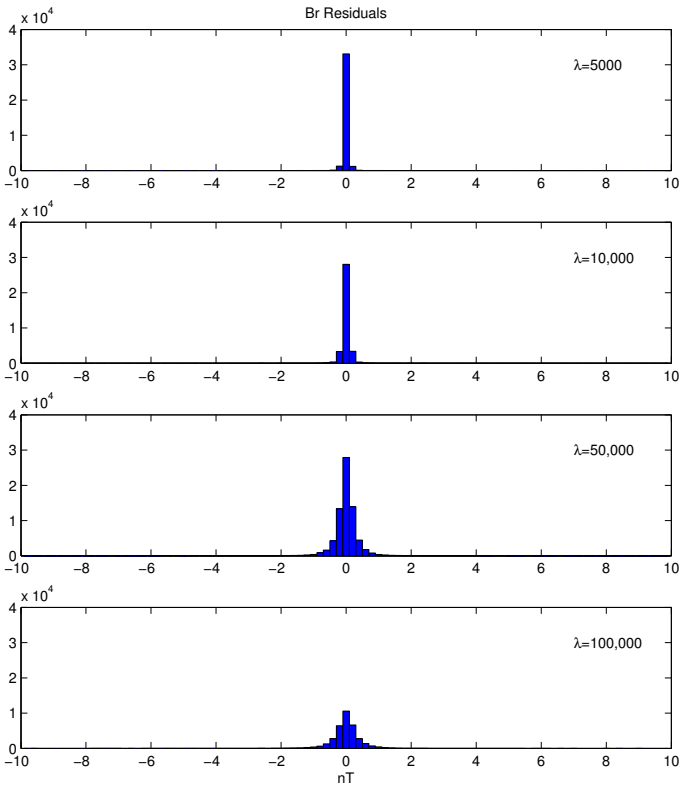

Figure 5.8: Histograms of the global exact residuals in the radial component of the field (predicted at 1° spaced locations) for a global model with 30 km thickness and damping parameters of 5000, 10,000, 50,000 and 100,000 from the three components of the spherical harmonic model data. Histogram bins are 0.2 nT. (Maximum residuals are ± 9.5 nT).

5.4.3 Selected model solutions

From the close up regions of Reiner Gamma and Descartes (Figure 5.6), the damping range from the trade-off curve of 5000-50,000 can be narrowed to 10,000-50,000 since the λ=10,000 solutions appear to still show less likely fluctuations and are hence 'underdamped'. However, increasing the damping parameter much more than this risks 'overdamping' the solutions and losing important magnetisation contrasts and hence the ability to reproduce the field. In addition, as the input data to these models from the spherical harmonic model is a minimum estimate of the field strength, this also favours less damping so as to not reduce the magnitude of the predicted field further.

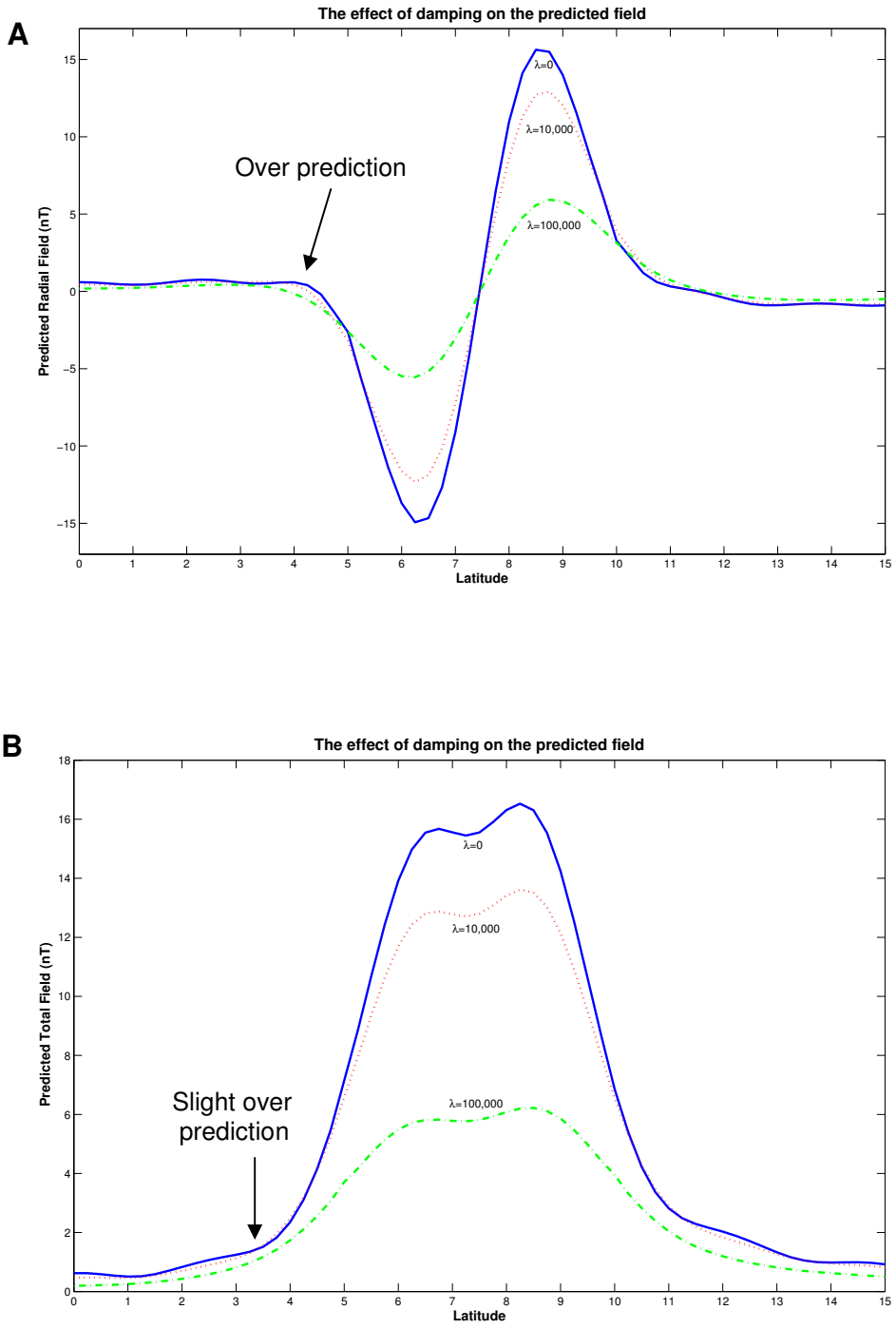

Figure 5.9: Profiles of A: The radial magnetic fields and B: the total magnetic fields predicted from models with damping parameters of 0 (blue, solid), 10,000 (red, dashed) and 100,000 (green, dot-dash), for the Reiner Gamma region at longitude 301.5° .

Looking at the misfit values for these models (Table 5.1), the damping range 10,000-50,000 produces models with misfits between ~0.1 and 0.4 nT depending on the thickness. To allow a comparison between models with different thicknesses (that are not too over or underdamped) a misfit of ~0.2 nT for each model thickness was achieved with λ=15,000 for the 10 km thick model, λ=20,000 for the 30 km thick model, and λ=16,000 for the 50 km thick model (Table 5.2). These models also have the same number of iterations despite their different damping parameters and thicknesses, and give very similar, and high, correlation coefficients. The total magnetisations for these models at the top and bottom of the layer, and the vertically integrated magnetisations are shown in figure 5.10. The spatially continuous magnetisation models also give magnetisation distributions similar in pattern and relative magnitude to the magnetic field components. The magnetisation amplitudes are also very similar to those produced from the equivalent source dipole models. Magnetisation solutions with the 30 km thick layer for the regions labelled in figure 2.3 can be found in Appendix 13.

5.4.4. The global distribution of residuals

Figure 5.11 shows the global distribution of the exact, absolute and normalised residuals for the components of magnetic field for the model with 30 km thickness and λ=20,000. These residuals are calculated as outlined in section 3.6. As expected, the largest residuals are on and around the strongest regions of magnetic field. The exact residual map is very similar to the magnetic field map, while the absolute residual map highlights that most, but not all, of the field is under predicted.

Thick. (km)	**Damp.** λ	**SSR** (nT^2)	**Norm** (A/m)	**Misfit** (nT)	**Iter.**	**VIM** (kA)	**Correlation coefficients** **Br**	**Bt**	**Bp**
10	15000	4581.43	1991.09	0.207	14	0.0936	0.997	0.997	0.996
30	20000	4227.49	1637.96	0.198	14	0.1390	0.994	0.993	0.991
50	16000	4163.61	1761.11	0.197	14	0.2077	0.993	0.989	0.986

Table 5.2: Solution parameters and model outputs for the chosen global models with 10 km, 30 km and 50 km thickness, from three components of the spherical harmonic model data.

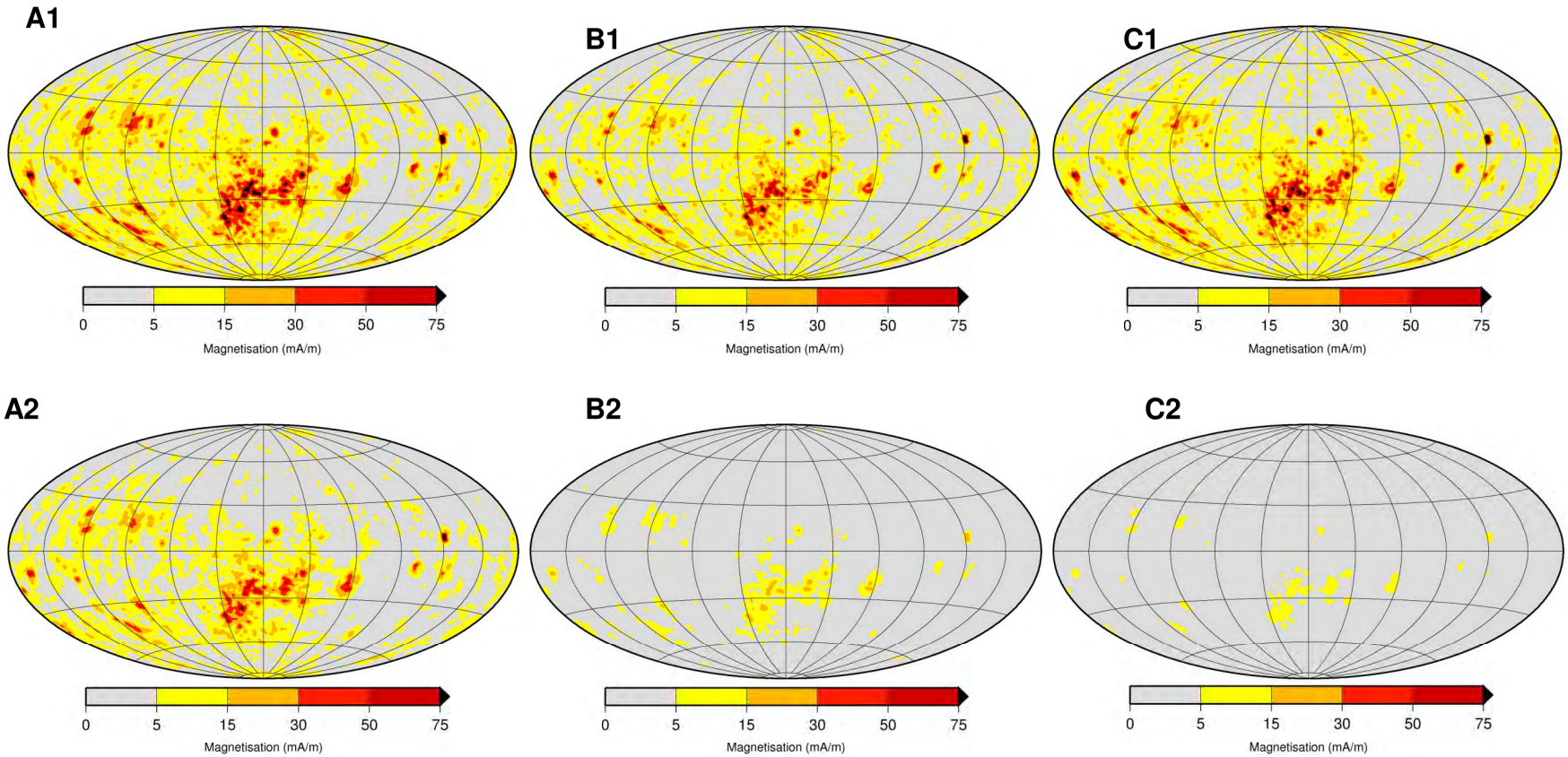

Figure 5.10, caption overleaf.

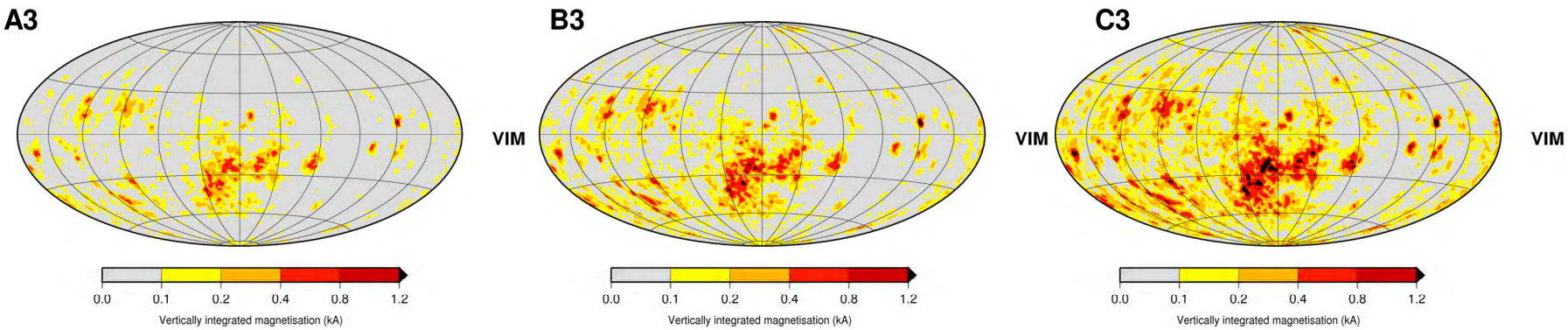

Figure 5.10: The total magnetisations at the surface (1) and at the base of the magnetised layer (2), and the vertically integrated magnetisation (3) for models with A: 10 km thickness and, λ=15,000, B: 30 km thickness and, λ=20,000, and C: 50 km thickness and, λ=16,000, from three components of the spherical harmonic model data. (Lambert projection centred on the far side, 0.5° gridded points).

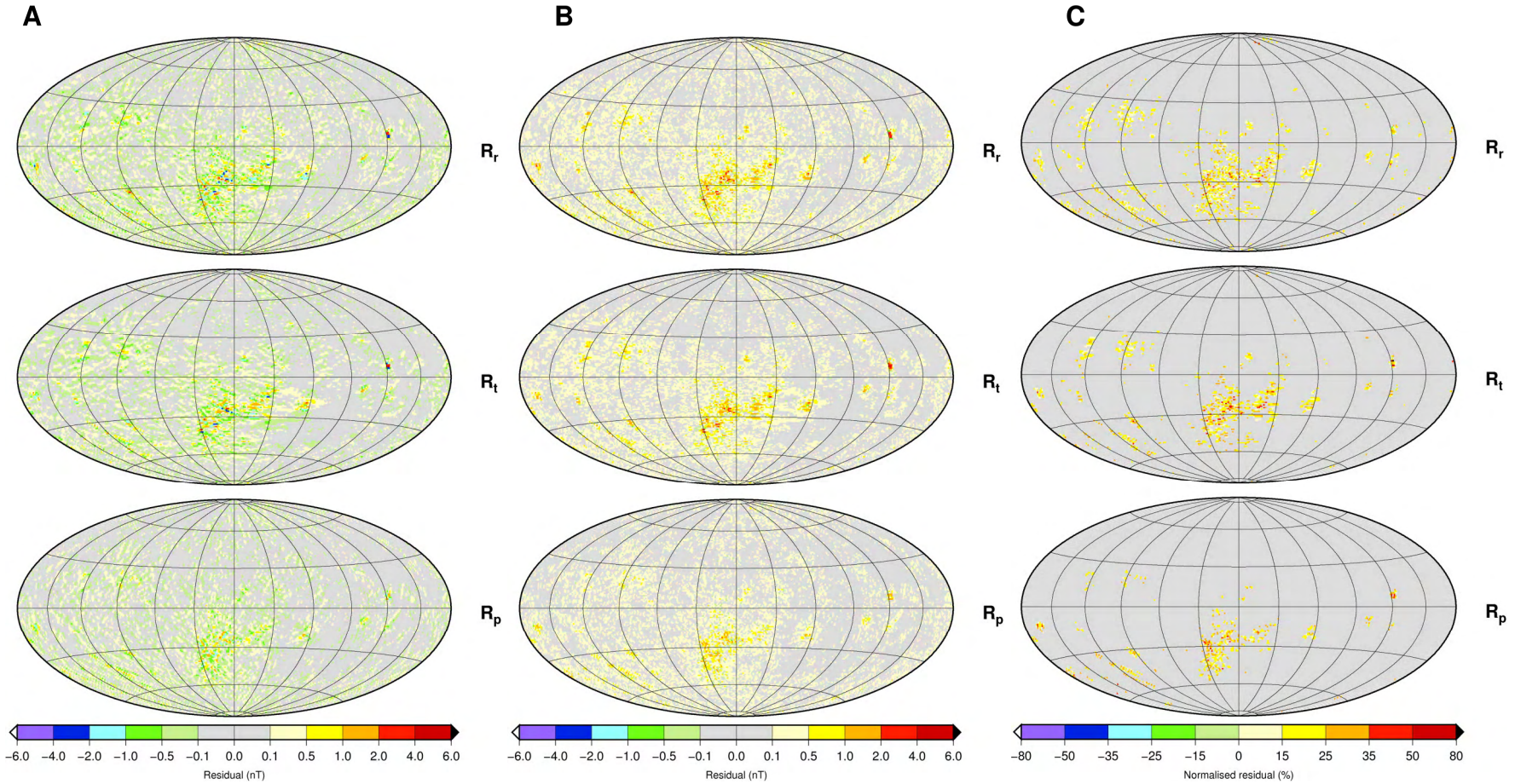

Figure 5.11: A: Exact residuals, B: Absolute residuals and C: Normalised residuals (grey where the total field < 2 nT), for the three components of magnetic field for a model with 30 km thickness and λ=20,000 from the three components of spherical harmonic model data (residuals at 1° spaced locations, lambert projection centred on the far side).

The predicted magnetic field exceeds the measured magnetic field (negative absolute residual) close to the strongest anomalies, as observed for the Reiner Gamma region in figure 5.9A.

For the selected damping parameters for the models with 10 km, 30 km and 50 km (Table 5.2), the global distribution of residuals is very similar. However, histograms of the component residuals for the 10 km, 30 km and 50 km thick models (Figure 5.12) show differences in the distributions of the residuals, with more small residuals in the model with 10 km thickness, and larger residuals in the model with 50 km thickness, despite these models having the same total misfit.

5.4.5. The effect of thickness on the model solution

As the damping parameter used in the inversion affects the model solution norm and SSR, when discussing the effect of the thickness of the layer it must be with respect to a constant value in another parameter. The effect of thickness is discussed with respect to models with the same damping parameter, the same VIM and the same global misfit. The pattern of the magnetisation solution however is stable with respect to the model thickness.

The same damping parameter

For models with the same damping parameter there are general trends which can be observed from table 5.1: Thinner layers require more iterations to converge to a solution because they retain fewer elements above the threshold. The threshold for the model with the thinnest layer (5 km) had to be decreased to 0.5 to give convergence within the maximum 500 iterations.

The 10 km layer also shows a higher solution norm for the same damping parameter, though the distinctions between the solution norms for each model is less apparent as the damping parameter increases, emphasising the loss of magnetisation information when a solution is heavily damped.

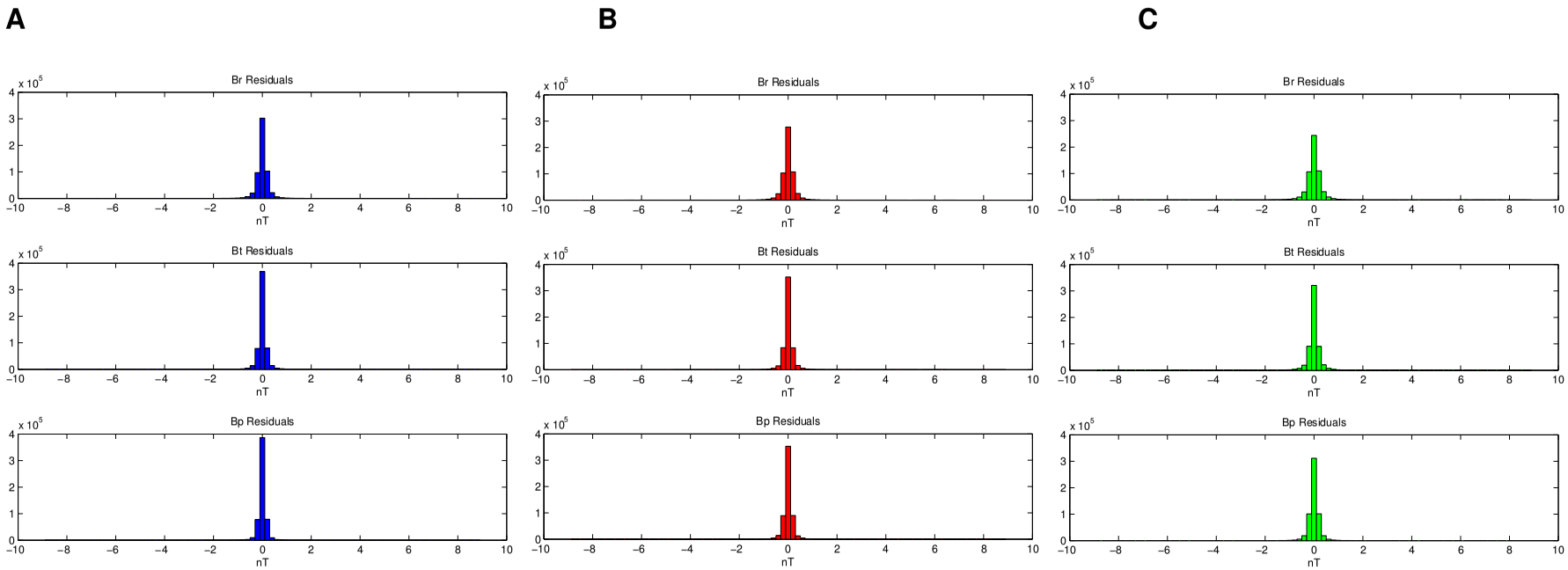

Figure 5.12: Histograms of component exact residuals (at 0.25° spacing) for models with A: 10 km thickness, λ=15,000, B: 30 km thickness, λ=20,000, and C: 50 km thickness, λ=16,000, from the three components of spherical harmonic model data. Histogram bins are 0.2 nT. (Maximum residuals are ± 9.5 nT).

The 'middle thickness' model, of 30 km, has the lowest norm and SSR for most damping parameters (table 5.1 and figure 5.4), suggesting a layer greater than 10 km but less than 50 km thick can provide the best fit to the magnetic field observations globally. This is in agreement with the spectrally derived average global thickness. However, it is not expected that all the magnetised regions will have the same thickness so there are likely to be regions over the globe which can be better described by thinner or thicker layers of magnetised crust (for example the thicker crust of the lunar farside may have thicker sources).

Figure 5.13 shows the variation in the misfit with the layer thickness for the same damping parameter. While the broad minima also suggests a preference for a layer 20-40 km thick, the variation in misfit for layers thicker than 10 km is not significant compared to the expected noise level in the data. The increase in the misfit with the thinnest layers in figure 5.13 may be due to lack of information retained in these models (due to the small values of the Gram matrix) or may be a sign of instabilities in the computations with very thin layers. This observation places a lower limit of layer thickness for spatially continuous magnetisation models of the Moon at ~10 km.

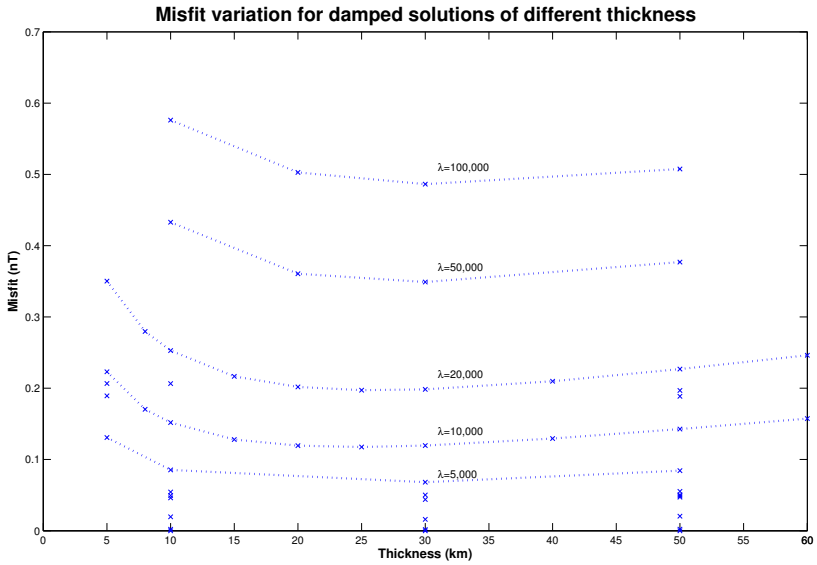

Figure 5.13: Variation in misfit with layer thickness for global models with the same damping parameter. (Points for smaller damping parameters with layer thicknesses of 5 km, 10 km, 30 km and 50 km not joined up).

The same vertically integrated magnetisation

The vertically integrated total magnetisation and the RMS VIM (in units of kA) was calculated from magnetisations produced at 6 different depths for the selected models with 10 km, 30 km and 50 km thickness and different damping parameters. The damping parameter was adjusted to produce models with the same (within ~3 %) RMS VIM of 0.1 kA for each of the three thicknesses (Table 5.3). Even with different solution norms and fits to the data, the distribution of VIM for each of these thicknesses is very similar. In this case it is the thinnest layer with the lowest misfit and highest correlation coefficients, although the 10 km model uses the lowest damping parameter. While the thickness of the layer may not be very well constrained, the similarity between the VIM maps for each thickness shows that the VIM, and hence the spatial extent of magnetisation, is robust, as observed already.

The same misfit

The model outputs for each model thickness which have the same global misfit are shown in table 5.2 and their magnetisations plotted in figure 5.10. The surface magnetisations and the VIM distributions are slightly different. The surface magnetisations are stronger for models with 10 km and 50 km thickness, and the sources in the VIM distribution are slightly broader and stronger for the 50 km thick model. Close ups of the magnetisation over the Reiner Gamma region (Figure 5.14) show some differences in the strengths and distribution for each thickness, but the extent of the main feature is very similar in each.

Thick. (km)	**Damp.** λ	**SSR** (nT^2)	**Norm** (A/m)	**Misfit** (nT)	**RMS VIM** (kA)	**Correlation coefficients** **Br**	**Bt**	**Bp**
10	10000	2475.23	2161.91	0.152	0.1027	0.998	0.998	0.998
30	50000	13087.66	1245.78	0.349	0.1053	0.985	0.983	0.980
50	100000	27672.58	892.62	0.508	0.1026	0.962	0.954	0.946

Table 5.3: Solution parameters for differently damped models with 10 km, 30 km and 50 km thickness with the same VIM.

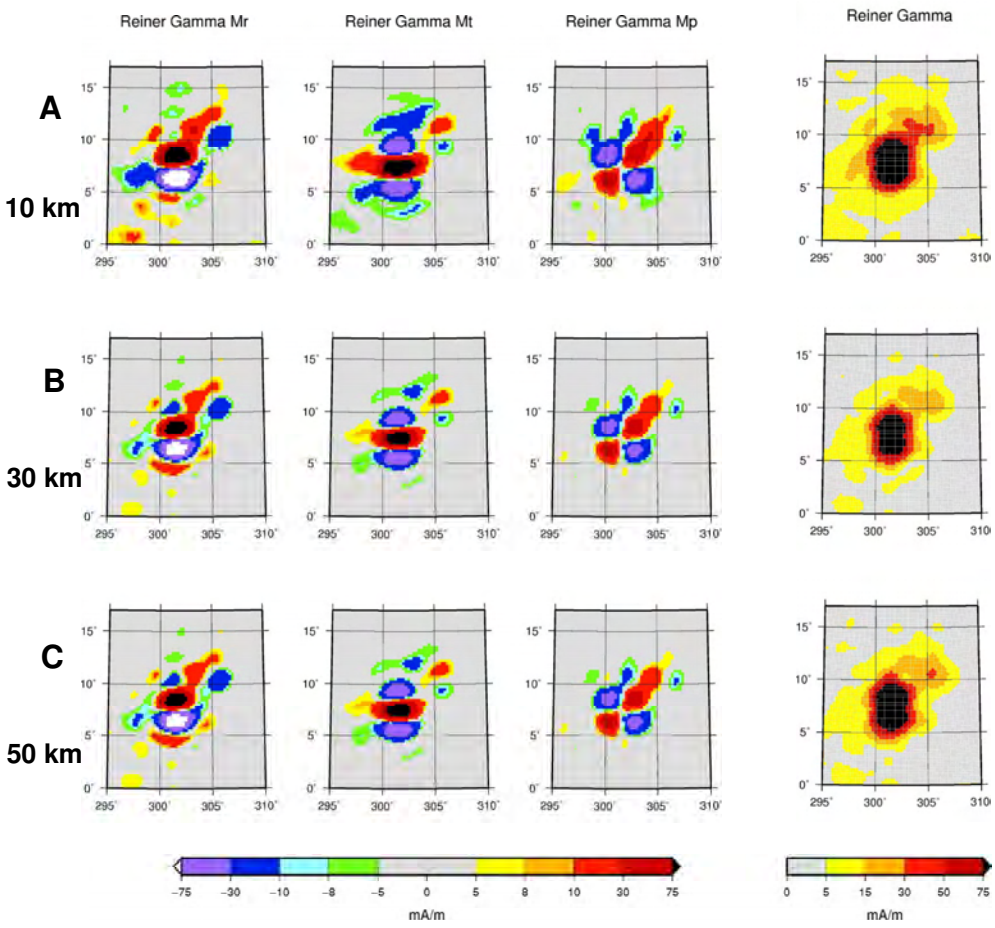

Figure 5.14: Three component and total magnetisations at surface for the Reiner Gamma region from global models with A: 10 km thickness, λ=15,000 B: 30 km thickness, λ=20,000, and C: 50 km thickness, λ=16,000. Lambert projection, gridded 0.25°.

While the differences in the magnetisation distributions will to some extent be related to the different damping parameters, the fact that these different distributions result in the same misfit means they can be compared in an attempt to determine which model thickness is better at reproducing the observed magnetic field. The predicted components of the magnetic field at 30 km altitude, and the absolute residuals for the three different thickness models for the Reiner Gamma region, are shown in figure 5.15. The main features of the field are predicted very well, but none of the models can reproduce the correct profile for the strongest regions of the magnetic field. The predicted features are spread out slightly with

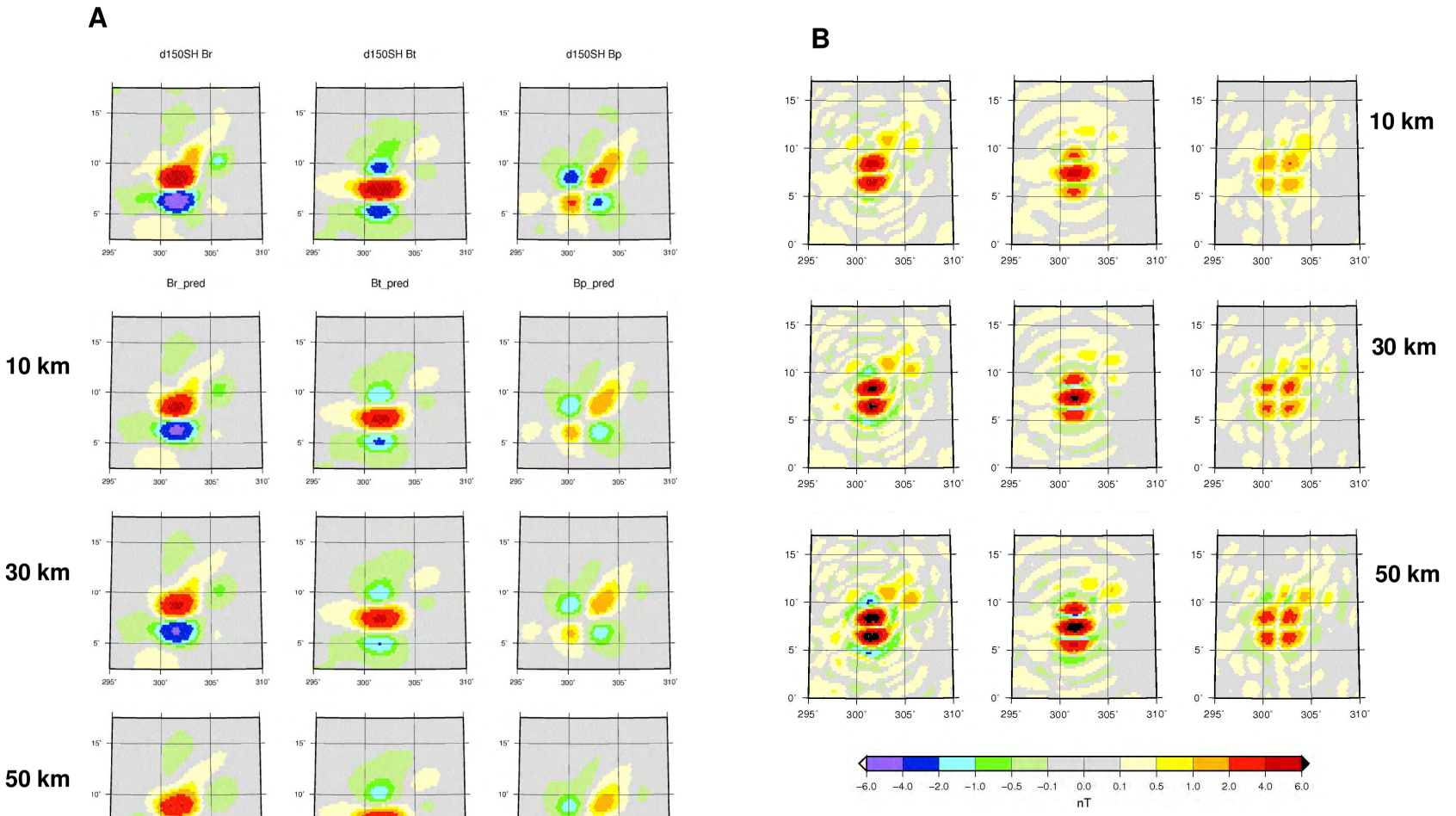

Figure 5.15: A: The components of the spherical harmonic model at 30 km altitude (top) and their predictions, and B: absolute residuals (on 0.25° grid), from global models with 10 km, 30 km and 50 km thickness. Note the slight difference in latitude coverage of figures A and B.

respect to the observed feature, resulting in the over prediction of the magnetic field components at the edge of the feature (shown by the negative absolute residuals).

Of the three selected model thicknesses, it is the 10 km thick model which gives the smallest residuals over the Reiner Gamma region and is hence better at producing the main features of the observed magnetic field. Lower residuals with the 10 km thick model and higher residuals with the 50 km thick model are also observed in most of the other regions of strong magnetic field labelled in figure 2.3, though some regions showed very little variation in residual distribution with the model thickness. The 10 km thick layer also requires the lowest damping parameter to give the same fit to the data.

5.4.6. Magnetisation variation with depth

The representation of magnetisation as a linear combination of Green's functions (equation 5.5) means that the magnetisation strength will decrease with depth from the surface, as observed in figure 5.10. The pattern of magnetisation remains constant with depth with the amplitude decreasing. The decrease with depth, shown in figure 5.16 for different magnitude surface magnetisations (in the Reiner Gamma region) depends on the location, the surface strength and the layer thickness.

While satellite observations are not expected to be able to resolve depth information, the low LP altitude of 30 km may allow some indication of the depth of sources. The difference in magnetisations for the top and bottom of the magnetised layers shown in 5.10 seems to suggest that the magnetised regions extend deeper than 10 km, but not quite as deep as 30 km for most regions. A cross section showing magnetisation with depth in the Reiner Gamma region for models with different thicknesses (Figure 5.17) shows the main magnetised region extending deeper than 10 km but not quite as deep as 30 km.

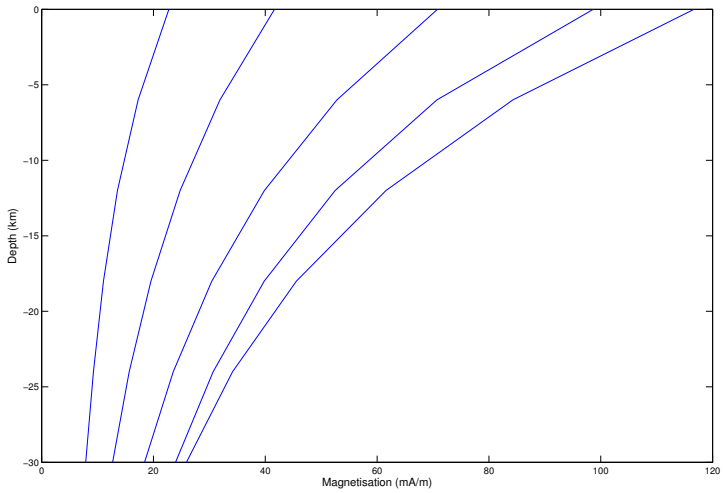

Figure 5.16: The decrease in magnetisation with depth in global magnetisation models for points with selected surface magnetisations (in the Reiner Gamma region) for the model with layer thickness 30 km and λ=20,000.

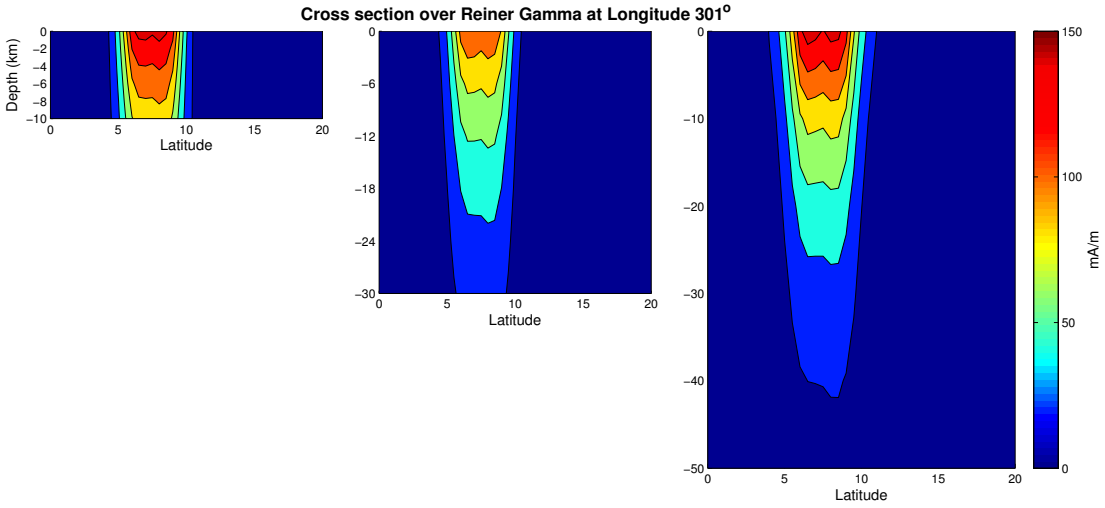

Figure 5.17: Cross sections showing magnetisation with depth at longitude 301° for the Reiner Gamma region for the models with 10 km thickness and λ=15,000 (left), 30 km thickness and λ=20,000 (centre) and 50 km thickness and λ=16,000 (right). Contours are 20 mA/m.

5.5. Surface predictions from the continuous models

The selected models with thicknesses of 10 km, 30 km and 50 km and damping parameters of 15,000, 20,000 and 16,000 respectively were used to predict the total surface magnetic field. Predictions of the 1°×1° binned ER data (binned and smoothed from predictions at the locations of the unbinned ER data) give very good agreement spatially with the ER observations (see figure 5.18 for the predictions from the 10 km thick model), with each model thickness giving the same correlation coefficient with the ER data (to 3 significant figures) of 0.639. However, the predictions under predict the strongest estimated total surface fields and over predict the weaker field regions, as observed with the surface predictions from the spherical harmonic model of the lunar crustal field (see section 2.7). The global misfits for the 1°×1° surface field predictions from the models with thicknesses of 10 km, 30 km and 50 km are high at 16.5 nT, 17.0 nT and 17.2 nT respectively.

On a regional scale, the surface predicted data show better spatial agreement in some regions more than others (Figure 5.19), for reasons discussed in section 2.7. For example, while the predicted field at altitude for the Reiner Gamma region shows excellent spatial agreement with the observations, the surface predictions for this region do not reproduce the observed distribution (Figure 5.19A). However, other regions, like the two anomalies near the Nectaris antipode, do show good spatial agreement with the ER data (Figure 5.19B).

The regional maps of the predicted surface field for different thickness models also show that in most regions the 10 km thick layer is better at fitting the ER observations, though the distinction is less obvious in some regions. The ER predictions from the 10 km thick layer for the regions labelled in figure 2.3 are given in Appendix 14.

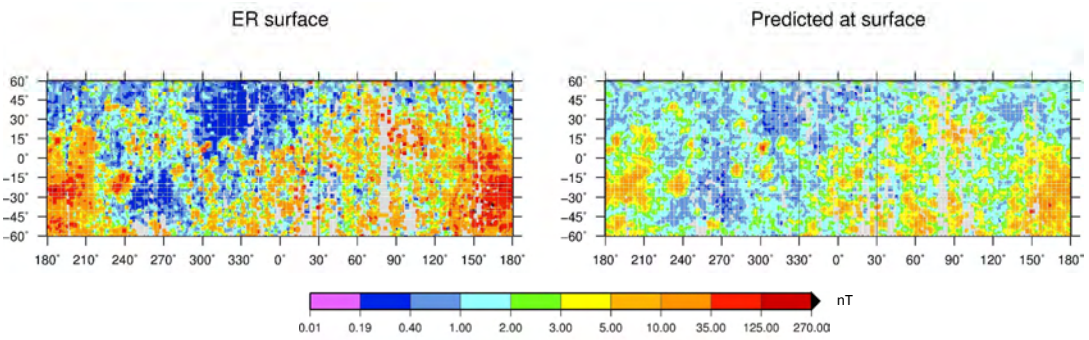

Figure 5.18: Comparison of the 1°×1° binned ER data (left) with the surface total field predictions at the same locations (right) from the global model with 10 km thickness and λ=15,000, for mid latitude regions. (Grey represents the absence of data.)

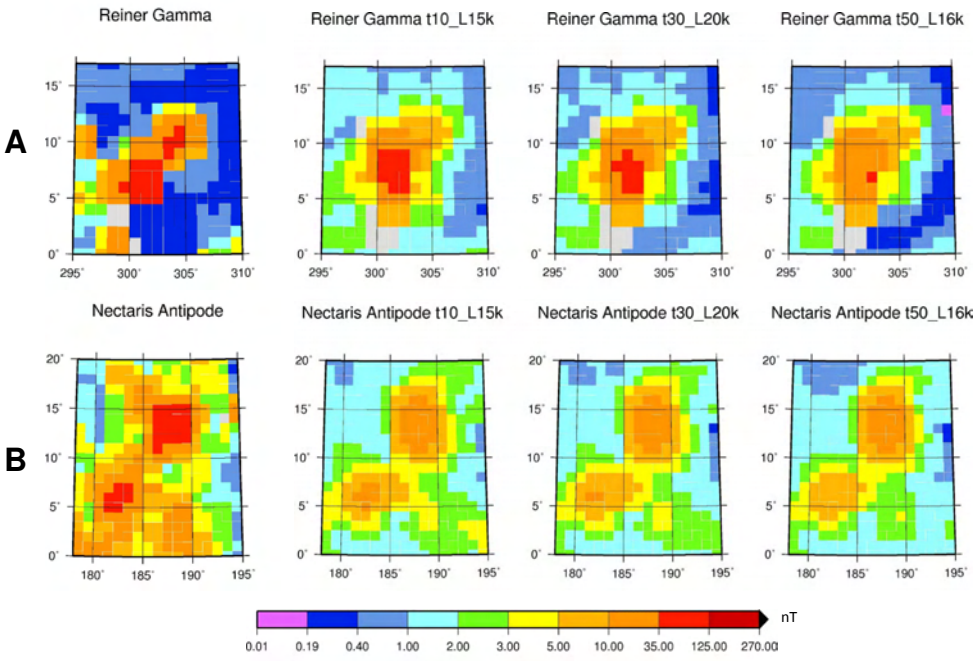

Figure 5.19: Comparison of the 1°×1° binned ER data (left) with the surface total field predictions from the models with 10 km thickness λ=15,000, 30 km thickness λ=20,000, and 50 km thickness λ=16,000 for A: the Reiner Gamma region and B: the anomalies near to the Nectaris antipode.

5.6. Magnetisation models from the radial magnetic field data

Use of the radial magnetic field data from different lunar regimes and on different polar coordinate subdivided grids allows the stability of the magnetisation solutions with respect to the 'cleanliness' of the input data to be assessed. These data still retain unsmoothed information from the satellite pass (unlike the spherical harmonic representation), and though altitude normalised, show different magnitudes depending on the initial pass altitude due to upward and downward continuation.

These models use 0.5° spaced data and a model layer thickness of 30 km (again with threshold of 1.5, retaining 3% of the matrix elements). Higher damping parameters than used for the models from the spherical harmonic input data were required to give sufficiently damped solutions. Table 5.4 shows the solution parameters and model outputs for damped models from radial data from all lunar regimes and from the wake and tail regions. The variability in the (non-smoothed) input data results in higher misfits and higher norms than the models produced with the spherical harmonic data, more so with the data from all the lunar regimes which contain more noise. The model outputs from the input data on the shifted grid were almost the same (to within 1 %) but the magnetisation solution distributions on a global and regional scale showed visible differences. These differences highlight an instability with respect to the selection of these unsmoothed data values, especially when utilising data from all lunar regimes, and allow an upper estimate of the intrinsic model uncertainty.

Data	Damping λ	SSR (nT^2)	Norm (A/m)	Misfit (nT)	Iterations
All regimes	20000	53308.66	2373.126	0.6104	20
	50000	80280.82	1381.397	0.7490	14
	100000	97862.51	917.9567	0.8270	11
Wake and tail only	50000	50427.34	1639.351	0.5937	15
	100000	69878.77	1239.134	0.6988	11

Table 5.4: Solution parameters and model outputs for differently damped models with layer thickness 30 km, produced from the radial magnetic field component in all lunar regimes and from wake and geomagnetic tail regions only.

5.6.1 Magnetisation solutions for the Reiner Gamma region

The magnetisation solutions for the Reiner Gamma region from the global model with the radial component of the magnetic field from all regions and from the wake and tail only are shown in figure 5.20. The use of the original crustal field data rather than the 'smoothed' data predictions from a spherical harmonic model gives more detail at the edges of the magnetised region, but the magnitudes and the patterns of these magnetisations are very similar to the solution from spherical harmonic data. There is also excellent agreement with the model solution from the equivalent source dipole technique for the Reiner Gamma region (see figure 4.34). However, the solution from the data from all regimes is smaller in extent and is missing the north-east extension of the main feature. This results from the 'suppression' of the magnetic field when in the solar wind [Purucker, 2008] and justifies the use of only the wake and tail data in magnetisation modelling.

5.6.2 Predictions and residuals

Figure 5.21 shows the radial magnetic field data from the wake and tail for the Reiner Gamma region, and predictions of this data and the absolute residuals from the damped model solutions. The variability in the input data accounts for the required high damping parameters and the reduced ability of the solution to be able to reproduce the input data. However, the prediction of the total surface magnetic field at the 1°×1° binned ER data points (Figure 5.22) shows a better fit to the observed shape of the surface feature than predicted from the magnetisation solutions from the spherical harmonic data. This supports the use of the original crustal field data for magnetisation modelling, rather than the data predictions from a spherical harmonic model.

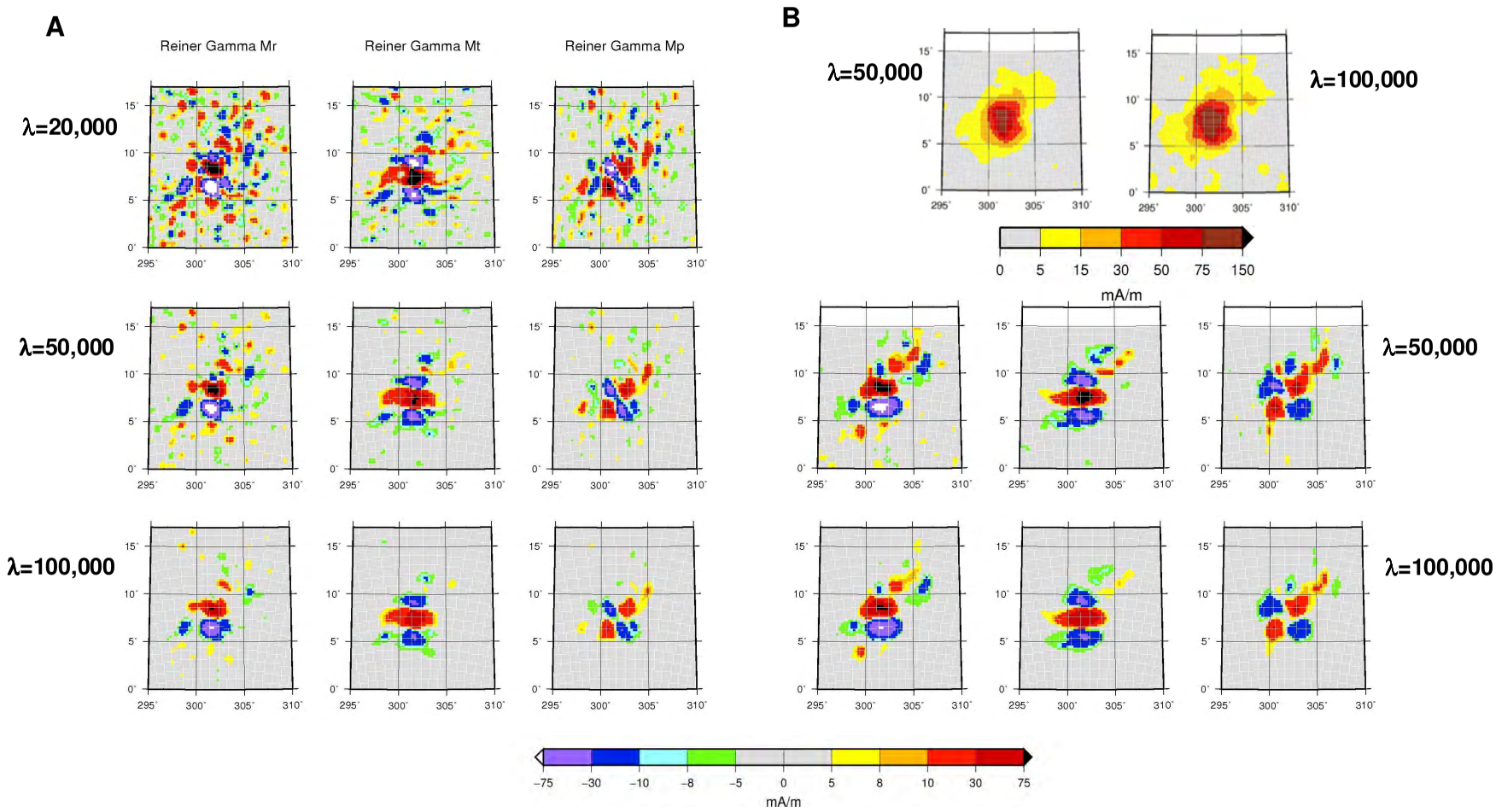

Figure 5.20: Three component (and total) magnetisations at the surface from global magnetisation models, for the Reiner Gamma region from 0.5° spaced radial magnetic field data at 30 km altitude with a 30 km thick layer and damping parameters of λ=20,000, λ=50,000 and λ=100,000 for data from A: all lunar regimes and B: wake and tail regions only (Note different latitude coverage on some figures). (Lambert projection, 0.25° gridded points).

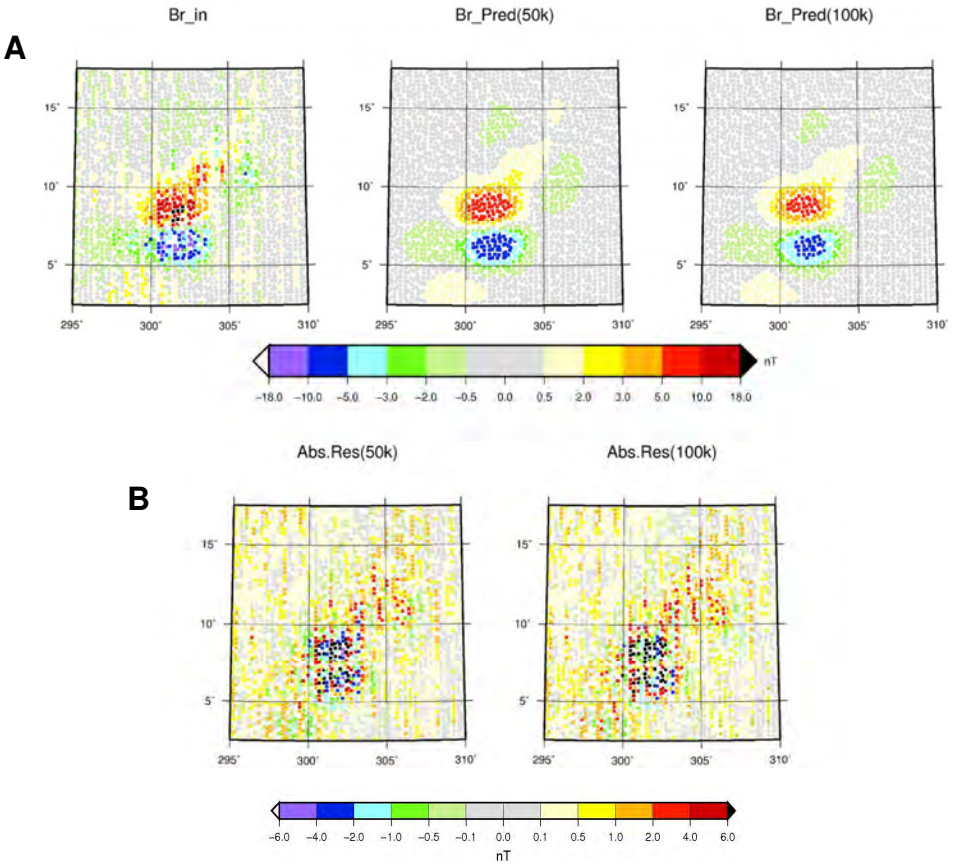

Figure 5.21: A: The input radial magnetic field at 30 km altitude for the Reiner Gamma region (left) and the predictions of this data from global models with layer thickness 30 km and damping parameters of λ=50,000 (50k) and λ=100,000 (100k), and B: the absolute residuals of these data. Note: As pass-by-pass data locations are plotted, grey represents low fields and white gaps are the absence of data.

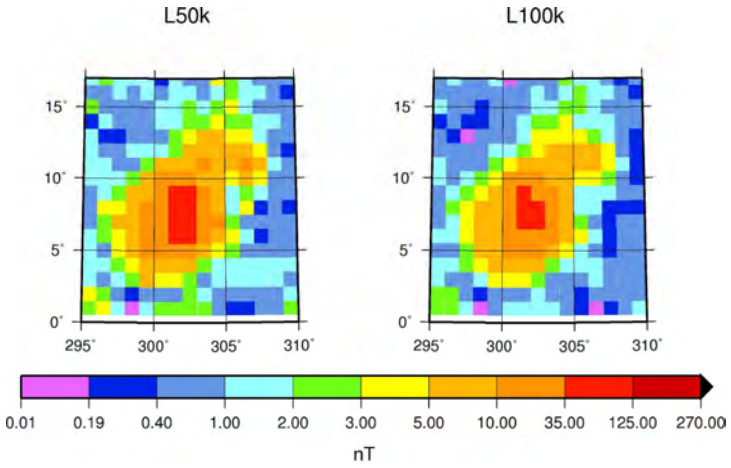

Figure 5.22: The predicted total surface magnetic field at the 1°×1° ER locations in the Reiner Gamma region from global models with wake and tail data and damping parameters of λ=50,000 (50k) and λ=100,000 (100k) and thickness 30 km.

5.7. Discussion of the continuous magnetisation models

This chapter has presented a range of solutions produced with different damping parameters and different crustal thicknesses. The amplitude and distribution of the crustal magnetisation remains considerably robust for a range of damping parameters and thicknesses, despite this model having no horizontal boundaries. The model solutions from differently processed data sets are also similar. Differences in the magnitude of the magnetisation solution occur with thinner layers, and with less damped models having stronger magnetisations. However, the magnetisation amplitudes for the suite of models with different thicknesses and damping parameters only differ by a factor of < 4, indicating stability in these model inversions, allowing a reasonable estimate of the likely lunar crustal magnetisations. This is unlike the spatially continuous models for the Martian crust which saw the RMS magnetisation vary by a factor of 20 for models with misfits different by only a factor of 2 [Whaler and Purucker, 2005].

The global nature of this model and the subtle differences between the models with different thicknesses make a choice of preferred layer thickness difficult. For the purposes of discussing the spatially continuous magnetisation models for the global lunar crust, the preferred solution is for a layer of 30 km thickness with damping parameter 20,000 shown in figure 5.23 (though regionally, thinner layers may be more suitable). Magnetisation solutions for the regions labelled in figure 2.3 can be found in Appendix 13.

5.7.1. Magnetisations

The maximum surface crustal magnetisations for the preferred solution are ± 120 mA/m, but these and other strong values of magnetisation are in localised regions only, where the maximum fields are observed. The average surface magnetisation is very weak at 5.4 mA/m, while the crustal average is 4.86 mA/m. The magnetisations in the radial direction are the strongest, and the magnetisations in the theta direction are the weakest. An upper value of the uncertainty in the model

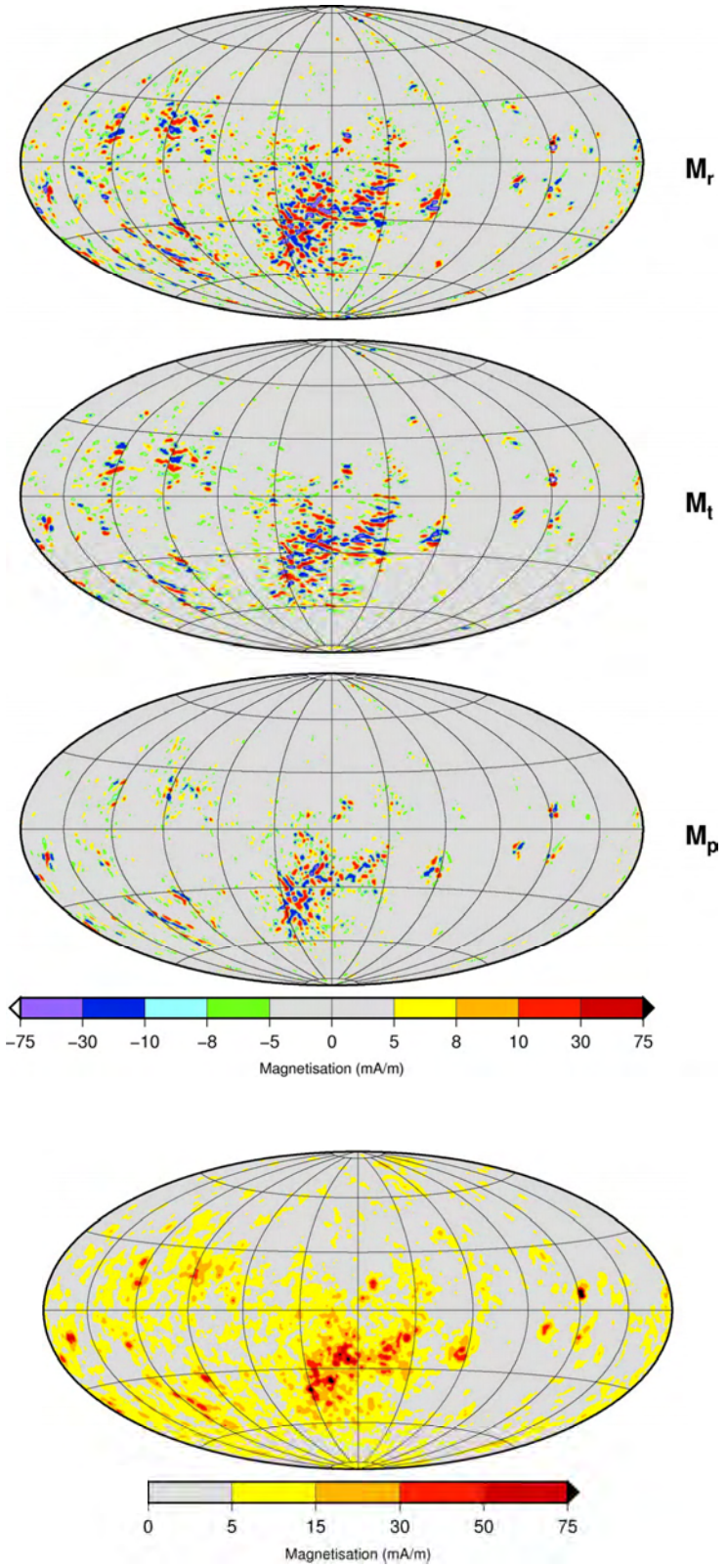

Figure 5.23: Three component and total magnetisations at the surface for the preferred global magnetisation model (with 30 km thickness and λ=20,000) from the three components of the spherical harmonic model data at 30 km altitude. Lambert projection centred on the far side, 0.5° gridded points.

parameters can be estimated from the differences between the magnetisation solutions produced when the input data grid was shifted. For the Reiner Gamma region, the maximum differences are 20-25 mA/m for the largest values of magnetisation, with a mean difference of ~ 4 mA/m for regions with magnetisation > 5 mA/m. The largest uncertainties are comparable to those estimated for the Reiner Gamma region using the covariance matrix for the equivalent source dipole technique.

The minimum norm magnetisation solution takes the same structure as the input magnetic field data (compare figure 5.23 with figure 2.5), though the exact details are not the same, as shown in figure 5.7. This means that although the magnetisation directions are robust, they are unlikely to be realistic. However, the distribution and amplitudes of the total magnetisation are likely to be related to the sources.

5.7.2. Inclinations and declinations

Despite the uncertainty in the component magnetisation direction, it is interesting to calculate values of inclination, I and declination, D (equations 1.5). As equations 1.5 involve ratios, if the component values of magnetisation are very small, values for I and D become unstable. Inclinations and declinations are only calculated for locations where the total magnetisation > 5 mA/m. Figure 5.24 shows the inclinations and declinations, where they are well defined, of the preferred global magnetisation model (with inset for the Reiner Gamma region). The inclination angles are very high and show rapid 'striping' from positive to negative. This may be due to the stronger values of radial magnetisation relative to the theta and phi magnetisations since high values of inclination will occur when

$$\left| \frac{-M_r}{\sqrt{M_\theta^2 + M_\phi^2}} \right| > 1 \ . \qquad (5.14)$$

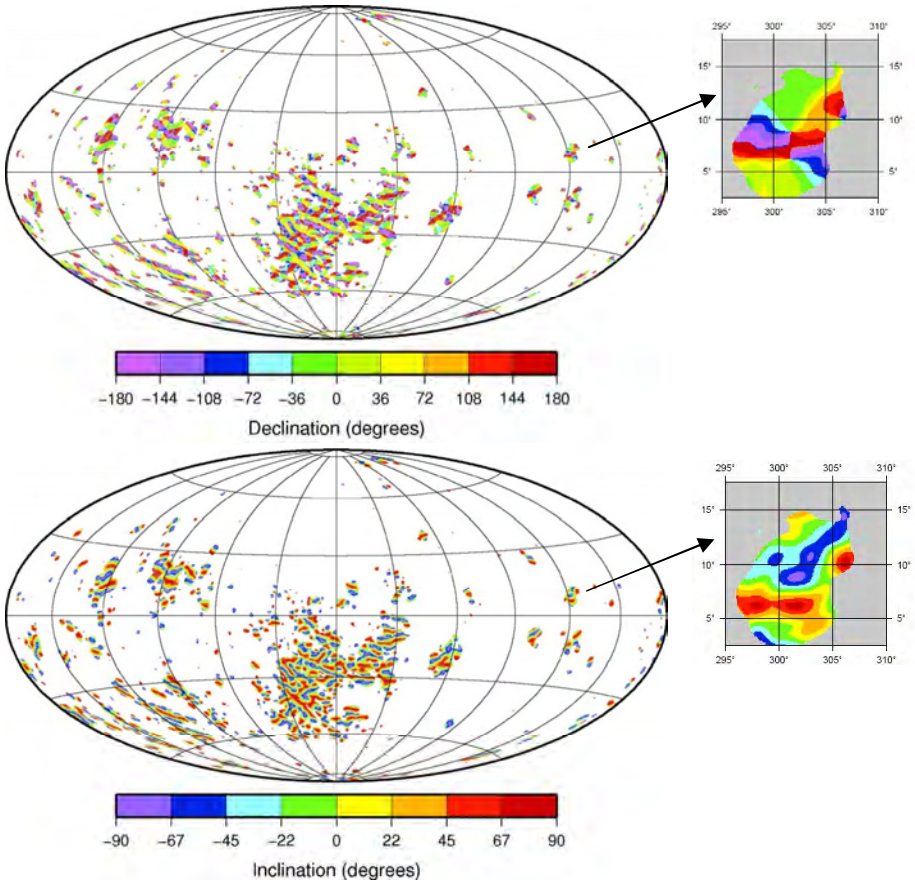

Figure 5.24: The inclination and declination of the surface magnetisation (where the total magnetisation > 5mA/m) for the preferred global magnetisation model (with 30 km thickness and λ=20,000), with inset for the Reiner Gamma region, from the three components of the spherical harmonic model data at 30 km altitude. Lambert projection centred on the far side, points at 0.25° spacing.

High inclinations affect the reliability of the declination angle, resulting in a 'sweeping' of the declination angles over a small region. While it is tempting to interpret the coherent and interesting patterns of the inclination and declination angles, magnetisation directions from minimum norm magnetisation models are unlikely to bear relation to the directions of the magnetising fields. The high inclinations and larger radial magnetisations might be a consequence of the use of the radial component of the field only in the production of the spherical harmonic model of the lunar crustal field data, however, this 'striping' and 'sweeping' of the inclinations and declinations is also observed on Mars (to be discussed in section 7.5.2).

5.7.3 The fit to the data

The global average misfit for all of these models is small. For the preferred model solution, the global misfit to the input data is only 0.2 nT. The largest residuals, ± 5 nT for the preferred model, occur where the measured field is maximum. A Laplacian rather than Gaussian form of the residuals (see figure 5.12) also occurred for spatially continuous magnetisation models for Mars [Whaler and Purucker, 2005] and may suggest that a one-norm minimisation (rather than a two-norm) would be a more appropriate inversion method [Walker and Jackson, 2000].

Residuals over some regions, and the agreement of predictions with surface field estimates, can be improved slightly if a thinner magnetised layer is used, though the reliability of very thin layers is suspect. However, a single layer thickness globally cannot predict the field well in all regions as the actual sources of lunar crustal magnetisation are more complex than can be expressed with a single global layer of magnetised crust with constant thickness.

Chapter 6

Inverse magnetisation models with the ER data

The surface magnetic field estimates obtained from the ER data can also be used to produce magnetisation models for the lunar crust using the equivalent source dipole technique. Being closer to the magnetised sources than the MAG data, the ER data are sensitive to fields from smaller scale structures that are not detected at altitude. The ER data thus can offer important constraints on the source magnitude and extent, both independent from the MAG data and jointly with the MAG data.

6.1 Non linear inversion

Magnetisation models using vector magnetic field data are based on linear equations, but the scalar ER data make the inverse problem non linear, requiring different methods than those employed for inversion of the vector MAG data. Representation of the total field at a location with equivalent source dipoles (with variable direction) results in a non linear relationship between the total field $B(\mathbf{r}_i)$ and the dipole parameters **m**:

$$B(\mathbf{r}_i) = \left[\left(G_{i_r} \cdot \mathbf{m} \right)^2 + \left(G_{i_\theta} \cdot \mathbf{m} \right)^2 + \left(G_{i_\phi} \cdot \mathbf{m} \right)^2 \right]^{1/2} \tag{6.1}$$

where G_{i_p} is the matrix of dipole source functions for the pth component of the model dipoles related to the surface observation locations.

6.1.1 Linearisation

The non linear relationship of equation 6.1 can be linearised to the form of equation 4.11 ($\mathbf{B} = \mathbf{Gm}$) with $\mathbf{m}$ containing combinations of the dipole parameters and $\mathbf{B}$ being the square of the total magnetic field, but this leads to an unnecessarily large and complicated matrix $\mathbf{G}$ and requires constraints that some of the parameters are positive. Instead, the relationship can be linearised using a Taylor series expansion [e.g Connerney, 1981].

For the non linear system, the *i*th datum y_i can be related to the model parameters by a (non linear) function $f_i(\mathbf{m})$. Assuming the function is locally linear, the data can be expressed using a Taylor expanded form of the function $f_i(\mathbf{m})$ around a starting model $\mathbf{m}_0$:

$$y_i = f_i(\mathbf{m_0}) + \sum_j \left.\frac{\partial f_i}{\partial m_j}\right|_{\mathbf{m_0}} \Delta m_j + \ldots \tag{6.2}$$

where $f_i(\mathbf{m}_0)$ are the initially predicted data from the starting model, and Δm_j is the increment to the *j*th parameter of the initial model which would improve the fit to the data:

$$\mathbf{m} = \mathbf{m}_0 + \Delta\mathbf{m} \tag{6.3}$$

Truncation of the Taylor expansion to first order terms in Δm_j is required to keep the problem tractable and thus requires that the values in Δm_j are small ($|\Delta m_j| << 1$). Other gradient methods for inversions such as the Newton method do consider higher order terms of expansion [e.g Avriel, 2003] but in this case, for such large numbers of data and parameters, the formation of the matrix of second partial derivatives (the Hessian matrix), becomes too computationally expensive.

Calculation of the residual Δy_i between the predicted data and the observed data allows equation 6.2 to take the form of equation 4.11, being linear in Δm_j:

$$\Delta y_i = y_i - f_i(\mathbf{m_0}) = \sum_j \left.\frac{\partial f_i}{\partial m_j}\right|_{\mathbf{m_0}} \Delta m_j \tag{6.4}$$

$$\Delta \mathbf{y} = \mathbf{P}\big|_{\mathbf{m_0}} \Delta \mathbf{m} \tag{6.5}$$

The matrix **P** (evaluated at the starting magnetisation), contains partial derivatives of the function $f_i(\mathbf{m})$ with respect to the model parameters, and is of size 'data × dipole parameters' ($mx \times 3nx$, for finding three components of magnetisation):

$$\mathbf{P} = \begin{bmatrix} \frac{\partial f_1}{\partial m_1} & \cdots & \cdots & \frac{\partial f_{mx}}{\partial m_{nx}} \\ \cdots & \cdots & & \\ \cdots & & \cdots & \\ \frac{\partial f_{mx}}{\partial m_1} & & & \frac{\partial f_{mx}}{\partial m_{nx}} \end{bmatrix} \tag{6.6}$$

With $\Delta\mathbf{y}$ in equation 6.4 the residuals between the ER data and the predictions of these data, the system of linear equations in equation 6.5 will be under constrained due to the fewer number of ER data points than model dipole parameters. The minimum increment $\Delta\mathbf{m}$ (minimum RMS $\Delta\mathbf{m}$) required to improve the fit to the data in this case (discussed in section 4.2.3) is:

$$\Delta \mathbf{m} = \mathbf{P}^T [\mathbf{P}\mathbf{P}^T + \lambda \mathbf{I}]^{-1} \Delta \mathbf{y} \tag{6.7}$$

As this inversion gives the minimum RMS increment $\Delta\mathbf{m}$, the updated model, $\mathbf{m} + \Delta\mathbf{m}$, may still give a large residual. The process of updating the model parameters to achieve a better fit can be repeated for z iterations until there is no longer a significant improvement in the fit to the data ($\|\Delta\mathbf{m}\|$ becomes vanishingly small), so that after z iterations,

$$\Delta y_i(z) = y_i - f_i(\mathbf{m}(z)) = \sum_j \left.\frac{\partial f_i}{\partial m_j}\right|_{\mathbf{m}(z)} \Delta m_j(z) \tag{6.8}$$

and in matrix form:

$$\boldsymbol{\Delta}\mathbf{y}(z) = \mathbf{P}\big|_{\mathbf{m}(z)} \boldsymbol{\Delta}\mathbf{m}(z) \tag{6.9}$$

With each iteration, the matrix **P** will change. To meet the criteria that the values in each Δm_j are small, significant damping of the matrix $\mathbf{P}\mathbf{P}^T$ is required. The damping term in equation 6.7 influences the size of the increment $\boldsymbol{\Delta}\mathbf{m}(z)$ and the misfit between the residuals $\boldsymbol{\Delta}\mathbf{y}(z)$ and the predicted residuals, $\mathbf{P}\big|_{\mathbf{m}(z)} \boldsymbol{\Delta}\mathbf{m}(z)$ rather than affecting the model **m** and the misfit to the data directly as in the linear case. The damping term will control the magnitude of $\boldsymbol{\Delta}\mathbf{m}(z)$ which will influence the number of iterations required to obtain a suitable model solution.

The function $f_i(\mathbf{m})$ for this linearisation could be either the function which results in the total field magnitude at the observation location (equation 6.10) (as in equation 6.1), or the square of this to give the squared total field magnitude at the observation location (equation 6.11).

$$f_i(\mathbf{m}) = \left[\left(G_{i_r}\cdot\mathbf{m}\right)^2 + \left(G_{i_\theta}\cdot\mathbf{m}\right)^2 + \left(G_{i_\phi}\cdot\mathbf{m}\right)^2\right]^{1/2} = \left[B_r^2 + B_\theta^2 + B_\phi^2\right]^{1/2} \tag{6.10}$$

$$f_i^{\,2}(\mathbf{m}) = \left(G_{i_r}\cdot\mathbf{m}\right)^2 + \left(G_{i_\theta}\cdot\mathbf{m}\right)^2 + \left(G_{i_\phi}\cdot\mathbf{m}\right)^2 = B_r^2 + B_\theta^2 + B_\phi^2 \tag{6.11}$$

The partial derivatives of these functions with respect to each model parameter (the components *p* of each dipole) gives:

$$\frac{\partial f_i}{\partial m_{j\,p}} = \frac{1}{2}\left(\frac{\partial f_i^{\,2}}{\partial m_{j\,p}}\right)\left[\left(G_{i_r}\cdot\mathbf{m}\right)^2 + \left(G_{i_\theta}\cdot\mathbf{m}\right)^2 + \left(G_{i_\phi}\cdot\mathbf{m}\right)^2\right]^{-1/2} \tag{6.12}$$

$$\frac{\partial f_i^2}{\partial m_{j\,p}} = 2G_{ij_{rp}}(G_{i_r}\cdot\mathbf{m}) + 2G_{ij_{\theta p}}(G_{i_\theta}\cdot\mathbf{m}) + 2G_{ij_{\phi p}}(G_{i_\phi}\cdot\mathbf{m}) \qquad (6.13)$$

where $G_{ij_{pq}}$ selects the element H_{pq} of the dipole source function matrix for the *j*th dipole at observation location $\mathbf{r}_i$ (now at the surface).

The size of the terms in equations 6.12 and 6.13, and hence the condition number of the matrix $\mathbf{PP}^T$, will depend on the distribution of the data and dipoles, the model parameters (depth, thickness and spacing) and the starting model values.

6.2 Inversion of the ER data for the Reiner Gamma region

The predictions of the ER surface data for the Reiner Gamma region from the equivalent source dipole models (Figure 4.42) and the continuous magnetisation models (Figure 5.22) show that while the magnetisation models for this region produced from the MAG data can predict the outline of the total surface field estimate, the magnitudes and contrast in magnitudes are not well reproduced. The Reiner Gamma region is again chosen as the location on which to produce a crustal magnetisation model from the ER data, which can be compared to the magnetisation models produced from the MAG data alone.

6.2.1 Input data and dipole grid

The formation of the matrix of partial derivatives, **P**, for the surface field estimates (equations 6.12 and 6.13) requires the matrix of dipole source functions **G** for the grid of dipoles and the surface observation locations, made with equations 4.8. The altitude of the surface observations was set to 0 km, with deviations from this value considered to asses the effect of this parameter on the model outputs given the uncertainty of the 'true' altitude of the estimated field and the local topography. The 'high resolution' dipole grid (with a central region 4126 dipoles at 0.25° spacing

with a 10° border region with 3571 dipoles at 0.5° spacing) was used again for this region, remembering that for surface observation locations the depth of the dipoles should be greater than the dipole spacing (see section 4.3.2). A fixed dipole depth of 15 km was used, with a layer thickness of 30 km for most models, and thicknesses of 10 km and 20 km to represent thin and thick buried layers.

To provide an even distribution of data locations, and to minimise the effect of a single large (and uncertain) estimate of the surface magnetic field on the magnetisation solution, the 1°×1° binned total surface magnetic field estimates from the ER data were used initially in this inversion. The unbinned ER data and the squared values of the 1°×1° binned ER data were also used as input data sets. There are 3374 unbinned ER data points and 1352 1°×1° binned data points over the extended region. As discussed in section 2.6.5, the unbinned ER data have very high values and high statistical uncertainties and are unevenly distributed. For this region, the average uncertainty in the unbinned ER data is 5 nT and these data do not offer good coverage of the Reiner Gamma region as shown in figure 6.1. The 1°×1° binned ER values for the extended region contain 83 empty bins, but only 6 empty bins over the central region (latitude 0°-17°).

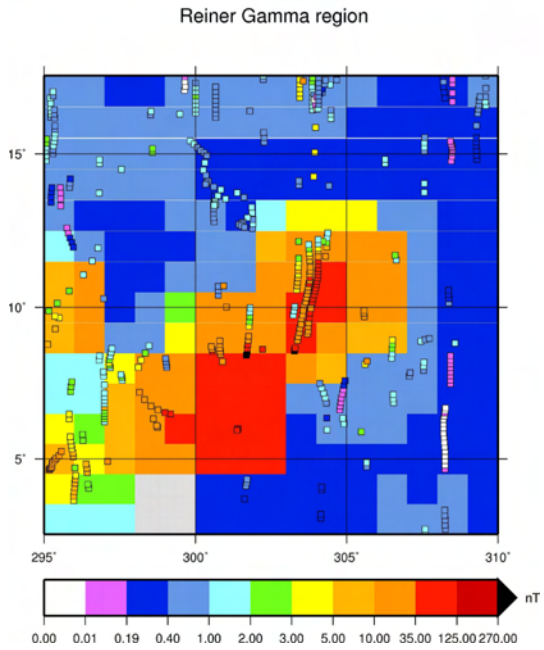

Figure 6.1: The 1°×1° binned ER data (background), and the unbinned ER data (small squares) for the Reiner Gamma region (repeat of figure 2.23).

The production of magnetisation models from the ER data will also suffer from non-uniqueness. Constraints on the magnetisation solutions in this case can come from the ability of the model solution to also reproduce the measured radial magnetic field at 30 km altitude in the wake and tail regions, referred to as the MAG data. The magnetisation solutions after each iteration were used to predict the radial magnetic field at 30 km using the matrix of dipole source functions for the model dipoles and the satellite observation locations. The misfit to the MAG and ER data, the correlation coefficients between the predicted and observed MAG and ER data, and the RMS magnetisation of the model solution, were calculated after each iteration.

6.2.2 Starting magnetisation distributions

The linearised form of the inversion of the ER data requires a non-zero starting magnetisation distribution, $\mathbf{m}_0$ to form the initial matrix **P** and the initial residuals between the data and the predictions from the starting magnetisation distribution. Because Δm_j must be small, and because equation 6.7 gives a solution for $\Delta\mathbf{m}$ with a minimum norm, it is likely that the starting magnetisation distribution will affect the final magnetisation distribution. In addition, there is no sign constraint on the magnetisation direction when using scalar data so starting directions could be reversed. Using the high resolution dipole grid for the Reiner Gamma region, three different types of starting model were used in the inversion of the ER data:

A priori: The three component magnetisation models for the Reiner Gamma region from the equivalent source dipole inversion of the MAG data (e.g figure 4.39) with appropriate depth and thickness. Models used are for dipole depths of 15 km and thicknesses 10 km (with λ=500), 20 km (with λ=1000) and 30 km (with λ=1000).

Random: Random magnetisations from a normal distribution, scaled by the standard deviation, assigned to each dipole component.

Constant: A constant magnetisation direction and magnitude for all of the model dipoles, in the radial, theta and phi directions separately.

6.2.3 Inversion of the 1°×1° binned ER data with different starting models

Using the unsquared 1°×1° binned ER surface field estimates as the input data, the dependence of a favourable magnetisation solution on the initial magnetisation model was assessed for dipoles at depth 15 km in a layer 30 km thick. A standard deviation and magnitude of 1 mA/m for the random and constant initial magnetisations was used to avoid biasing the magnetisation with a strong initial value (standard deviations of 10 mA/m and 5 mA/m were too strong).

For the random, constant and a priori initial magnetisation distributions, a damping parameter of 10^5 (in equation 6.7) was required to give $|\Delta m_j| < 0.05$ for each iteration. For Δm_j values much larger than this, the iterative process was not stable, giving sporadic rather than smooth changes to the fit to the data and the RMS magnetisation, while for Δm_j values much smaller than this, the increment was too small to give a convergent solution in a sensible number of iterations. The features of each model are set from the first iteration, showing a dependence on the starting distribution.

From each of these starting models, 20 iterations were sufficient for the misfits to the ER and MAG data, and the RMS magnetisation of the solution to converge. With each iteration, the fit to the ER data improves rapidly (Figure 6.2A and B) giving similar misfit values of less than 0.25 nT, and correlation coefficients greater than 0.99 for models from each of the initial starting magnetisations. Although the models can predict the ER data very well, given the uncertainties in the unbinned ER data, a larger misfit is preferable. The misfit to the MAG data increases with each iteration, and converges to a different misfit for each starting magnetisation model (Figure 6.2C). The misfits and also the correlation coefficients between the predicted and observed MAG data (Figure 6.2D) show very poor fits to

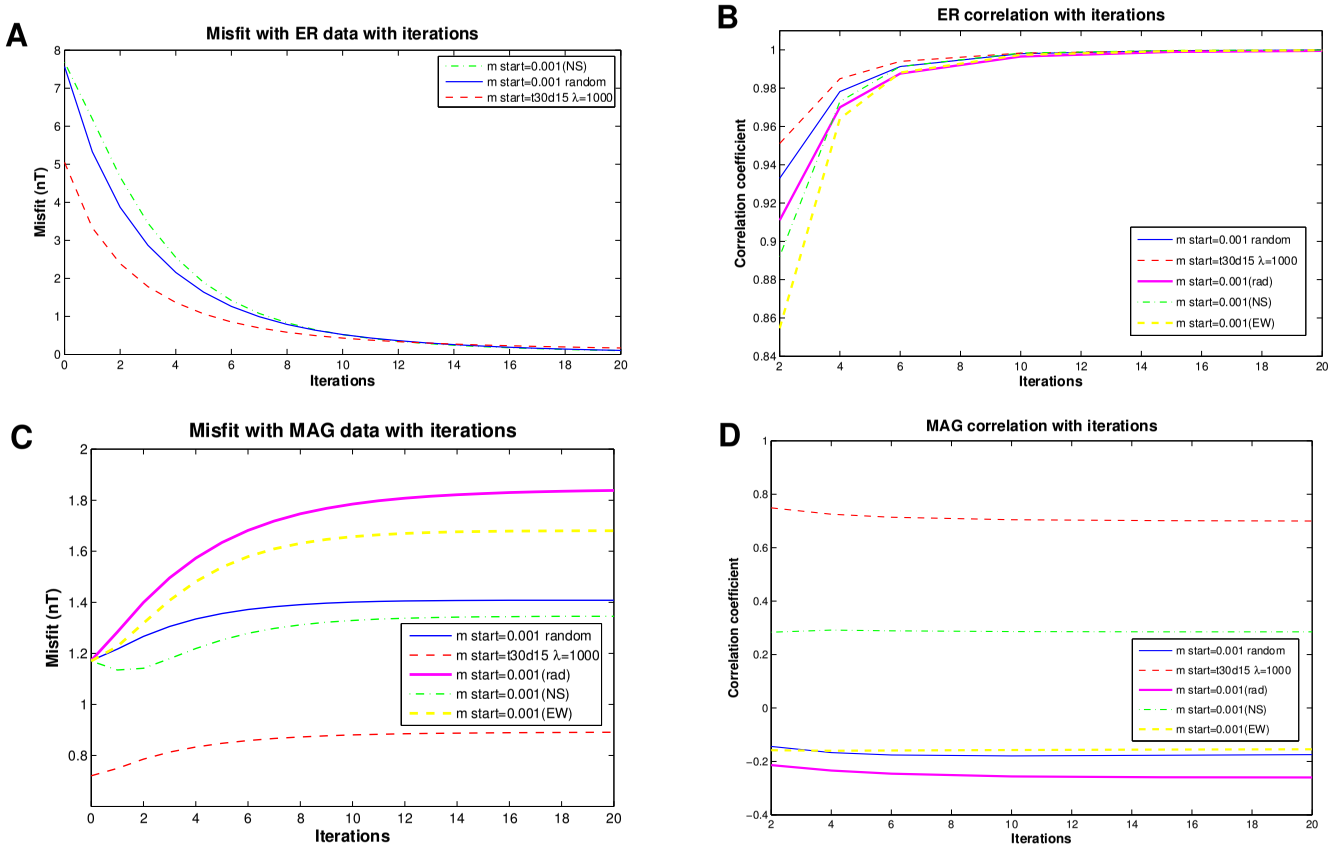

Figure 6.2: Misfits and correlation coefficients between the predicted and observed data with iteration for A and B: the ER data, and C and D: the MAG data for the Reiner Gamma region from starting magnetisation distributions (m start) constant in the radial (rad, pink thick solid), north-south (NS, green dashed) and east-west (EW, yellow thick dashed) directions with magnitude 1 mA/m, randomly distributed magnetisations with standard deviation 1 mA/m (blue solid) and an a priori magnetisation distribution (t30d15, red dashed). Selected misfits only are given in A with the misfits from the north-south constant starting distribution similar to the misfits with the east-west and radial starting distributions.

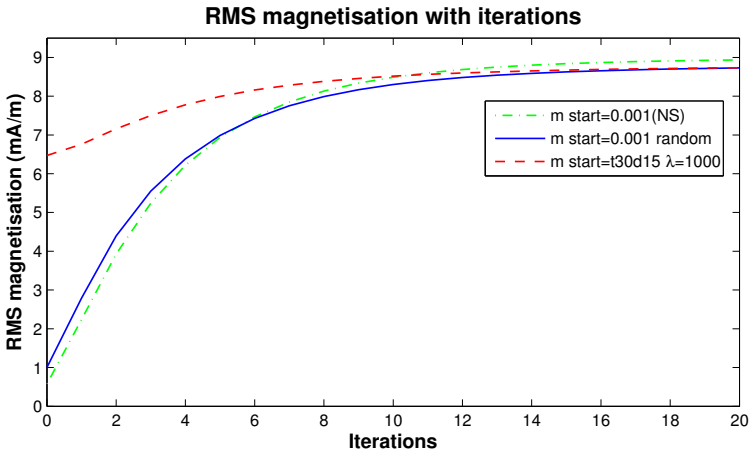

Figure 6.3: The RMS magnetisation of the model dipoles after each iteration for the Reiner Gamma region from starting magnetisation distributions (m start) constant in the north-south(NS, green dashed) direction with magnitude 1 mA/m, randomly distributed magnetisations with standard deviation 1 mA/m (blue solid) and an a priori magnetisation distribution (t30d15, red dashed). RMS magnetisations for the north-south constant starting distribution are similar to the RMS magnetisations with the east-west and radial starting distributions.

the MAG data from all but the a priori starting magnetisation distribution. The RMS magnetisations also increase with each iteration (Figure 6.3) up to about 9 mA/m.

Each of these starting distributions produces different initial misfits to the ER and MAG data, with the a priori distribution giving the best fit to the MAG data. Although the initial distributions have different RMS magnetisations, the final RMS magnetisations from each model are similar at about 9 mA/m. The component and total magnetisation solutions after 20 iterations from each of the starting magnetisation distributions are shown in figure 6.4. The components of each magnetisation solution are very different for similar misfits to the ER data. However, the total magnetisation (and the RMS magnetisation) from each starting model is very similar and follows the outline of the area of the region of the strongest ER data points, with maximum magnetisations in some locations of up to 200 mA/m. The total magnetisation strength and distribution is also similar to that produced for the Reiner Gamma region in the equivalent source dipole models with the MAG data and from the spatially continuous magnetisation models.

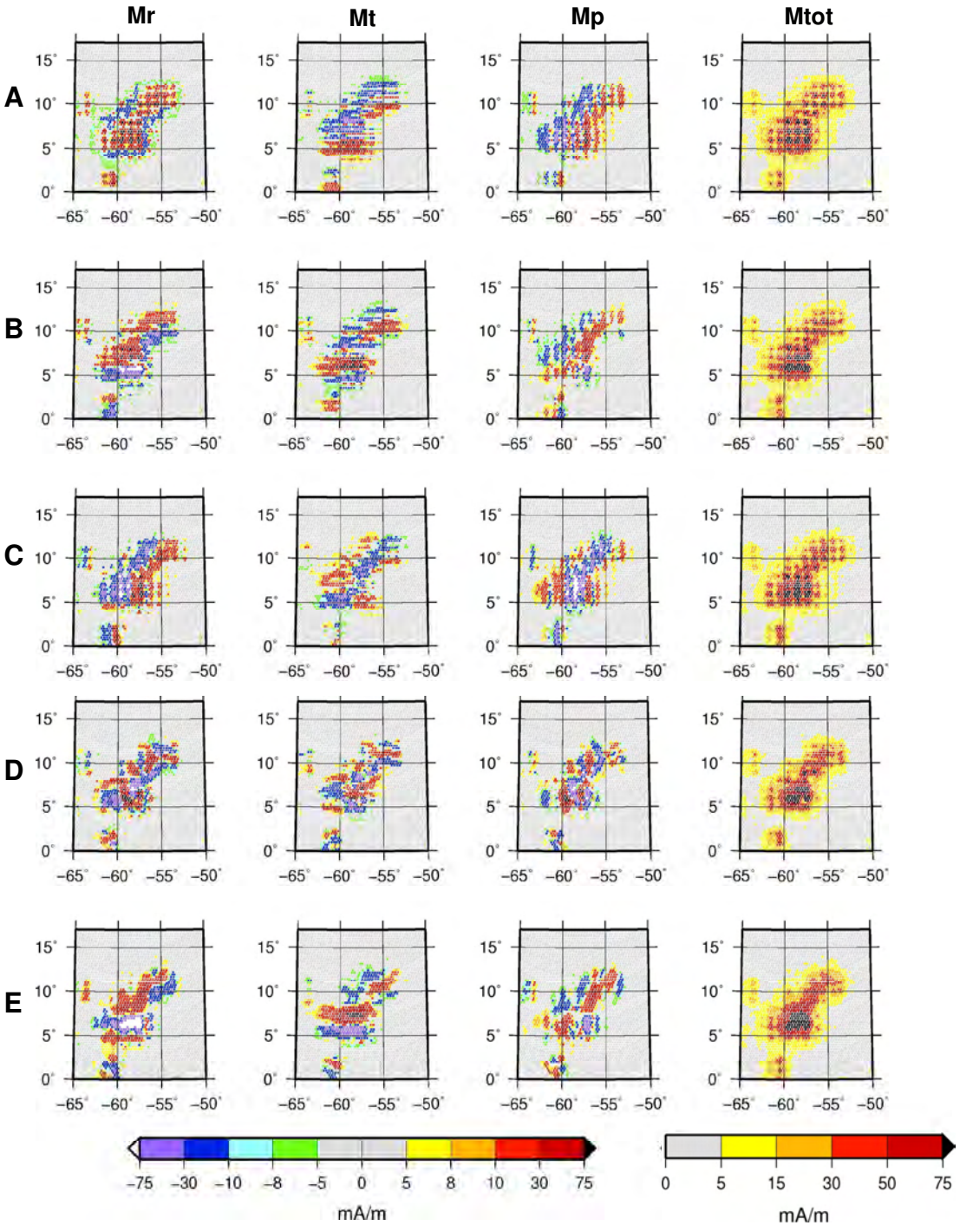

Figure 6.4: The three component and total magnetisation for the Reiner Gamma region after 20 iterations of the inversion with the unsquared 1°×1° binned ER data, from starting magnetisation distributions constant in A: the radial direction, B: the north-south direction, and C: the east-west direction with magnitude 1 mA/m, and D: randomly distributed magnetisations with standard deviation 1 mA/m, and E: an a priori magnetisation distribution. Model thickness 30 km, depth 15 km.

Each of these models forms a rather 'blocky' distribution, with groups of dipoles beneath each 1°×1° binned data point taking strong and parallel magnetisations to fit that data point (this remains even with more iterations). Unlike the direct inversion of equation 4.18, this iterative inversion solves for the minimum norm increment to the model parameters which then builds up the best fitting model solution so that the magnitudes of some dipoles can change more than others, particularly where the residuals are largest.

The magnetisation solutions from the constant direction starting models spread into the other component directions as observed in the direct inversions with the MAG data. The solution from the random starting model changes when a different random starting model is used. Increments to the a priori magnetisation model (Figure 6.4E) reduce the strength of some of the dipoles and adds smaller scale features (compare to figure 4.39C) to the south of the main feature and in the north east extension of the feature, where the ER data gives strong fields.

When the solutions of figure 6.4 are used to predict the ER data and the MAG data (Figures 6.5 and 6.6), again the main features of the predicted fields are 'set' after the first iteration, and converge towards their final solution with each iteration. Each of the model solutions fits the ER data very well, matching the shape and strengths of the main feature, with slight over prediction of the weaker fields surrounding the stronger region.

The constraint of being able to fit the MAG data as well as the ER data is important in this inversion where the different starting magnetisations result in different model solutions. The ability of these magnetisation models to also predict the MAG observations depends strongly on the starting model, as suggested by the misfits and correlation coefficients in figures 6.2C and 6.2D. The magnetisation solution from the a priori starting model is the best at reproducing the radial field observations at altitude (Figure 6.6E), and the starting model in the theta direction only also leads to a model that predicts the main features of the MAG data well (Figure 6.6B). However in the case of the starting distribution fixed in the theta direction, the predicted field can be opposite to the observed field if the initial fixed direction is reversed, resulting from the lack of sign constraint in the inversion from

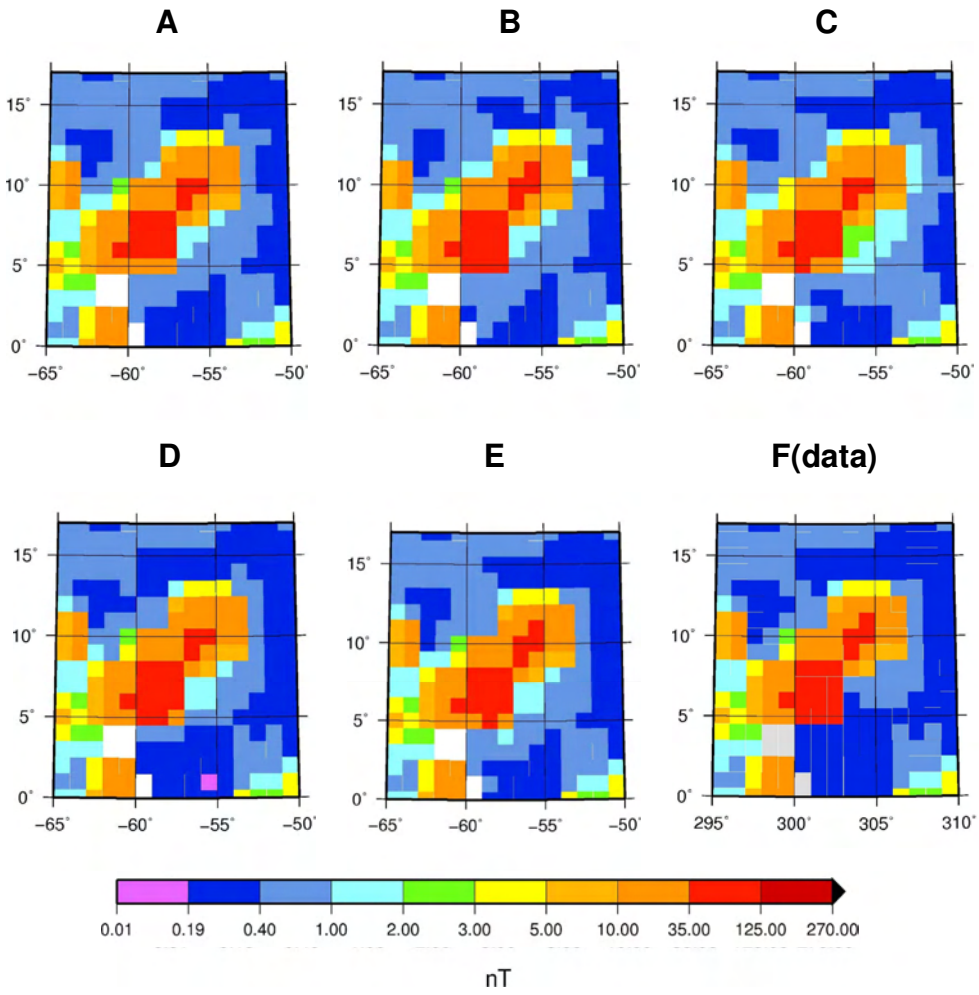

Figure 6.5: Predictions of the 1°×1° binned ER surface data for the Reiner Gamma region after 20 iterations of the inversion with the unsquared 1°×1° binned ER data from starting magnetisation distributions constant in A: the radial direction, B: the north-south direction and C: the east-west direction with magnitude 1 mA/m, and D: randomly distributed magnetisations with standard deviation 1 mA/m, and E: an a priori magnetisation distribution, shown with F: the actual data. Model thickness 30 km, depth 15 km.

the scalar ER data. The magnetisation solutions from the random starting distribution, and with the starting distributions fixed in the radial and phi directions cannot reproduce the radial field observations at altitude (Figure 6.6D, A and C), emphasising the importance of having an additional constraint to choose a unique solution.

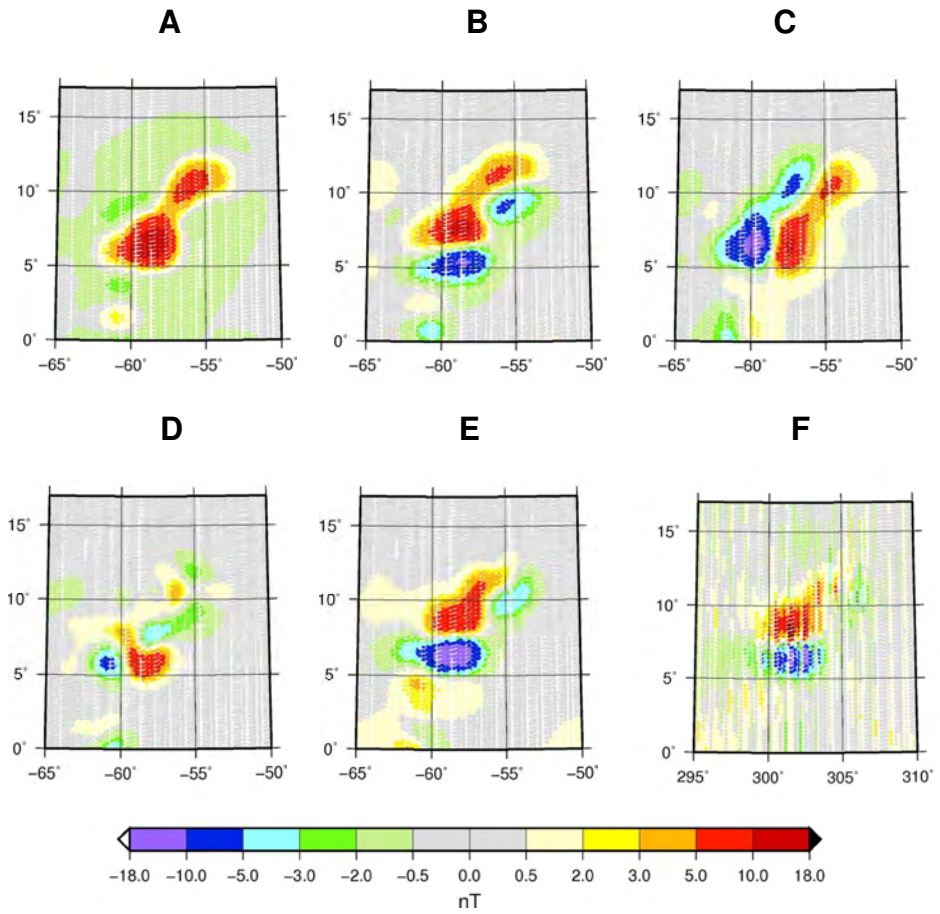

Figure 6.6: As figure 6.5, for the radial component of the MAG data. (White gaps show absence of data.)

A suitable magnetisation model from the inversion of the unsquared 1°×1° binned ER surface estimates can be produced by making small changes to an a priori magnetisation distribution produced from inversion of the MAG data, or from an independent starting distribution with the dipole directions initially fixed in the theta (north-south) direction, pointing south. There are only a limited number of starting magnetisation distributions for inversion of the ER data that lead to final models capable of adequately fitting the MAG data. The starting magnetisation models fitting the MAG data in this case are initially compatible with the MAG data.

6.2.4 Inversions with the unbinned ER data

The unbinned ER surface field estimates were also used as the input data to the inversion with model dipoles at depth 15 km in a layer 30 km thick, with the a priori magnetisation distribution as the starting distribution. With more data points than the 1°×1° binned ER data (but still under constrained), and an uneven distribution of data points, the **P** matrix for this set up was less well conditioned than the **P** matrix for the 1°×1° binned ER data and a larger damping parameter of 5×10^6 was required to give $|\Delta m_j| < 0.05$ for each iteration. With each iteration, the misfit to the ER data decreases and the RMS magnetisation and the misfit to the MAG data increase as with the inversion with the 1°×1° binned ER data. However, even after 200 iterations, there was no convergence of the misfits and RMS values.

Looking at the solution after 200 iterations, the strong individual data points result in large magnetisations (RMS magnetisation ~ 19 mA/m), especially in the north-east extension of the Reiner Gamma region (Figure 6.7) where there is a concentration of strong data points (see figure 6.1). The model solution lacks the extra southern feature required to fit the 1°×1° binned ER data. The misfit to the

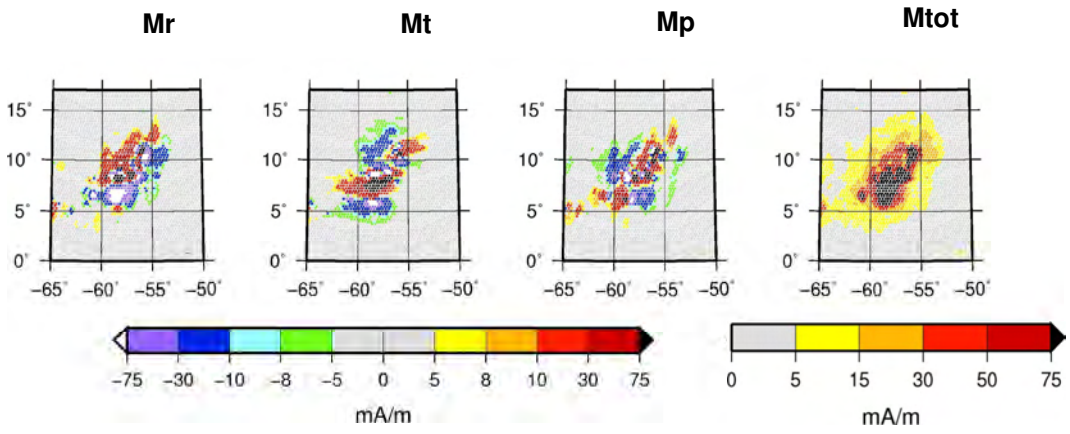

Figure 6.7: The three component and total magnetisation solutions for the Reiner Gamma region after 200 iterations of the inversion with the unsquared unbinned ER surface field estimates, with an a priori magnetisation distribution. Model thickness 30 km, depth 15 km.

unbinned ER data after 200 iterations is ~8 nT, and although the magnetisation solution can predict the distribution and direction of the MAG data at altitude, the predicted values are too high. Due to the high uncertainties and long computation times to achieve a convergence, the 1°×1° binned ER data are preferred for inversion for the Reiner Gamma region.

6.2.5 Inversions with the squared 1°×1° binned ER data

The functions $f_i(\mathbf{m})$ and their partial derivatives with respect to each model parameter required for the linearisation of the ER inversion can be for either the total field magnitude at the observation location, or the square of the total field magnitude (equations 6.10-6.13). With model dipoles at depth 15 km in a layer 30 km thick, with the a priori magnetisation distribution as the starting distribution, the squared values of the 1°×1° binned ER data were used as input data for the inversion. This inversion required a very large damping parameter of 10^8 to give $|\Delta m_j| < 0.05$ for each iteration.

Again, the misfit to the (now squared) ER data decreases with each iteration and the RMS magnetisation and the misfit to the MAG data increase. There is very little difference between the magnetisation solutions and their predictions of the ER and MAG data from this inversion and the inversion with the unsquared 1°×1° binned ER data; however, this inversion requires more iterations to converge (~40), with the misfit to the ER data slightly higher than the equivalent solution from the unsquared data, but the misfit to the MAG data slightly lower. Despite the expressions for the partial derivatives for the squared data being simpler than those for the unsquared data (equations 6.12 and 6.13) this did not offer an advantage to the convergence of the solution.

6.2.6 Inversions with shifted altitude surface data

The surface ER estimates are assumed to be at an altitude of 0 km, however for the Reiner Gamma region, the average elevation is -1.6 km (see figure 4.25). To take into account the uncertainty in the actual vertical location of the mirror point for the reflecting electrons in the ER technique, and the local topography, the 'altitude' of the ER data points was changed to -2 km, and also to +2 km. Again 20 iterations were made with a damping parameter of 10^5 with the unsquared 1°×1° binned ER data for the model dipoles at depth 15 km in a layer 30 km thick from the a priori magnetisation distribution.

The misfits and the correlation coefficients for both the ER and MAG data show an improved fit for the model with the ER data points at -2 km and reduced fit for the model with the ER data points at 2 km (see figure 6.8 for misfits). This is consistent with the local elevation if the electron mirror locations are at the surface. The magnetisation distributions produced from these models with shifted altitude surface data points were very similar (Figure 6.4E for altitude 0 km), with very slightly weaker total magnetisations for the best fitting model with the ER data points at -2 km altitude resulting in a smaller RMS magnetisation than for the other models (Figure 6.9).

6.2.7 Inversions with different thicknesses

The model parameters were altered to assess if the inversion of the unsquared 1°×1° binned ER data could provide information on preferable depths and thicknesses of the magnetised source responsible for the Reiner Gamma anomaly. For dipoles at 15 km, the thickness was changed to 10 km and 20 km to represent a thin and thick buried layer, using the a priori magnetisation distributions for those thicknesses. With a damping parameter of 10^5, the thinner layers required more iterations to converge, with the thin buried layer requiring > 100 iterations. Each of these different thickness layers converged to the same misfits and correlations with the ER and MAG data, reproducing both data sets well. The converged RMS

magnetisations however, were very different (Figure 6.10), being much larger with the thinner layers. The magnetisation solutions for the layers with thicknesses of 10 km, 20 km and 30 km after 100, 40 and 20 iterations respectively are stronger and broader for the thinner layers (Figure 6.11), and though the distributions are different, it is not possible to determine which is most suitable.

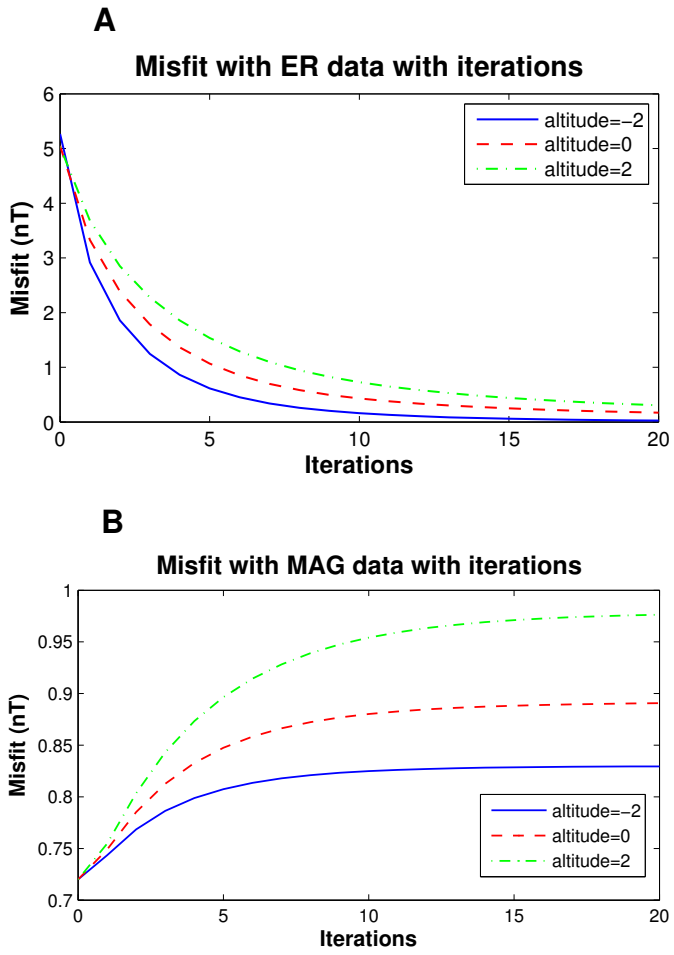

Figure 6.8: The misfit with iteration of A: the ER data and B: the MAG data, for the Reiner Gamma region from an a priori starting magnetisation distribution with the ER data locations at altitudes of -2 km (blue solid), 0 km (red dashed) and 2 km (green dot-dash). Model thickness 30 km, depth 15 km.

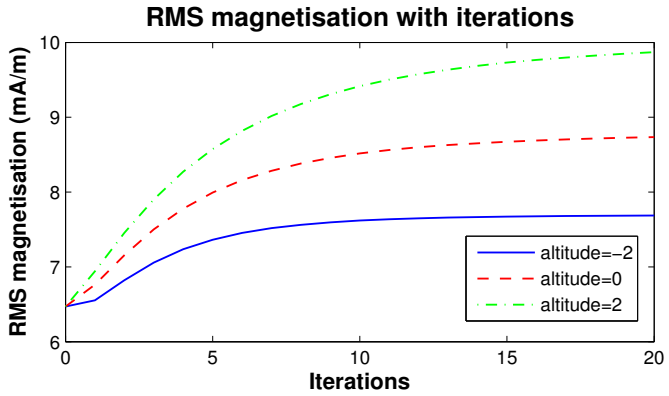

Figure 6.9: The RMS magnetisation of the model dipoles after each iteration for the Reiner Gamma region from an a priori starting magnetisation distribution with the ER data locations at altitudes of -2 km (blue solid), 0 km (red dashed) and 2 km (green dot-dash). Model thickness 30 km, depth 15 km.

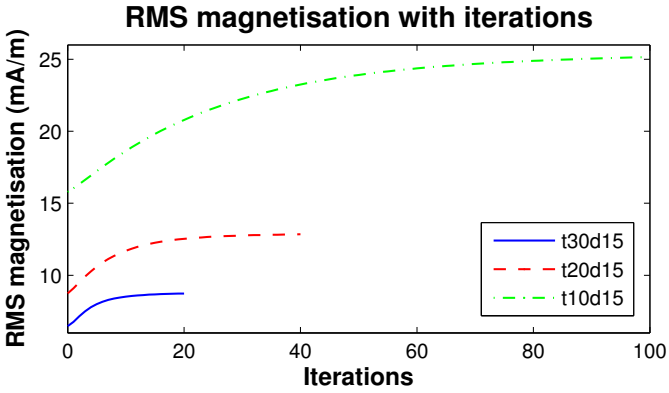

Figure 6.10: The RMS magnetisation of the model dipoles after each iteration for the Reiner Gamma region from an a priori starting magnetisation distribution with dipoles at depth 15 km and thicknesses of 10 km (green dot-dash), 20 km (red dash) and 30 km (blue solid).

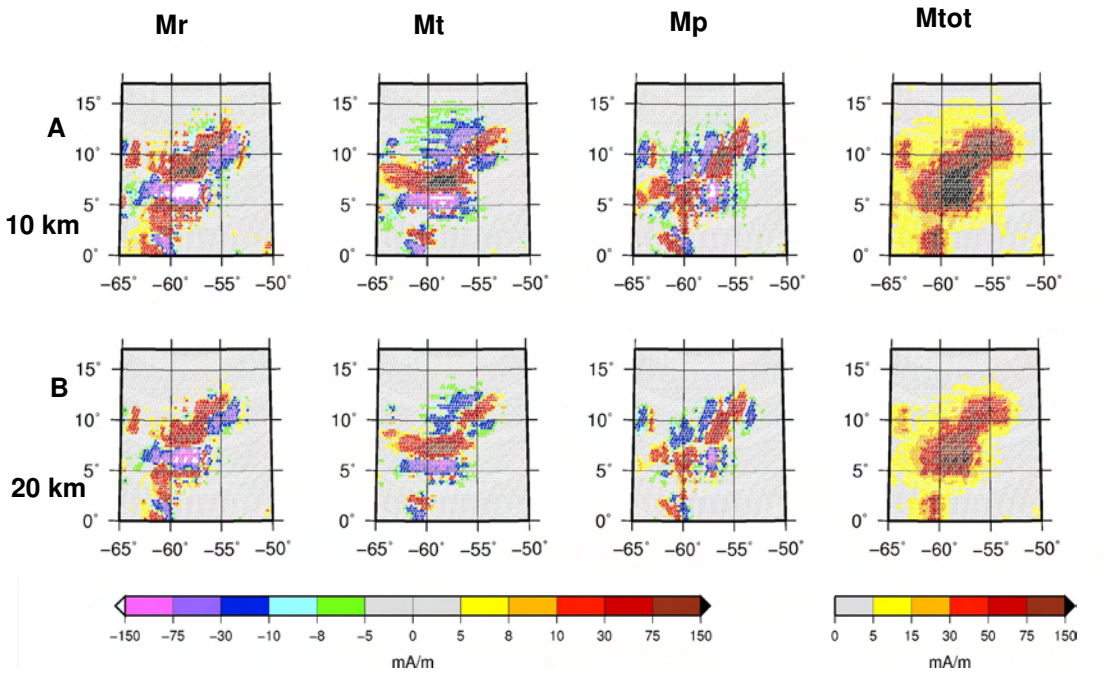

Figure 6.11: The three component and total magnetisations for the Reiner Gamma region from inversion with the unsquared 1°×1° binned ER surface field estimates, from an a priori magnetisation distribution for dipoles with depth 15 km and A: thickness 10 km after 100 iterations, B: thickness 20 km after 40 iterations. (With extended amplitude scale.)

6.2.8 Discussion of inversions with the ER data

The iterative inversion of the ER data is successful in producing magnetisation models with very small misfits to the ER data, and excellent correlations, from a variety of starting magnetisation distributions. These model solutions can also predict the MAG data at altitude reasonably well if there is an element of the starting magnetisation which is compatible with the observations at altitude, such as a favourable direction or the solution from the MAG inversion. The fact that the inversion from the random starting distribution can not reproduce the field at altitude shows the importance of selecting a suitable starting magnetisation model. The improved fit to the data when using the regional surface altitude for the

ER data points rather than 0 km shows that local topography could be considered for inversions with the ER data but is not essential for the production of suitable models.

While the blocky nature of these magnetisation solutions are to some extent an artefact of the iterative technique, the magnetisation distributions required to fit the ER data undoubtedly contain more smaller scale and higher magnitude features and have a higher RMS magnetisation than the magnetisation distributions found from the inversion of the MAG data at altitude only. Small scale features are required to fit the ER data. However the total magnetisation is not significantly stronger in these models. From the a priori starting magnetisation distribution, small but significant changes to the dipole moments, both increasing and decreasing in magnitude, are made to fit the ER data well. The very good fits to each of the data sets from selected magnetisation models does not allow a choice of a best fitting model to be made. Small scale yet strong magnetisations are expected from the strong ER surface field estimates and from the Apollo surface fields, while coherence on a larger scale is also required to give the magnetic field observed at altitude.

6.3 Joint inversion with the ER and MAG data

The equivalent source dipole technique to model crustal magnetisation has produced magnetisation models for the Reiner Gamma region using the MAG and the ER data independently. Selected models produced from each data set are capable of predicting the other data set reasonably well, showing that the models are representative solutions for the crustal magnetisation in this area. The fact that independent inversion with either data set results in magnetisation solutions that can predict the other data set shows that despite the differences in the processing and the uncertainties with the ER data in particular, the MAG and ER data sets are compatible for the Reiner Gamma region. The linearisation of the inversion of the ER data makes it possible to carry out a joint inversion of the MAG and ER data, producing a magnetisation model that simultaneously satisfies both data sets by design rather than selection.

6.3.1 Formulation of the joint iterative inversion

The linerisation of the iterative relationship between the model parameters and the ER data in equation 6.9 solves for the increment to initial model parameters that improves the fit to the data. To include the MAG data in this inversion, the linear relationship between the MAG data and the model parameters (equation 4.11) which solves for the model parameters directly, needs to instead be reformulated to solve for increments to the model parameters iteratively from a starting magnetisation distribution.

For the matrix of dipole source functions for the model dipoles and the satellite observation locations **G**, the increment $\Delta\mathbf{m}$ to a starting magnetisation distribution $\mathbf{m}_0$ is found from the inversion of the initial misfit $\Delta\mathbf{d}$ between the MAG data **B**, and the initial predictions of this data $\mathbf{d}_0$:

$$\Delta\mathbf{d} = \mathbf{B} - \mathbf{d}_0 = \mathbf{G}\mathbf{m} - \mathbf{G}\mathbf{m_0}$$
$$\Delta\mathbf{d} = \mathbf{G}\Delta\mathbf{m} \tag{6.14}$$

Equation 6.14 after z iterations can be combined with equation 6.9, to provide the formulation for the iterative inversion of both the ER and the MAG data:

$$\begin{pmatrix} \Delta\mathbf{d}(z) \\ -- \\ \Delta\mathbf{y}(z) \end{pmatrix} = \begin{pmatrix} \mathbf{G} \\ -- \\ \mathbf{P}\big|_{\mathbf{m}(z)} \end{pmatrix} \Delta\mathbf{m}(z) \tag{6.15}$$

$$\Delta\mathbf{D}(z) = \mathbf{J}(z)\Delta\mathbf{m}(z)$$

where $\Delta\mathbf{D}(z)$ is the combined vector of residuals after z iterations and $\mathbf{J}(z)$ is the joint matrix containing the dipole source functions at the satellite observation locations, and the matrix of partial derivatives which changes with each iteration. Equation 6.15 can again be solved by a damped least squares inversion, with this set of linear equations now over constrained giving:

$$\Delta\mathbf{m}(z) = \left[\mathbf{J}(z)^T\mathbf{J}(z) + \lambda\mathbf{I}\right]^{-1}\mathbf{J}(z)^T\Delta\mathbf{D}(z) \tag{6.16}$$

The most computationally expensive procedure in the inversion of equation 6.16 is the formation of the product of the functions matrix $\mathbf{J}(z)^T\mathbf{J}(z)$. While the matrix of partial derivatives $\mathbf{P}(z)$ changes with each iteration, the dipole source function matrix $\mathbf{G}$ remains the same. The calculation time of the formation of $\mathbf{J}(z)^T\mathbf{J}(z)$ can be greatly reduced by noticing that the matrices $\mathbf{G}$ and $\mathbf{P}(z)$ can be treated independently and then combined (see Appendix 15) so that only the smaller matrix multiplication $\mathbf{P}\big|^T_{\mathbf{m}(z)}\mathbf{P}\big|_{\mathbf{m}(z)}$ needs to be carried out at each iteration:

$$\begin{pmatrix} \mathbf{G} \\ -- \\ \mathbf{P}\big|_{\mathbf{m}(z)} \end{pmatrix}^T \begin{pmatrix} \mathbf{G} \\ -- \\ \mathbf{P}\big|_{\mathbf{m}(z)} \end{pmatrix} = \mathbf{G}^T\mathbf{G} + \mathbf{P}\big|^T_{\mathbf{m}(z)}\mathbf{P}\big|_{\mathbf{m}(z)} \tag{6.17}$$

Although the ER and MAG data have different uncertainties and different magnitudes (due to their distance from the source), as long as the ER part of the inversion uses the unsquared ER data, the magnitudes of the residuals $\Delta\mathbf{d}(z)$ and $\Delta\mathbf{y}(z)$ in equation 6.15 will not be significantly different and the inversion should not preferentially fit one residual set over the other (if the squared ER are used, the larger squared ER residuals might require scaling to prevent certain larger values having more weight in the solution).

6.4 Joint inversion of the ER and MAG data for the Reiner Gamma region

Using the high resolution dipole grid for the Reiner Gamma region, joint iterative inversions of the extended data sets of the unsquared 1°×1° binned ER data (with altitude set at 0 km) and the radial MAG data for this region were carried out from different starting magnetisation distributions and with different layer thicknesses. For the extended region over Reiner Gamma, there are ~30 times more

MAG data than ER data points. The ER values range from 0.2 to > 400 nT, and the MAG data range from 0 to ± 25 nT.

6.4.1 Joint inversion with different starting models

For dipole depths of 15 km in a 30 km thick layer, starting magnetisation distributions with random orientation and standard deviation 1 mA/m, constant initial magnetisation of strength 1 mA/m, and an a priori initial magnetisation distribution were used. A damping parameter of 10^5 was required to give $|\Delta m_j| < 0.05$ for each iteration from each starting model. Looking at the values of the residuals $\Delta\mathbf{d}$ and $\Delta\mathbf{y}$, their magnitudes are not significantly different, as expected (the difference in the means of 0.44 nT and 2.5 nT respectively is much smaller than the maximum values in $\Delta\mathbf{d}$), and the large number of data points in $\Delta\mathbf{d}$ means that the inversion should not require scaling of the ER residuals. As each iteration requires a matrix inversion, the iterative inversion is computationally expensive, even with the 'matrix shortcut' of equation 6.17. The misfits and correlation coefficients to each of the data sets, and the RMS magnetisation were calculated after each iteration.

From each of the starting distributions, approximately 20 iterations were again sufficient for the misfits to the ER and the MAG data to be close to convergence, with the fit to the ER data again improving rapidly (Figure 6.12A). The fit to the MAG data also improves with each iteration in this joint inversion for all but the a priori starting model (which is already a minimum least squares fit to the MAG data) (Figure 6.12B). However, the fit to the MAG data in this case is still better than the fit from the model with the inversion of the ER data alone with the a priori starting magnetisation distribution. The RMS magnetisations again increase after each iteration (Figure 6.13) but had not converged after 50 iterations, even though they were higher than the RMS magnetisations of the solutions from the MAG and ER inversions independently.

The RMS magnetisation of the solutions from each starting model (with thickness 30 km), except the starting model of dipoles fixed in the radial direction, increase in a similar fashion. The higher RMS magnetisation from the radial starting

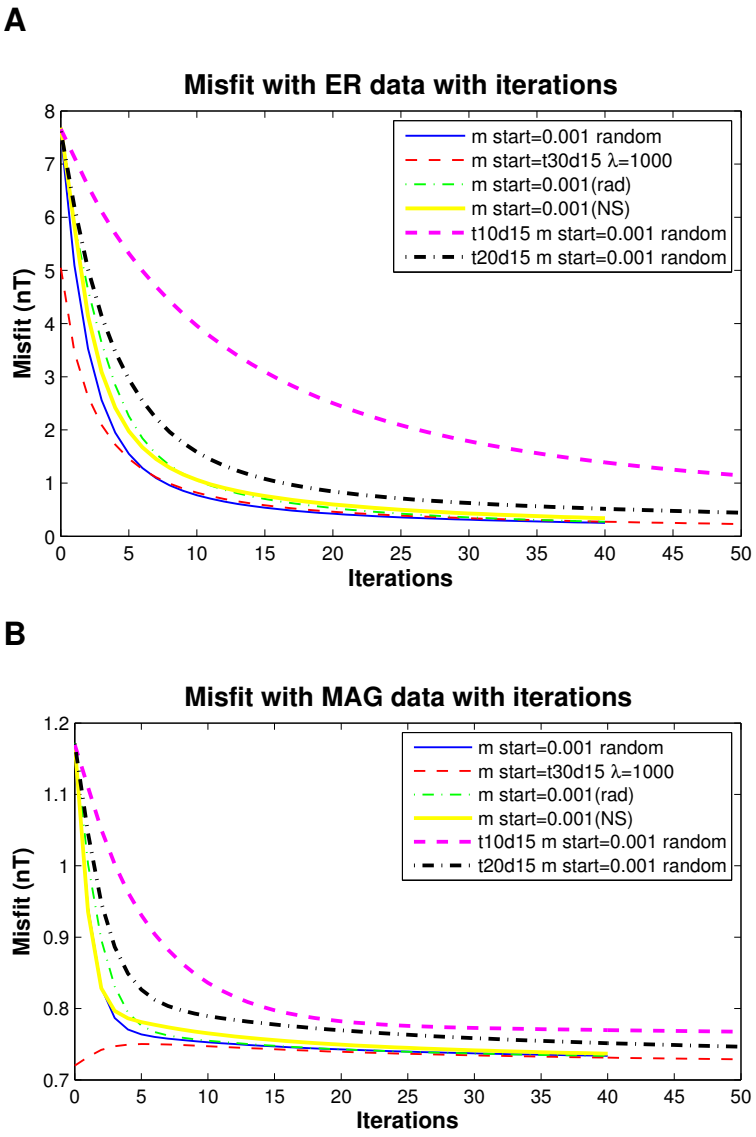

Figure 6.12: The misfit with iteration (up to 40 and 50) of A: the ER data and B: the MAG data, for the Reiner Gamma region from different starting magnetisation distributions and different thicknesses (depth 15 km). Starting magnetisations (m start) are, for the 30 km thick layer, constant in the radial (rad, green dot-dash), and north-south (NS, yellow thick solid) directions with magnitude 1 mA/m, randomly distributed magnetisations with standard deviation 1 mA/m (blue solid), and an a priori magnetisation distribution (red dash), and for a 10 km and 20 km thick layer, randomly distributed magnetisations with standard deviation 1 mA/m (pink thick dash, and black thick dot-dash respectively).

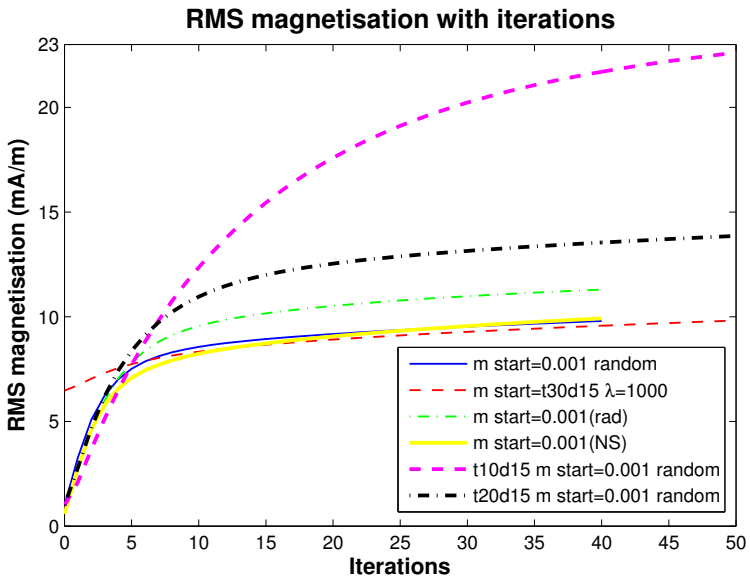

Figure 6.13: As 6.12 for the RMS magnetisation of the model dipoles after each iteration from different starting magnetisation distributions and different thicknesses (depth 15 km).

model may suggest this direction is less compatible with both sets of observations. This slight increase rather than convergence of the RMS magnetisation with each iteration, results in small changes to the model parameters in an attempt to improve the fit to both data sets, giving the final magnetisation solution many small scale features.

Figure 6.14 shows the three components and total magnetisations for the model solutions after 20 iterations from the 4 different starting magnetisation distributions. The magnetisation solutions are again slightly 'blocky' from the iterative inversion. It is interesting that in this joint inversion, the magnetisation solution is less dependent on the starting magnetisation distribution, and that each of the starting distributions results in the familiar large scale dipolar pattern for the Reiner Gamma region with small scale features imposed on this pattern.

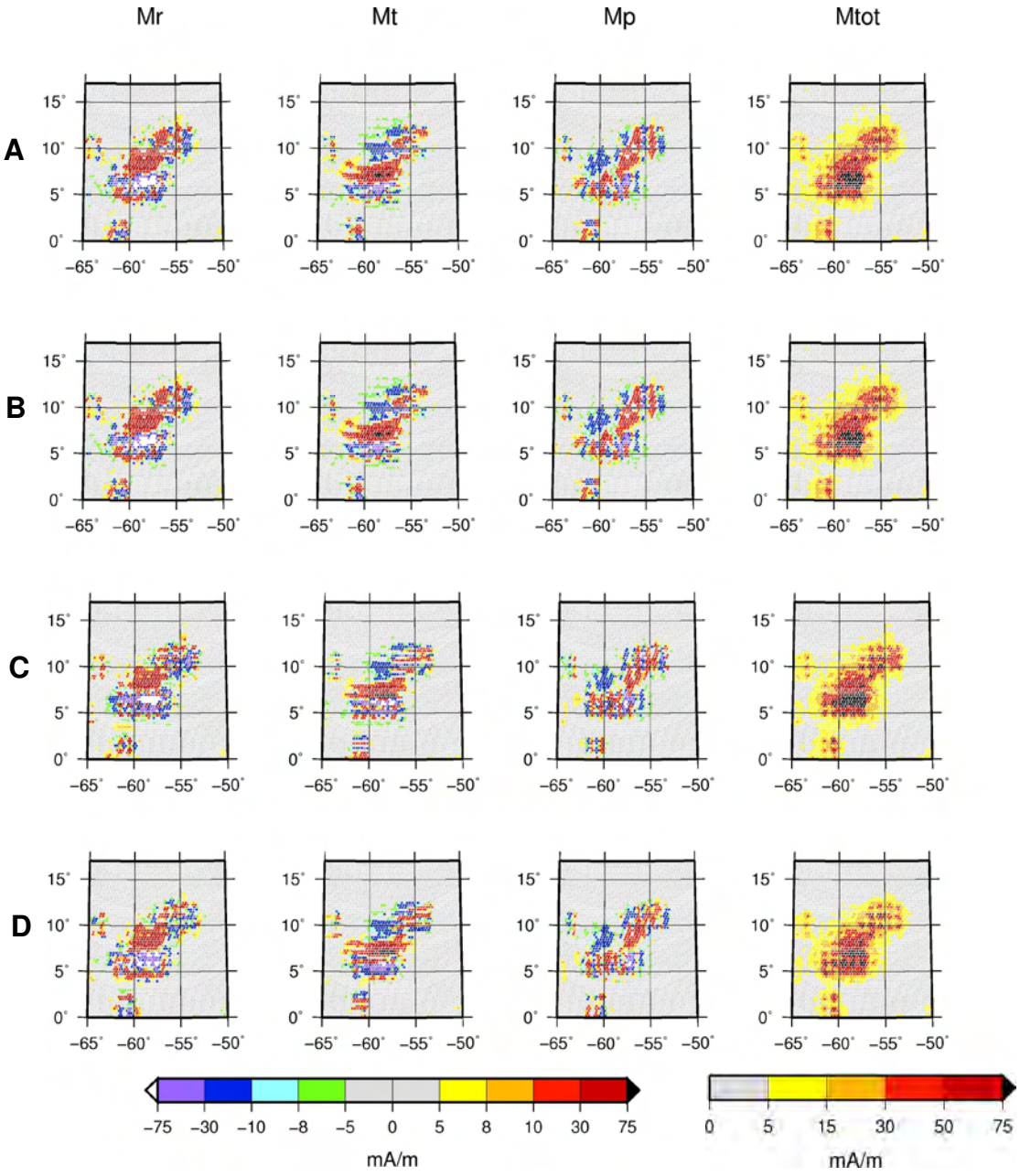

Figure 6.14: The three component and total magnetisation for the Reiner Gamma region after 20 iterations of the inversion with the unsquared 1°×1° binned ER data and the MAG data, from starting magnetisation distributions A: randomly distributed magnetisations with standard deviation 1 mA/m, B: an a priori magnetisation distribution, and constant in the C: radial direction and D: north-south direction with strength 1 mA/m. Model thickness 30 km, depth 15 km.

6.4.2 Joint inversion for the Reiner Gamma region with different thicknesses

The dipole layer thickness was again altered to 10 km and 20 km to represent a thin and thick buried layer, using a random starting magnetisation distribution. Similarly to the inversion with the ER data only, these thinner, buried layer models required more iterations for the misfits to converge (Figure 6.12) and resulted in stronger and broader magnetisation solutions (Figure 6.15) with larger and still increasing RMS magnetisations (Figure 6.13). With similar values for misfits and correlation coefficients for predictions from the models with different thicknesses, particularly for the ER data, from the joint inversion it is also not possible to determine which layer thickness is most suitable. However, predictions from the 30 km thick layer (at depth 15 km) do give a slightly better fit to the MAG data than the thinner layers after the same amount of iterations.

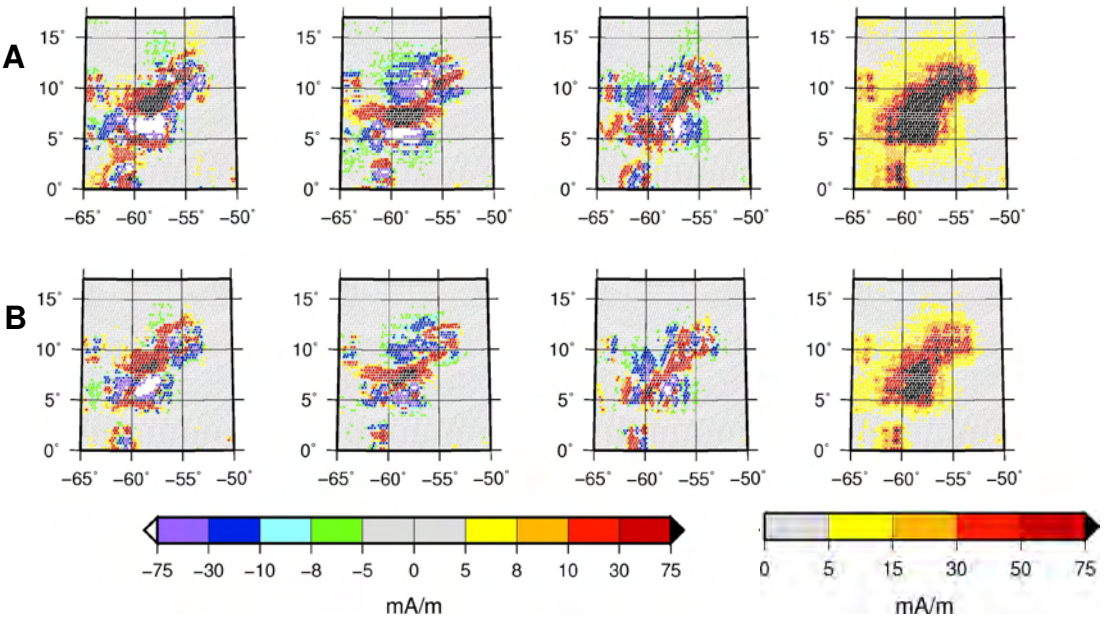

Figure 6.15: The three component and total magnetisation for the Reiner Gamma region from inversion with the unsquared 1°×1° binned ER data and the MAG data from a random starting magnetisation distribution with standard deviation 1 mA/m for dipoles with depth 15 km and A: thickness 10 km, after 50 iterations, and B: thickness 20 km, after 20 iterations

6.4.3 Discussion of the joint inversion

The magnetisation solutions from the joint inversion are very similar to the magnetisation solutions from the inversion of the ER data alone with the theta direction and a priori starting magnetisation distributions. The converged misfit values for the final model solutions for each of the data sets are very close to the misfit values from inversions with each data set independently (see table 6.1, highlighted values). The inclusion of the MAG data in this inversion means that the small scale features in these models can now better predict the data at altitude than the inversion with just the ER data. In fact, the correlation coefficient between the predicted and observed MAG data is highest for the models produced from the joint inversion.

The joint inversion produces magnetisation solutions with higher RMS magnetisations than the single data set inversions (Table 6.1), and with RMS magnetisation values that do not converge. This non-convergence may be an indication that the surface and altitude data in this region are not 100% consistent, or that the model parameters cannot adequately represent the true features of magnetisation in this region. However, given the noise and uncertainty in the data

Input data (and starting model and iterations)	**MAG misfit** (nT)	**ER misfit** (nT)	**RMS mag.** (mA/m)	**Correlation coefficients** **MAG**	**ER**
MAG, Br wake and tail	**0.720**	5.13	6.50	0.745	0.704
ER, 1°x1° binned (random, 21 iterations)	1.41	**0.105**	8.73	-0.175	>0.999
ER 1°x1° binned (a priori, 21 iterations)	0.891	**0.170**	8.73	0.700	>0.999
MAG and ER (random, 41 iterations)	**0.734**	**0.25**	9.80	0.779	>0.999
MAG and ER (a priori, 51 iterations)	**0.729**	**0.230**	9.82	0.782	>0.999

Table 6.1: Misfit values for the MAG and ER data, and RMS magnetisations for the final solutions from inversions with MAG and ER data independently and jointly for the Reiner Gamma region with dipoles at depth 15 km and in a layer of thickness 30 km. Bold values show the misfits from the MAG and ER inversions independently and jointly.

sets, complete compatibility would not be expected, and limitations in the model parameters are more likely to become apparent when trying to fit different data sets simultaneously.

The components of magnetisation in this joint inversion again show the dipolar pattern, similar to the pattern of the magnetic field for this region, even from the random starting magnetisation distribution. The larger number of MAG data points used in this inversion and hence the dominating presence of the large **G** matrix in the joint matrix **J** (equation 6.15) may act as a control for the final magnetisation distribution. The recurrence of this dipolar pattern magnetisation distribution from an iterative inversion highlights the problems of a minimum solution norm inversion for inferring paleodirections. However, the total magnetisation solution from all of these models shows the robustness of the amplitudes and of the total magnetisation for the Reiner Gamma region.

The joint inversion of the MAG and ER data for the Reiner Gamma region has been successful, but relies on the consistency of the two data sets and on the representation of the magnetisation distribution with the model parameters. Other anomaly regions may not be suited to a joint inversion if the MAG and ER data sets show considerable disagreement in the location and spatial extent of the anomaly field. A joint inversion may then offer a means of highlighting errors in the location of the ER data points in certain regions and correcting them. In addition, the computational expense of the production of the matrices in equation 6.15 for a global grid of dipoles and data makes regional rather than global models of crustal magnetisation from joint inversion more practical.

Chapter 7

Summary and Discussion

Magnetisation models in this thesis have been produced from several inverse modelling techniques with different lunar crustal magnetic field data sets. The resulting distributions of crustal magnetisation can account for the observed magnetic fields at the surface and at altitude. Crustal magnetisation models for the Reiner Gamma region allow comparison of the different modelling techniques and the use of different data sets.

7.1 Summary of models

The different modelling techniques and the input data used in the inversion for the magnetisation models in this thesis are listed in table 7.1. Spatially continuous global crustal magnetisation models have been produced from the radial component of the MAG data from all lunar regimes and from the wake and tail regions only, and from the three components of the magnetic field from the degree 150 spherical harmonic model of the lunar crustal field. The equivalent source dipole technique, applied to the Reiner Gamma region, has produced magnetisation models from direct inversion of the radial magnetic field data from the wake and tail regions only. These magnetisation distributions have a minimum RMS magnetisation for a given least squares fit to the data, controlled by a damping parameter. The requirement of a damping parameter for these inversions resulted in a suite of possible magnetisation solutions for layers of different thicknesses and depths, rather than providing a single model outcome. The linearisation of the relationship between the scalar ER data and

Input data / Modelling technique	Spatially continuous (global)	ESD (Reiner Gamma)	Joint (ESD, Reiner Gamma)
Br (all regimes, 30 km)			
Br (wake & tail only, 30 km)		*Direct*	
SH model (30 km)			
ER (1°x1° binned)		*Iterative*	
ER (unbinned)		*Iterative*	

Table 7.1 Summary of modelling techniques and data sets used.

the dipole magnetisations, using an iterative inversion method, allowed the production of magnetisation models for the Reiner Gamma region from the 1°×1° binned ER data, and the unbinned ER data, and the ER data jointly with the MAG data.

Crustal magnetisation models for the Reiner Gamma region representing the modelling techniques and input data sets in table 7.1 are shown in figures 7.1-7.3 using an extended amplitude scale to view the differences in the more strongly magnetised areas. These models are discussed in this chapter.

7.2 Observations

The most obvious observation to make of the inverse models in this thesis is the almost 'one to one' correspondence of the directions of magnetisation and the vector components of the crustal field. The magnetised regions are directly beneath the observed magnetic features despite neither inversion fixing source locations. This appears to be a consequence of the minimisation of the RMS magnetisation and is also observed in crustal magnetisation models at Mars and the Earth (to be discussed in section 7.5). Though the magnetisation directions of these models are unlikely to be representative of the true magnetisation directions of the magnetised sources, the magnetisation magnitudes from each of the inversion methods used are robust.

7.2.1 Directions

An advantage of these magnetisation modelling techniques is that they could avoid constraining the source magnetisation directions. However, the co-estimation of each magnetisation component has perhaps been restricting by increasing the number of non-unique solutions, and resulting in the smearing of the magnetisation solutions into the three component directions. In addition, the choice of the solution with minimum RMS magnetisation places no constraint on the spatial variation of the solution so that the magnetisation shows variation in direction over small regions. Even if magnetisation directions are fixed, the solutions still reverse polarity over a small region and thus the magnetisation modelling methods used in this thesis are not conducive to producing large regions with uniform magnetisation direction.

If it is assumed that magnetisation direction is parallel to the paleofield direction, the magnetising field would be required to vary in direction over small spatial scales. However, magnetisations inferred from satellite data for the Earth do not give directions parallel (or antiparallel) to a dipolar field (to be discussed in section 7.5). Without a uniform direction for a magnetised region, calculation of inclination and declination, and of paleopoles, is not meaningful. The different inclination and declination values for the same magnetic anomaly would result in very different paleopole locations, as observed for adjacent model dipoles in equivalent source dipole models for Martian crustal magnetisation by Langlais et al. (2004).

While some of the spatially rapid directional variation in the magnetisation models in this thesis result from the modelling methods, smaller scale variation such as that observed in the magnetisation models with the ER data may be real features of lunar crustal magnetisation. Solutions with less directional variation may be possible to produce if a more severe solution norm were employed in the inversion, constraining the amount of spatial variation, rather than amplitude variation. This is discussed in section 7.6.1.

7.2.2 Magnitudes

For magnetisation confined to layers with thicknesses from 10 to 50 km, magnetisation amplitudes of at least 75 mA/m are required to produce the strongest observed magnetic fields. Each of the models with different techniques and data sets provided solutions with magnetisation above the Parker bound for that layer thickness [Parker, 2003]. Average values in magnetised regions are ~30-40 mA/m, while maximum values in the magnetisation models for the Reiner Gamma region produced using the ER data are up to 200 mA/m. As these model solutions have the minimum RMS magnetisation for the fit to the data, the magnetisation magnitudes are minimum estimates of lunar crustal magnetisation. True magnetisations are expected to be as strong as, and stronger than the magnitudes in these models, especially for thinner layers and for smaller scale features. The damping parameter also reduces the RMS magnetisation, and the magnetic field data used in these models are under estimates of the actual crustal fields, giving lower magnetisation estimates; the ER data and the spherical harmonic model predictions are lower bound estimates on field strengths, and the amplitude of the radial component of the MAG data used in this thesis has recently been shown to be underestimated [Purucker and Nicholas, 2010].

To compare the magnetisations from these models to those measured in the Apollo rocks, the magnetisation (A/m) for a dipole in a block with 0.25°×0.25° surface area and thicknesses from 10 to 50 km was converted to a mass normalised dipole moment (Am^2kg^{-1}) using a range of lunar rock densities (1500-3000 kgm^{-3}). The measured NRMs (stable and unstable) for the different lunar samples ranged from 10^{-7} -10^{-1} Gcm^3g^{-1} [Fuller and Cisowski, 1987]. Conveniently, the units Gcm^3g^{-1} are equivalent to Am^2kg^{-1}. For the model magnetisation values of 0.5-200 mA/m, the mass normalised dipole moments are ~ 4×10^{-8} - 1×10^{-4} Am^2kg^{-1}, within the range of the measured NRMs.

Though smaller than some of the measured NRMs, the agreement in magnitude of the model magnetisations with measured NRMs shows that models from satellite data for minimum magnetisation within a layer can give reasonable estimates for the magnetisation of the lunar crust.

An independent estimate for uniformly magnetised impact melt in the Imbrium basin (beneath the mare) based on the weak fringing fields of craters within this basin, was given as 10^{-6} Gcm^3g^{-1} [Mitchell et al., 2008]. Measurements of NRMs in differentiated meteorites and chondrites, and the mass normalised dipole moment for the asteroid Gaspra are of the order 10^{-3} Am^2kg^{-1} [Kivelson et al., 1993].

7.2.3 Model thicknesses and source depths

Both the spatially continuous magnetisation model and the equivalent source dipole model used layers with different thicknesses (and depths of dipoles) to try to find the best fitting model to the MAG data globally, and the MAG and ER data in the Reiner Gamma region. For the global spatially continuous model, a layer thickness of 30 km gave the smallest misfit and smallest RMS magnetisations for a range of damping parameters. Both thicker and thinner layers globally required a larger RMS magnetisation to give the same misfit as the 30 km layer, and this is observable in the Reiner Gamma region in figure 7.2. Although the difference in misfits between the 30 km layer and the 10 and 50 km layers were small, this might suggest that globally the magnetised sources of the lunar crust are better represented by a layer ~30 km thick, consistent with the spectral thickness calculated in section 3.5.2. However, predictions of the surface magnetic fields from the different thickness layers gave slightly better fits to the ER data with the 10 km thick layer.

The study of the Reiner Gamma region with the equivalent source dipole models, also did not give a 'best fitting layer' as each model thickness (and depth) provided good fits to the data and similar magnetisation distributions for a range of damping parameters. With a layer of dipoles, thinner layers of dipoles and buried layers required larger RMS magnetisations, observable in figure 7.2A and 7.2B.

The lack of information about source depth and thickness available from these inversions of satellite data are probably a consequence of the resolution and sensitivity of the data, and/or loss of information in the field during altitude normalisation of the MAG data. Within this limitation, the assumption of a spherical Moon (with no consideration of topography) is justified, although the models with

the ER data for the Reiner Gamma region did respond to changing the level of the surface data points.

From the magnetisation solutions it is possible to estimate an alternative layer thickness using the method of Parker (2003) in a reverse sense; if the magnetisations are the minimum required to give the fields at altitude, the Parker bound plot in figure 3.4, shows that layers could be as thin as 3 km for the strongest magnetisations, but the average magnetisations give thicknesses of 10-15 km. Modelling crustal magnetisation for thinner layers (< 10 km) was not possible with these methods due to the spacing requirement of the dipoles in the equivalent source dipole method, and instabilities in the computations with very thin layers in the spatially continuous model.

7.2.4 Magnetised sources

Due to the global response of the magnetisation solution in the continuous models, where the solution for a region depends on the global compromise of fit to the data and RMS magnetisation, a regional rather than global magnetisation model is more conducive to trying to understand sources of magnetisation. For the Reiner Gamma region, magnetisation models with a variety of thicknesses and depths each give good fits to the data. However, in this region, the best fits to the data are from surface (or near surface) layers rather than buried layers. This is compatible with theories that the magnetised source in this region is impact ejecta [e.g Hood et al., 2001], though the layer would likely be thinner than modelled here. The horizontal extent of the source, though coincident with the high albedo feature, may be more compact than the magnetisation models show, due to the spreading of the magnetisation solution across the modelled layer.

The ‘one to one’ correspondence of the directions of magnetisation and the vector components of the crustal field in these models means that there is no additional information about signatures associated with particular lunar structures. In addition, in some regions, care is required in the interpretation of the magnetised sources; what appears as a linear feature in one or more magnetisation components

(especially when the magnetisation direction is fixed) may not be linear when the total, or other magnetisation components are considered.

7.3 Comparison of modelling techniques

From the models presented and discussed in Chapters 4, 5 and 6, the different modelling and inversion techniques and data sets give very similar magnetisation distributions for the Reiner Gamma region. Comparisons of the equivalent source dipole and continuous models for the regions of Descartes, Firsov and Crisium in section 4.10 and in Appendix 13 also show great similarities. Although similarity of the solutions from the continuous and equivalent source dipole techniques is expected given that each produces the minimum RMS magnetisation solution for a given least squares fit to the data, and was observed for the Mars case [Whaler and Purucker, 2005], the similarities of the models produced using the scalar ER data with those from the vector MAG data should not be taken for granted.

7.3.1 Comparison of the ESD and spatially continuous models

To make a direct comparison of the different inversion methods with the MAG data, figure 7.1 shows the magnetisation models for the Reiner Gamma region for a 30 km thick layer produced from the equivalent source dipole technique and the spatially continuous technique from the radial component of the MAG data in the wake and tail. Despite the large damping parameter (50,000) required for a suitable global magnetisation solution, the agreement between the two models in both the magnitude and direction of the components, and the extent and details of the feature, is impressive. The correlation coefficient for the total magnetisation is 0.973. The comparable resolution of features shows that the 0.25° spaced dipoles are adequate representations of the continuous magnetisation distribution in the crustal layer.

The selected magnetisation models for the Reiner Gamma region for layer thicknesses of 10 km, 20 km and 30 km with equivalent source dipoles, and layer thicknesses of 10 km, 30 km and 50 km from the global continuous model (now with

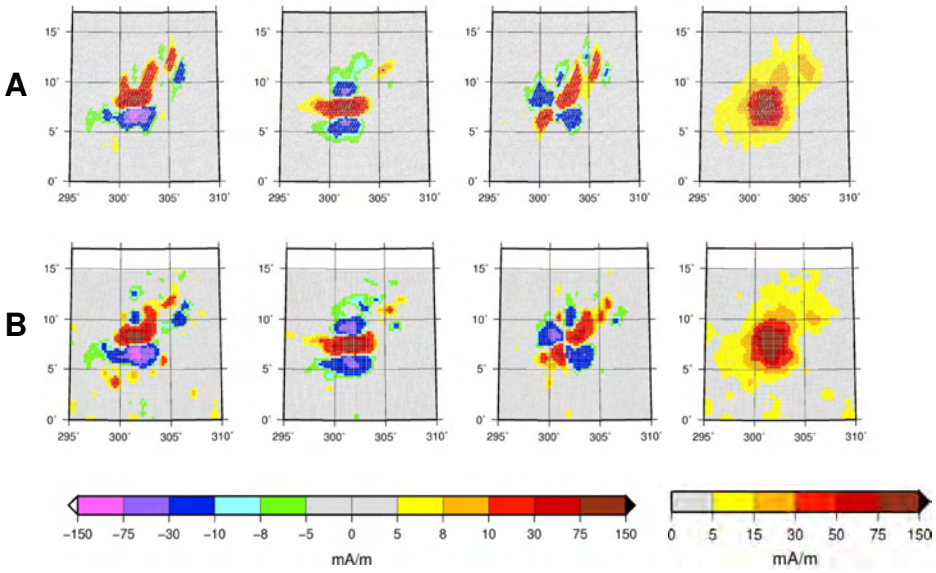

Figure 7.1 Three component and total magnetisations for the Reiner Gamma region from the radial component of the MAG data in the wake and tail for a 30 km thick layer from A: the equivalent source dipole technique with λ=1000, and B: the spatially continuous technique with λ=50,000, evaluated at the surface.

the spherical harmonic model data) are shown in figure 7.2. The spatially continuous model with the three components of the spherical harmonic model data as input looses some of the finer scale detail of the feature and increases the size of the central magnetised region slightly (Figure 7.2D-F), as the spherical harmonic model acts to smooth out some of the features of the crustal field (and is at a lower resolution).

The increase in magnetisation magnitude with decrease in layer thickness is observed in the equivalent source dipole models (Figure 7.2A-C), while it is the 10 km and 50 km thick layers from the continuous model which have the larger magnetisations (Figure 7.2D-F). The 10 km thick model layers from both techniques show the most agreement in magnitude and extent of the magnetisation, with a correlation coefficient of 0.992 (though correlation coefficients for the rest of the models in figure 7.2 are also high at > 0.96).

While the agreement between the solutions from the equivalent source dipole technique and the spatially continuous technique is very good, for the study of a region it is better to include only the data for that region (with a border) rather than

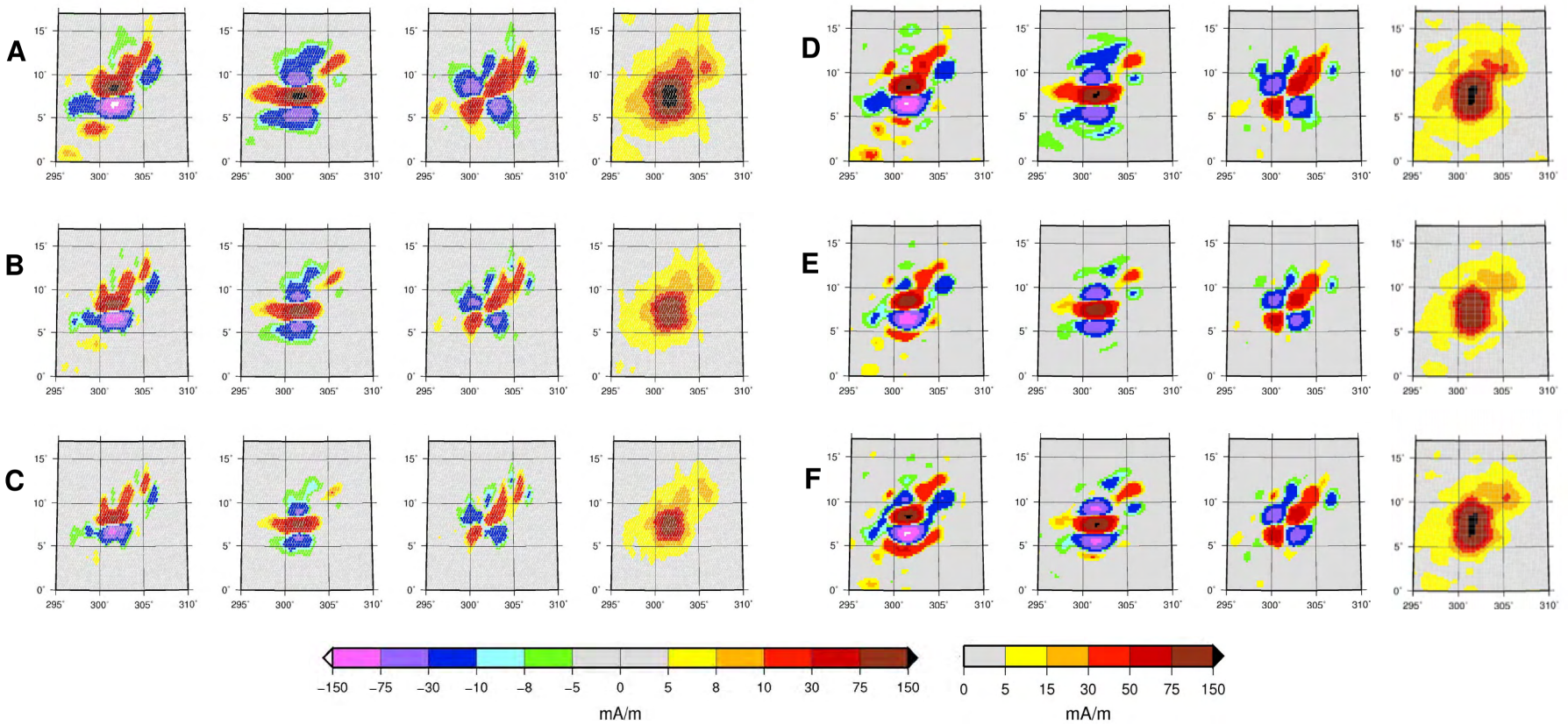

Figure 7.2: Three component and total magnetisations for the Reiner Gamma region from the radial component of the MAG data in the wake and tail for A: a 10 km thick layer, B: a 20 km thick layer and C: a 30 km thick layer, from the equivalent source dipole technique with λ=1000 and dipole depth 15 km, and from the three components of the spherical harmonic model data at 30 km altitude for D: a 10 km thick layer (λ=15,000) , E: a 30 km thick layer (λ=20,000), and F: a 50 km thick layer (λ=16,000), from the spatially continuous technique, evaluated at the surface.

settling for a compromise for the region based on the global data set. However, the global model represents a fast way to produce magnetisation models for regions of interest on the Moon.

7.3.2 Comparison of magnetisation solutions from MAG and ER data

Selected magnetisation model solutions with different layer thicknesses for the Reiner Gamma region, from the iterative inversion of the different forms of the ER data, and from different starting magnetisations are shown in figure 7.3. The equivalent source dipole solution for the 30 km thick layer from the MAG data is also shown for comparison.

When the 1°×1° binned ER data are used to produce magnetisation models, there is not a significant increase in the strength of the magnetisation, compared to the solution from the MAG data, except for the north-east extension of the Reiner Gamma feature (e.g figure 7.3B). This suggests that the magnetised sources in this region are smaller scale and/or shallower than the rest of the Reiner Gamma region. Finer scale details are added in the component magnetisations to meet the stronger ER data on a coarser grid, giving a slight blocky nature to the total magnetisation distribution compared to the models from the higher resolution MAG data. As with the MAG data where the radial field in the wake and tail regions gave a little more structure to the magnetisation models than the data from the spherical harmonic model, there is finer scale detail added when the unbinned ER data are used (Figure 7.3D), in this case having much stronger magnitudes. These stronger magnitudes hint at the strength of magnetisations required to account for the strongest surface fields. However, the smallest scale features of the crustal fields as observed from the Apollo surface measurements are perhaps not detectable with the ER technique [Halekas et al., 2010] suggesting even stronger magnetisations are likely.

For the models from the ER data alone (Figure 7.3A,B) to also fit the MAG data, it was necessary to include some a priori information in the starting magnetisation distribution, resulting in the familiar distribution in component directions. The difference in the components of magnetisation for the models of

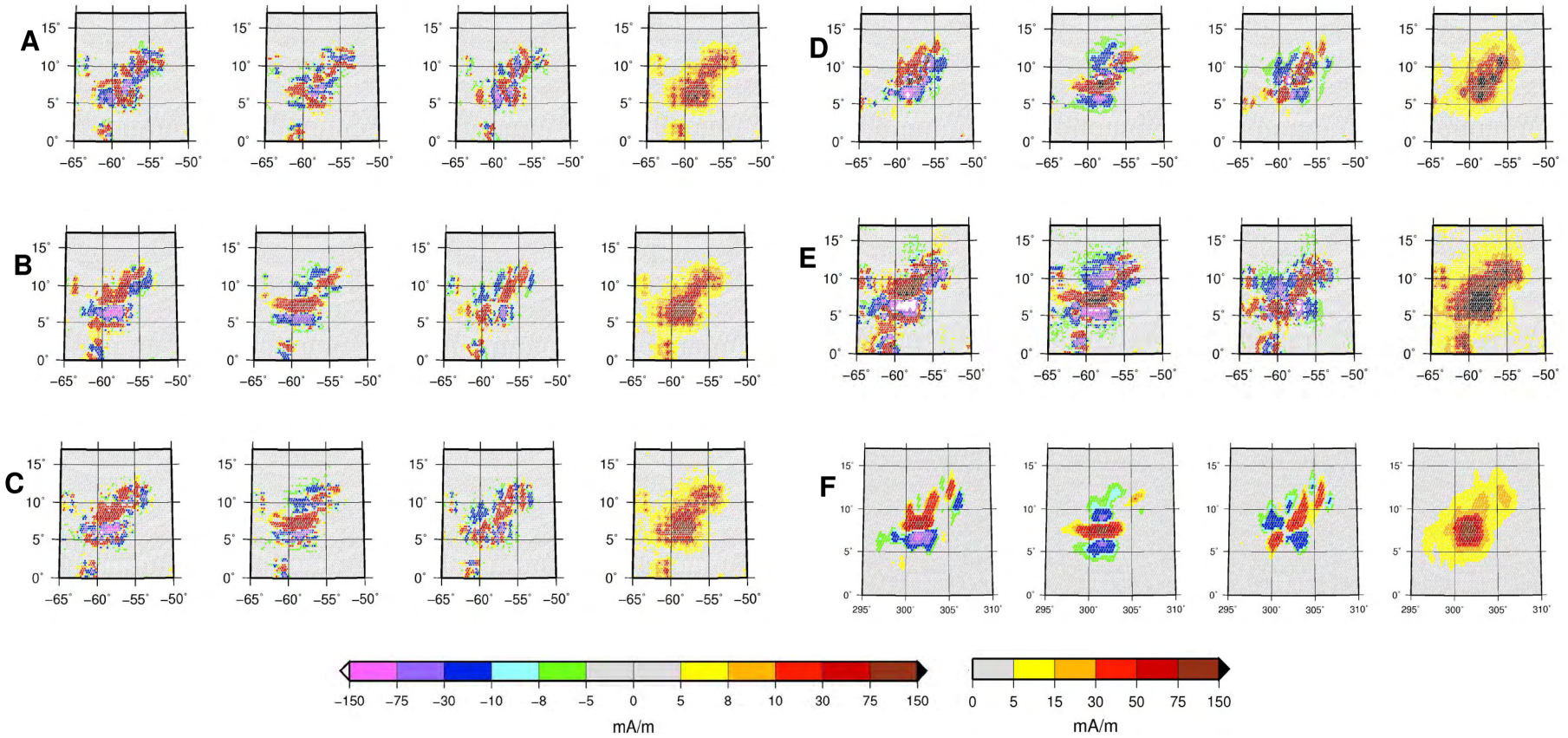

Figure 7.3: Three component and total magnetisations for the Reiner Gamma region with layer thickness 30 km (except E) and dipole depth 15 km from A: the 1°×1° binned ER data with a random starting magnetisation, B: the 1°×1° binned ER data with an a priori starting magnetisation, and C: a joint inversion of the ER and MAG data, all after 20 iterations, D: the unbinned ER data with an a priori starting model after 200 iterations, and E: a joint inversion with layer thickness 10 km, after 50 iterations. Shown with F: from the radial component of the MAG data in the wake and tail.

figures 7.3A and B show the non-uniqueness inherent in the total magnetic field also, but again the total magnetisation is robust. When the ER and MAG data are used jointly in the inversion, the resulting solution is very similar to both the solutions from the ER and MAG data independently. A thinner layer again gives stronger magnetisations (Figure 7.3E).

The fact that only small changes are required to the magnetisation distributions produced from each data set alone, in order to fit both data sets almost as well as the individual models, shows that the ER and MAG data are compatible for the Reiner Gamma region. Although at altitude, the MAG data alone can give a good estimation of crustal magnetisation strengths and distributions

7.4 Comparisons with other magnetisation models

The Reiner Gamma feature is a 'favourite' in the study of lunar magnetism. The first magnetisation estimates for the lunar crust modelled the Reiner Gamma feature as a polygonal plate 10 m thick over the main high albedo feature [Hood et al., 1979]. For such a thin layer, the magnetisation calculated was large at 5.2 ± 2.4 Am^2kg^{-1}. Recent estimates of the magnetisation for the central region of the Reiner Gamma feature used LP MAG data with equivalent source dipoles [Nicholas et al., 2007], and MAG data from the Japanese satellite Kaguya, with magnetic monopoles as sources [Toyoshima et al., 2008].

7.4.1 Another magnetic dipole model

Nicholas et al. (2007) used equivalent source dipoles with 0.25° spacing with their magnetisation direction fixed in the theta direction to model the magnetisation of the Reiner Gamma region over the central high albedo feature. This model required magnetisations of up to 0.4 A/m, with opposite polarities, for a 40 km thick layer over the central feature (Figure 7.4A). When compared to the magnetisation models of this region with dipoles fixed in the theta direction from this thesis (Figure

7.4B), the Nicholas et al. model shows more variation in magnitude and direction over this small region. The different magnetisation strengths and directions in their model compared to the models in this thesis may result from the different processing of the MAG data in each model, or the absence of border dipoles in the model of Nicholas et al. (2007). However, there is agreement in the order of magnitude of the magnetisation.

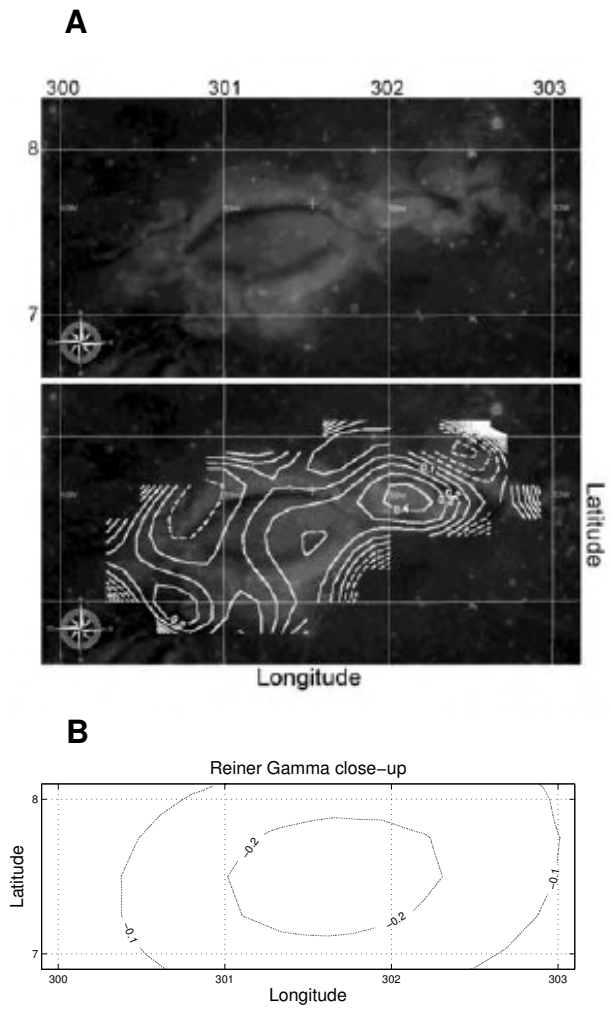

Figure 7.4: A: Grey-scale image of the centre of the Reiner Gamma feature (from Clementine UV camera) and overlay of the magnitude of magnetisations for a 40 km thick layer in a northerly direction over Reiner Gamma. (From Nicholas et al. (2007)), and B: a contour plot of magnetisation in a 30 km thick layer (from figure 4.36), for dipoles fixed in the theta direction. Contour intervals at 0.1 A/m. (solid lines are positive, dashed lines are negative).

7.4.2 A magnetic monopole model

Models of the Reiner Gamma region using magnetic monopoles required 'charges' of the magnetic monopoles with 0.16° spacing of up to ± 10 Wb [Toyoshima et al., 2008]. The polarity of the magnetic charges (Figure 7.5A) is similar to the radial distribution of dipoles in the models of the Reiner Gamma region in this thesis (Figure 7.5B), and include the north-east extension of the Reiner Gamma feature. Monopole sources give a more compact source region for the Reiner Gamma feature. Although not directly comparable to magnetisations of dipoles, equating the magnetic dipole moment Am^2 to Wbm, magnetisations of 100 mA/m for 0.25° spaced dipoles in the Reiner Gamma region from my inverse models are equivalent to magnetic charges of 7 Wb.

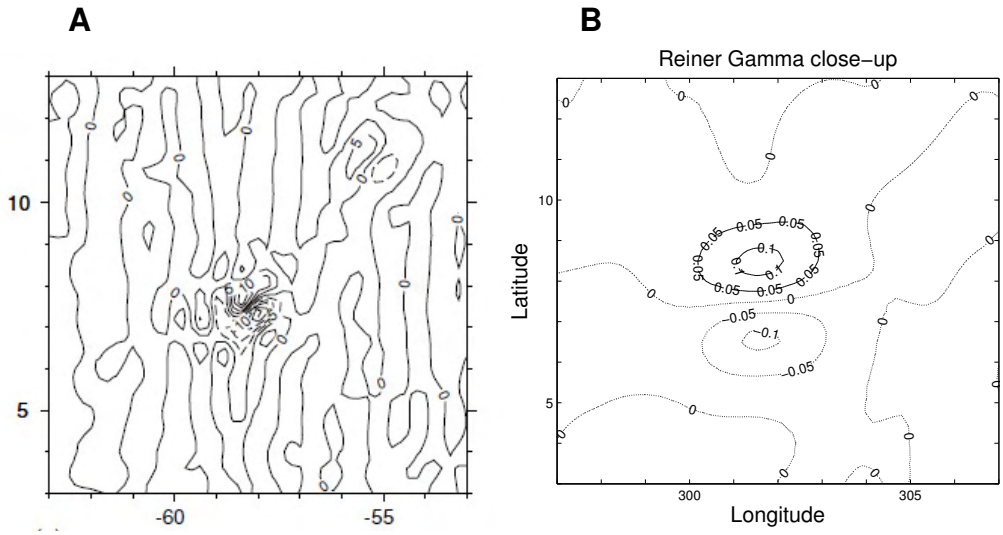

Figure 7.5: A: Contour map of magnetic charges of magnetic monopoles used to represent the crustal field at Reiner Gamma. The contour interval is 5 Wb. (From Toyoshima at al. (2007)), and B: a contour plot of magnetisation in a 30 km thick layer (from figure 4.36), for dipoles fixed in the radial direction. The contour interval is 0.05 A/m. (solid lines are positive, dashed lines are negative).

7.5 Comparative planetology

The global lunar crustal magnetisation model can be compared with the global crustal magnetisation models produced for the Earth and Mars from satellite data. Figure 7.6 shows the three components of the crustal magnetisation and the total magnetisation for the Earth, Mars and the Moon, from spatially continuous magnetisation models from Whaler and Purucker (2010), Whaler and Purucker (2005), and this study respectively. The lunar magnetisation features are much higher resolution and finer scale than can be produced from satellite observations at the Earth or Mars given the low altitude of LP and the size of the Moon.

7.5.1 Magnetisation magnitudes

As with the magnitudes of the crustal fields (section 1.3), the lunar crustal magnetisations are very much weaker than those on Earth and Mars for layers of comparable thickness. In fact, the highest magnetisations in the lunar models of ~0.2 A/m are barely significant compared to the lowest significant magnetisations for the terrestrial and Martian models. The strengths of magnetisations on Mars are also rarely observed on the Earth. Thinner layers and smaller scale features on each of these bodies will have much stronger magnetisations than the maximum values for a layer with constant global thickness, however the lunar magnetisations are still unlikely to be comparable in magnitude to those on Earth and Mars at 10s A/m.

The large magnetisations on Mars and the Earth result from the different content of magnetic minerals, and the strengths of the magnetising fields. The oxidising atmospheres of Earth and Mars and the presence of iron (and titanium on Earth) are conducive to the existence of many magnetic carriers. The strong magnetisation values on Mars may be attributable to a thick magnetised crust, a higher and/or different magnetic mineral content, and/or a stronger magnetising field.

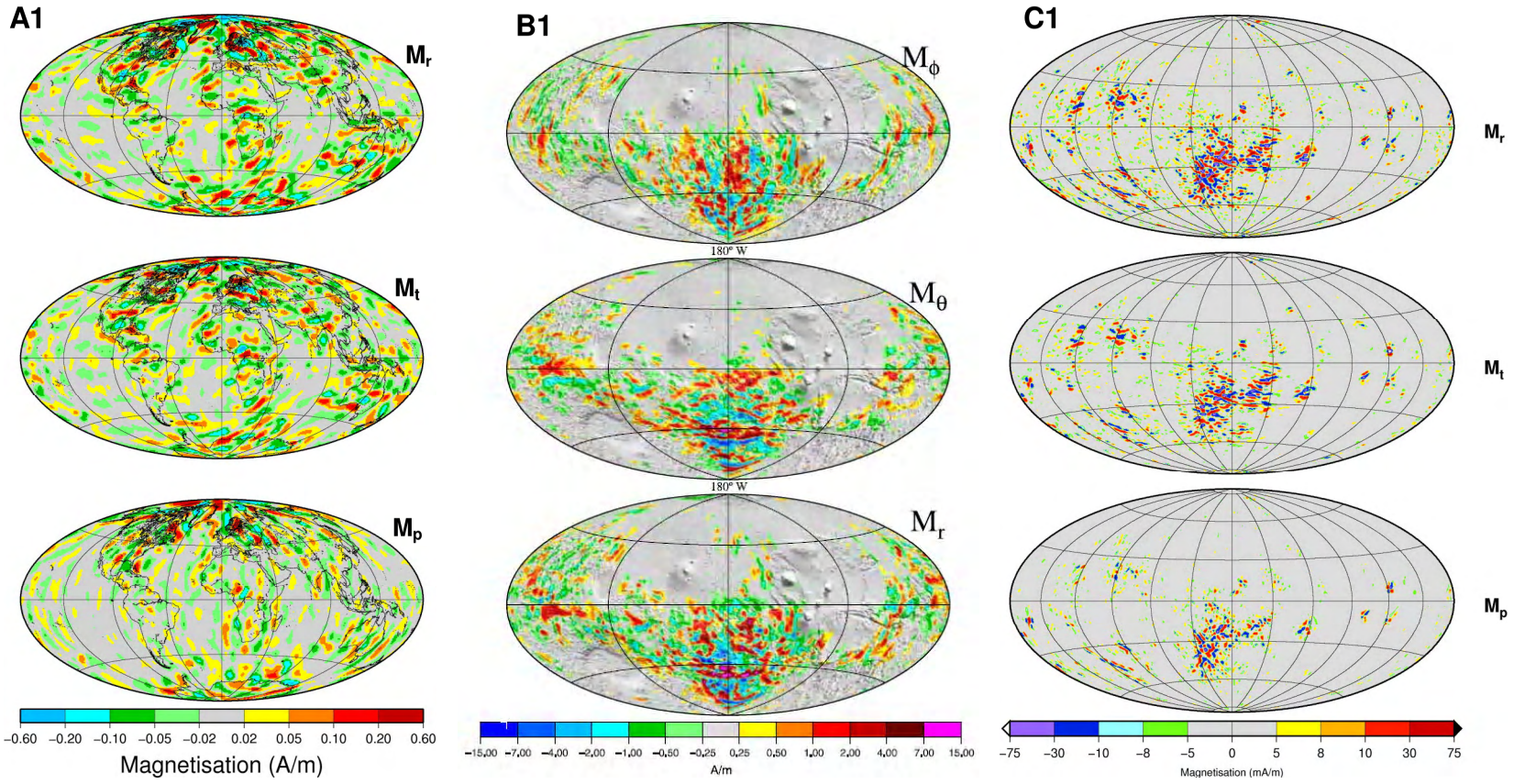

Figure 7.6, caption overleaf.

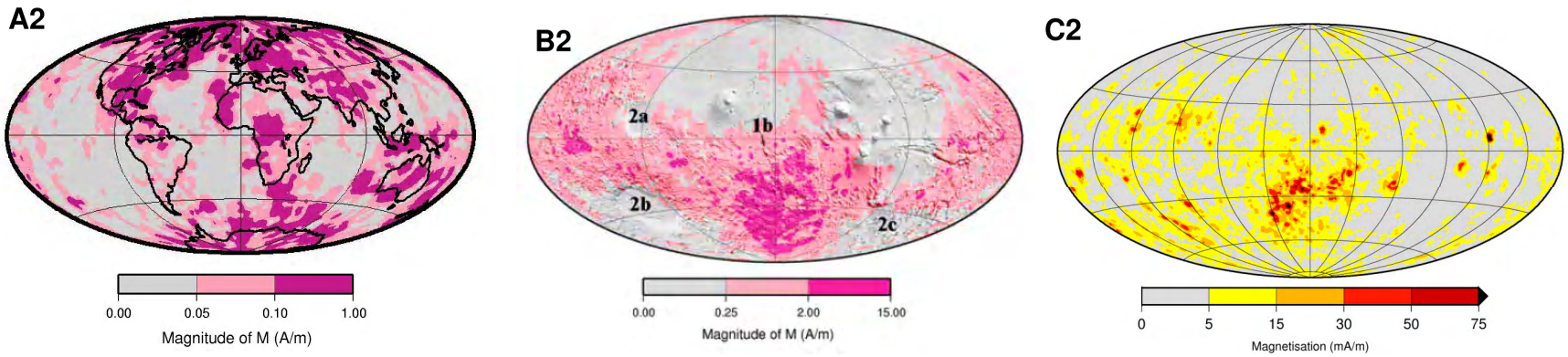

Figure 7.6: Three component magnetisations (1) and total magnetisation (2) for preferred models for A: the Earth with a 40 km thick layer (from Whaler and Purucker (2010)), B: Mars with a 40 km thick layer (from Whaler and Purucker (2005)), and C: the Moon with a 30 km thick layer (this study). Note the very different scales of magnetisation and the different ordering of the components.

7.5.2 Comparison of features

The components of magnetisation in the models for the Earth, Mars and the Moon in figure 7.6 each show almost 'one to one' correspondence with the component directions of their crustal fields (not shown). As mentioned for the Moon in section 2.1.4, several of the anomalies on Earth and Mars also take the characteristic form of a magnetic field resulting from a small homogeneously magnetised body (see figure 2.6). There are two features near the Martian equator at longitude ~100° and 140° with this pattern, and a feature on Earth off the south west of Australia. The occurrence of this feature on a variety of scales and latitudes across these three terrestrial planets (albeit in the field data rather than in crustal magnetisation) is perhaps suggestive of source bodies magnetised in a similar way.

The similarity of the results from minimum RMS magnetisation modelling is also evident in the structures seen in the inclination and declination calculated from the component magnetisations (Figure 7.7). Despite being magnetised in a dipolar dynamo field, the terrestrial magnetisation directions from the magnetisation model of Whaler and Purucker (2010) are not parallel or antiparallel to a dipole field aligned close to the rotation axis. Inclinations stripe from -90° to +90° over magnetic anomalies at all latitudes, with declinations sweeping from -180° to +180° at these same locations, as observed for the Moon. This 'striping' and 'sweeping' is observed in the inclinations and declinations calculated for Mars, though is less obvious with the colour scale in figure 7.7B.

7.6 Suggestions for future work

The lack of confidence in the magnetisation directions in these models and inconclusive estimates of thicknesses and depths means that is has not been possible to directly address some of the key issues surrounding lunar magnetism, namely the magnetised sources and the origin of the magnetising fields. Suggestions for further work to address some of these short comings and extend the work in this study are:

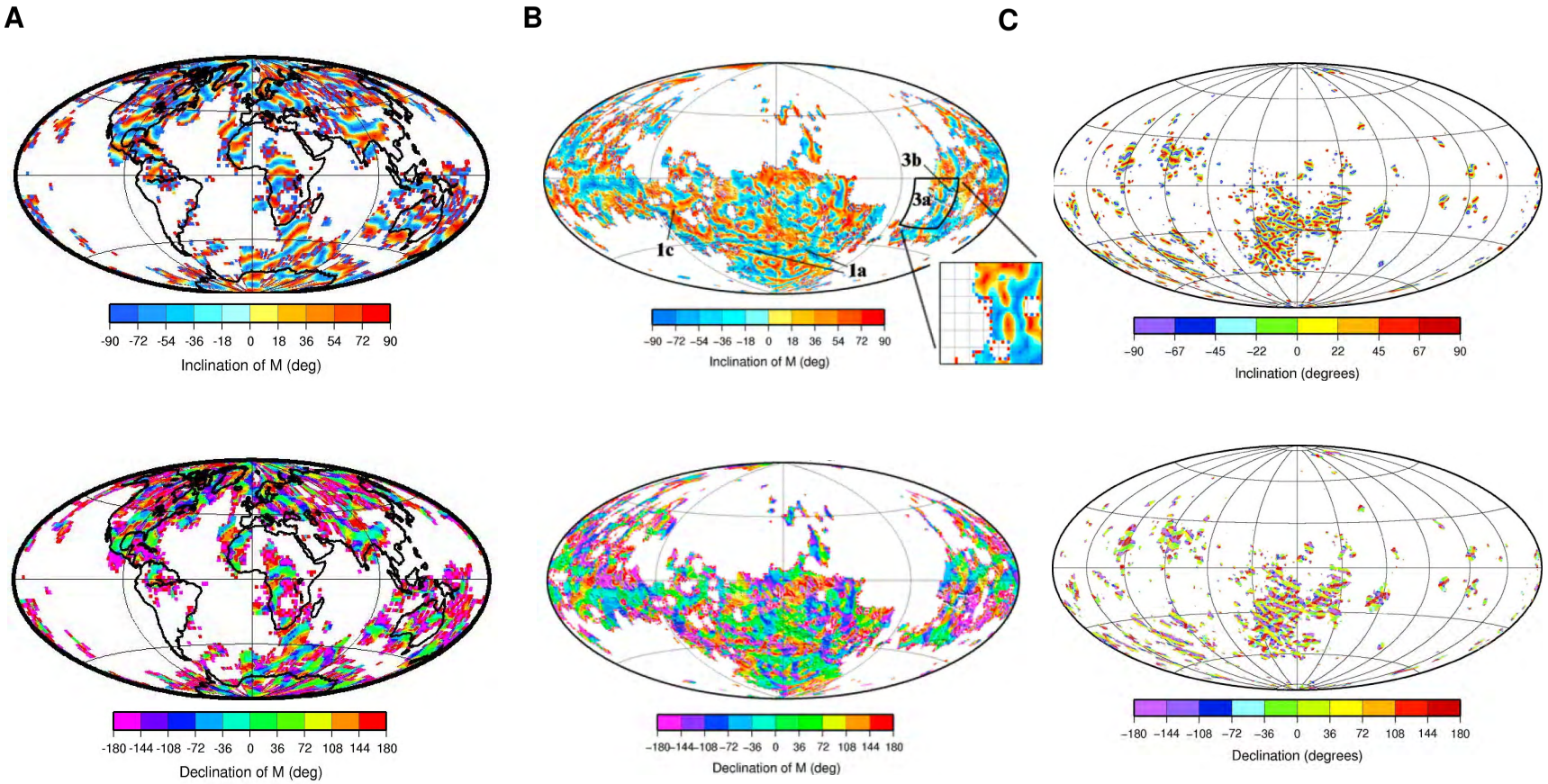

Figure 7.7: Inclinations (top) and declinations (bottom) of magnetisation direction relating to the magnetisation components in figure 7.6 (where the strength of magnetisation is sufficient for the angle to be defined) for A: Earth's continents (from Whaler and Purucker (2010)), B: Mars (from Whaler and Purucker (2005)), and C: the Moon (this study).

1. Improvements of estimations of crustal magnetisation, especially directional constraints
2. Improving understanding of the magnetised sources
3. Further development of the ER and joint MAG-ER inversions
4. Making use of magnetisation models to contribute to lunar science.

7.6.1 Improving estimations of magnetisation

The magnetisation solutions for the models in this thesis are chosen to have the minimum RMS magnetisation for a given fit to the data, controlled by a damping parameter. While these solutions represent the minimum amplitude required to fit the data, the choice of minimum amplitude norm may not permit the true magnetisation direction to be represented.

It may be possible to produce a smoothly varying solution with less directional variation by minimising the spatial gradient of the solution rather than the amplitude. Smoothly varying magnetisation solutions can be produced by incorporating a minimum roughness norm constraint within the **D** matrix of equation 3.8a and the definition of the elements of the Gram matrix $\mathbf{\Gamma}$ in equation 3.8b, with the parameter λ acting as a smoothing factor (described in section 3.3.2). The use of a different norm in these inversions would test the sensitivity of the magnetisation solution to the choice of the solution norm applied as a constraint, and may provide a more meaningful magnetisation solution to these damped, minimum RMS magnetisation models.

7.6.2 Improving understanding of the sources

With the excellent coverage of the LP and Kaguya MAG data, and now new models of the internal magnetic field [Purucker and Nicholas, 2010], it is not necessarily the resolution or coverage of the crustal field measurements which is limiting the conclusions on the sources of lunar crustal magnetism (though surface

surveys such as that from a lunar rover would of course provide valuable information); rather, as in the terrestrial case also, it is the deciphering of the exact sources of the fields which is still lacking.

It would be interesting to apply some of the analysis techniques used with terrestrial aeromagnetic data utilising gradients for the lunar crustal magnetic field (see section 3.4.1). Spatial gradients for the low altitude MAG data could be calculated and used to try to provide more tractable estimates of source depth and to locate source edges. In addition, utilisation of the MAG data at their original altitudes rather than the normalised or modelled data may allow better control on the estimation of source thickness and depth, by reducing the non-uniqueness of the problem.

Ultimately, a better understanding of the magnetisation of the lunar crust will come from more lunar samples, and new geophysical data. Ground truth magnetisation directions and compositions for regions like Reiner Gamma and impact antipodes, coupled with, for example, seismic and/or radar surveys may be able to constrain the true sources of these anomalies and their magnetising fields. Re-analysis of the magnetic properties of the Apollo samples is on-going to improve the understanding of the magnetic and paleomagnetic properties of the lunar rocks. The mechanism of shock remanent magnetisation is also being studied experimentally [e.g Gattacceca et al., 2007, 2008] to assist in the interpretation of SRMs in the lunar samples.

7.6.3 Further development of the ER and joint MAG-ER inversions

With the success of the inversions with the ER data for the Reiner Gamma region, further inversions with these data can be carried out for more regions. Additional starting models could be investigated for use in the ER inversions for different regions, such as the model solution from the MAG inversion with some perturbation. The sensitivity of the ER data to the data altitude using surface topography could also be tested further.

In the case of the joint inversion, a suggestion for further work would be the reduction of the number of MAG data points used, to decrease the influence of the **G** matrix in the joint inversion matrix **J** of equation 6.15 to optimise the inversion. Difficulties in the reproduction of the ER and MAG data from the joint models may identify regions with errors in the location of the ER data points, and processes could be developed to correct this as a key anticipated use of the joint inversion.

7.6.4 Utilising crustal magnetisation models

As already mentioned, crustal magnetisation models allow prediction of the crustal field contribution to the magnetic field around the Moon at any location. A particular suggestion for the use of this is to use the field predictions from crustal field models to trace the path of electrons to the lunar surface, offering 'correction' of the locations of surface fields inferred from the ER technique. A similar method with synthetic magnetic field data was used by Halekas et al., (2010) to assess the sensitivity of the ER technique. Charged particle tracking is also useful for the study of weathering of the lunar surface [e.g Hood and Williams, 1989], and the shielding properties of the crustal fields against the solar wind. The interaction of the solar wind with the lunar crustal fields, especially their shielding properties is an area of interest for the planning of lunar bases in the near future.

Chapter 8

Concluding remarks

This thesis has presented the first global models of lunar crustal magnetisation and has successfully combined the vector MAG data and scalar ER data in an inversion to produce a magnetisation model for the Reiner Gamma region. The implications of the magnetisation models produced in this thesis can be discussed in terms of the aims of this thesis and the issues surrounding lunar magnetism.

Distribution of crustal magnetisation

The magnetisation models of this thesis, produced from inverse modelling techniques with different data sets, account well for the observed lunar crustal magnetic fields at the surface and at altitude. These models thus offer a means of representing and reproducing the lunar crustal field. It has been shown that both a regional equivalent source dipole technique and a global spatially continuous magnetisation distribution, each solving for a minimum RMS magnetisation and least squares fit to the data, give consistent solutions.

Both the equivalent source dipole and continuous models did not allow conclusive estimations of source parameters of thickness and depth. However, there was a global preference for a magnetised layer approximately 30 km thick, with thinner sources expected, and providing better fits to the data, in the Reiner Gamma region as an example.

It has not been possible to determine magnetisation directions with the modelling techniques used, but the magnitudes of magnetisation in models are robust. Models with layer thicknesses > 10 km require magnetisation magnitudes that are comparable to those measured in the Apollo samples. While such magnetisations are considered strong for lunar samples, lunar crustal magnetisation is weak compared to that at Earth and Mars.

Joint inversion with ER and MAG data

The successful joint inversion of the ER and MAG data in this thesis is a significant outcome. The inclusion of the ER data into crustal magnetisation models without any special treatment (e.g weighting) has shown that the two different magnetic field data sets of the MAG and ER at the Moon are compatible. Inversion with the MAG data alone provides minimum estimates for the magnitudes of magnetisation of source regions, and is sufficient for determining larger scale features. Inclusion of the ER data improves the magnetisation models by revealing and hinting at smaller scale magnetisation features and stronger magnetisation magnitudes, anticipated from the Apollo surface magnetometer measurements and terrestrial crustal magnetisation.

Implications for magnetising fields

Even without directions, the strengths of the magnetisations in these models can be used to discuss the origin of the magnetising fields. While not ruling out either of the two main theories, an ancient lunar dynamo or impact generated transient fields, the inferences from the magnetisation models in this thesis are not sufficient to say with any certainty which is more likely.

The magnetisation models in this thesis require magnitudes similar to those measured in the Apollo samples, suggesting that magnetising fields with strengths of a few μT (as deduced for some Apollo samples) might have been present on the

Moon. The persistence of these magnetisation strengths at depth (> 10 km) requires the magnetising field to exist in, or be able to penetrate into, the lunar crust. As transient fields generated in impacts are thought to only exist only near the surface, an internal field from a dynamo may be more consistent with the coherent magnetisation of such thick layers in these models. In addition, if the some of the magnetisation was acquired during cooling (TRM), a dynamo field is the only viable magnetising field remaining steady over long periods of time.

However, magnetisation in a dynamo field may not be able to explain all of the features of the magnetisation models. Regions of uniform magnetisation direction would be expected if the magnetising field were of dynamo origin, but the addition of smaller scale variations in the magnetisation models with the ER data, and the variations in magnetisation direction observed over small distances on the lunar surface, suggest that the directions of the magnetising fields may have varied on small spatial scales. Such small scale variation within a magnetising field may only be possible in impact generated magnetic fields.

As concluded in most other studies of the lunar magnetic fields, the observed features may not be explicable with a single theory for a magnetising field and it is likely that a variety of different processes were responsible for the magnetisation of the lunar crust as observed today. The mystery of the origin of the magnetising fields at the Moon, and the sources themselves, still remain over 40 years after their discovery.

Bibliography

Acuña, M.H., Connerney, J.E.P., Wasilewski, P., Lin, R.P., Anderson, K.A., Carlson, C.W., McFadden, J., Curtis, D.W., Réme, H., Cros, A., Médale, J.L., Sauvaud, J.A., d'Uston, C., Bauer, S.J., Cloutier, P., Mayhew, M., and Ness, N.F. (1992) Mars Observer Magnetic Fields Investigation, *Journal of Geophysical Research, Vol. 97-E5, p. 7799-7814.*

Acuña, M.H., Connerney, J.E.P., Wasilewski, P., Lin, R.P., Anderson, K.A., Carlson, C.W., McFadden, J., Curtis, D.W., Mitchell, D., Reme, H., Mazelle, C., Sauvaud, J.A.,d'Uston. C., Cros, A., Medale, J.L., Bauer, S.J., Cloutier, P., Mayhew, M., Winterhalter, D., and Ness, N.F. (1998) Magnetic Field and Plasma Observations at Mars: Initial Results of the Mars Global Surveyor Mission, *Science, Vol. 279, p. 1676-1679.*

Anderson, K.A., Lin, R.P., McGuire, R.E., and McCoy, J.E. (1975) Measurement of Lunar and Planetary Magnetic fields by reflection of low energy electrons, *Space Science Instrumentation, Vol. 1, p. 439-470.*

Anderson, K.A., Lin, R.P., McGuire, R.E., McCoy, J.E., Russell, C.T., and Coleman, P.J., Jr (1977) Linear magnetization feature associated with Rima Sirsalis, *Earth and Planetary Science Letters, Vol. 34-1, p. 141-151.*

Anderson, B.J., Acuña, M.H., Korth, H., Purucker, M.E., Johnson, C.L. Slavin, J.A., Solomon, S.C., and McNutt, R.L. (2008) The Structure of Mercury's Magnetic Field from MESSENGER's First Flyby, *Science, Vol. 321-5885, p. 82-85.*

Arkani-Hamed, J., and Boutin, D. (2003) Polar Wander of Mars: Evidence from Magnetic Anomalies, *6th International Conference on Mars, July 20-25 2003, Pasadena, California, abstract No. 3051.*

Avriel, M. (2003) Nonlinear Programming: Analysis and Methods, *Dover Publishing.*

Backus, G., Parker, R., and Constable, C. (1996) Foundation of Geomagnetism, *Cambridge University Press, UK.*

Binder, A.B. (1998) Lunar Prospector: Overview, *Science, Vol. 281-5382, p. 1475.*

Blakely, R.J. (1996) Potential Theory in Gravity and Magnetic Applications, *Cambridge University Press, UK.*

Cain, J.C., Ferguson, B.B., and Mozzoni, D. (2003) An n = 90 internal potential function of the Martian crustal magnetic field, *Journal of Geophysical Research, Vol. 108-E2, p. 2-1, doi:10.1029/2000JE001487.*

Carlson, C.W., Curtis, D.W., Paschmann, G., and Michael, W. (1982) An instrument for rapidly measuring plasma distribution functions with high resolution, *Advances in Space Research, Vol. 2-7, p. 67-70.*

Carporzen, L., Gilder, S.A., and Hart, R.J. (2005) Palaeomagnetism of the Vredefort meteorite crater and implications for craters on Mars, *Nature, Vol. 435, p.198–201.*

Chiao, L-Y., Lin, J-R., and Gung, Y-C. (2006) Crustal magnetization equivalent source model of Mars constructed from a hierarchical multiresolution inversion of the Mars Global Surveyor data, *Journal of Geophysical Research, Vol. 111-E12, doi: 10.1029/2006JE002725.*

Christensen, P.R., Morris, R.V., Lane, M.D., Bandfield, J.L., and Malin, M.C. (2001) Global mapping of Martian hematite mineral deposits: Remnants of water-driven processes on early Mars, *Journal of Geophysical Research, Vol. 106-E10, p. 23873-23886.*

Cisowski, S., Fuller, M., Rose, M.E., and Wasilewski, P.J (1973), Magnetic effects of experimental shocking of lunar soil, *Proceedings of the 4th Lunar Science Conference, Vol. 3, p.3003-3017.*

Cisowski, S.M., Fuller, M.D., Wu, Y.M., Rose, M.F., and Wasilewski, P.J. (1975) Magnetic effects of shock and their implications for magnetism of lunar samples**,** In: *Proceedings of the 6th Lunar Science Conference, Houston, Texas, Vol. 3. p. 3123-3141.*

Cohen, B.A., Swindle, T.D., and Kring, D.A. (2000) Support for the Lunar Cataclysm Hypothesis from Lunar Meteorite Impact Melt Ages, *Science, Vol. 290, p.1754-1756.*

Collinson, D.W. (1993) Magnetism of the Moon - a lunar core dynamo or impact magnetization? *Surveys in Geophysics, Vol. 14-1, p.89-118.*

Connerney, J.E.P (1981) The Magnetic field of Jupiter: A Generalized inverse Approach, *Journal of Geophysical research, Vol. 86-A9, p. 7679-7693.*

Connerney, J.E.P., Acuña, M.H., Wasilewski, P.J., Ness, N.F., Reme, H., Mazelle, C., Vignes, D., Lin, R.P., Mitchell, D.L., and Cloutier, P.A. (1999) Magnetic lineations in the ancient crust of Mars, *Science, Vol. 284-5415, p. 794-798.*

Constable, S.C., Parker, R.L., and Constable, C.G. (1987) Occam's Inversion: A practical algorithm for generating smooth models from electromagnetic sounding data, *Geophysics, Vol. 52-3, p. 289-300.*

Covington, J. (1993) Improvement of equivalent source inversion technique with a more symmetric dipole distribution model, *Physics of the Earth and Planetary Interiors, Vol. 76-3-4, p. 199-208.*

Crawford, D.A., Schultz, P.H. (1988) Laboratory observations of impact-generated magnetic fields, *Nature, Vol. 336, p. 50-52.*

de Pater, I., and Lissauer, J.J. (2001) Planetary Sciences, *Cambridge University Press, Cambridge UK.*

Dolginov, Sh.Sh., Yeroshenko, E.G., Zhuzgov, L.N., and Pyshkov, N.V. (1966) Measurements of the magnetic field in vicinity of the Moon by the artificial satellite Luna 10. Translated from: *Doklady A.N.SSSR Geofizika, Vol. 170-3, p. 574-577.*

Dunlop, D.J., and Özdemir, Ö. (1997) Rock Magnetism, Fundamentals and frontiers, Cambridge studies in Magnetism, *Cambridge University Press, UK.*

Dyal, P., and Gordon D. I. (1973) Lunar Surface Magnetometers, *IEEE Transactions on Magnetics, Vol. 9-3, p. 226-231.*

Dyal, P., and Parkin, C.W. (1972) Measurements of the lunar magnetic field interaction with the solar wind, *Nature, Vol. 236-5347, p. 381-385.*

Dyal, P., Parkin, C.W., and Sonett, C.P. (1970) Apollo 12 Magnetometer: Measurement of a Steady Magnetic Field on the Surface of the Moon, *Science, Vol. 169-3947, p. 762-764.*

Dyal, P., Parkin C.W., and Daily, W.D (1974) Magnetism and the Interior of the Moon, *Reviews of Geophysics and Space Physics, Vol. 12, p. 568-591.*

Dyment, J., and Arkani-Hamed, J. (1988) Equivalent Source Magnetic Dipoles Revisited, *Geophysical Research Letters, Vol. 25-11, p 2003-2006.*

Fowler, C.M.R. (2005) In: The Solid Earth, second edition, *Cambridge University Press UK.*

Frey, S., Halekas, J.S., Mitchell, D.L., and Lin, R.P. (2002) Cluster Analysis of Lunar Magnetism, Gravity Anomalies, and Topology, *33rd Annual Lunar and Planetary Science Conference, March, Houston, Texas, abstract No.2048.*

Fuller, M. (1974), Lunar Magnetism, *Reviews of Geophysics and Space Physics, Vol. 12, p. 23-70.*

Fuller, M. (1998) Lunar magnetism—a retrospective view of the Apollo sample magnetic studies, *Physics and Chemistry of The Earth, Vol. 23-7-8, p. 725-735.*

Fuller, M., and Cisowski, S.M (1987) Lunar Paleomagnetism. In: Geomagnetism, Volume 2 (Jacobs, J.A. ed.), *Academic Press.*

Fuller, M., and Halekas, J.S. (2008) The Role of Impact Related Shock in Lunar Magnetism, *39th Lunar and Planetary Science Conference, Houston, Texas, Abstract No.1391, p.1430.*

Garrick-Bethell, I., Weiss, B.P., Shuster, D.L., and Buz, J. (2009) Early Lunar Magnetism, *Science, Vol. 323-5912, p. 356-359.*

Gattacceca, J., Lamali, A., Rochette, P., Boustie, M., and Berthe, L. (2007) The effects of explosive-driven shocks on the natural remanent magnetization and the magnetic properties of rocks, *Physics of the Earth and Planetary Interiors, Vol. 162-1-2, p. 85-98.*

Gattacceca, J., Berthe, L., Boustie, M., Vadeboin, F., Rochette, P., and de Resseguier, T. (2008) On the efficiency of shock magnetization processes, *Physics of the Earth and Planetary Interiors, Vol. 166-1-2, p. 1-10.*

Gold, T., and Soter, S. (1976) Cometary impact and the magnetization of the moon, *Planetary and Space Science, Vol. 24, p. 45-54.*

Gubbins, D. (1983) Geomagnetic field analysis – I. Stochastic Inversion, *Geophysical Journal of the Royal Astronomical Society, Vol. 73, p. 641-652.*

Halekas, J. S. (2003) Origins of lunar crustal magnetic fields, *PhD Thesis, University of California, Berkeley*.

Halekas, J.S., Mitchell, D.L., Lin, R.P., Frey, S., Acuña, M.H., Hood, L.L., and Binder, A.B. (2000) Mapping of the Lunar magnetic field by Lunar Prospector, *31st Annual Lunar and Planetary Science Conference, Houston, Texas, abstract No.1436.*

Halekas, J.S., Mitchell, D.L., Lin, R.P., Frey, S., Hood, L.L., Acuña, M.H., and Binder, A.B. (2001) Mapping of crustal magnetic anomalies on the lunar nearside by the Lunar Prospector electron reflectometer, *Journal of Geophysical Research, Vol. 106-E11, p. 27841-27852.*

Halekas, J.S., Mitchell, D.L., Lin, R.P., Hood, L.L., Acuña, M.H., and Binder, A.B. (2002) Demagnetization signatures of lunar impact craters, Geophysical Research Letters, Vol. 29-13, p. 23-1.

Halekas, J.S., Lin, R.P., and Mitchell, D.L. (2003) Magnetic fields of lunar multi-ring impact basins, *Meteoritics and Planetary Science, Vol. 38-4, p.565-578.*

Halekas, J.S., Lillis, R.J., Lin, R.P., Manga, M., Purucker, M.E., and Carley, R.A. (2010) How strong are lunar crustal magnetic fields at the surface?: Considerations from a re-examination of the electron reflectometry technique, *Journal of Geophysical Research, Vol. 115-E3, doi: 10.1029/2009JE003516.*

Hapgood, M.A (1992) Space Physics Coordinate Transformations: A User Guide, *Planetary and Space Science, Vol. 40-5, p. 711-717.*

Harnett, E.M., and Winglee, R.M. (2003) 2.5-D fluid simulations of the solar wind interacting with multiple dipoles on the surface of the Moon, *Journal of Geophysical Research, Vol. 108-A2, doi:10.1029/2002JA009617.*

Hartmann, W.K., and Davis, D.R (1975) Satellite-sized planetesimals and lunar origin, *Icarus, Vol. 24, p. 504-515.*

Hayashida, A., Shibuya, H., Tsunakawa, H., Takahashi, F., Shimizu, H., and Matsushima, M. (2009) Quantitative comparison of lunar magnetic field observed by Kaguya and Lunar Prospector missions, *American Geophysical Union, Fall Meeting 2009, abstract #P23C-1270.*

Heiken, G. H., Vaniman, D.T., and French, B. M. (eds.) (1991), Lunar Sourcebook; a user's guide to the moon, *Cambridge University Press.*

Hemant, K., and Maus, S. (2005) Geological modelling of the new CHAMP magnetic anomaly maps using a geographical information system technique, *Journal of Geophysical Research, Vol. 110-B12, doi:10.1029/2005JB003837.*

Hemant, K., and Purucker, M.E. (2008) Magnetic Anomalies Antipodal to Large Impact Basins on the Moon, *American Geophysical Union, Fall Meeting, abstract No. GP21C-0788.*

Hiesinger, H and Head, J.W (2006) New Views of Lunar Geoscience: an Introduction and Overview. In: New Views of the Moon (Jolliff, B.L.,Wieczorek, M.A., Shearer, C.K., Neal, C.R., eds.), *p. 221–364, Mineralogical Society of America, Chantilly.*

Hood, L.L. (1986) Geophysical constraints on the lunar interior, In *Origin of the Moon* (Hartmann, W.K., Phillips, R.J., and Taylor, G.J., eds.), *p. 361–410, Lunar and Planetary Institute, Houston.*

Hood L. L. (1987) Magnetic field and remanent magnetization effecs of basin-forming impacts on the Moon. *Geophysical Research Letters, Vol. 14, p. 844–847.*

Hood, L.L (1994) Frozen fields, *Earth, Moon, and Planets, Vol. 67-1-3, p. 131-142.*

Hood, L.L., and Artemieva, N.A. (2008) Antipodal effects of lunar basin-forming impacts: Initial 3D simulations and comparisons with observations, *Icarus, Vol. 193-2, p. 485-502.*

Hood, L.L. and Huang, Z. (1991) Formation of Magnetic Anomalies Antipodal to Lunar Impact Basins: Two-Dimensional Model Calculations, *Journal of Geophysical Research, Vol. 96, p. 9837-9846.*

Hood, L.L., and Schubert, G. (1980) Lunar magnetic anomalies and surface optical properties, *Science, Vol. 208, p. 49-51.*

Hood, L.L., and Vickery, A. (1984) Magnetic field amplification and generation in hypervelocity meteoroid impacts with application to lunar paleomagnetism, *Journal of Geophysical Research, Vol. 89, p. C211 - C223.*

Hood, L.L., and Williams, C.R. (1989) The lunar swirls - Distribution and possible origins, *19th Lunar and Planetary Science Conference, Houston, Texas, p. 99-113.*

Hood, L. L., and Zakharian, A. (2001) Mapping and modelling of magnetic anomalies in the northern polar region of Mars, *Journal of Geophysical Research, Vol. 106-E7, p. 14601-14620.*

Hood, L.L., Russell, C.T., and Coleman, P.J. (Jr) (1978) The magnetization of the lunar crust as deduced from orbital surveys, *Proceedings of the 9th Lunar and Planetary Science Conference, Houston, Texas, Vol.3, p.3057-3078.*

Hood, L. L., Coleman, P.J. (Jr) Russell, C.T., and Wilhelms, D.E. (1979a) Lunar magnetic anomalies detected by the Apollo subsatellite magnetometers, *Physics of the Earth and Planetary Interiors, Vol. 20, p. 291-311.*

Hood, L.L., Coleman, P.J., and Wilhelms, D.E (1979b) The Moon: Sources of the crustal magnetic anomalies, *Science, Vol. 204, p. 53-57.*

Hood, L.L., Russell, C.T., and Coleman, P.J. (1981) Contour maps of lunar remanent magnetic fields, *Journal of Geophysical Research, Vol. 86, p. 1055-1069.*

Hood, L.L., Mitchell, D.L., Lin, R.P., Acuna, M.H., and Binder, A.B. (1999) Initial measurements of the lunar induced magnetic dipole moment using Lunar Prospector magnetometer data, *Geophysical Research Letters, Vol. 26-15, p. 2327-2330.*

Hood, L.L., Zakharian, A., Halekas, J., Mitchell, D.L., Lin, R.P., Acuña, M.H., and Binder, A.B. (2001) Initial mapping and interpretation of lunar crustal magnetic anomalies using Lunar Prospector magnetometer data *Journal of Geophysical Research, Vol. 106-E11, p.27825-27839.*

Hood P.J and McClure D.J. (1965) Gradient Measurements in Ground Magnetic Prospecting, *Geophysics, Vol. 30-3, p. 403-410.*

Housley, R.M., Grant, R.W., Paton, N.E. (1973) Origin and Characteristics of Fe metal in lunar glass welded aggregates, *Proceedings of the 4th Lunar Science Conference, Houston, Vol. 3, p. 2737-2749.*

Howe, H.C., Lin, R.P., McGuire, R.E., Anderson, K.A. (1974) Energetic electron scattering from the lunar remanent magnetic field, *Geophysical Research Letters, Vol. 1, p. 101-104.*

Hughes, C.G., Blewett, D.T., Hawke, B.R., and Richmond, N.C. (2006) Optical Maturity and Magnetic Studies of Lunar Swirls, *37th Annual Lunar and Planetary Science Conference, Houston, Texas, abstract No.1230.*

Jackson, A. (1990) Accounting for crustal magnetization in models of the core magnetic field, *Geophysical Journal International, Vol. 103, p. 657-673*.

Katanforoush, A and Shahshahani, M. (2003) Distributing points on a sphere I, *Experimental Mathematics, Vol. 12-2, p.119.*

Khan, A., and Mosegaard, K. (2002) An inquiry into the lunar interior: A nonlinear inversion of the Apollo lunar seismic data, *Journal of Geophysical Research, Volume 107-E6, p. 3-1.*

Khan, A., Mosegaard, K., and Rasmussen, K.L. (2000) A new seismic velocity model for the Moon from a Monte Carlo inversion of the Apollo lunar seismic data, *Geophysical Research Letters, Vol. 27-11, p.1591-1594.*

Khurana, K.K., Kivelson, M.G., Stevenson, D.J., Schubert, G., Russell, C.T., Walker, R.J., and Polanskey, C. (1998) Induced magnetic fields as evidence for subsurface oceans in Europa and Callisto, *Nature, Vol. 395- 6704, p. 777-780.*

Kivelson, M.G., Bargatze, L.F., Khurana, K.K., Southwood, D.J., Walker, R.J., and Coleman, P.J. (1993) Magnetic field signatures near Galileo's closest approach to Gaspra, *Science, Vol. 261-5119, p. 331 – 334.*

Konopliv, A.S., Binder, A.B., Hood, L.L., Kucinskas, A.B., Sjogren, W.L., and Williams, J.G. (1998) Improved Gravity Field of the Moon from Lunar Prospector, *Science, Vol. 281-5382, p. 1476.*

Korotev, R.L. (1994) Compositional Variation in Apollo 16 Impact-Melt Breccias and Inferences for the Geology and Bombardment History of the Central Highlands of the Moon, *Geochimica et Cosmochimica Acta, Vol. 58, p. 3931.*

Kurata, M., Tsunakawa, H., Saito, Y., Shibuya, H., Matsushima, M., and Shimizu, H. (2005) Mini-magnetosphere over the Reiner Gamma magnetic anomaly region on the Moon, *Geophysical Research Letters, Vol. 32-24, doi:10.1029/2005GL024097.*

Langel, R.A., and Hinze, W.J. (1998) The Magnetic field of the Earth's lithosphere: The satellite perspective, *Cambridge University Press, Cambridge UK.*

Langlais, B., Purucker, M.E., and Mandea, M., (2004) Crustal magnetic field of Mars, *Journal of Geophysical Research, Vol. 109-E2, doi:10.1029/2003JE002048.*

Langlais, B., Lesur, V., Purucker, M.E., Connerney, J.E.P., and Mandea, M. (2009) Crustal Magnetic Fields of Terrestrial Planets, *Space Science Reviews, Vol. 152, Numbers 1-4.*

Lawrence, K., Johnson, C., Tauxe, L., and Gee, J. (2008) Lunar paleointensity measurements: Implications for lunar magnetic evolution, *Physics of the Earth and Planetary Interiors, Vol. 168-1-2, p. 71-87.*

Lesur, V., Wardinski, I., Rother, M. and Mandea, M. (2008) GRIMM: the GFZ Reference Internal Magnetic Model based on vector satellite and observatory data. *Geophysical Journal International, Vol. 173-2, p. 382-394.*

Lin R.P., Anderson K.A., Bush R., McGuire R.E., and McCoy J.E. (1976) Lunar surface remanent magnetic fields detected by the electron reflection method. *Proceedings of the 7th Lunar Science Conference, Houston, Texas, Vol. 3, p. 2691-2703.*

Lin, R.P. (1979) High spatial resolution measurements of surface magnetic fields of the lunar frontside, *Proceedings from the 10th Lunar and Planetary Science Conference, Houston, Texas, Vol. 3, p. 2259-2264.*

Lin, R.P., Anderson K.A., and Hood L.L. (1988) Lunar surface magnetic field concentrations antipodal to young large impact basins. *Icarus, Vol. 74, p. 529–541.*

Lin, R.P., Mitchell, D.L., Curtis, D.W., Anderson K.A., Carlson, C.W., McFadden, J., Acuña, M.H., Hood L.L., and Binder. A. (1988) Lunar surface magnetic fields and their interaction with the Solar Wind: Results from Lunar Prospector. *Science, Vol. 281, p. 1480.*

Lognonné, P., Gagnepain-Beyneix, J., and Chenet, H. (2003) A new seismic model of the Moon: implications for structure, thermal evolution and formation of the Moon, *Earth and Planetary Science Letters, Vol. 211-1-2, p.27-44.*

Lorrain, P., Corson, D.R., and Lorrain, F. (1988) Electromagnetic fields and waves, *W. H. Freeman and Co, New York.*

Lowes, F.J. (1966) Mean square values on the sphere of spherical harmonic vector fields. *Journal of Geophysical Research, Vol. 71, p. 2179.*

Lucey, P.G., Taylor, G.J., and Malaret, E. (1995) Abundance and Distribution of Iron on the Moon, *Science, Vol. 268-5214, p. 1150-1153.*

Lucey, P., Korotev, R.L., Gillis, J.J., Taylor, L.A., Lawrence, D., Campbell, B.A., Elphic, R., Feldman, W., Hood, L.L., Hunten, D., Mendillo, M., Noble, S., Papike, J.J., Reedy, R.C., Lawson, S., Prettyman, T., Gasnault, O., and Maurice, S. (2006) Understanding the Lunar Surface and Space-Moon Interactions**,** In: New Views of the Moon (Jolliff, B.L.,Wieczorek, M.A., Shearer, C.K., Neal, C.R., eds.), *p. 83–219, Mineralogical Society of America, Chantilly.*

Maus, S. and Haak, V. (2003) Magnetic field annihilators: invisible magnetization at the magnetic equator, *Geophysical Journal International, Vol. 155, p. 509-513.*

Maus, S., Rother, M., Holme, R., Lühr, H., Olsen, N., and Haak, V. (2002) First scalar magnetic anomaly map from CHAMP satellite data indicates weak lithospheric field, *Geophysical Research Letters, Vol. 29-14, p. 47-1.*

Mayhew, M.A. (1979) Inversion of satellite magnetic anomaly data, *Journal of Geophysics, Vol. 45-2, p. 119-128.*

Menke, W. (1989) Geophysical data analysis: Discrete inverse theory, *International Geophysics Series, Vol. 45, Academic Press.*

Mihalov, J.D., Sonett, C.P., Binsack, J.H., Moutsoulas, M.D. (1971) Possible Fossil Lunar Magnetism Inferred from Satellite Data, *Science, Vol.171-3974, p. 892-895.*

Milbury, C., Schubert, G., Raymond, C.A., Smrekar, S.E (2008) Joint Analysis of Gravity and Magnetic Anomalies on the Moon, *NLSI Lunar Science Conference, California, abstract No. 2164.*

Miller H.G. and Singh V. (1994) Potential field tilt-a new concept for location of potential field sources, *Journal of Applied Geophysics, Vol. 32, p. 213-217.*

Mitchell, D.L., Lin, R.P., Mazelle, C., Rème, H., Cloutier, P.A., Connerney, J.E.P., Acuña, M.H., Ness, N.F. (2001) Probing Mars' crustal magnetic field and ionosphere with the MGS Electron Reflectometer, *Journal of Geophysical Research, Vol.106-E10, p. 23419-23428.*

Mitchell, D.L., Halekas, J.S., Lin, R.P., Frey, S., Hood, L.L., Acuña, M.H., and Binder, A. (2008) Global mapping of lunar crustal magnetic fields by Lunar Prospector, *Icarus, Vol. 194-2, p. 401-409.*

Moore, H.J., Hodges, C.A., and Scott, D.H. (1974) Multiringed basins - Illustrated by Orientale and associated features, *Proceedings of the 5th Lunar Science Conference, Houston, Texas, Vol. 1, p. 71-100.*

Murray, B., Malin, M.C., and Greeley, R. (1981) Earthlike planets: Surfaces of Mercury, Venus, Earth, Moon, Mars, *W. H. Freeman and Co, New York.*

Nagata, T., Ishikawa, Y., Kinoshita, H., Kono, M., Syono, Y., and Fisher, R.M. (1970) Magnetic Properties of the Lunar Crystalline Rock and Fines, *Science, Vol. 167-3918, p. 703-704.*

Nagata, T., Fisher, R.M., and Schwerer, F.C. (1972) Lunar Rock Magnetism, *The Moon, Vol. 4-1-2, p. 160-186.*

Nazarova, K.A. (1994) Serpentinized peridotites as a possible source for oceanic magnetic anomalies, *Marine Geophysical Research, Vol. 16, p. 455–462.*

Ness, N.F (1970) Magnetometers for Space Research, *Space Science Reviews, Vol. 11-4, p. 459-554.*

Ness, N.F., Behannon, K.W., Lepping, R.P., Whang, Y.C., and Schatten, K.H. (1974) Magnetic Field Observations near Mercury: Preliminary Results from Mariner 10, *Science, Vol. 185-4146, p. 151-160.*

Nicholas, J.B., Purucker, M.E., and Sabaka, T.J. (2007) Age spot or youthful marking: Origin of Reiner Gamma, *Geophysical Research Letters, Vol. 34-2.*

Nicolosi, I., Blanco-Montenegro, I., Pignatelli, A., and Chiappini, M. (2006) Estimating the magnetization direction of crustal structures by means of an equivalent source algorithm, *Physics of the Earth and Planetary Interiors, Vol. 155-1-2, p. 163-169.*

Ono, T., Kumamoto, A., Nakagawa, H., Yamaguchi, Y., Oshigami, S., Yamaji, A., Kobayashi, T., Kasahara, Y., and Oya, H. (2009) Lunar Radar Sounder Observations of Subsurface Layers Under the Nearside Maria of the Moon, *Science, Vol. 323-5916, p. 909-912.*

Parker, R.L. (1971) The determination of seamount magnetism, *Geophysical Journal International, Vol. 24-4, p. 321-324.*

Parker, R.L. (2003) Ideal bodies for Mars magnetics, *Journal of Geophysical Research, Vol.108-E1, p. 6-1, doi:10.1029/2001JE001760.*

Parker, R. L., Shure, L., and Hildebrand, J. (1987) The application of inverse theory to seamount magnetism, *Reviews of Geophysics and Space Physics, Vol. 25, p.17.*

Peeples, W.J., Sill, W.R., May, T.W., Ward, S.H., Phillips, R.J., Jordan, R.L., Abbott, E.A., and Killpack, T.J. (1978) Orbital radar evidence for lunar subsurface layering in Maria Serenitatis and Crisium, *Journal of Geophysical Research, Vol. 83, p. 3459-3468.*

Pilkington, M. and Grieve, R.A.F. (1992) The geophysical signature of terrestrial impact craters, *Reviews of Geophysics, Vol. 30-2, p. 161-181.*

Press, W.H., Teukolsky, S.A., Vetterling, W.T., and Flannery, B.P. (1992) Numerical Recipes in Fortran, *Second edition, Cambridge University Press, UK.*

Purucker, M.E., and Nicholas, J.B. (2010) Global spherical harmonic models of the internal magnetic field of the Moon based on sequential and coestimation approaches, *Journal of Geophysical Research, Vol. 115-E12, doi:10.1029/2010JE003650.*

Purucker, M.E. (2008) A global model of the internal magnetic field of the Moon based on Lunar Prospector magnetometer observations, *Icarus, Vol. 197-1, p. 19-23.*

Purucker, M. E., and Whaler, K.A. (2007), Crustal Magnetism, In: Geomagnetism, Volume 5 (Kono, M., ed.), *Elsevier Treatise on Geophysics.*

Purucker, M.E., Sabaka, T.J., and Langel, R.A. (1996) Conjugate gradient analysis: A new tool for studying satellite magnetic data sets, *Geophysical Research Letters, Vol. 23, p. 507-510.*

Purucker, M.E., Ravat, D., Frey, H., Voorhies, C., Sabaka, T., and Acuña, M. (2000) An altitude-normalized magnetic map of Mars and its interpretation, *Geophysical Research Letters, Vol. 27-16, p. 2449-2452.*

Purucker, M.E., Sabaka, T.J., Halekas, J.S., Olsen, N., Tsyganenko, N., and Hood, L.L. (2006) The Lunar Magnetic Field Environment: Interpretation of new maps of the Internal and external fields, *37th Annual Lunar and Planetary Science Conference, Houston, Texas, abstract No.1933.*

Quesnel, Y., Langlais, B., and Sotin, C. (2007) Local inversion of magnetic anomalies: Implication for Mars' crustal evolution, *Planetary and Space Science, Vol. 55-3, p. 258-269.*

Ravat, D. (2006) Uncertainty in magnetization directions derived from planetary magnetic anomalies in view of numerical experiments with coalesced anomalies from Earth, *American Geophysical Union, Fall Meeting, abstract No. GP11B-0076.*

Reid, A. B., Allsop, J.M., Granser, H., Millet, A.J., and Somerton, I.W. (1990) Magnetic interpretation in three dimensions using Euler deconvolution, *Geophysics, Vol. 55, p. 80–91.*

Richmond, N.C., and Hood, L.L. (2008) A preliminary global map of the vector lunar crustal magnetic field based on Lunar Prospector magnetometer data, *Journal of Geophysical Research, Vol.113-E2, doi:10.1029/2007JE002933.*

Richmond, N.C., Hood, L.L., Halekas, J.S., Mitchell, D.L., Lin, R.P., Acuña, M., and Binder, A.B. (2003) Correlation of a strong lunar magnetic anomaly with a high-albedo region of the Descartes mountains, *Geophysical Research Letters, Vol. 30-7, p. 48-1.*

Richmond, N.C., Hood, L.L., Mitchell, D.L., Lin, R.P., Acuña, M.H., and Binder, A.B. (2005) Correlations between magnetic anomalies and surface geology antipodal to lunar impact basins, *Journal of Geophysical Research, Vol.110-E5, doi:2005JGRE..11005011R.*

Richter, I., Brinza, D.E., Cassel, M., Glassmeier, K.-H., Kuhnke, F., Musmann, G., Othmer, C., Schwingenschuh, K., and Tsurutani, B.T. (2001) First direct magnetic field measurements of an asteroidal magnetic field: DS1 at Braille. *Geophysical Research Letters, Vol. 28-10, p.1913-1916.*

Roberts, J.H., Lillis, R.J., and Manga, M. (2009) Giant impacts on early Mars and the cessation of the Martian dynamo, *Journal of Geophysical Research, Vol. 114-E4, doi:10.1029/2008JE003287.*

Rochette, P., Gattacceca, J., Chevrier, V., Hoffmann, V., Lorand, J.P., Funaki, M., Hochleitner, R. (2005) Matching Martian crustal magnetization and meteorite magnetic properties, *Meteoritics and Planetary Science, Vol. 40, p. 529–540.*

Runcorn, S.K. (1975) On the interpretation of Lunar magnetism, *Physics of the Earth Planetary Interiors, Vol. 10, p.37-335.*

Runcorn, S.K. (1980) Lunar polar wandering, *Proceedings of 11th the Lunar and Planetary Science Conference, Houston, Texas, Vol. 3, p. 1867-1877.*

Runcorn, S.K., Collinson, D.W., O'Reilly, W., Stephenson, A., Greenwood, N.N., Battey, M.H. (1970) Magnetic Properties of Lunar Samples, *Science, Vol. 167-3918, p. 697-699.*

Russell, C.T. (1993) Magnetic fields of the terrestrial planets, *Journal of Geophysical Research, Vol. 98-E10, p. 18,681-18,695.*

Russell, C.T., and Lichtenstein, B.R. (1975) On the source of lunar limb compressions, *Journal of Geophysical Research, Vol. 80, p. 4700-4711.*

Russell, C.T, Coleman, P.J. (Jr), and Schubert, G. (1977) On deducing the magnetization of the lunar surface from orbital surveys, *Physics of the Earth and Planetary interiors, Vol. 13, 386-390.*

Sabaka, T.J., Olsen, N., and Purucker, M.E. (2004) Extending Comprehensive Models of the Earth's magnetic field with Orsted and CHAMP data, *Geophysical Journal International, Vol. 159, p.521-547.*

Salem, A., Williams, S., Fairhead, D., Smith, R., and Ravat, D. (2008) Interpretation of magnetic data using tilt-angle derivatives, *Geophysics, Vol. 73-1.*

Schaler, E.W., and Purucker, M.E. (2007) Lunar south pole hydrogen and water ice deposits: Constraints from lunar prospector magnetic field observations, *38th Lunar and Planetary Science Conference, Houston, Texas, abstract No.1034.*

Schultz, P.H. and Gault, D.E. (1975) Seismic effects from major basin formations on the moon and Mercury, *The Moon, Vol. 12, p. 159-177.*

Schultz, P.H., and Srnka, L.J. (1980) Cometary collisions on the moon and Mercury, Cometary collisions on the moon and Mercury, *Nature, Vol. 284, p. 22-26.*

Shure, L., Parker, R.L., and Backus, G.E. (1982) Harmonic Splines for geomagnetic modelling. *Physics of the earth and planetary interiors, Vol. 28, p.215-229.*

Sonett, C.P. (1982) Electromagnetic induction in the Moon. *Reviews of Geophysics and Space Physics, Vol. 20, p. 411–456.*

Srnka, L.J. (1977) Spontaneous magnetic field generation in hypervelocity impacts, *Proceedings of the 8th Lunar Science Conference, p. 792–795.*

Srnka, L.J., Hoyt, J.L., Harvey, J.V.S., and McCoy, J.E. (1979) A study of the Rima Sirsalis lunar magnetic anomaly, *Physics of the Earth and Planetary Interiors, Vol. 20, p. 281-290.*

Stacey, F.D and Lovering, J.E. (1959) Natural Magnetic Moments of Two Chondritic Meteorites, *Nature, Vol. 183-4660, p. 529-530.*

Starukhina, L.V., and Shkuratov, Y.G. (2004) Swirls on the Moon and Mercury: meteoroid swarm encounters as a formation mechanism, *Icarus, Vol. 167-1, p. 136-147.*

Stavrev, P., Gerovska, D., and Araúzo-Bravo, M. J. (2009) Depth and shape estimates from simultaneous inversion of magnetic fields and their gradient components using differential similarity transforms, *Geophysical Prospecting, Vol. 57-4, p. 707-717.*

Stegman, D.R., Jellinek, A.M, Zatman, S.A, Baumgarder, J.R, and Richards, M.A. (2003), An early lunar core dynamo driven by thermochemical mantle convection, *Nature, Vol. 421, p. 143-146.*

Stern, D.P (1976) Representation of magnetic fields in space, *Reviews of Geophysics and Space Physics, Vol. 14, p. 199-214.*

Stevenson, D.J. (1983) Planetary magnetic fields, *Reports on Progress in Physics, Vol. 46, May 1983, p. 555-620.*

Stevenson, D.J. (2001) Mars' core and magnetism, *Nature, Vol. 412-6843, p. 214-219.*

Stevenson, D.J. (2003) Planetary magnetic fields, *Earth and Planetary Science Letters, Vol. 208-1-2, p. 1-11.*

Strangway, D.W., Gose, W.A., Pearce, G.W., and Carnes, J.G. (1973a) Magnetism and the History of the Moon, In Magnetism and Magnetic Minerals - 1972 (Graham, C.D. (Jr) and Rhyne, J.J. eds.), *American Institute of Physics, New York, pp. 1178-1187.*

Strangway D.W., Gose W., and McConnell R.K. (1973b) Lunar magnetic anomalies and the Cayley Formation, *Nature, Vol. 246, p. 112-114.*

Toyoshima, M. Shibuya, H. Matsushima, M. Shimizu, H. and Tsunakawa, H. (2008) Equivalent source mapping of the lunar crustal magnetic field using ABIC, *Earth, Planets and Space, Vol. 60, p. 365-373.*

Tsunakawa, H., Shibuya, H., Takahashi, F., Shimizu, H., Matsushima, M., Matsuoka, A., Nakazawa, S., Otake, H., and Iijima, Y. (2010) Lunar Magnetic Field Observation and Initial Global Mapping of Lunar Magnetic Anomalies by MAP-LMAG Onboard SELENE (Kaguya), *Space Science Reviews (May 2010), p. 1-33-33.*

van de Moortèle, B., Reynard, B., Rochette, P., Jackson, M., Beck, P., Gillet, P., McMillan, P.F., and McCammon, C.A. (2007) Shock-induced metallic iron nanoparticles on olivine-rich Martian meteorites, *Earth and Planetary Science Letters, Vol. 262-1-1, p.37-49.*

Vine, F. J., and Matthews, D.H. (1963) Magnetic anomalies over ocean ridges, *Nature*, *Vol. 199, p. 947-949.*

Von Frese, R.R.B., Hinze, W.J., and Braile, L.W. (1981) Spherical Earth gravity and magnetic anomaly analysis by equivalent point source inversion, *Earth and Planetary Science Letters, Vol. 53, p. 69-83*

Voorhies, C. V., Sabaka, T. J., and Purucker, M.E. (2002) On magnetic spectra of Earth and Mars, *Journal of Geophysical Research, Vol.107-E6, p. 1-1, doi:10.1029/2001 JE001534*

Walker, M. R., and Jackson, A. (2000) Robust modelling of the Earth's magnetic field, *Geophysical Journal International, Vol.143-3, p. 799-808.*

Wasilewski, P., and Mayhew, M.A., (1982) Crustal xenolith magnetic properties and long wavelength anomaly source requirements, *Geophysical Research Letters, Vol. 9-4, p. 329-332.*

Wasilewski, P. J., Thomas, H. H., and Mayhew, M. A. (1979) The Moho as a magnetic boundary, *Geophysical Research Letters, Vol. 6, p. 541-544.*

Wessel, P., and Smith, W. H. F. (1998) New, improved version of generic mapping tools released, *Eos, Transactions American Geophysical Union, Vol. 79-47, p. 579-579.*

Whaler, K.A. (1994) Downward continuation of Magsat lithospheric anomalies to the Earth's surface, *Geophysical Journal International, Vol. 116-2, p. 267-278.*

Whaler, K.A., and Langel, R.A. (1996) Minimal crustal magnetizations from satellite data, *Physics of the Earth and Planetary Interiors Vol. 98, p.303-319.*

Whaler, K.A., and Purucker, M.E. (2005) A spatially continuous magnetization model for Mars, *Journal of Geophysical Research, Vol. 110, doi:10.1029/2004JE002393.*

Whaler, K.A. and Purucker, M.E. (2010) Magnetization models derived from high resolution satellite lithospheric anomaly fields, In: *Proceedings of ESA's Second Swarm International Science Meeting,* (http://www.congrex.nl/09c24/S2_Posters/S2_P10_Whaler_paper.pdf)

Wieczorek, M. A., and Weiss, B.P. (2010) Testing the Lunar Dynamo Hypothesis Using Global Magnetic Field Data, *41st Lunar and Planetary Science Conference, Houston, Texas, abstract No. 1625.*

Wieczorek, M.A., Jolliff, B.L., Khan, A., Pritchard, M.E., Weiss, B.P.,Williams, J.G., Hood, L.L., Righter, K., Neal, C.R., Shearer, C.K., Mc-Callum, I.S., Tompkins, S., Hawke, B.R., Peterson, C., Gillis, J.J., and Bussey, B., (2006) The constitution and structure of the lunar interior. In: New Views of the Moon (Jolliff, B.L.,Wieczorek, M.A., Shearer, C.K., Neal, C.R., eds.), *p. 221–364, Mineralogical Society of America, Chantilly.*

Williams, J.G., Boggs, D.H., Yoder, C.F., Ratcliff, J.T., and Dickey, J.O. (2001) Lunar rotational dissipation in solid body and molten core, *Journal of Geophysical Research, Vol.106-E11, p. 27933-27968.*